

# **Dissertation**

submitted to the  
Combined Faculty of Mathematics, Engineering and Natural Sciences  
of the Ruperto-Carola University of Heidelberg, Germany  
for the degree of

**Doctor of Natural Sciences**

Put forward by

**Philip Sebastian Boyd**

born in: Ludwigsburg, Germany

Oral examination: June 29th, 2022



**Mapping intracellular pH of tumors in vivo  
using CEST-MRI:  
methodological development and preclinical investigation**

Referees: Prof. Dr. Peter Bachert

Prof. Dr. Michael Hausmann



**Mapping intracellular pH of tumors in vivo  
using CEST-MRI:  
methodological development and preclinical investigation**

Chemical exchange saturation transfer (CEST) magnetic resonance imaging (MRI) allows to non-invasively obtain information about the micromolecular environment of living tissues, particularly, intracellular pH ( $\text{pH}_i$ ). In this thesis, a method for quantitative CEST-based  $\text{pH}_i$  mapping was developed enabling, for the first time, compensation of all concomitant effects on CEST signals in tumor tissues, such as unknown concentration changes and superimposing contributions.

To this end, a novel model was established enabling direct translation of magnetization exchange rates between protons in proteins and water into pH. This model utilizes (i) the reliable extraction of exchange rates, accomplished by an optimized isolation of measured CEST signals at  $B_0 = 9.4$  T, and (ii) a calibration procedure exploiting a newly identified, distinct functional behavior of CEST signals. Porcine brain lysates mimicking in vivo conditions were employed for calibration and to demonstrate reliable pH mapping in the physiologically relevant range of 6.2–8.0. Application in vivo to lesions of tumor-bearing mice showed a median  $\text{pH}_i$  of approximately 7.2, further validating the developed method. This novel approach, now, allows to robustly assess the potential of  $\text{pH}_i$  as imaging biomarker for cancer diagnosis or treatment monitoring in preclinical settings, representing an important milestone towards application in humans.



**Bildgebung des intrazellulären pH in Tumoren in vivo  
mittels CEST-MRT:  
methodische Entwicklung und präklinische Untersuchung**

Die Chemical Exchange Saturation Transfer (CEST) Magnetresonanztomographie (MRT) ermöglicht es nicht-invasiv Informationen über das mikromolekulare Umfeld in lebenden Geweben zu erhalten, insbesondere, über den intrazellulären pH-Wert ( $\text{pH}_i$ ). In dieser Arbeit wurde eine Methode zur quantitativen CEST-basierten  $\text{pH}_i$ -Bildgebung entwickelt, welche erstmalig alle auftretenden Effekte auf CEST-Signale in Tumorgeweben gleichzeitig kompensiert, wie beispielsweise unbekannte Konzentrationsänderungen und überlagerte Signalbeiträge.

Zu diesem Zweck wurde ein neues Modell entwickelt, welches es ermöglicht die Magnetisierungsaustauschraten zwischen Proteinprotonen und Wasserprotonen direkt in pH-Werte umzuwandeln. Dieses Modell nutzt hierfür (i) die zuverlässige Bestimmung von Austauschraten, welche durch eine optimierte Isolierung gemessener CEST-Signale bei  $B_0 = 9,4 \text{ T}$  ermöglicht wurde, und (ii) ein Kalibrierungsverfahren, das auf einer neu identifizierten funktionalen Abhängigkeit von CEST-Signalen beruht. Um die Gegebenheiten in vivo nachzuahmen wurde die Kalibrierung in Schweinehirnlysaten durchgeführt. Zudem konnte in Schweinehirnlysaten eine zuverlässige pH-Bildgebung im physiologisch relevanten Bereich von 6,2–8,0 gezeigt werden. Angewendet auf Läsionen tumortragender Mäuse wurde ein  $\text{pH}_i$ -Median von ungefähr 7,2 ermittelt, was die Anwendbarkeit der entwickelten Methode in vivo weiter bekräftigt. Mit diesem neuen Ansatz kann nun das Potential des  $\text{pH}_i$  als Bildgebungsbiomarker in der Krebsdiagnose oder Krebstherapieüberwachung im präklinischen Rahmen robust erprobt werden, was einen bedeutenden Meilenstein zur Anwendung im Menschen darstellt.



# Contents

<b>List of Abbreviations</b>	<b>v</b>
<b>1 Introduction</b>	<b>1</b>
<b>2 Fundamental Principles</b>	<b>7</b>
2.1 Nuclear magnetic resonance . . . . .	7
2.1.1 Nuclear spin and Zeeman effect . . . . .	7
2.1.2 Macroscopic magnetization . . . . .	9
2.1.3 Time evolution, relaxation and Bloch equations . . . . .	12
2.1.4 MR signal . . . . .	16
2.1.5 Chemical shift . . . . .	18
2.2 Magnetic resonance imaging . . . . .	20
2.2.1 Spatial encoding . . . . .	20
2.2.2 Imaging pulse sequences . . . . .	23
2.3 Magnetization transfer . . . . .	25
2.3.1 Chemical exchange . . . . .	26
2.3.2 Exchange-relayed nuclear Overhauser effect . . . . .	28
2.3.3 Semi-solid magnetization transfer . . . . .	28
2.4 Chemical exchange saturation transfer . . . . .	30
2.4.1 Saturation transfer . . . . .	31
2.4.2 The Z-spectrum . . . . .	32
2.4.3 Endogenous CEST signals . . . . .	33
2.4.4 The CEST pulse sequence . . . . .	34
2.5 Theory of saturation transfer and quantitative CEST . . . . .	36
2.5.1 Pool model . . . . .	36
2.5.2 Bloch McConnell equations . . . . .	36
2.5.3 Analytical solution of the Bloch McConnell equations . . . . .	38
2.5.4 CEST contrasts . . . . .	41
2.6 The pH value . . . . .	42

<b>3</b>	<b>A novel model enabling quantitative CEST-based pH mapping</b>	<b>47</b>
3.1	Principle of pH mapping using the amide or the guanidyl signal . . . . .	47
3.2	Calibration of the exchange rate characterizing constant $k_c$ . . . . .	49
3.3	Symmetry of $MTR_{\text{Rex}}$ as a function of pH . . . . .	51
3.4	Extraction of exchange rates $k_{\text{ex}}$ . . . . .	52
3.4.1	The power ratiometric approach ( $\text{CEST}_{\text{ratio}}$ ) . . . . .	53
3.4.2	A robust $MTR_{\text{Rex}}$ -based contrast- $B_1$ -correction approach . . . . .	54
3.5	On the pH sensitivity of CEST signals . . . . .	56
3.6	Reliable pH mapping using a combination of the amide and guanidyl signals	59
<b>4</b>	<b>Materials and Methods</b>	<b>63</b>
4.1	MR imaging system and experimental setup . . . . .	63
4.1.1	MR scanner . . . . .	63
4.1.2	RF coils . . . . .	63
4.1.3	Heating system . . . . .	64
4.1.4	Preparation of examinations . . . . .	65
4.2	Model systems . . . . .	66
4.2.1	Porcine brain lysates . . . . .	68
4.2.2	Creatine model solutions . . . . .	70
4.2.3	Tumor-bearing mice . . . . .	71
4.3	Data acquisition . . . . .	73
4.3.1	CEST pulse sequence, mean $B_1$ and presaturation pulse shape $c_c$ .	73
4.3.2	The CEST-MRI data set . . . . .	74
4.3.3	Image readout . . . . .	74
4.3.4	MR data acquisition protocol . . . . .	76
4.4	Data processing and evaluation . . . . .	77
4.4.1	$B_0$ and $B_1$ field mapping . . . . .	78
4.4.2	CEST data post-processing and pH mapping workflow . . . . .	79
4.4.3	Calibration of $k_c$ . . . . .	88
<b>5</b>	<b>Results</b>	<b>91</b>
5.1	In vitro validation using porcine brain lysates . . . . .	91
5.1.1	Extraction of pH-dependent signals from background . . . . .	94
5.1.2	Calibration of $k_c$ for the amide and guanidyl signal . . . . .	98
5.1.3	pH mapping . . . . .	100

5.2	In vivo application . . . . .	107
5.2.1	Prerequisites for a robust and reliable pH <sub>i</sub> mapping in vivo . . . . .	108
5.2.2	pH <sub>i</sub> mapping in tumor-bearing mice . . . . .	112
5.3	Transfer to pulsed CEST . . . . .	118
<b>6</b>	<b>Discussion</b>	<b>123</b>
6.1	Isolation of pH-dependent signal contributions from concomitant effects . . . . .	123
6.1.1	Extraction of pH-dependent signals from Z-spectra . . . . .	124
6.1.2	Concentration independence . . . . .	127
6.2	A novel model using a single k <sub>c</sub> describing one CEST pool . . . . .	128
6.2.1	Underlying assumptions . . . . .	128
6.2.2	Sensitivity towards pH <sub>i</sub> . . . . .	129
6.2.3	Describing the amide and guanidyl signals with one k <sub>c</sub> each . . . . .	129
6.2.4	Transferability of in vitro-calibrated k <sub>c</sub> for examinations in vivo . . . . .	130
6.2.5	Influence of temperature . . . . .	131
6.2.6	The sensitivity of the pH <sub>combi</sub> approach . . . . .	132
6.2.7	Further applications . . . . .	133
6.3	Remaining challenges . . . . .	134
6.4	Towards application in humans . . . . .	136
6.4.1	Further evaluation of using a pulsed presaturation . . . . .	136
6.4.2	pH <sub>i</sub> mapping in humans . . . . .	137
<b>7</b>	<b>Summary and Conclusion</b>	<b>139</b>
<b>A</b>	<b>Appendix</b>	<b>I</b>
A.1	Measurement of labile proton fraction $f_s$ . . . . .	I
A.1.1	Quantification for one CEST pool . . . . .	I
A.1.2	Ratio between two CEST pools . . . . .	II
A.2	Complete lists of frequency offsets for sampling of Z-spectra . . . . .	II
A.3	Complete lists of simulation parameters used in Figures . . . . .	III
	<b>List of Figures</b>	<b>V</b>
	<b>List of Tables</b>	<b>VII</b>
	<b>Bibliography</b>	<b>IX</b>

*Contents*

<b>List of Scientific Contributions</b>	<b>XXIX</b>
<b>Acknowledgements   Danksagung</b>	<b>XXXIII</b>
<b>Declaration   Erklärung</b>	<b>XXXV</b>

## List of Abbreviations

$\alpha$	labeling efficiency
$\gamma$	gyromagnetic ratio (for $^1\text{H}$ in water, $\frac{\gamma}{2\pi} = 42,576 \frac{\text{MHz}}{\text{T}}$ )
$\delta\omega_s$	CS between labile and water protons [ppm]
$\Delta\omega$	frequency offset (to water resonance)
$\Delta B_0$	$B_0$ field inhomogeneities
$\Delta B_1$	$B_1$ field inhomogeneities
$\omega_0$	Larmor frequency ( $\omega_0 = \gamma B_0$ )
$\omega_1$	Rabi frequency given by RF amplitude ( $\omega_1 = \gamma B_1$ )
$\vec{B}_0$	static magnetic field
$\vec{B}_1$	RF excitation field
$\vec{B}_{eff}$	effective magnetic field in the rotating frame
$f_s$	relative proton fraction (labile to water proton ratio)
$M$	magnetization
$M_0$	thermal equilibrium magnetization
$M_{sat}$	magnetization after presaturation
$R_1$	longitudinal relaxation rate
$R_{1\rho}$	longitudinal relaxation rate in the rotating frame
$R_2$	transversal relaxation rate
$R_{2s}$	transversal relaxation rate of solute pool
$R_{eff}$	water relaxation rate in the rotating frame
$R_{ex}$	exchange-dependent relaxation rate in the rotating frame
$s$	solute pool (labile protons of CEST pool)
$T_1$	longitudinal relaxation time

## Contents

$T_2$	transversal relaxation time
$t_d$	delay time
$t_p$	pulse duration
$t_{rec}$	recovery time
$t_{sat}$	saturation duration
$w$	water pool (abundant free water protons)
$w_{amide}$	weightings of $pH_{amide}$ used for calculation of $pH_{combi}$
$w_{gua}$	weightings of $pH_{gua}$ used for calculation of $pH_{combi}$
$^1H$	atomic nucleus of hydrogen (proton)
<b>ADC</b>	analog to digital converter
<b><math>B_0</math></b>	static magnetic field strength
<b><math>B_1</math></b>	RF amplitude
<b>BM</b>	Bloch McConnell equations
<b>BW</b>	band width
<b><math>c_1</math></b>	form factor for pulsed CEST encompassing the intra-pulse DC
<b><math>c_2</math></b>	form factor for pulsed CEST encompassing the presaturation pulse shape
<b>CA</b>	contrast agent
<b>CE</b>	chemical exchange
<b>CESL</b>	chemical exchange-sensitive spin lock
<b>CEST</b>	chemical exchange saturation transfer
<b>CEST<sub>ratio</sub></b>	ratio of the same CEST signal at two different $B_1$
<b>CS</b>	chemical shift
<b>CT</b>	X-ray computed tomography
<b>cw</b>	continuous wave
<b>DC</b>	duty cycle ( $DC = t_p / (t_p + t_d)$ )
<b>DICOM</b>	digital imaging and communications in medicine
<b>DKFZ</b>	Deutsches Krebsforschungszentrum (German Cancer Research Center)
<b>DS</b>	direct water saturation

<b>DWI</b>	diffusion weighted imaging
<b>FA</b>	flip angle
<b>FE</b>	frequency encoding
<b>FID</b>	free induction decay
<b>FISP</b>	fast imaging with steady state precession
<b>fMRI</b>	functional magnetic resonance imaging
<b>FOV</b>	field of view
<b>FS</b>	full saturation limit ( $\delta\omega_s \gg \omega_1 \gg k_{ex} + R_{2s}$ at label scan)
<b>FT</b>	Fourier transform
<b>FWHM</b>	full width at half maximum
<b>GRE</b>	gradient echo, or gradient-recalled echo
<b><math>k_c</math></b>	exchange rate characterizing constant at a fixed temperature
<b><math>k_{ex}</math></b>	exchange rate (solute to water)
<b>LS</b>	large-shift limit ( $\delta\omega_s \gg \omega_1$ at label scan)
<b>MITK</b>	medical imaging interaction toolkit
<b>MR</b>	magnetic resonance
<b>MRI</b>	magnetic resonance imaging
<b>MRS</b>	magnetic resonance spectroscopy
<b>MRSI</b>	magnetic resonance spectroscopic imaging
<b>MRT</b>	Magnetresonanztomographie
<b>MT</b>	magnetization transfer
<b>MTC</b>	magnetization transfer contrast (contrast arising from ssMT)
<b>MTR</b>	magnetization transfer ratio
<b><math>MTR_{Rex}</math></b>	inverse metric yielding $R_{ex}$ (relaxation-compensated   spillover-corrected)
<b>NMR</b>	nuclear magnetic resonance
<b>NMRS</b>	nuclear magnetic resonance spectroscopy
<b>NOE</b>	nuclear Overhauser effect
<b>PBS</b>	phosphate-buffered saline

## Contents

<b>PE</b>	phase encoding
<b>PET</b>	positron emission tomography
<b>pH</b>	<i>potential of hydrogen</i> (measure to specify the acidity and basicity of aqueous solutions)
<b>pH<sub>amide</sub></b>	pH calculated from the amide proton CEST signal
<b>pH<sub>combi</sub></b>	pH calculated from weighted combination of pH <sub>amide</sub> and pH <sub>gua</sub>
<b>pH<sub>e</sub></b>	extracellular pH
<b>pH<sub>gua</sub></b>	pH calculated from the guanidyl proton CEST signal
<b>pH<sub>i</sub></b>	intracellular pH
<b>pH<sub>max</sub></b>	position of the maximum of MTR <sub>ReX</sub> (pH)
<b>pH<sub>titrated</sub></b>	titrated pH measured with a pH meter
<b>PTE</b>	proton transfer enhancement
<b>QUESP</b>	quantification of exchange rate using varying saturation power
<b>RARE</b>	rapid acquisition with relaxation enhancement
<b>RF</b>	radio frequency
<b>RMS</b>	root mean square
<b>rNOE</b>	exchange-relayed NOE
<b>ROI</b>	region of interest
<b>SAR</b>	specific absorption rate
<b>SNR</b>	signal-to-noise ratio
<b>SD</b>	spillover dilution
<b>SE</b>	spin echo
<b>SL</b>	spin lock
<b>ssMT</b>	semi solid MT
<b>STD</b>	standard deviation
<b>TE</b>	echo time
<b>TMS</b>	tetramethylsilane
<b>TR</b>	repetition time

<b>tSNR</b>	temporal signal-to-noise ratio
<b>UHF</b>	ultra-high field strength
<b>RF</b>	radio frequency
<b>WASABI</b>	water shift and $B_1$ mapping (simultaneous $B_0$ and $B_1$ field mapping method)
<b>wlog</b>	without loss of generality
<b>Z</b>	Z-spectrum signal, i.e. normalized $z$ -magnetization after saturation ( $Z = M_{sat} / M_0$ )
<b>Z<sub>lab</sub></b>	Z value of the label pool (pool of interest)
<b>Z<sub>ref</sub></b>	Z value of the reference (all other pools without the pool of interest)



# 1 Introduction

The foundation of the experimentally detected nuclear magnetic resonance (NMR) lies in the postulation of a quantum mechanical phenomenon – the nuclear spin – and its subsequent discovery in the 1920s. In 1938, Isidor I. Rabi et al. unveiled and described the phenomenon of NMR in the gaseous phase by inducing transitions between discrete energy levels using oscillating magnetic fields [1], for which Rabi was awarded a Nobel prize in physics in 1944. In the following decade, Felix Bloch et al. [2] and Edward M. Purcell et al. [3] built upon this knowledge and, independently of one another, demonstrated the phenomenon of NMR in condensed matter in 1946, yielding both a shared Nobel prize in physics in 1952. The empirical equations Bloch discovered, which properly describe the spin dynamics of NMR experiments performed in liquids, introduced two important parameters, i.e. the longitudinal relaxation time ( $T_1$ ) and the transversal relaxation time ( $T_2$ ). These so-called *Bloch equations* enabled the theoretical description of a radio frequency (RF) irradiation of nuclear spins and their subsequent relaxation towards thermal equilibrium. A few years later, in 1950, it was observed that the resonance frequency of nuclear spins, i.e. their Larmor frequency ( $\omega_0$ ), strongly depends on the specific chemical environment [4, 5]. The discovery of this chemical shift (CS) effect led to the development of magnetic resonance spectroscopy (MRS), which became an important tool for many applications in physics and an indispensable standard procedure in analytical biochemistry.

The use of magnetic resonance (MR) as one of the most important tools in diagnostic medicine – magnetic resonance imaging (MRI) – started in 1973, when Lauterbur [6] and Mansfield [7] realized that the spatial distribution of nuclear spins within the MR signal can be encoded by using magnetic field gradients, for which both were awarded the Nobel prize in medicine in 2003. MRI enables to non-invasively obtain information, for instance, about anatomical structures by exploiting the strong signal of hydrogen nuclei ( $^1\text{H}$ , i.e. protons) due to the huge number of water molecules ( $\text{H}_2\text{O}$ ) in biological tissues. One of the benefits of MRI is its excellent soft-tissue contrast, stemming from the surprisingly strong differences in  $T_1$  and  $T_2$  of various biological tissues. Apart from  $T_1$  and

## 1 Introduction

$T_2$  weighted contrasts, numerous contrast mechanisms such as magnetic resonance spectroscopic imaging (MRSI), functional magnetic resonance imaging (fMRI), or diffusion weighted imaging (DWI), to name but a few, were developed. Essentially, this versatility of MR allows for deeper insights not only into anatomy but also into physiologic or metabolic processes. Moreover, in contrast to other imaging modalities such as X-ray computed tomography (CT) or positron emission tomography (PET), MR does not rely on ionizing radiation or radionuclides. Consequently, MRI rapidly established itself as a standard method in medical diagnostics and monitoring of many diseases.

In order to better understand pathologies such as cancer, which is one of the primary causes of death in industrialized countries [8, 9], molecular imaging contrasts are desirable. Particularly, the mapping of pH is a valuable contrast, as it plays a central role in many metabolic processes and acid-base homeostasis [10–13]. Thus, so far, many non-invasive MR-based techniques have been developed to achieve localized measurements of pH *in vivo* [14–16]. Importantly, *in vivo* a distinction is made between intracellular pH ( $\text{pH}_i$ ) and extracellular pH ( $\text{pH}_e$ ). In healthy tissues, generally speaking,  $\text{pH}_i$  is more acidic than  $\text{pH}_e$  (i.e.  $\text{pH}_i < \text{pH}_e$ ) whereas, conversely, in cancerous tissues  $\text{pH}_i$  is known to be typically increased (i.e.  $\text{pH}_i > \text{pH}_e$ ) [17–24]. Consequently,  $\text{pH}_i$  is an especially valuable marker for the assessment of cancer.

In the last few decades, accordingly, MRS-based approaches such as  $^1\text{H}$ -MRSI [14] or, in particular, phosphorous ( $^{31}\text{P}$ )-MRSI [25–27] have been established as gold standard procedures for non-invasive, localized assessment of  $\text{pH}_i$  by exploiting endogenous organic compounds which naturally occur in the cytosol of living tissues. However, while MRS-based techniques exhibit an excellent specificity in detecting  $\text{pH}_i$  values, these approaches, in fact, suffer from low signal-to-noise ratio (SNR) due to the direct detection of low-concentrated organic compounds leading to long acquisition times and low spatial resolutions ( $\sim 50$  min and  $\sim 12$  mm<sup>3</sup>) [25–27], thus hampering clinical applicability.

In contrast, chemical exchange saturation transfer (CEST) [28–33] is an emerging MRI technique which enables the non-invasive detection of low-concentrated organic compounds in living tissue with a comparable resolution to conventional MRI. In CEST-MRI, this is accomplished by utilizing a frequency-selective RF preparation prior to a conventional MRI readout which magnetically labels chemical exchange (CE) processes occurring between labile protons of low-concentrated biomolecules and protons of the

abundant free water pool. Hence, in CEST-MRI information about biomolecules in biological tissues, such as metabolites [34–45] or proteins and peptides [46–50], is obtained indirectly via the direct detection of the modified water signal. In comparison to the direct detection of the low-concentrated metabolites in MRS-based methods, the indirect detection via the modified water signal yields a powerful amplification, thus, enabling spatial resolutions in the order of  $\sim 1 \text{ mm}^3$ . Consequently, CEST-MRI offers the possibility to combine the spectral selectivity of MRS with the high SNR of conventional MRI.

Importantly, due to the underlying process of CE, CEST signals are intrinsically sensitive to pH [46, 51]. In vivo, the most prominent CEST signals stem from amide and guanidyl protons which are mainly associated with mobile proteins and peptides within cells [46, 47, 50, 52, 53], whereas the guanidyl signal, in addition, is also associated with creatine [39, 40, 54, 55] which is an organic compound primarily present in muscle as well as brain tissue and also mainly intracellular. For this reason, high-resolution pH<sub>i</sub> mapping of tumors in vivo is, in principle, feasible by means of CEST-MRI.

However, in vivo and especially in tumors, the amide and guanidyl signals are severely influenced by concomitant effects which impede a straightforward isolation of the pH-dependency. More specifically, the concomitant effects, which can all strongly vary in an unpredictable manner in tumors [56], are mainly:

1. The intrinsically unknown concentration of the CEST pool (i.e. the relative concentration of amide or guanidyl protons with respect to the water protons).
2. Other superimposing and interfering CEST signals.
3. The pronounced background of semi-solid magnetization transfer contrast (MTC, i.e. a strong background signal due to semi-solid structures in vivo, such as cell membranes, surface proteins or the cytoskeleton).
4. Spillover dilution (i.e. the dilution of CEST signals due to mostly relaxation properties of the water signal but also other magnetization transfer signals [57, 58]).

In order to isolate the pH-dependency of CEST signals from some of the aforementioned concomitant effects, several CEST-MRI-based approaches have already been proposed [16, 59–87] and, in principle, can be roughly grouped as follows (some methods are allocated in multiple categories):

## 1 Introduction

- Measurement of  $\text{pH}_e$  [59, 76, 88, 89], i.e. by injecting known concentrations of exogenous contrast agents (CA), which are not transported into cells (applications in tumors but also other tissues).
- Examinations aiming at investigating pH changes during acute ischemic stroke [64–66, 73, 78, 81, 86], where changes in concentration are assumed to be negligible.
- Applications for pH-weighted tumor imaging [63, 67, 69, 83, 85, 87], which only allow for a detection of relative pH changes (both  $\text{pH}_i$  and  $\text{pH}_e$ ).
- Ratiometric approaches [59–62, 76], which compensate for changes in concentration by utilizing the ratio of CEST signals (both  $\text{pH}_i$  and  $\text{pH}_e$ ).

However, state-of-the-art methods do not enable simultaneous compensation of all aforementioned concomitant effects on CEST signals in tumor tissues. Thus, endogenous CEST-based, quantitative  $\text{pH}_i$  mapping in vivo is currently not yet applicable for cancer imaging.

The aim of this thesis was to develop a quantitative  $\text{pH}_i$  mapping method based on the endogenous amide and guanidyl CEST signals, which is applicable for tumor imaging in vivo. To this end, a novel model is established (chapter 3), which is based on the finding that, at a fixed temperature (e.g.  $37^\circ\text{C}$  in vivo), the pH-dependency of the magnetization transfer exchange rates ( $k_{\text{ex}}$ ) between amide or guanidyl protons and water protons is completely characterized by only one rate constant ( $k_c$ ). For both, the amide and guanidyl signal, this theoretical framework enables a direct translation of extracted  $k_{\text{ex}}$  into pH, i.e. yielding  $\text{pH}_{\text{amide}}$  and  $\text{pH}_{\text{gua}}$  (section 3.1). A robust and reliable approach allowing for a precise calibration of  $k_c$  in vitro is presented (section 3.2) exploiting a newly identified, distinct functional behavior of isolated CEST signals as a function of pH (section 3.3). The developed method utilizes the reliable extraction of  $k_{\text{ex}}$  which was accomplished by an optimized isolation and processing procedure of the measured amide and guanidyl CEST signals exhibiting a high spectral selectivity at a static magnetic field strength of  $B_0 = 9.4$  T. In this context, an optimized fitting procedure based on the theory of relaxation- and spillover-corrected CEST signals ( $\text{MTR}_{\text{REX}}$ ) [57, 58, 90] was implemented (section 3.4) allowing for concentration-independent extraction of  $k_{\text{ex}}$  and, thus, pH from data acquired at multiple RF amplitudes ( $B_1$ ). Using the developed model, the pH sensitivity of CEST signals was explored yielding further insights into the nature of CEST (section 3.5). Based on the determined complementary pH sensitivities of

amide and guanidyl protons, the two individually obtained  $\text{pH}_{\text{amide}}$  and  $\text{pH}_{\text{gua}}$  maps were combined into a final pH map enabling a broader total range of high pH sensitivity, i.e. yielding  $\text{pH}_{\text{combi}}$  (section 3.6).

To evaluate and validate the proposed method under in vivo-like conditions, porcine brain lysates mimicking the in vivo composition of proteins and peptides were employed for calibration of  $k_c$ . Moreover, porcine brain lysates were utilized to demonstrate the feasibility of reliable, quantitative pH mapping across a broad range of physiologically relevant pH values between 6.2 and 8.0 (section 5.1). Using the insights and calibration obtained from porcine brain lysates, applicability for examinations in vivo was demonstrated in the lesions of tumor-bearing mice showing a physiologically plausible median  $\text{pH}_i$  of approximately 7.2, independent of tumor size, further validating the developed method (section 5.2). In addition, in an effort towards translating the developed method for examinations in humans where a pulsed presaturation is a prerequisite, creatine model solutions were investigated using a pulsed presaturation scheme. In creatine model solutions, the possibility of tuning the pH sensitivity by variation of the presaturation pulse shape was demonstrated (section 5.3).

Altogether, the developed method, now, allows to robustly assess the potential of  $\text{pH}_i$  as a valuable imaging biomarker for cancer diagnosis, treatment planning and monitoring in a preclinical setting, representing an important milestone towards the prospective application in humans.



## 2 Fundamental Principles

In this chapter, the fundamental principles and phenomena are described in a condensed manner. A broad overview is presented, which covers the essential physical and biochemical basics as well as the applied techniques utilized within the scope of this thesis. For any further and more detailed descriptions, the interested reader may refer to standard textbooks such as [91–94], just to mention a few.

### 2.1 Nuclear magnetic resonance

The underlying physical principle, essentially, is the phenomenon of NMR. In the following sections, the basics of NMR are briefly explained.

#### 2.1.1 Nuclear spin and Zeeman effect

In general, all matter encountered in the universe can be categorized into two classes: ordinary and exotic matter. More specifically, one can define ordinary matter to be composed of fermionic elementary particles with spin  $\frac{1}{2}$  (i.e. quarks and leptons). In particular, all matter we encounter in everyday life (i.e. composite particles such as atoms and molecules) consists of merely three elementary particles: the up quark, the down quark and the electron. Up and down quarks form the building blocks of nucleons (i.e. protons and neutrons), which together with electrons form atoms. Since all nucleons are fermions with half-integer spins which satisfy the Fermi-Dirac statistics, they cause atomic nuclei with an odd number of protons and/or neutrons to have a non-zero total nuclear spin  $\vec{I} \neq 0$ . According to the spin-statistics theorem, this quantum mechanical nuclear spin is fundamentally limited to discrete values ( $\vec{I} = \frac{1}{2}, 1, \frac{3}{2}, \dots$ ). The nucleus of the simplest atom (i.e. hydrogen,  $^1\text{H}$ ) consists of a single proton and has a spin quantum number of  $\vec{I} = \frac{1}{2}$  which, hereafter, is simply referred to as spin  $I$ . This spin  $I$  complies with the

## 2 Fundamental Principles

quantum-mechanical commutator relations for angular momentum via

$$[\hat{I}_i, \hat{I}_j] = i\hbar\epsilon_{ijk}\hat{I}_k \quad (2.1)$$

$$[\hat{I}^2, \hat{I}_i] = 0, \quad (2.2)$$

where  $i, j, k \in [x, y, z]$ . Application of these operators on the eigenstates  $|I, m\rangle$  yields the corresponding eigenvalues

$$\hat{I}^2 |I, m\rangle = \hbar^2 I(I+1) |I, m\rangle \quad (2.3)$$

$$\hat{I}_z |I, m\rangle = \hbar m |I, m\rangle, \quad (2.4)$$

which are the observables of the nuclear spin system. Here,  $\hbar = \left(\frac{h}{2\pi}\right) \approx 1.05 \cdot 10^{-34}$  Js is the reduced Planck constant and  $m = (-I, -I+1, \dots, I-1, I)$  is the magnetic quantum number (i.e.  $m = \pm\frac{1}{2}$  for  $^1\text{H}$ ), with the selection rule of  $\Delta m = 1$  for photon absorption or emission. The physical quantity of the quantized angular momentum is given by  $|\vec{I}| = \hbar\sqrt{I(I+1)}$ . Moreover, any non-zero nuclear spin  $\vec{I}$  is associated with a magnetic moment  $\vec{\mu}$  via

$$\vec{\mu} = \gamma\vec{I}. \quad (2.5)$$

Here,  $\gamma$  is the gyromagnetic ratio which is specific for each nucleus. For any given nucleus,  $\gamma$  depends on the Landé factor  $g_I$  as well as the nuclear magneton  $\mu_N$  through

$$\gamma = g_I \cdot \frac{\mu_N}{\hbar} = g_I \cdot \frac{e}{2m_p}, \quad (2.6)$$

where  $e$  is the elementary charge ( $e \approx 1.602 \cdot 10^{-19}$  C) and  $m_p$  the proton rest mass ( $m_p \approx 1.673 \cdot 10^{-27}$  kg). The experimentally determined value for a hydrogen proton in water is  $\gamma = \frac{g_p \mu_N}{\hbar} = 2,675 \cdot 10^8 \text{ rad} \cdot \text{s}^{-1} \cdot \text{T}^{-1}$  and, accordingly,  $\frac{\gamma}{2\pi} = 42,576 \frac{\text{MHz}}{\text{T}}$ . Furthermore, it is observed that nuclei with  $\vec{\mu} \neq 0$  interact with an external static magnetic field  $\vec{B} = (0, 0, B_0)^t$ , without loss of generality (wlog) aligned in  $z$ -direction. This interaction is described by the Hamiltonian  $\hat{\mathcal{H}}$  via

$$\hat{\mathcal{H}}_z = -\hat{\vec{\mu}}\vec{B} = -\hat{\mu}_z B_0 = -\gamma\hat{I}_z B_0. \quad (2.7)$$

Because the angular momentum  $\hat{I}_z$  and the Hamiltonian  $\hat{\mathcal{H}}_z$  are linearly related, they have the same eigenstates  $|I, m\rangle$ . Therefore, the time-independent Schrödinger equation

$\hat{\mathcal{H}}_z |I, m\rangle = E_m |I, m\rangle$  can be applied to calculate the eigenvalues according to

$$E_m = \langle I, m | \hat{\mathcal{H}}_z | I, m \rangle = -\gamma B_0 \langle I, m | \hat{I}_z | I, m \rangle = -m\hbar\gamma B_0. \quad (2.8)$$

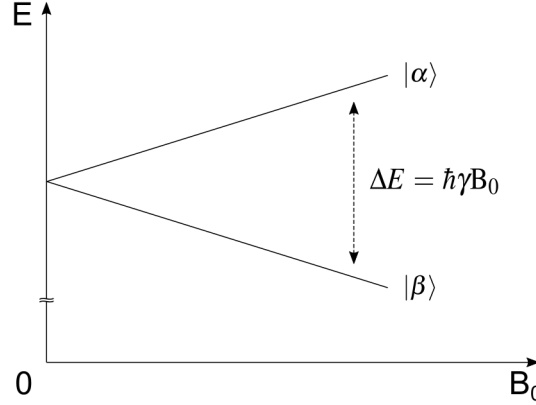


**Figure 2.1:** The Zeeman effect leads to a splitting into  $2I + 1$  discrete energy levels for a nucleus inside an external magnetic field  $B_0 > 0$ . For  $^1\text{H}$  with  $I = \frac{1}{2}$ , this results in two equidistant energy levels. The energy difference  $\Delta E = \hbar\gamma B_0$  between the two states  $|\alpha\rangle$  and  $|\beta\rangle$  increases linearly with the strength of the magnetic field.

Consequently, this results in an equidistant splitting into  $(2I + 1)$  discrete energy levels. This is the so-called *Zeeman effect* (Figure 2.1), which in the case of the hydrogen nucleus yields an energy difference  $\Delta E$  of the two possible eigenstates  $|\alpha\rangle = |\frac{1}{2}, -\frac{1}{2}\rangle$ , and respectively,  $|\beta\rangle = |\frac{1}{2}, +\frac{1}{2}\rangle$  given by

$$\Delta E = E_\alpha - E_\beta = \hbar\gamma B_0 = \hbar\omega_0. \quad (2.9)$$

Here, the resonance frequency  $\omega_0 = \gamma B_0$  is the so-called *Larmor frequency*. In this thesis, a static magnetic field strength<sup>1</sup> of  $B_0 = 9.4$  T is used. For  $^1\text{H}$  at  $B_0 = 9.4$  T, the Larmor frequency is often given by  $\nu_0 = \frac{\omega_0}{2\pi} \approx 400$  MHz. Also, transitions between these adjacent energy levels can be induced using time-varying magnetic fields.

### 2.1.2 Macroscopic magnetization

All previous considerations merely describe the quantum-mechanical behavior of a single nuclear spin. A realistic NMR experiment, however, almost certainly always deals

<sup>1</sup> Technically, magnetic flux density. However, by convention and for the sake of simplicity, from here on referred to as magnetic field strength.

## 2 Fundamental Principles

with huge quantities of nuclear spins. Typically,  $N > 10^{16}$  nuclei have to be considered, whereas each spin within this so-called macroscopic ensemble obeys the rules depicted in the preceding section 2.1.1. Consequently, for each spin, the energy levels are split into  $(2I + 1)$  states inside an static external magnetic field (again, i.e.  $\vec{B} = (0, 0, B_0)^t$  wlog). In thermal equilibrium, this large number of spins results in a population probability  $p_m$  of the energy states which is governed by the *Boltzmann statistics* according to

$$p_m = \frac{1}{Z} e^{-E_m/(k_B T)}. \quad (2.10)$$

Here,  $Z = \sum_{m=-I}^I (e^{-E_m/(k_B T)})$  is the partition function describing the number of states of the canonical ensemble,  $k_B$  the Boltzmann constant and  $T$  the thermal equilibrium temperature. For  $N$  nuclei of  $^1\text{H}$  with  $I = \frac{1}{2}$ , and thus two energy states  $|\alpha\rangle$  and  $|\beta\rangle$ , the expected value of the  $z$ -component of the magnetic moment  $\vec{\mu}$  is given by

$$\begin{aligned} \langle \hat{\mu}_z \rangle &= \gamma \langle \hat{I}_z \rangle = \gamma \left[ p_{-\frac{1}{2}} \langle \alpha | \hat{I}_z | \alpha \rangle + p_{+\frac{1}{2}} \langle \beta | \hat{I}_z | \beta \rangle \right] \\ &= \gamma \frac{\hbar}{2} \left[ p_{+\frac{1}{2}} - p_{-\frac{1}{2}} \right] \\ &= \gamma \frac{\hbar}{2} P, \end{aligned} \quad (2.11)$$

where  $P$  is the polarization of the ensemble determined by the difference in population probabilities between the two occupied states. Therefore,  $P$  is also known as the normalized difference in population which is calculated via

$$P = p_{+\frac{1}{2}} - p_{-\frac{1}{2}} = \frac{\Delta N}{N}. \quad (2.12)$$

By inserting the energy eigenvalues  $E_m$  obtained through equation (2.8) into the population probability (2.10) one obtains

$$P = \frac{e^{\frac{\gamma B_0 \hbar}{2k_B T}} - e^{-\frac{\gamma B_0 \hbar}{2k_B T}}}{e^{\frac{\gamma B_0 \hbar}{2k_B T}} + e^{-\frac{\gamma B_0 \hbar}{2k_B T}}} = \tanh \left( \frac{\gamma \hbar B_0}{2k_B T} \right). \quad (2.13)$$

For all intents and purposes within the scope of this thesis<sup>2</sup>, it is appropriate to assume that  $\gamma \hbar B_0 \ll k_B T$ , since  $T \geq 300$  K and  $B_0 = 9.4$  T. Hence, one can approximate the hyperbolic tangent in equation (2.13) by a Taylor expansion around  $x = 0$ . The resulting

---

<sup>2</sup> For investigations at in vivo temperature and ultra-high field strength (UHF), i.e.  $B_0 \geq 7$  T.

first order approximation of the polarization is given by

$$P \approx \frac{\gamma \hbar B_0}{2k_B T}. \quad (2.14)$$

This means that, within the experimental circumstances of this thesis, a polarization in the order of  $P \approx 5 \cdot 10^{-6}$  is present. The macroscopic magnetization  $\vec{M}_0$  of a spin ensemble is defined as the sum of all magnetic moments  $\langle \hat{\vec{\mu}} \rangle$  within a given volume  $V$ . Accordingly,  $\vec{M}_0$  is proportional to the polarization and is calculated by

$$\vec{M}_0 = \sum_{i=1}^N \frac{\langle \hat{\vec{\mu}} \rangle}{V} = \frac{N}{V} \langle \hat{\vec{\mu}} \rangle = \gamma \frac{\hbar N}{2V} \vec{P} \approx \frac{1}{4} \frac{N}{V} \frac{\gamma^2 \hbar^2}{k_B T} \vec{B}. \quad (2.15)$$

This inverse proportionality  $\vec{M}_0 \propto T^{-1}$  is also known as the *Curie law*. In NMR experiments,  $\vec{M}_0 \propto$  signal which is why, in principle, one can increase the signal by either (i) increasing the Number  $N$  of spins (e.g. by measuring a sample with a larger volume  $V$  or higher density of spins  $\rho_I = \frac{N}{V}$ ), (ii) choosing a nucleus with a higher gyromagnetic ratio  $\gamma$ , (iii) decreasing the temperature  $T$  of the sample, or (iv) increasing the magnetic field strength  $\vec{B}$ . It should be pointed out that  $\vec{M}_0$  has a quadratic dependency on  $\gamma$  which is specific for each nucleus and has the largest value of all stable nuclei for  $^1\text{H}$ . Consequently,  $^1\text{H}$ -NMR experiments typically yield a superior SNR compared to other nuclei<sup>3</sup> with  $\vec{I} \neq 0$ .

In addition,  $\vec{M}_0$  depends linearly on  $\vec{B}$  which is the main reason why scientists, physicists, chemists, engineers and radiologists etc. alike strive for ever stronger magnetic fields. This is especially important in living tissue, where  $\vec{B}$  is essentially the only parameter which can be adjusted to increase signal<sup>4</sup>. For temperatures in vivo and field strengths commonly used in modern MR scanners (i.e.  $37^\circ\text{C}$ ,  $T \approx 310\text{ K}$  and  $B_0 \sim 1$  to  $10\text{ T}$ ), the small fraction of  $P \sim 10^{-6}$  effectively only yields a measurable signal intensity  $\propto \vec{M}_0$  due to the high biological<sup>5</sup> as well as natural<sup>6</sup> abundance of  $^1\text{H}$ .

<sup>3</sup> In the field of NMR, the  $^1\text{H}$  nucleus is simply referred to as proton while all other nuclei are collectively referred to as so-called X-nuclei.

<sup>4</sup> At least, if one uses thermally polarized magnetization as opposed to NMR hyperpolarization techniques.

<sup>5</sup> The counteracting huge number of  $^1\text{H}$  within biological tissues, essentially, i.e. the protons of hydrogen nuclei in water with  $\frac{N}{V} \approx 10^{19} \text{ mm}^{-3}$ .

<sup>6</sup> The fact that virtually all hydrogen isotopes are  $^1\text{H}$ , which has a relative abundance of  $\approx 99.99\%$ .

### 2.1.3 Time evolution, relaxation and Bloch equations

All previous considerations are time-independent and merely involve static magnetic fields. In the following, varying (i.e. time-dependent) magnetic fields are introduced to the spin system and the consequent dynamics are considered. In such a time-dependent magnetic field  $\vec{B}(t)$ , the dynamics of a single spin are described using the time-dependent *Schrödinger equation*

$$i\hbar \frac{\partial}{\partial t} |I, m\rangle = \hat{\mathcal{H}}(t) |I, m\rangle, \quad (2.16)$$

in which  $\hat{\mathcal{H}}(t) = -\hat{\vec{\mu}} \cdot \vec{B}(t)$  denotes the time-dependent Hamiltonian. By applying the *Ehrenfest theorem*, which states that the expectation value of a quantum-mechanical operator complies with the associated classical equation of motion, one can determine the expectation value of the time-dependent magnetic moment via

$$\frac{d}{dt} \langle \hat{\mu}_j \rangle = \frac{i}{\hbar} \langle [\hat{\mathcal{H}}, \hat{\mu}_j] \rangle + \left\langle \frac{\partial \hat{\mu}_j}{\partial t} \right\rangle. \quad (2.17)$$

By exploiting the commutator relations, which are given by equations (2.1) and (2.2), one obtains

$$\frac{d}{dt} \langle \hat{\vec{\mu}} \rangle = \langle \hat{\vec{\mu}} \rangle \times \gamma \vec{B}(t). \quad (2.18)$$

In the macroscopic limit, however, quantum-mechanical systems must comply with the description of classical physics. This is known as the *correspondence principle*, which significantly simplifies the actually underlying physical properties. Accordingly, it is sufficient enough to describe the system by means of the expectation value known from the classical macroscopic magnetization, and thus, equation (2.18) is transformed to

$$\frac{d}{dt} \vec{M}(t) = \vec{M}(t) \times \gamma \vec{B}(t). \quad (2.19)$$

According to equation (2.19), the magnetization  $\vec{M}$  is subject to a torque if it has a component perpendicular to  $\vec{B}(t)$ . In such a case,  $\vec{M}$  undergoes a precession motion perpendicular to  $\vec{B}(t)$  with the Larmor frequency  $\omega(\vec{B}(t))$  which, ultimately, is used for signal generation in NMR experiments.

### Rotating frame of reference and effective field

In order to generate a measurable signal (essentially, i.e. magnetization precessing perpendicular to the main, static magnetic field  $\vec{B}_0$ ), a time-dependent RF excitation field  $\vec{B}_1(t)$ <sup>7</sup>, with the frequency  $\omega_{RF}$  and wlog oscillating in the  $x$ - $y$ -plane, is superimposed on  $\vec{B}_0$  resulting in a total time-dependent magnetic field given by

$$\vec{B}_{tot}(t) = \vec{B}_0 + \vec{B}_1(t) = \begin{pmatrix} 0 \\ 0 \\ B_0 \end{pmatrix} + B_1 \begin{pmatrix} \cos(\omega_{RF}t) \\ \sin(\omega_{RF}t) \\ 0 \end{pmatrix}. \quad (2.20)$$

Accordingly, the dynamics of  $\vec{M}(t)$  can be obtained by inserting  $\vec{B}_{tot}(t)$  into equation (2.19). However, it is rather complicated to describe the entire time evolution using the laboratory system. For this reason, all dynamic processes are typically described by a transformation of the laboratory system into a coordinate system which rotates about the  $z$ -axis with frequency  $\omega_{RF}$  (i.e. collectively with  $\vec{B}_1(t)$ ). In this so-called rotating frame of reference, the new coordinates are consequently given by  $(x', y', z' = z)$  and equation (2.19) is expressed via

$$\frac{d}{dt}\vec{M}'(t) = \vec{M}'(t) \times \gamma\vec{B}'_{tot}. \quad (2.21)$$

By definition,  $\vec{B}_0$  as well as  $\vec{B}_1(t)$  can, in the rotating frame, be considered as static magnetic fields which significantly simplifies all further considerations. By convention, the RF field  $\vec{B}_1$  is aligned in the  $x'$ -direction which simplifies the description of the total magnetic field (equation (2.20)) to

$$\vec{B}_{eff} = \begin{pmatrix} B_1 \\ 0 \\ B_0 - \frac{\omega_{RF}}{\gamma} \end{pmatrix}, \quad (2.22)$$

which, in the rotating frame, is referred to as the effective magnetic field  $\vec{B}_{eff}$  (Figure 2.2).

---

<sup>7</sup> Within this thesis,  $B_1$  only refers to the transmit field power (as opposed to the receive field power). In some literature, the transmit field is denoted as  $B_1^+$  and the receive field as  $B_1^-$ .

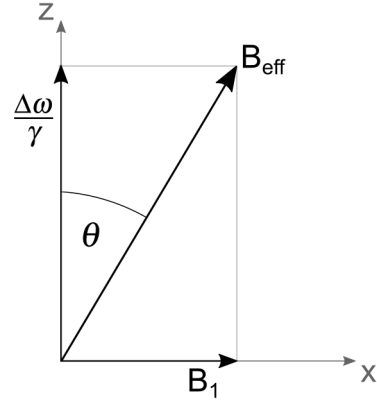


**Figure 2.2:** In the rotating frame of reference solely the effective magnetic field  $\vec{B}_{eff}$  appears to induce all dynamic processes.  $B_{eff}$  is composed of the RF amplitude  $B_1$  in  $x'$ -direction and the residual field  $B_0 - \frac{\omega_{RF}}{\gamma} = \frac{\Delta\omega}{\gamma}$  in  $z$ -direction, which is determined by the off-resonance  $\Delta\omega = \omega_{RF} - \omega_0$ . The angle  $\theta = \arctan\left(\frac{\omega_1}{\Delta\omega}\right)$  describes the tilt relative to the static magnetic field  $B_0$ . If the resonance condition is fulfilled, all components other than the  $x'$ -component vanish.

### Resonance condition and flip angle

Interestingly, if the RF field exactly oscillates with the Larmor frequency of the nuclear spins, it follows that  $\omega_{RF} = \omega_0 = \gamma B_0$ . This so-called resonance condition is of uttermost importance for the phenomenon of NMR<sup>8</sup>. If the resonance condition is fulfilled, equation (2.22) yields a vanishing  $z$ -component of the effective field  $\vec{B}_{eff}$ , due to  $B_0 = \frac{\omega_{RF}}{\gamma}$ . Accordingly, the residual effective magnetic field only acts on the  $x'$ -direction which, in turn, results in the magnetization precessing about the  $x'$ -direction (i.e. in the  $y'$ - $z$ -plane) with the frequency

$$\omega_1 = \gamma B_1. \quad (2.23)$$

Consequently, such an on-resonant RF irradiation of the spin system which fulfills the resonance condition is referred to as tipping pulse. In the laboratory system, in contrast, a tipping pulse causes a spiral trajectory of the macroscopic magnetization  $\vec{M}(t)$ . The flip angle  $\alpha$  between the magnetization and the  $z$ -axis is calculated by

$$\alpha = \int_0^{t_p} \omega_1(t) dt = \int_0^{t_p} \gamma B_1(t) dt, \quad (2.24)$$

<sup>8</sup> Hence, the name nuclear magnetic *resonance*.

where  $t_p$  refers to the tipping pulse duration. In the simple case of a constant amplitude of  $B_1$ , which is shortly turned on during  $t_p$ , equation (2.24) even further simplifies to

$$\alpha = \gamma B_1 t_p. \quad (2.25)$$

Hence,  $\alpha$  can be increased by either increasing the amplitude ( $B_1$ ) or the length ( $t_p$ ) of the tipping pulse. All components of  $\vec{M}$  transversal to  $B_{eff}$  always precess around the effective field axis. Thus, as soon as the RF field is turned off again, the transversal components of the magnetization  $\vec{M}$  again start to precess in the  $x$ - $y$ -plane around the effective field (here again, i.e. the static magnetic field  $\vec{B}_0$ ) with the Larmor frequency  $\omega_0$ . According to *Faraday's law of induction*, the movement of this rotating magnetization induces an alternating voltage inside a receiver coil. In other words, the varying voltage which is picked up by the receiver coil(s) gives rise to the actual signal which is measured in NMR experiments (see section 2.1.4).

### Relaxation and Bloch equations

Until now, no relaxation effects were taken into account, meaning that a transversal component would precess endlessly about the  $z$ -axis. However, in reality the magnetization is always driven back to thermal equilibrium (i.e. during and after the RF irradiation is performed). This process of a spin system's tendency towards its thermal equilibrium magnetization is called *relaxation*. It has been experimentally demonstrated that the parallel component of the magnetization to  $\vec{B}_0$  (i.e.  $M_z$ ) relaxes with a rate which is proportional to the difference between the momentary  $M_z$  and the equilibrium magnetization  $M_0$ . In contrast, the transversal components (i.e.  $M_x$  and  $M_y$ ) decay proportionally to their momentary transversal magnitude. These processes occur due to interactions of the spins with their surrounding environment as well as with each other. In order to comply with the relaxation processes observed in nature, equation (2.19) has to be separated into its components and expanded by additional terms. The phenomenologically found, so-called *Bloch equations*, which take this into account, are given by [95]

$$\frac{d}{dt}M_{x'} = \gamma(\vec{M} \times \vec{B})_{x'} - \frac{M_{x'}}{T_2}, \quad (2.26)$$

$$\frac{d}{dt}M_{y'} = \gamma(\vec{M} \times \vec{B})_{y'} - \frac{M_{y'}}{T_2}, \quad (2.27)$$

$$\frac{d}{dt}M_z = \gamma(\vec{M} \times \vec{B})_z - \frac{M_z - M_0}{T_1} \quad (2.28)$$

## 2 Fundamental Principles

and are considered to be the fundamental equations of magnetic resonance. Here,  $T_2$  is the transversal relaxation time,  $T_1$  the longitudinal relaxation time and  $M_0$  the equilibrium magnetization. The relaxation times strongly depend on their environment. As a consequence of this, many biological tissues have specific  $T_1$  and  $T_2$  values, which can, for instance, be used to discriminate between them. The underlying reason of transversal relaxation processes are spin-spin interactions, leading to a phase shift of the individual spin packages among each other (i.e. spin dephasing). Therefore,  $T_2$  is sometimes referred to as the *spin-spin* relaxation time. In such a  $T_2$  relaxation process, energy is exchanged between distinct spin packages but not transferred to the environment. On the contrary, the longitudinal relaxation is caused by the coupling of the spin system with the thermal reservoir (i.e. the so-called lattice). Consequently, such a  $T_1$  relaxation process is stimulated by the Brownian motion of molecules via induced, time-varying magnetic fields. Therefore,  $T_1$  is also known as the *spin-lattice* or *thermal* relaxation time. Ultimately, this unrecoverable, dissipative energy loss due to the transfer of heat during a  $T_1$  process promotes relaxation towards the thermal equilibrium magnetization. Another useful concept in MR are the relaxation rates  $R_2$  and  $R_1$ , which are defined as the inverse of each corresponding relaxation time

$$R_2 = \frac{1}{T_2}, \quad (2.29)$$

$$R_1 = \frac{1}{T_1}. \quad (2.30)$$

In biological tissues at 9.4 T, relaxation times are typically in the order of  $T_2 \sim (30 - 100)$  ms and  $T_1 \sim (1 - 3)$  s.

### 2.1.4 MR signal

The Bloch equations (2.26), (2.27) and (2.28) can be reformulated by means of complex numbers and the notation  $M_{\perp}(t) := M_{xy}(t) = M_x(t) + iM_y(t)$  and  $M_{\parallel}(t) := M_z(t)$ . Under the assumption that the pulse duration is negligible (i.e.  $t_p \ll T_{1,2}$ ), the Bloch equations are solved by

$$M_{\perp}(t) = M_{\perp}(0)e^{i\omega_0 t} e^{-t/T_2}, \quad (2.31)$$

$$M_{\parallel}(t) = M_0 - (M_0 - M_{\parallel}(0))e^{-t/T_1}, \quad (2.32)$$

where  $M_{\perp}(0)$  and  $M_{\parallel}(0)$  denote the transverse, and respectively, longitudinal component of the magnetization at the beginning of the relaxation (e.g. immediately after excitation). Equation (2.31) yields a damped oscillation in the transverse plane and equation (2.32) a recovery towards the  $z$ -direction. In fact, however, in real NMR experiments an even shorter transversal relaxation time denoted by  $T_2^*$  is observed with

$$\frac{1}{T_2^*} = \frac{1}{T_{2, \text{intrinsic}}} + \frac{1}{T_{2, \text{inhom}}}. \quad (2.33)$$

$T_2^*$  originates from an additional dephasing of the spin packages due to magnetic field inhomogeneities ( $\Delta B$ ), which is superimposed on the intrinsic dephasing arising from spin-spin interactions. A direct consequence of this additional dephasing is the faster decay of transverse magnetization governed by the observed  $T_2^*$  (with  $T_2^* < T_2$ ). The rotation of this decaying magnetization  $M_{\perp}(t)$  about the  $z$ -axis induces a time-varying magnetic flux, as already briefly mentioned in the previous section 2.1.3. Accordingly, this over time changing magnetic flux yields an electromotive force which, in turn, can be measured as a time-dependent voltage  $U_{ind}$  within a receiver coil. Hence, the MR signal of a volume  $V$  is given by

$$S(t) = U_{ind} \propto \int_V \rho(\vec{r}) e^{i\omega_0 t} d\vec{r}, \quad (2.34)$$

with the spatial density distribution  $\rho(\vec{r})$  of the individual spins. However, because the transversal component decays with the time constant  $T_2^*$ , the actually measured signal is given by

$$S(t) = S_0 e^{i\omega_0 t} e^{-t/T_2^*}. \quad (2.35)$$

Historically, this characteristic MR signal is referred to as free induction decay (FID). By performing the Fourier transform (FT) of this oscillating exponential decay, one obtains a Lorentzian line shape in the frequency domain (Figure 2.3). Accordingly, one can calculate the underlying resonance frequency (i.e. the Larmor frequency  $\omega_0$ ) as well as the full width at half maximum (FWHM) which is given by  $\Gamma = \frac{2}{T_2^*}$ . Remarkably, however, even within a perfectly homogeneous and constant static magnetic field multiple resonances can occur. Yet, these different resonances have to originate from corresponding differing Larmor frequencies  $\omega_0$ . An explanation of this phenomenon is given in the subsequent section 2.1.5.

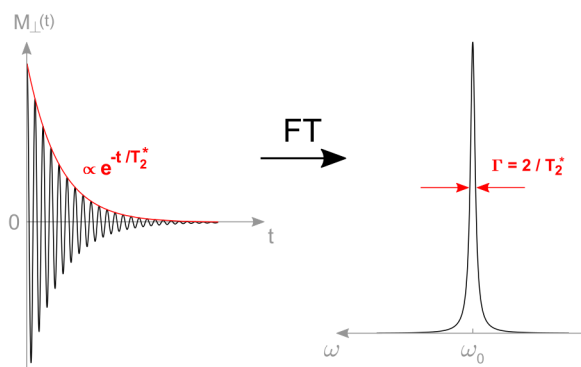


**Figure 2.3:** After application of a Fourier transform (FT), the free induction decay (FID) signal which decays with the relaxation constant  $T_2^*$  (time domain, left) yields a Lorentzian line shape at the resonance frequency  $\omega_0$  (frequency domain, right), i.e. at the Larmor frequency.

### 2.1.5 Chemical shift

Until now it was assumed that the static magnetic field strength  $B_0$  is constant, resulting in only one resonant frequency  $\omega_0$  which, accordingly, is identical for all  $^1\text{H}$  nuclei. However, while in principle correct, this assumption only holds true for free protons and can no longer be applied to bound protons (i.e.  $^1\text{H}$  within different chemical groups of molecules). Depending on the local chemical environment, the electron cloud of the atom shields the nucleus to a greater or lesser extent from the external magnetic field  $B_0$ . Thus, the altered, local magnetic field strength at the position of the nucleus is given by

$$\vec{B}_{loc} = \vec{B}_0 + \delta\vec{B} = \vec{B}_0(1 - \sigma), \quad (2.36)$$

with the shielding tensor<sup>9</sup>  $\sigma$ , which strongly depends on the specific chemical environment of the considered proton and the structure of the molecule, respectively. This shift of  $\vec{B}_{loc}$  leads to a shift of the resonance frequency according to

$$\delta\omega = \gamma\delta\vec{B}, \quad (2.37)$$

which is referred to as chemical shift (CS). According to (2.37), the CS depends on  $B_0$  which leads to a different CS at different  $B_0$  even for protons in identical chemical environments. Hence, in order to define a  $B_0$ -independent quantity, the CS usually is

<sup>9</sup> Within the scope of this thesis,  $\sigma$  can be assumed to be represented by a dimensionless constant, i.e. isotropic shielding.

given as the normalized difference with respect to a reference frequency  $\omega_{ref}$  in the unit of parts per million via

$$\delta_i [\text{ppm}] = \frac{\omega_i - \omega_{ref}}{\omega_{ref}} \cdot 10^6. \quad (2.38)$$

In a NMR-spectrum, by convention, higher values of CS are plotted to the left (Figure

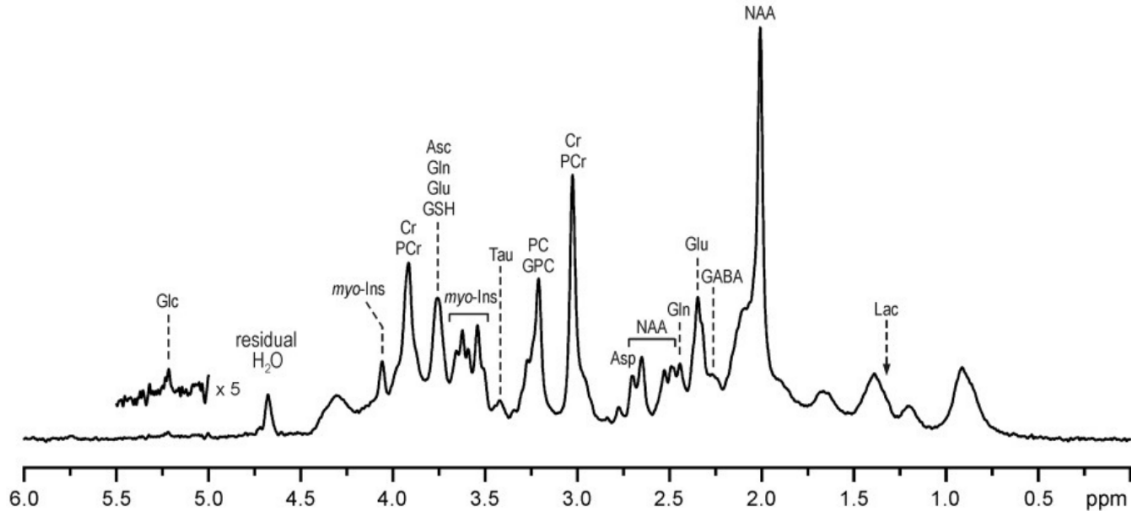


**Figure 2.4:**  $^1\text{H}$  NMR spectrum of the human brain acquired at  $B_0 = 7$  T. The chemical shift (CS) effect enables to distinguish between different chemical groups by means of magnetic resonance spectroscopy (MRS). In the human brain, the most prominent resonances are N-acetylaspartate (NAA), phosphocreatine (PCr) and creatine (Cr). Here, the strong water signal is severely suppressed (resonating at  $\delta \approx 4.7$  ppm with respect to TMS). Conversely, in CEST-MRI the water resonance is used as reference frequency, thus, by definition resonating at  $\delta = 0$  ppm. Edited, original Figure taken from [96].

2.4). Accordingly,  $\omega_0$  increases from right to left whereas the shielding decreases from right to left. Per definition, the used reference frequency  $\delta_{ref} := \delta \hat{=} 0$  ppm is given by the Larmor frequency of any suitable reference substance. In MRS, tetramethylsilane (TMS) is commonly used as a reference [94], which has the chemical structure  $\text{Si}(\text{CH}_3)_4$ . In contrast, the reference substance in water-mediated magnetization transfer (MT) experiments, which are described in further detail in section 2.3, is water itself ( $\text{H}_2\text{O}$ ). More specifically, the resonance frequency of free water protons is assigned to the chemical shift of zero (i.e.  $\delta_w := \delta \hat{=} 0$  ppm). Consequently, by applying this, the shift of the resonance frequency  $\delta\omega_i$  of any given chemical environment  $i$  compared to the water signal

## 2 Fundamental Principles

is given via

$$\delta\omega_i = \omega_i - \omega_w = \delta_i\omega_w \quad (2.39)$$

### 2.2 Magnetic resonance imaging (MRI)

So far, the acquired MR signal (and accordingly also the NMR spectrum) is obtained by measuring the superimposed signal coming from the entire sample itself after some form of RF excitation. However, to allow for an image to be reconstructed, MR signals coming from different locations within the sample need to be distinguishable from each other (i.e. each signal needs to be allocated to its specific location within the measured volume). In other words, in order to resolve anatomical structures the signal has to depend on its spatial location. This procedure is called spatial encoding.

#### 2.2.1 Spatial encoding

Typically, spatial encoding is performed by intentionally superimposing spatially varying linear magnetic fields, which are referred to as a gradient fields  $(G_x, G_y, G_z)^t = \vec{G}$ , on the static magnetic field  $\vec{B}_0$  via

$$\vec{B}(\vec{r}) = \vec{B}_0 + (\vec{G} \cdot \vec{r}) = B_0 + (\vec{G} \cdot \vec{r}). \quad (2.40)$$

According to equation (2.40), the superimposed gradient field changes the local field strength at each location  $\vec{r} = (x, y, z)^t$  which, in turn, leads to spins at different positions having different resonance frequencies. Hence, following equation (2.9), the position of each spin package is encoded by its resonance frequency  $\omega_0(\vec{B}(\vec{r}))$ , yielding

$$\omega_0(\vec{r}) = \gamma(B_0 + \vec{G}(\vec{r})). \quad (2.41)$$

By convention,  $\vec{G}(\vec{r}) \parallel \vec{B}_0$  in order to preserve the original quantization axis of the nuclear spins. This local variation of the static magnetic field by means of gradient fields is the underlying principle of MRI. However, because there are three dimensions  $(x, y, z)$ , it is necessary to encode each dimension in a different way. In the following, it is briefly explained how a conventional MRI pulse sequence manages to encode each of the three dimensions in order to unambiguously assign each signal to its right location.

### Slice selection

The first step consists of the slice selection<sup>10</sup>. Here, the magnetic field  $B_0$  is superimposed with a gradient field  $\vec{G}(z)$  in  $z$ -direction, yielding

$$\omega_0(z) = \gamma(B_0 + G_z \cdot z). \quad (2.42)$$

Importantly, this superposition of  $\vec{G}(z)$  is performed while the excitation pulse  $\omega_{RF}$  is applied. Accordingly, by excitation of only a particular Larmor frequency  $\omega_0(z)$ , this enables the selection of a two-dimensional slice (i.e., since only spins within this slice fulfill the resonance condition). In reality, however, a block (cuboid with a certain width  $\Delta z$ ) is excited rather than a 2D slice because the excitation pulse has a finite bandwidth  $\Delta\omega_{RF}$ . The exact position of the slice is defined by the center frequency  $\omega_{RF}$  of the excitation pulse, whereas the width  $\Delta z$  depends on the bandwidth  $\Delta\omega_{RF}$  as well as the strength of the gradient via

$$\Delta z = \frac{\Delta\omega_{RF}}{2\pi\gamma G_z}. \quad (2.43)$$

This means that, for example, if one wants to excite a thinner slice either (i) the excitation bandwidth needs to be decreased, or similarly, (ii) the gradient strength increased.

### Frequency encoding

After having performed the slice excitation, any subsequent signals to be acquired must, without exception, come from within the excited cuboid, since only these spin packages yield transversal magnetization in the first place. So, the only two remaining dimensions of the signal which have to be encoded are the  $x$  and  $y$  directions. Therefore, a second gradient which encodes the signal in the  $x$ -direction<sup>11</sup> is additionally applied while the signal is acquired (i.e. during the readout<sup>12</sup>), given by

$$\omega_0(x) = \gamma(B_0 + G_x \cdot x). \quad (2.44)$$

Equation (2.44) implies that the measured signal no longer consists out of a single frequency (i.e. even ignoring CS effects). In fact, the MR signal instead contains the sum

<sup>10</sup> wlog performed in  $z$ -direction.

<sup>11</sup> Again, wlog in  $x$ -direction. Also, technically in  $x'$ -direction, but for the sake of simplicity referred to as  $x$ -direction.

<sup>12</sup> Hence, the FE direction is also often referred to as readout direction.

## 2 Fundamental Principles

of all frequencies which is why it is called a frequency spectrum. Now, by applying a first FT in the  $x$ -direction, these frequencies (or rather their intensities) can be assigned to their actual signal distribution as a function of  $x$ . However, as of now, the MR signal at each position  $x$  is still the sum across each line in the residual  $y$ -direction (i.e. so-called frequency projections).

### Phase encoding

Lastly, the remaining spatial dimension is encoded by manipulating the phase of the precessing spin packages. Again, similar to the frequency encoding (FE), a linear gradient  $G_y$  is utilized to encode the missing third dimension. However, in contrast to (i) the slice selection gradient which is applied during RF excitation and (ii) the FE gradient which is applied during the signal acquisition, importantly, (iii) the phase encoding (PE) gradient is applied in between the excitation and readout. During this phase encoding period  $t_{PE}$ , the magnetization along the  $y$ -direction<sup>13</sup> accumulates a phase  $\phi(y)$  which specifically depends on its exact  $y$ -location, given by

$$\underbrace{\phi(y) = \frac{\gamma}{2\pi} \int_{t_0}^{t_{PE}} G_y(t) \cdot y dt}_{N_y \text{ times}} \quad (2.45)$$

Remarkably, this phase accumulation remains unchanged during the subsequent signal acquisition (i.e. during the aforementioned FE which is performed along with the readout). However, in order to obtain an image with a resolution of  $N_y$  data points (i.e.  $N_y$  pixel in the  $y$ -direction) this process must be repeated  $N_y$  times with a different gradient strength  $G_y$  for every repetition. After  $N_y$  repetitions, the final image is calculated by applying a second FT in the  $y$ -direction, which converts the frequency projections obtained from the FE step into a 2D image. In addition, it should be pointed out that frequency and phase encoding are mathematically equivalent. Nevertheless, in reality PE is more prone to e.g. motion-induced artifacts simply because it takes longer than FE.

To summarize, a conventionally acquired 2D image is obtained by manipulating the frequencies and phases of spin packages using linear magnetic gradient fields to encode the MR signal in a specific manner. As the direction, strength, timing and duration of these gradient fields are known, the encoded and subsequently acquired signals can be used to non-invasively image, for instance, anatomical structures by calculating a 2D FT (i.e.

<sup>13</sup>Again, technically the  $y'$ -direction of the rotating frame of reference.

essentially, the local proton density distribution is mapped, along with  $T_1$  and  $T_2$  effects, as explained in subsection 2.2.2).

### **k-space**

The raw data acquired during an MR experiment is recorded in the so-called *k-space*. In principle, the k-space is just an array of complex numbers directly obtained from the signal acquisition via an analog to digital converter (ADC), e.g. by measuring a FID. In fact, depending on the applied imaging pulse sequence, the encoded MR signal is recorded to fill up k-space in a specific manner. However, the location in k-space represents a spatial frequency (i.e.  $k_x$  and  $k_y$  in the 2D case) rather than a position in the real space (i.e.  $x$  and  $y$  in image-space). Consequently, this means that every point in k-space contains information about the spatial frequency and phase of the entire final image (i.e. one k-space point has information about all pixels). Therefore, the center of k-space (i.e. low spatial frequencies) contributes to the basic contrast (i.e. brightness) as well as coarse shapes of the image. On the contrary, the periphery of k-space (i.e. high spatial frequencies) determines sharp edges, sudden intensity changes as well as delicate details within the image. By applying a 2D FT, as briefly summarized above, this frequency representation of the spatial information (i.e. k-space) is converted into its spatial domain (i.e. image-space) which, ultimately, yields the desired MR image.

### **2.2.2 Imaging pulse sequences**

For the actual image acquisition an imaging pulse sequence is applied. There exist various methods which all excite and manipulate the MR signal in such a manner that the previously explained spatial encoding and acquisition of k-space can actually occur. In principle, however, MR imaging sequences can be classified into two types, i.e. (i) spin echo (SE) and (ii) gradient echo, or gradient-recalled echo (GRE) sequences. Within the scope of this thesis, both types of imaging sequences are used. Therefore, in the following, the basic concept of each type of pulse sequence is briefly described.

#### **Spin echo**

The underlying principle of the SE sequence is the manipulation of the FID signal. To accomplish this, SE sequences employ a pair of two successive RF pulses, typically a  $90^\circ$  followed by a  $180^\circ$  pulse. The first pulse (i.e.  $90^\circ$ ) tips the magnetization into the transversal plane, thus, generating a FID which immediately starts decaying  $\propto e^{-t/T_2^*}$ .

## 2 Fundamental Principles

Interestingly, this decay is dominated by field inhomogeneities, as indicated by  $T_2^*$  (see equation (2.33)). Consequently, those spins which reside in a slightly stronger local magnetic field precess somewhat faster compared to others in slightly weaker magnetic fields (i.e. they gain phase relative to others, thus, effectively damping the macroscopic transversal magnetization). However, after time  $t = \frac{TE}{2}$ , the second RF pulse (i.e.  $180^\circ$ ) is applied which, accordingly, turns the entire spin system by  $180^\circ$ . As a result, the spins which had just gained phase now essentially lack behind. Yet, as they continue to precess faster, they eventually rephase again with the slower precessing spins, thus, generating a signal recovery at the echo time (TE). This signal recovery is accordingly named spin echo and was first observed by Erwin Hahn<sup>14</sup> in 1949. After a certain repetition time (TR), this entire procedure is repeated. In total,  $N_y$  repetitions are performed until the entire k-space is filled up (i.e.  $N_y$  PE steps). The MR signal intensity produced by such a SE sequence is given by

$$S_{SE} \propto \kappa \cdot \rho \cdot \left(1 - e^{-TR/T1}\right) \cdot e^{-TE/T2}. \quad (2.46)$$

Here,  $\kappa$  is a instrumental scaling constant (i.e. encompassing electronic signal amplification etc.) and  $\rho$  is the proton density (i.e. encompassing the local distribution of spins).

### Gradient echo

Again, the underlying principle behind GRE sequences is the manipulation of the FID signal. However, GRE sequences manipulate the FID itself (i.e. before the underlying  $T_2^*$  decay considerably weakens the FID signal). In order to generate an echo, a GRE sequence exploits the rapid dephasing and subsequent rephasing of the FID signal by applying gradient fields. After irradiation of a RF pulse, a first gradient field is applied across the entire field of view (FOV) (i.e. the dephasing gradient). Accordingly, during the application of the dephasing gradient, spins at different locations along the gradient direction have different resonance frequencies, which results in an accelerated dephasing of the FID. Shortly afterwards, after the time  $\frac{TE}{2}$  has passed, a second gradient field is applied with the exact same strength but with opposite polarity (i.e. the rephasing gradient). As a result of this rephasing gradient pointing in the opposite direction, exactly those spins which were just dephased are now effectively refocused again, and thus, the signal of the FID is recovered<sup>15</sup> again at time  $t = TE$ . Therefore, this type of signal

<sup>14</sup> Originally, Hahn used two  $90^\circ$  pulses. In fact, two successive RF pulses of any flip angle (FA) yield an echo, which is why a SE generated by two FA other than  $90^\circ$ - $180^\circ$  also is referred to as *Hahn echo*.

<sup>15</sup> Except for the continuous underlying  $T_2^*$  decay.

recovery is referred to as gradient echo. Following that, any residual transversal magnetization is then crushed by means of spoiler gradients. Finally, after a certain TR, which for GRE sequences can be extremely short, the whole process is repeated until the entire k-space is traversed and recorded. Because the TR is so short there is not enough time for a complete recovery of magnetization towards  $z$ -direction (i.e.  $TR \ll T_1$ ). Therefore, after several repetitions of duration TR, the flip angle (FA) yielding maximal transversal magnetization is significantly smaller than  $90^\circ$ . This optimal FA is referred to as *Ernst angle*<sup>16</sup> and it is given by

$$\alpha_E = \arccos(e^{-TR/T_1}). \quad (2.47)$$

Effectively, using  $FA = \alpha_E$  allows the residual magnetization in  $z$ -direction to be maximized, which after a several repetitions TR approaches a so-called imaging steady-state. Moreover, the MR signal intensity produced by such a GRE sequence with optimal FA is given by

$$S_{GRE} \propto \kappa \cdot \rho \cdot \sin(\alpha_E) \frac{1 - e^{-TR/T_1}}{1 - \cos(\alpha_E)e^{-TR/T_1}} e^{TE/T_2^*}. \quad (2.48)$$

Again,  $\kappa$  is a instrumental scaling constant and  $\rho$  the proton density. Note that, compared to the SE pulse sequence signal acquisition (2.46), the signal acquired with a GRE sequence is compromised by a factor of  $e^{TE/T_2^*}$  as opposed to  $e^{TE/T_2}$  (i.e. SE sequences intrinsically compensate for magnetic field inhomogeneities, assuming perfect  $180^\circ$  inversion pulses). However, TE as well as TR can significantly differ between various pulse sequences.

## 2.3 Magnetization transfer (MT)

$^1\text{H}$  MR experiments in biological tissues resulted in the finding that magnetization from one compartment within the biological tissues can be transferred to another. The discovery of this MT between different compartments led to the pool model, wherein a pool of protons  $i$  (with identical chemical shifts  $\delta_i$ , relaxation times  $T_{1i}$  and  $T_{2i}$ , as well as exchange rates  $k_{ij}$ ) inter-exchanges magnetization with a second distinct pool  $j$ . In diluted aqueous solutions (such as biological tissues), there fundamentally exist three separate exchange mechanisms which enable MT:

---

<sup>16</sup> First described by Richard R. Ernst.

## 2 Fundamental Principles

**(i) Chemical exchange:** Chemically bound protons physically swap positions with protons of other chemicals (i.e. other pools). Effectively, magnetization is traded between different pools as nuclei are transferred from one type of molecule to another. Importantly, the quantum-mechanical state of the nuclear spin is not changed during this chemical exchange (CE). The effect mainly depends on the exchange rate (i.e. the reaction rate) and the CS between the exchanging pools. A more detailed description of this process is provided in section 2.3.1.

**(ii) Dipolar interactions:** Various spin systems are coupled through dipolar interactions. Essentially, this results in cross-relaxation pathways between interacting pools, enabling MT. Primarily, the intensity of dipolar interaction effects depends on the specific types of involved spins, the distance and angle between them as well as their relative motion to each other. This mechanism is also known as the nuclear Overhauser effect (NOE). A specific case of such a process is explained in section 2.3.2.

**(iii) Molecular exchange:** Depending on the macromolecular environment and its actual physical geometry, one specific molecule can essentially either be in a free or bound state of motion. Accordingly, as the molecule diffuses through the different compartments its chemical shift and relaxation rates vary. Hence, magnetization is transferred between different pools. This is exploited in the semi solid MT (ssMT) which is explained in section 2.3.3.

### 2.3.1 Chemical exchange (CE)

As already briefly mentioned, CE is the physical exchange of protons of individual pools [97]. These chemical reactions between primarily water and other labile protons bound in, for instance, functional groups of proteins, peptides or metabolites are governed by acid-base-reactions. They are characterized by the exchange rate  $k_{sw}$ <sup>17</sup> between the solute pool  $s$  and the water pool  $w$ . For first order chemical reactions, which are proportional to the concentration  $c$ , this is approximated by [97, 98]

$$k_{ex} := k_{sw} = k_{base} \cdot c[OH^-] + k_{acid} \cdot c[H_3O^+] + k_{buffer}, \quad (2.49)$$

---

<sup>17</sup> Throughout this thesis  $k_{ex}$  refers to  $k_{sw}$ , i.e. the exchange rate from low-concentrated solutes  $s$  to the abundant water pool  $w$ .

where  $c[\text{OH}^-]$  and  $c[\text{H}_3\text{O}^+]$  are the concentrations of hydroxide and hydronium ions, respectively.  $k_{\text{base}}$ ,  $k_{\text{acid}}$  and  $k_{\text{buffer}}$  are the base-, acid-, and respectively, buffer-catalyzed reaction rates. The rather diverse complexity of the involved catalysis mechanisms<sup>18</sup> is, for the sake of simplicity, encompassed by  $k_{\text{buffer}}$ . Moreover,  $k_{\text{base}}$ ,  $k_{\text{acid}}$  and  $k_{\text{buffer}}$  all exhibit a strong temperature dependence<sup>19</sup> which is mathematically described by the *Arrhenius law* [99]. By utilizing the definition of the pH- and pOH-value (explained in detail in subsection 2.6), as well as the dissociation constant of water ( $pK_w := -\log_{10}K_w = \text{pH} + \text{pOH}$ ) equation (2.49) can be rearranged to [99]

$$k_{\text{ex}}(\text{pH}, T) = k_{\text{base}}(T) \cdot 10^{\text{pH} - pK_w(T)} + k_{\text{acid}}(T) \cdot 10^{-\text{pH}} + k_{\text{buffer}}(\text{pH}, T, c_{\text{buffer}}). \quad (2.50)$$

Depending on the pH milieu, the temperature  $T$  and the type of functional group the ex-

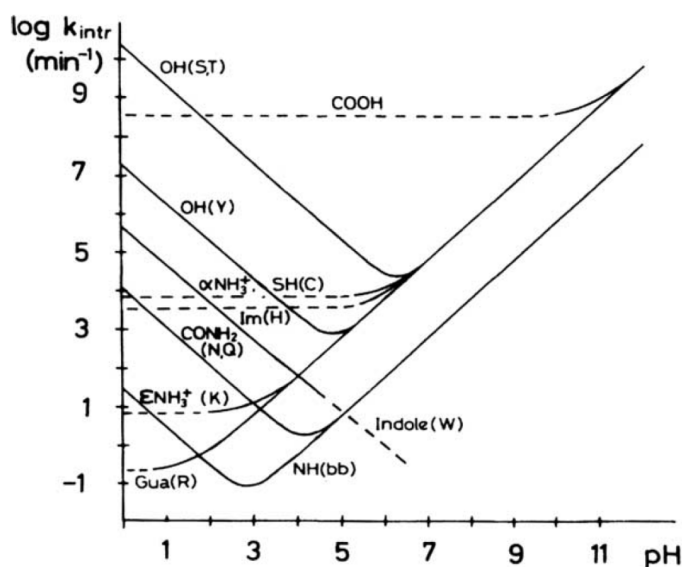


**Figure 2.5:** Illustration of the exchange rates  $k_{\text{ex}}$  for various functional groups in amino acids as a function of pH at  $T = 25^\circ\text{C}$ . The amino acids are denoted by their one-letter code [100], whereas (bb) refers to the backbone of the amino acid chain. Gua and NH (denoted at the bottom) refer to guanidyl ( $(\text{NH}_2)_2^+$ ) and amide (NH) protons, respectively, which are both used for pH mapping in the developed method. Note the logarithmic axis of ordinates, the notation of  $k_{\text{intr}}$  and the unit of  $\text{min}^{-1}$  (as opposed to  $k_{\text{ex}}$  and Hz, respectively, which are used throughout this thesis). Figure taken from [101].

change rate can vary by several orders of magnitude (Figure 2.5). In general, the exchange

<sup>18</sup> Severely depending on e.g. the specific functional group.

<sup>19</sup> As, in principle, every chemical reaction rate.

rate depends exponentially on temperature [40, 102].

### 2.3.2 Exchange-relayed nuclear Overhauser effect (rNOE)

Certainly, not all  $^1\text{H}$  in biological molecules can physically change their location. However, the non-exchanging, covalent bound protons can still transfer magnetization through space via dipolar interactions. This dipolar coupling between nuclear spins is known as the NOE [103]. If such a bound nuclear spin is excited (e.g. by application of a RF field), the magnetization can then be distributed through the entire molecule via so-called spin diffusion (i.e. intra-molecular MT). Importantly, this process enables the transport of magnetization from immobile, non-exchanging protons to labile, exchanging ones. Consequently, the latter can transfer magnetization to free water protons by means of chemical exchange (i.e. inter-molecular MT). This combination of (i) intra-molecular spin diffusion and subsequent (ii) inter-molecular CE is the dominant pathway of MT between non-exchanging, bound protons in mobile macromolecules and the water pool [30, 104, 105]. It is accordingly called the exchange-relayed NOE (rNOE) [106] and is schematically depicted in Figure 2.6a. Because the rNOE pathway depends on the relatively slow intra-molecular process of spin diffusion<sup>20</sup>, the effective rNOE exchange rates are in the order of  $\sim (2 - 5)$  Hz [107].

### 2.3.3 Semi-solid magnetization transfer (ssMT)

One important characteristic of biological tissues is the presence of large macromolecular structures. They primarily consist of immobile, semi-solid<sup>21</sup> textures within cells such as cell membranes, surface proteins or the cytoskeleton, for instance. Interactions which result in a transfer of magnetization between protons of this so-called macromolecular matrix and those of free water molecules are collectively referred to as the ssMT, which is depicted in Figure 2.6b. This process exploits the increased correlation time of water molecules, originating from their reduced mobility while being temporarily bound to the surface of the molecular matrix. Essentially, magnetization from within the matrix is transferred via (i) intra-molecular spin diffusion, (ii) inter-molecular NOE, and (iii) CE to water protons residing close to the matrix surface [30], as described in the previous subsections. Lastly, these water molecules (bound to the molecular matrix) diffuse into the free water state via the continuous process of (iv) molecular exchange [108]. Effectively,

<sup>20</sup> Effectively, acting like the bottle neck of the entire MT pathway of rNOE processes.

<sup>21</sup> Not truly rigid, but exhibiting solid-like characteristics.

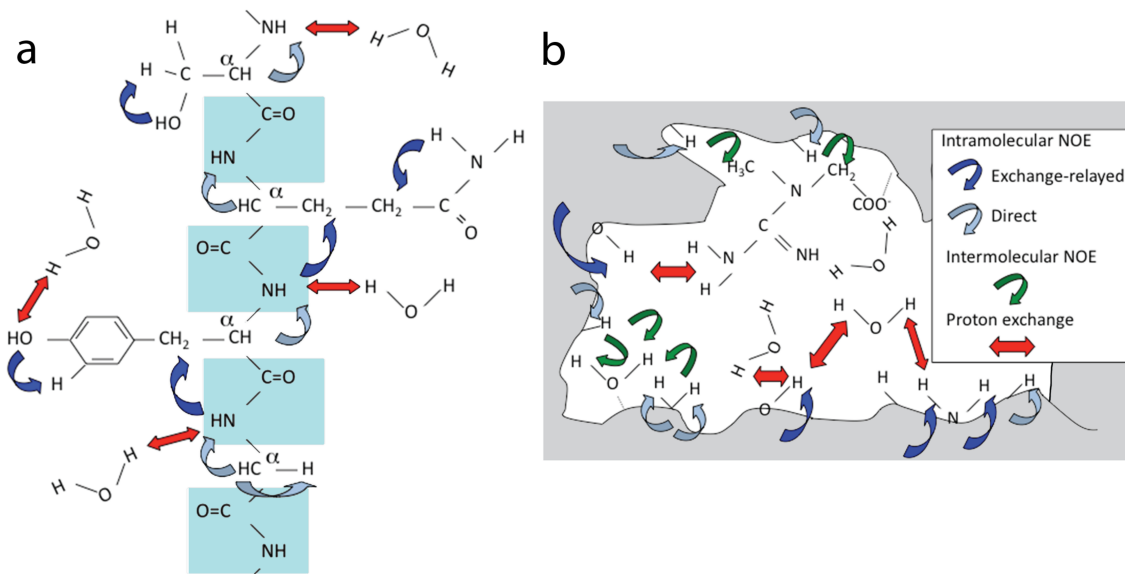


**Figure 2.6:** (a) The magnetization transfer (MT) pathway of the exchange-relayed NOE (rNOE) is a two-step process enabling MT from non-exchanging, covalent bound protons of macromolecules (e.g.  $-\text{CH}_2-$ ) to water protons. Firstly, magnetization is transferred via intra-molecular pathways (i.e. spin diffusion, blue and gray arrows) to protons of chemically exchanging groups (e.g.  $-\text{OH}$ ) within the same molecule. Secondly, further transfer of magnetization to water protons is achieved via chemical exchange (CE) (red arrows). (b) The MT pathway of semi solid MT (ssMT) enables the transfer of magnetization between the macromolecular matrix (gray background) and water protons. Firstly, magnetization is distributed within the macromolecular matrix via intra-molecular processes (blue and gray arrows). Thereafter, magnetization is transferred to water molecules, which are temporarily bound to the molecular matrix, via intermolecular dipolar interactions (green arrows) as well as chemical exchange (red arrows). Edited, both original figures taken from [30].

the resulting exchange rates are in the order of  $\sim 40$  Hz [109]. Similar to solid structures, the protons of the semi-solid molecular matrix have short relaxation times  $T_2$  in the range of  $\sim \mu\text{s}$ . Consequently, after application of a FT, this short  $T_2$  results in a relatively broad line width  $\Gamma$  of several kHz (cf. Figure 2.3), which is why a direct detection is a quite difficult task. Nevertheless, the ssMT can be used to obtain a so-called magnetization transfer contrast (MTC)<sup>22</sup> [110] even at large offsets (i.e. several ppm). The MTC is indirectly achieved via the direct measurement of the modified (i.e. attenuated) water signal.

<sup>22</sup> As MTC is the contrast obtained via ssMT effects, both notations (MTC and ssMT) are often used interchangeably within the field of MT-MRI and also in this thesis.

## 2.4 Chemical exchange saturation transfer (CEST)

Chemical exchange saturation transfer (CEST) [28–33] allows the indirect detection of low-concentrated biomolecules with concentrations in the millimolar (mM) range. In a CEST experiment, this is achieved by exploiting the  $^1\text{H}$  magnetization transfer from the low-concentrated solute pool  $s$  to the abundant free water pool  $w$ . More specifically, CEST-MRI utilizes a frequency-selective RF preparation prior to a conventional MRI readout which magnetically labels CE processes occurring between labile protons of low-concentrated biomolecules with a concentration in the order of  $c_s \sim 10$  mM (e.g. hydrogen nuclei of amide and guanidyl groups in proteins and peptides, see subsection 2.4.3) and water protons with a concentration of  $c_w \approx 55.5 \text{ M}^{23}$ . Consequently, the CEST experiment exploits the benefits of MRS and MRI by combining

- (1) the different chemical shift properties of protons in different functional groups (high spectral resolution and specificity of MRS) with
- (2) the signal acquisition of water protons (high spatial resolution and strong signal intensities of MRI).

In other words, CEST utilizes the magnetization transfer in order to modify<sup>24</sup> the strong water signal, thus, enabling the indirect detection of low-concentrated biomolecules. In comparison to the direct detection of low-concentrated biomolecules (MRS), the indirect detection via the modified water signal yields a  $^1\text{H}$  signal amplification which is referred to as the proton transfer enhancement (PTE). The PTE is governed by the longitudinal relaxation time of protons in free water molecules ( $T_{1w}$ ) and the exchange rate of the involved magnetization transfer pathway ( $k_{ex}$ ). Assuming a low-concentrated solute pool  $s$  in comparison to the water pool  $w$ , the PTE is approximated via [111]

$$\text{PTE} \approx k_{sw} \cdot T_{1w} = k_{ex} \cdot T_{1w} = \frac{k_{ex}}{R_{1w}} \quad (2.51)$$

In words, the PTE signal enhancement depends on how fast magnetization is transferred to the water signal ( $k_{ex}$ ) and how long the magnetization is stored within the modified water signal ( $T_{1w}$ ). Because of this essentially higher SNR of the strong water signal, CEST-MRI enables the visualization of low-concentrated biomolecules with spatial resolutions in the order of  $\sim 1 \text{ mm}^3$  compared to MRS-based methods in the order of  $\sim 1 \text{ cm}^3$ .

<sup>23</sup> With  $1 \text{ M} = 1 \frac{\text{mol}}{\text{l}}$ , where  $1 \text{ mol} \triangleq N_A \approx 6.022 \cdot 10^{23}$ .

<sup>24</sup> More specifically, water signal attenuation due to frequency-selected, magnetically labeled labile protons exchanging magnetization with water protons through the process of CE.

Equation (2.51) implies an increase of the CEST effect with increasing exchange rates  $k_{ex}$  which, in principle, holds true. In reality, however, too fast exchange rates can not be resolved by means of CEST ( $k_{ex}$  values within the so-called fast-exchange regime, i.e.  $k_{ex} > \delta\omega_s$ , subsection 2.5.3). Typical exchange rates relevant for CEST effects in vivo are found in the slow to intermediate exchange regime.

### 2.4.1 Saturation transfer

In principle, the CEST experiment consists of two separate elements:

- (1) The frequency specific saturation phase (presaturation).
- (2) The subsequent acquisition of the modified water signal.

In the context of magnetization transfer experiments, the term *saturation* is used to describe the reduction of magnetization of a distinct pool of nuclear spins. More specifically, considering spin  $I = \frac{1}{2}$  ensembles (i.e. two energy state systems), saturation corresponds to the equal occupation of both states  $|\alpha\rangle$  and  $|\beta\rangle$ . As a consequence, the polarization is zero and, thus, the macroscopic magnetization of a completely saturated two state spin ensemble is zero.

In the simplest CEST experiment, frequency-selective saturation of a solute pool  $s$  is realized using a continuous wave (cw) RF-irradiation of a specific frequency ( $\omega_{RF}$ ), saturation duration ( $t_{sat}$ ) and RF amplitude ( $B_1$ ), which hereafter simply is collectively referred to as the presaturation. The selectivity of the presaturation pulse in the frequency domain (i.e. the spectral width  $\delta\nu$ ) is inversely related to its duration in the time domain ( $t_{sat}$ ), i.e.  $\delta\nu \propto t_{sat}^{-1}$ . During the presaturation phase, in which the pool  $s$  is saturated, the saturation of pool  $s$  is (partially<sup>25</sup>) transferred to the free water pool  $w$  by means of magnetization transfer mechanisms described in section 2.3, e.g. via chemical exchange. The resulting accumulation of saturation in the water signal is the reason for the signal amplification due to the PTE, equation (2.51). Consequently, this leads to a reduction of the water magnetization. Immediately after the presaturation phase, the  $z$ -component<sup>26</sup> of the modified water signal  $M_{zw}(\omega_{RF})$  is acquired.

<sup>25</sup> For complete saturation in the living organism,  $t_{sat}$  must at least equal several times the longitudinal relaxation time, typically  $t_{sat} \approx (3 - 5) \times T_{1w}$ , i.e. several seconds (Figure 5.9).

<sup>26</sup> Hence, CEST was historically also referred to as Z-spectroscopy.

### 2.4.2 The Z-spectrum

By repeating this procedure consisting of (1) a presaturation followed by (2) the subsequent water signal acquisition at various frequency offset ( $\Delta\omega$ ) and normalizing the acquired water signals with the unsaturated thermal equilibrium magnetization of water ( $M_{zw}^0$ ), one obtains the so-called Z-spectrum via

$$Z(\Delta\omega) = \frac{M_{zw}(\Delta\omega)}{M_{zw}^0} \quad (2.52)$$

where  $\Delta\omega = \omega_{RF} - \omega_w$  represents the frequency offset of the applied RF presaturation pulse ( $\omega_{RF}$ ) with respect to the water signal resonance ( $\omega_w$ ). Importantly, if the water signal acquisition is performed using e.g. a conventional MRI readout<sup>27</sup>, this results in one distinct Z-spectrum in every single pixel of the acquired MR image. Vice versa, each acquired data point at frequency offset  $\Delta\omega$  in the Z-spectrum corresponds to an entire image.

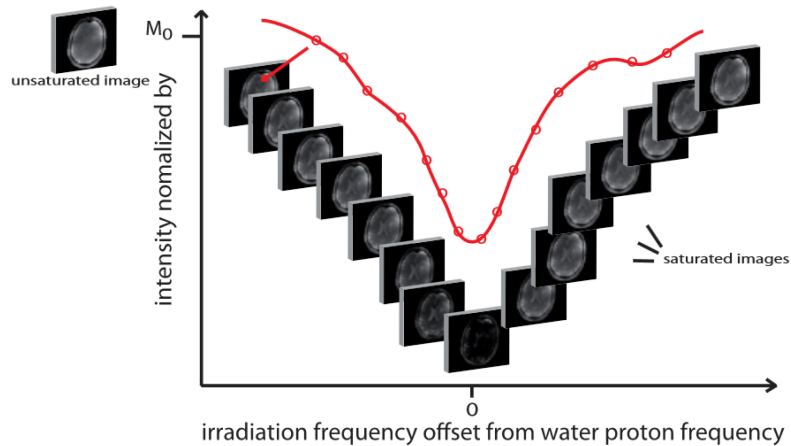


**Figure 2.7:** In a CEST-MRI experiment, immediately after presaturation an MR image is acquired for each frequency offset  $\Delta\omega$  within the Z-spectrum. By normalizing all images with an additionally acquired unsaturated image  $M_0 \hat{=} M_{zw}^0$  (thermal equilibrium magnetization of water), one obtains an individual Z-spectrum with values  $\in [0, 1]$  for each pixel (i.e. equation (2.52)). Depending on the specific frequency offset, the images exhibit different signal intensities. Edited, original taken from [58]).

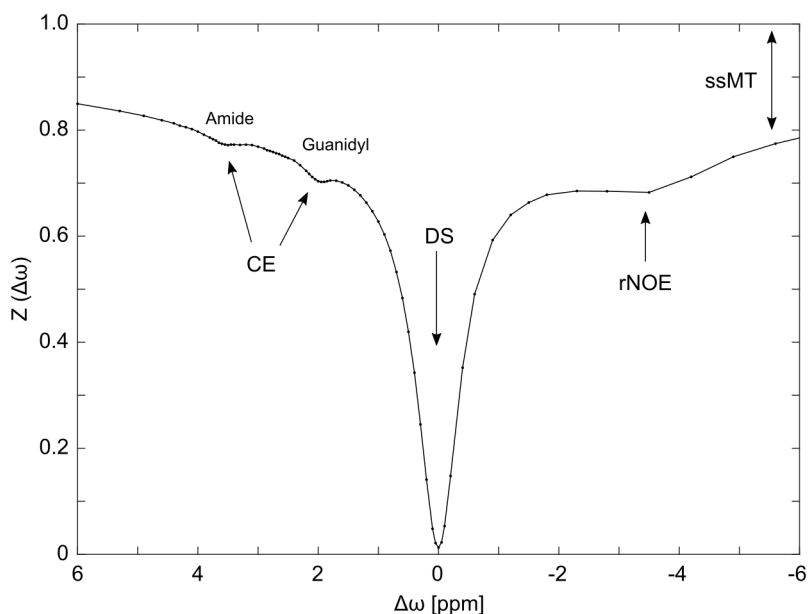


**Figure 2.8:** In vivo Z-spectrum of a tumor lesion in a tumor-bearing mouse ( $B_0 = 9.4$  T,  $B_1 = 1$   $\mu$ T). Apart from the direct water saturation (DS), which occurs if the RF presaturation is close to the water resonance, the most noticeable effect in vivo is the broad and pronounced vertical offset due to the semi solid magnetization transfer (ssMT). In comparison, contributions to the in vivo Z-spectrum due to chemical exchange (CE) or the exchange-related nuclear Overhauser effect (rNOE) are significantly smaller. The developed method, uses the amide and guanidyl signals which resonate at  $\Delta\omega_{amide} \approx 3.6$  and  $\Delta\omega_{gua} \approx 2.0$  ppm, respectively. By convention, the higher frequencies are plotted to the left.

### 2.4.3 Endogenous CEST signals

An in vivo Z-spectrum is presented in Figure 2.8. If a CEST experiment is performed in a living organism (in vivo), several concomitant MT effects simultaneously occur (section 2.3). The most prominent are:

- The direct water saturation (DS), which occurs if the RF presaturation is close to the water resonance (i.e.  $Z(\Delta\omega \approx 0) \approx 0$ ). The DS dominates the Z-spectra close to the water resonance.
- The semi solid magnetization transfer (ssMT), which is the most noticeable effect in vivo apart from the DS. The ssMT is responsible for the broad and pronounced vertical offset in an in vivo Z-spectrum in the range of approximately  $\pm 50$  ppm and

<sup>27</sup> As opposed to e.g. the simple acquisition of an unlocalized FID.

## 2 Fundamental Principles

has its maximum at around  $\Delta\omega \approx -2.5$  ppm. The ssMT gives rise to the magnetization transfer contrast (MTC).

- Effects due to chemical exchange (CE), which originate from exchanging protons of endogenous functional groups e.g. in mobile proteins and peptides or metabolites. The most prominent CE effects *in vivo* are due to amide (-NH) and guanidyl  $(-\text{NH}_2)_2^+$  protons resonating at a frequency offset of  $\Delta\omega(\text{amide}) \approx 3.6$  and  $\Delta\omega(\text{gua}) \approx 2.0$  ppm, respectively. In this thesis, the amide and guanidyl CEST signals are utilized for pH mapping. Amide protons have exchange rates of 30 to 280 Hz [31, 40, 46, 58, 105, 112–114] whereas guanidyl protons have exchange rates of 600 to 1600 Hz [38, 40, 97, 112]. Another CE contribution to the *in vivo* Z-spectrum is due to fast exchanging amine protons (-NH<sub>2</sub>), resonating at  $\Delta\omega(\text{amine}) \approx 2.7$  ppm with exchange rates in the range of 700 to 10,000 Hz [42, 97]. The amine signal contribution to an *in vivo* Z-spectrum is not well resolved, due to the fast exchange rates leading to excessive peak broadening.
- Exchange-relayed nuclear Overhauser effects (rNOE), which originate from non-exchanging, covalent bound aliphatic protons (e.g. in macromolecules) at frequency offsets in the range of approximately -0.5 to -6.0 ppm. In addition, also rNOE effects on the positive frequency offset axis (i.e. downfield) are present which originate from aromatic protons.

### 2.4.4 The CEST pulse sequence

Fundamentally, the data acquisition in CEST-MRI consists of two separate elements:

- (1) The presaturation<sup>28</sup> block which enables the desired contrast, i.e. frequency selective magnetic labeling (Figure 2.9, green).
- (2) The subsequent image readout block which records the modified water signal, i.e. acquisition of MR images (Figure 2.9, blue).

In order to detect the decaying CEST contrast, the image acquisition needs to be performed immediately after the presaturation preparation. Therefore, fast imaging techniques are required in CEST-MRI. To acquire a Z-spectrum, the presaturation and subsequent image acquisition are repeated for each frequency offset  $\Delta\omega$ , until all offsets of the desired  $Z(\Delta\omega)$ -spectrum are recorded (Figure 2.7). In other words,  $\Delta\omega$  is changed

---

<sup>28</sup> Within this thesis also interchangeably referred to as saturation.

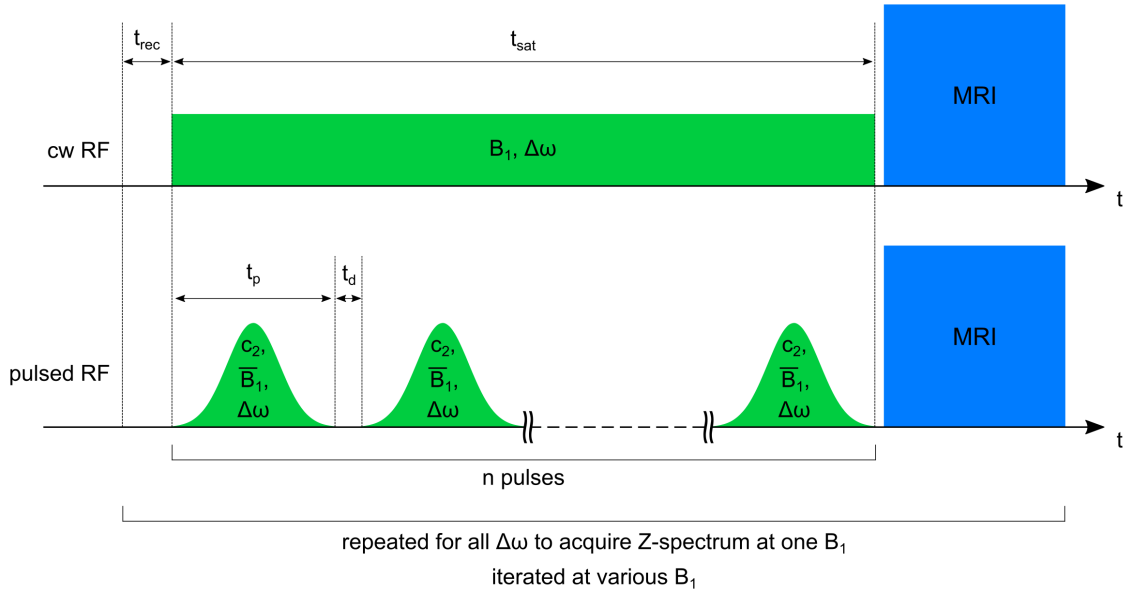


**Figure 2.9:** The CEST pulse sequence consists of a frequency-selective presaturation block (green) and the subsequent acquisition of the modified water proton signal, i.e. the imaging block (blue). In this thesis, either a cw (top, one rectangular pulse) or a pulsed presaturation (bottom,  $n$  Gaussian-shaped pulses) were used. During the frequency selective presaturation phase, magnetization is transferred e.g. from a low-concentrated solute pool to the abundant water pool. Immediately afterwards, the modified water signal is used for image acquisition.

for each acquired image  $M(\Delta\omega)$ . Presaturation is achieved using either a cw saturation scheme or a pulsed saturation scheme. For a cw saturation, a rectangular RF pulse of duration  $t_{sat}$  and well-defined  $B_1$  is applied (Figure 2.9, top). In contrast, for a pulsed saturation, a pulse series<sup>29</sup> of  $n$  RF pulses<sup>30</sup> is applied, each with a duration of  $t_p$  and an associated mean amplitude  $B_1$  (Figure 2.9, bottom). For a pulsed presaturation, the delay time  $t_d$ <sup>31</sup> or increased in order to decrease the specific absorption rate (SAR) of RF energy in the tissue. In this context, the DC is defined via

$$DC = \frac{t_p}{t_p + t_d}, \quad (2.53)$$

<sup>29</sup> Also referred to as pulse train.

<sup>30</sup> In this thesis, Gaussian-shaped pulses were used for the pulsed CEST experiments in creatine model solutions although, in principle, the pulses can have any shape.

<sup>31</sup> To completely dephase any residual transversal magnetization.

## 2 Fundamental Principles

which is also used to determine the total saturation time of pulsed experiments via

$$t_{sat} = n \cdot t_p + (n - 1) \cdot t_d = (n - 1) \cdot \frac{t_p}{DC} + t_p. \quad (2.54)$$

For a cw presaturation, it holds true that  $DC = c_1 = c_2 = 1$ .

## 2.5 Theory of saturation transfer and quantitative CEST

This section covers the theoretical approach on magnetization transfer experiments, such as CEST. For any further and more detailed descriptions, the interested reader may refer to review articles such as [30–32, 58].

### 2.5.1 Pool model

The pool model mathematically describes the magnetization transfer processes. The simplest pool model is the two-pool model which takes into account the free abundant water proton pool  $w$  and the labile protons of a low concentrated solute pool  $s$ , e.g. amide or guanidyl protons. Importantly, each pool is defined as a set of protons exhibiting identical resonance frequencies, relaxation rates and exchange rates. In 1958, McConnell [115] used such a system consisting of two distinct pools to mathematically formulate the magnetization transfer between these pools via, essentially, expanding the conventional Bloch equations (2.26) to (2.28) by additional terms.

### 2.5.2 Bloch McConnell equations (BM)

The Bloch McConnell equations (BM) allow for a mathematical description of the time-evolution of the magnetizations of the two pools  $w$  and  $s$  ( $\vec{M}_w$  and  $\vec{M}_s$ , respectively), which

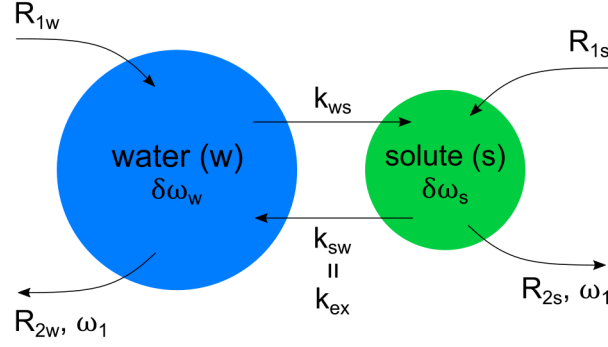


**Figure 2.10:** The two-pool model describes the magnetization transfer between the abundant free water proton pool ( $w$ ,  $c_w \approx 55.5$  M) and the low-concentrated solute proton pool ( $s$ ,  $c_s \sim 10$  mM), e.g. representing amide or guanidyl protons. Importantly, both pools ( $i = w, s$ ) are completely characterized by their specific relaxation rates  $R_{1i}$  and  $R_{2i}$ , and frequency offset  $\delta\omega_i$ . The exchange of magnetization between both pools is governed by the exchange rates  $k_{sw} \hat{=} k_{ex}$  and  $k_{ws}$ , respectively.

exchange magnetization amongst each other:

$$\frac{d}{dt}M_{xw} = -\Delta\omega_w M_{yw} - R_{2w}M_{xw} + k_{sw}M_{xs} - k_{ws}M_{xw} \quad (2.55)$$

$$\frac{d}{dt}M_{yw} = +\Delta\omega_w M_{xw} - R_{2w}M_{yw} + \omega_1 M_{zw} + k_{sw}M_{ys} - k_{ws}M_{yw} \quad (2.56)$$

$$\frac{d}{dt}M_{zw} = -\omega_1 M_{yw} - R_{1w}(M_{zw} - M_{zw}^0) + k_{sw}M_{zs} - k_{ws}M_{zw} \quad (2.57)$$

$$\frac{d}{dt}M_{xs} = -\Delta\omega_s M_{ys} - R_{2s}M_{xs} - k_{sw}M_{xs} + k_{ws}M_{xw} \quad (2.58)$$

$$\frac{d}{dt}M_{ys} = +\Delta\omega_s M_{xs} - R_{2s}M_{ys} + \omega_1 M_{zs} - k_{sw}M_{ys} + k_{ws}M_{yw} \quad (2.59)$$

$$\frac{d}{dt}M_{zs} = -\omega_1 M_{ys} - R_{1s}(M_{zs} - M_{zs}^0) \underbrace{-k_{sw}M_{zs} + k_{ws}M_{zw}}_{\text{exchange terms}} \quad (2.60)$$

More specifically, the BM equations describe the dynamics of pool  $w$  and  $s$ , respectively, i.e. equations (2.55) to (2.57) and (2.58) to (2.60), respectively. Here, by using  $i = w, s$ , (i) the relaxation rates of a particular pool  $i$  is given by  $R_{1i}$  and  $R_{2i}$ , (ii) the shift of the RF irradiation frequency compared to the Larmor frequency of that pool is given by  $\Delta\omega_i$  with  $\Delta\omega_i = \Delta\omega - \delta_i$ , and (iii) the exchange rates of the pools  $i, j = w, s$  is given by  $k_{ij}$  with  $w \neq s$ . Importantly, both pools are coupled to each other via  $k_{ij}$  in the exchange terms of

## 2 Fundamental Principles

each individual equation. The equilibrium condition defines the exchange rates via

$$k_{ws} \cdot M_{zw}^0 = k_{sw} \cdot M_{zs}^0 = k_{ex} \cdot M_{zs}^0, \quad (2.61)$$

with the thermal equilibrium magnetizations  $M_{zw}^0$  and  $M_{zs}^0$ , respectively (note, that in this thesis  $k_{ex} = k_{sw}$ ).  $M_{zw}^0$  and  $M_{zs}^0$  also define the relative population difference between the pools  $f_s$ , i.e. their relative concentrations or proton fractions, given by

$$f_s = \frac{M_{zs}^0}{M_{zw}^0} = \frac{k_{ws}}{k_{sw}} = \frac{k_{ws}}{k_{ex}}. \quad (2.62)$$

Furthermore, by utilizing equation (2.15),  $f_s$  can be expressed in terms of the total number of protons  $N_i$  of each pool  $i = w, s$  (i.e. their molecular concentrations  $c_i$ ) and the number of labile protons per molecule  $n_i$  (i.e. the number of exchanging protons per molecule) via

$$f_s = \frac{N_s}{N_w} = \frac{c_s \cdot n_s}{c_w \cdot n_w}. \quad (2.63)$$

In principle, the two-pool model can be expanded by incorporating additional solute pools (accordingly named  $s_2, s_3, s_4 \dots$ ). In analogy, such a model is then referred to as a multi-pool model in which each pool added to the system yields three additional equations, i.e. one equation for each spatial dimension. Importantly, this assumes that each solute pool  $i \neq w$  only interacts with the water pool  $w$  and not with other solute pools, which holds true if  $N_s \ll N_w \iff f_{i \neq w} \ll 1$ . However, for CE experiments in vivo this is a valid approach due to the dominating concentration of the water pool compared to the low-concentrated solute pools.

### Longitudinal relaxation rate in the rotating frame of reference ( $R_{1\rho}$ )

Analogous to  $T_1$ , the inverse of  $T_{1\rho}$  is defined as the longitudinal, or spin-lattice, relaxation rate in the rotating frame of reference ( $R_{1\rho}$ )

$$R_{1\rho} = \frac{1}{T_{1\rho}} \quad (2.64)$$

### 2.5.3 Analytical solution of the Bloch McConnell equations

The BM equations are a coupled system of first-order linear differential equations. This allows for an analytical solution by employing an eigenspace ansatz [57, 58, 116] given

by

$$\vec{M}(t) = \sum_{n=1}^6 \left( e^{\lambda_n t} \vec{v}_n \right) + \vec{M}^{ss}, \quad (2.65)$$

in which (i)  $\vec{M}(t)$  represents the magnetization vector of the two-pool system<sup>32</sup> described via equations (2.55) to (2.60), (ii)  $\lambda_n$  represents the eigenvalues of the corresponding eigenvectors  $\vec{v}_n$  and (iii)  $\vec{M}^{ss}$  represents the steady-state solution. Remarkably, the only relevant contribution in realistic<sup>33</sup> CE experiments is represented by  $\lambda_1$  (i.e. the smallest eigenvalue) which is collinear to the effective field  $\vec{B}_{eff}$ . Furthermore, in the rotating frame of reference (Figure 2.2),  $\lambda_1$  is equivalent to  $-R_{1\rho}$  [57, 117]

$$\lambda_1 = -R_{1\rho}. \quad (2.66)$$

Importantly, this simplifies the complicated system of coupled first-order linear differential equations to a one-dimensional problem, thus allowing for an analytical solution of the BM equations. In a CEST experiment, the water magnetization decays along the axis of  $\vec{B}_{eff}$  with the relaxation rate  $R_{1\rho}$  during application of the presaturation pulse  $t_{sat}$ . For a two-pool system,  $R_{1\rho}$  is given by

$$R_{1\rho}(\Delta\omega) = R_{eff}(\Delta\omega) + R_{ex}(\Delta\omega) = \underbrace{(R_{1w} \cos^2\Theta(\Delta\omega) + R_{2w} \sin^2\Theta(\Delta\omega))}_{R_{eff}} + R_{ex}, \quad (2.67)$$

in which (i)  $R_{eff}$  represents the intrinsic relaxation rate of pool  $w$ , (ii)  $R_{ex}$  represents the exchange dependent rate encompassing the additional relaxation rate due to the exchanging pool  $s$  and (iii)  $\Theta$  represents the angle of the rotating frame of reference (Figure 2.2), i.e. the angle between  $\vec{B}_0$  and  $\vec{B}_{eff}$ , given by

$$\Theta = \arctan \left( \frac{\omega_1}{\Delta\omega} \right). \quad (2.68)$$

Note, that  $R_{1\rho}$  is usually dominated by the water relaxation rate  $R_{eff}$ . However, in the presence of MT the additional term  $R_{ex}$  is necessary to fully characterize the MT contributions to the relaxation rate. As any additional relaxation pathway is mathematically

<sup>32</sup> Hence,  $n = 6$ .

<sup>33</sup> Assuming, that by the time the signal is measured all other components of the magnetization along other eigenvectors are completely decayed.

## 2 Fundamental Principles

described by  $R_{ex}$ , these MT contributions encompass not only CE processes, but also MT interactions in general. If no magnetization is transferred between pools, e.g. in pure water,  $R_{1\rho}$  is given by [117]

$$R_{1\rho}(\text{water only}) = R_{eff}(\Delta\omega) = R_{1w} \cos^2\Theta(\Delta\omega) + R_{2w} \sin^2\Theta(\Delta\omega) \quad (2.69)$$

$$= R_{1w} + (R_{2w} - R_{1w}) \frac{\omega_1^2}{\omega_1^2 + \Delta\omega^2} \quad (2.70)$$

Altogether, the eigenspace approach allows for the analytical description of the water magnetization at all times. By Normalization with the thermal equilibrium magnetization of water, one yields the complete solution of the Z-value (after a presaturation at the frequency offset  $\Delta\omega$  which was performed for a time period of  $t_{sat}$ ) given by

$$Z(\Delta\omega, t_{sat}) = \frac{M_{zw}(\Delta\omega, t_{sat})}{M_{zw}^0} \quad (2.71)$$

$$= [Z_i \cos^2\Theta(\Delta\omega) - Z^{ss}(\Delta\omega)] e^{-R_{1\rho}(\Delta\omega)t_{sat}} + Z^{ss}(\Delta\omega). \quad (2.72)$$

Equation (2.71) represents a mono-exponential decay of the initial magnetization  $Z_i$  towards the steady-state  $Z^{ss}$ , which is described by the decay rate  $R_{1\rho}(\Delta\omega)$  given by equation (2.67). The steady-state magnetization in equation (2.71) is given by

$$Z^{ss}(\Delta\omega) = \frac{R_{1w} \cos^2\Theta(\Delta\omega)}{R_{1\rho}(\Delta\omega)} \quad (2.73)$$

### Dependency of $R_{ex}$ in general

In general, the exchange-dependent relaxation rate in the rotating frame  $R_{ex}$  depends on several parameters. By assuming that the water pool dominates the sparsely distributed labile solute pool (i.e.  $f_w \gg f_s$ ,  $k_{ex} \gg k_{ws}$  and a negligible  $R_{1s} \ll k_{ex}$ ), the complete analytical formula of  $R_{ex}$  can be written as [58]

$$R_{ex}(\Delta\omega) = f_s \cdot \left[ \underbrace{k_{ex} \frac{\delta\omega_s^2}{\omega_1^2 + \Delta\omega^2}}_{w\text{-peak}} \underbrace{\frac{\omega_1^2}{\frac{\Gamma^2}{4} + \Delta\omega_s^2}}_{s\text{-peak}} + \underbrace{R_{2s} \frac{\omega_1^2}{\frac{\Gamma^2}{4} + \Delta\omega_s^2}}_{R_{2s}\text{-term}} + \underbrace{k_{ex} \sin^2\Theta \frac{R_{2s}(R_{2s} + k_{ex})}{\frac{\Gamma^2}{4} + \Delta\omega_s^2}}_{\text{cross-term}} \right] \quad (2.74)$$

$\underbrace{\hspace{15em}}_{k_{ex}\text{-term}}$

in which  $\delta\omega_s = \omega_s - \omega_w$ ,  $\Delta\omega_s = \Delta\omega - \delta\omega_s$  and the full width at half maximum (FWHM) of the line width  $\Gamma$  is given by

$$\Gamma = 2\sqrt{\frac{R_{2s} + k_{ex}}{k_{ex}}\omega_1^2 + (R_{2s} + k_{ex})^2} \quad (2.75)$$

Concerning conditions in vivo, i.e. assuming  $k_{ex} \gg R_{2s}$ ,  $R_{ex}$  in equation (2.74) is completely dominated by the  $k_{ex}$ -term and can consequently be approximated via

$$R_{ex}(\Delta\omega) = f_s k_{ex} \frac{\delta\omega_s^2}{\omega_1^2 + \Delta\omega^2} \frac{\omega_1^2}{\omega_1^2 + k_{ex}^2 + \Delta\omega_s^2} \quad (2.76)$$

### Dependency of $R_{ex}$ in the large-shift limit (LS)

Moreover,  $R_{ex}$  can be further simplified as its sensitivity depends on the frequency offset  $\Delta\omega$  of the irradiated RF ( $\omega_1$ , with  $\omega_1 = \gamma B_1$ ) with respect to the water resonance. Assuming that the large-shift limit (LS) holds true, i.e.  $\delta\omega_s \gg \omega_1$ , equation (2.76) can further be simplified to [118]

$$R_{ex}(\Delta\omega = \delta\omega_s) = f_s k_{ex} \frac{\omega_1^2}{\omega_1^2 + k_{ex}(k_{ex} + R_{2s})} \approx f_s k_{ex} \frac{\omega_1^2}{\omega_1^2 + k_{ex}^2}, \quad (2.77)$$

in which

$$\alpha := \frac{\omega_1^2}{\omega_1^2 + k_{ex}(k_{ex} + R_{2s})} = \frac{(\gamma B_1)^2}{(\gamma B_1)^2 + k_{ex}(k_{ex} + R_{2s})} \quad (2.78)$$

is the so-called labeling efficiency (see Figure 3.2). Importantly, the exchange-dependent relaxation rate  $R_{ex}$  depends on  $B_1 = \frac{\omega_1}{\gamma}$  and  $k_{ex}$ .

### 2.5.4 CEST contrasts

The goal of any CEST contrast metrics is to compensate for concomitant magnetization transfer effects. This is important, particularly in vivo, as various exchanging sites are simultaneously present. Therefore, it is crucial to isolate the individual pools from the various interfering and superimposing MT effects.

**Asymmetry analysis ( $MTR_{asym}$ )** The most common contrast metric is the so-called asymmetry analysis. The asymmetry analysis is based on the assumption, that the concomitant effects like DS and ssMT are symmetric with respect to the water signal. Thus,

## 2 Fundamental Principles

the signal contributions of DS and ssMT cancel each other if a difference of two  $Z$ -values which lie on opposite sides of the  $Z$ -spectrum (zero-order-spillover correction). The magnetization transfer ratio (MTR) one obtains in this manner is given via [46, 111]

$$MTR_{asym}(\Delta\omega) = Z^{ss}(-\Delta\omega) - Z^{ss}(+\Delta\omega) = Z_{ref}^{ss} - Z_{lab}^{ss}, \quad (2.79)$$

where *ss* refers to steady-state, *ref* to the reference scan and *lab* to the label scan (i.e. the specific offset of interest). This allows to isolate CEST signals, if confounding contributions are symmetric around the water signal. However, in vivo the assumption is not valid. This is because, the in vivo  $Z$ -spectrum is asymmetric (Figure 2.8). Therefore,  $MTR_{asym}$  can not be used for a quantitative investigation of CEST experiments.

**Magnetization transfer ratio of  $R_{ex}$  ( $MTR_{Rex}$ )** In contrast, the inverse metric ( $MTR_{Rex}$ ) [57, 58, 90, 119] allows for a quantitative investigation of CEST experiments. Importantly, the  $MTR_{Rex}$  contrast metric which is given by

$$MTR_{Rex}(\Delta\omega) = \frac{1}{Z_{lab}^{ss}(\Delta\omega_{lab})} - \frac{1}{Z_{ref}^{ss}(\Delta\omega_{ref})} = \frac{R_{ex}}{R_{1w}} = \frac{f_s \cdot k_{ex} \cdot \alpha}{R_{1w}} \quad (2.80)$$

is independent of DS and ssMT effects. For a pulsed presaturation,  $MTR_{Rex}$  is given by

$$MTR_{Rex}^{pulsed}(\Delta\omega) = DC \cdot c_1 \cdot \frac{f_s \cdot k_{ex}}{R_{1w}} \cdot \frac{(\gamma B_1)^2}{\underbrace{(\gamma B_1)^2 + k_{ex}(k_{ex} + R_{2s}) \cdot c_2^2}_{\alpha}} \quad (2.81)$$

with the form factors  $c_1$  and  $c_2$ . The intra-pulse DC is represented by  $c_1$  and the presaturation pulse shape is represented by  $c_2$  (Figure 4.4). For a cw presaturation, it holds true that  $DC = c_1 = c_2 = 1$ .

## 2.6 The pH value

In this section the basics of the pH value are described. The interested reader is referred to e.g. [99, 120].

**Law of mass action**

Reversible chemical reactions of first order<sup>34</sup> are described via



where the educts are represented by  $A$  and  $B$ , the products by  $X$  and  $Y$ , and the stoichiometric coefficients by  $a$ ,  $b$ ,  $x$  and  $y$  in the unit mol. Due to the reversibility, a chemical equilibrium will occur after a certain time which is described by

$$K_c = \frac{c^x[X] \cdot c^y[Y]}{c^a[A] \cdot c^b[B]}, \quad (2.83)$$

with the equilibrium constant  $K_c$  and the concentrations  $c$  of the products and educts. Equation (2.83), which states the ratio of the concentrations of the products and educts in chemical equilibrium, is referred to as the law of mass action. Consequently,  $K_c$  is a measure for the position of the chemical equilibrium (i.e. a large value of  $K_c$  corresponds to a high concentration of products, and vice versa). It should be noted that equation (2.83) is an approximation which, in principle, only holds true for diluted aqueous solutions<sup>35</sup>. However, the law of mass action also holds true for solutions with high concentrations if the concentrations  $c$  of substances in equation (2.83) are replaced with their respective activities  $a$  given by

$$a(X) = f(X) \cdot c[X], \quad (2.84)$$

with the coefficient of activity  $f$ . For all intents and purposes within this thesis, it can be assumed that  $f(X) = 1$  for all substances, thus, leading to  $a(X) \hat{=} c[X]$ .

**Autoprotolysis of water**

In pure liquid water ( $\text{H}_2\text{O}$ ), self-ionization occurs leading to hydronium ( $\text{H}_3\text{O}^+$ ) and hydroxide ions ( $\text{OH}^-$ ). Accordingly, this so-called autoprotolysis of water given by



<sup>34</sup> Reactions, in which the reaction rate is linearly dependent on the concentration.

<sup>35</sup> With concentrations of up to  $\sim 100\text{mM}$ .

## 2 Fundamental Principles

can be described by the law of mass action yielding the equilibrium constant of water via

$$K_c = \frac{c[\text{H}_3\text{O}^+] \cdot c[\text{OH}^-]}{c^2[\text{H}_2\text{O}]} \quad (2.86)$$

Because the value of  $K_c$  in water is small, the chemical equilibrium is dominated by the left side of equation (2.85). For this reason, the concentration of water molecules can, essentially, be assumed to be constant with a value of  $c[\text{H}_2\text{O}] = 55.6 \frac{\text{mol}}{\text{l}} = 55.6 \text{ M}$ . Therefore,  $c[\text{H}_2\text{O}]$  and the equilibrium constant  $K_c$  in equation (2.86) can be combined which results in the simplified equation of

$$K_w := K_c \cdot c^2[\text{H}_2\text{O}] = c[\text{H}_3\text{O}^+] \cdot c[\text{OH}^-] = 1 \cdot 10^{-14} \frac{\text{mol}^2}{\text{l}^2}, \quad (2.87)$$

in which  $K_w$  is referred to as the ionic product of water. Importantly, the value of  $K_w$  is strongly dependent on temperature with a value of  $K_w = 1 \cdot 10^{-14} \frac{\text{mol}^2}{\text{l}^2}$  at standard conditions ( $T = 298.15 \text{ K} = 25 \text{ }^\circ\text{C}$  and  $p = 1 \text{ atm} = 1013.25 \text{ hPa}$ ). For higher temperatures, the equilibrium in equation (2.85) is shifted to the right side yielding higher values for  $K_w$ , which means that the concentration of hydronium and hydroxide ions in water increases with increasing temperature.

### The logarithmic pH scale

By applying the decimal logarithm to equation (2.87), the following fundamental relations can be defined:

$$pH := -\log_{10}(c[\text{H}_3\text{O}^+]), \quad (2.88)$$

$$pOH := -\log_{10}(c[\text{OH}^-]), \quad (2.89)$$

$$pK_w := -\log_{10}(K_w). \quad (2.90)$$

Using the definition of the  $p$ -value<sup>36</sup> (i.e. the negative of the decimal logarithm) in equations (2.88) to (2.90) allows to describe the concentrations of hydronium and hydroxide ions in water while avoiding powers of 10. Accordingly, the logarithmized ionic product of water is given by

$$pK_w = pH + pOH = 14. \quad (2.91)$$

---

<sup>36</sup> Historically, the  $p$  denotes the *potential* or *power* of hydrogen.

which is obtained by inserting equations (2.88) to (2.90) into equation (2.87). As pure water<sup>37</sup> consists of equal amounts of  $c[\text{H}_3\text{O}^+] = c[\text{OH}^-] = 1 \cdot 10^{-7} \text{ M}$ , the pH value of  $\text{pH} = \frac{pK_w}{2} = 7$  is referred to as neutral<sup>38</sup>. Aqueous solutions with  $\text{pH} < 7$  are called acidic (i.e. higher concentrations of  $\text{H}_3\text{O}^+$ ). In contrast, aqueous solutions with  $\text{pH} > 7$  are called basic (i.e. higher concentrations of  $\text{OH}^-$ ). Therefore, the pH value is a measure to specify the acidity or basicity of aqueous solutions.

---

<sup>37</sup> At standard conditions.

<sup>38</sup> The exact neutral value of the pH scale depends on temperature, e.g. at temperatures higher than 25°C the neutral value is lower than 7 (for pure water at 37°C  $\approx 6.8$ ).



## 3 A novel model enabling quantitative CEST-based pH mapping

In the following, the underlying theory of the developed pH mapping method is introduced. Ultimately, the proposed analytical model enables to directly translate measured exchange rates  $k_{\text{ex}}$  into pH values and, inter alia, allows for a stable and robust calibration in vitro. The entire pH mapping method is based on the finding that, for amide and guanidyl protons at a fixed temperature (e.g. at 37 °C in vivo), the dependency of the exchange rate  $k_{\text{ex}}$  on pH is completely characterized by only one rate constant  $k_{\text{c}}$  (section 3.1). Moreover, a stable and robust method to precisely calibrate  $k_{\text{c}}$  in vitro is presented (section 3.2) which is based on the symmetric dependency of CEST signals as a function of pH and is a fundamental insight of this thesis (section 3.3). Furthermore, a contrast- $B_1$ -correction fit model based on  $\text{MTR}_{\text{Rex}}$  theory is introduced which allows for concentration-independent extraction of  $k_{\text{ex}}$  from data acquired at multiple  $B_1$  (section 3.4). Also, the behavior of the pH sensitivity of CEST signals is explored yielding many interesting insights (section 3.5). Finally, a method is presented which enables robust and reliable pH mapping by combining the two individually obtained pH maps from the amide and guanidyl signal into a final pH map using a weighted approach based on the theoretical pH sensitivity of each proton species (section 3.6). Parts of this chapter have already been published in [121].

### 3.1 Principle of pH mapping using the amide or the guanidyl signal

In general, the exchange rate  $k_{\text{ex}}$  depends on many terms and parameters (i.e. equation (2.50)). However, it is already well-established that, within the physiologically relevant range (i.e.  $\text{pH} \simeq 6$  to 8), the exchange rates  $k_{\text{ex}}$  of amide as well as guanidyl protons are dominated by base-catalyzed processes [97] (cf. Figure 2.5). Accordingly, the generally complicated relation between  $k_{\text{ex}}$  and pH can, for each proton species separately, be

### 3 A novel model enabling quantitative CEST-based pH mapping

expressed in a simplified manner via [97]

$$k_{ex}(pH, T) = k_b(T) \cdot 10^{pH - pK_w(T)}. \quad (3.1)$$

Here,  $k_b(T)$  is the base-catalyzed exchange rate constant and  $K_w(T)$  the dissociation constant of water, which both are functions of the temperature  $T$ . Therefore, if the temperature of the system is constant, all temperature dependent terms can be separated from the rest and equation (3.1) once again simplifies to

$$k_{ex}(pH, T = \text{const.}) = \underbrace{k_b(T) \cdot 10^{-pK_w(T)}}_{=: k_c(T)} \cdot 10^{pH} = k_c(T) \cdot 10^{pH}. \quad (3.2)$$

Consequently, for any given fixed temperature (e.g. 37 °C in vivo), the dependency of  $k_{ex}$  on pH is completely characterized by only one rate constant  $k_c$  (Figure 3.1a), which is unique for each proton species and temperature<sup>1</sup>, respectively. Thus, by rearranging equation (3.2) and with prior knowledge of the exchange rate characterizing constant  $k_c$ , it is possible to map pH values by simply measuring  $k_{ex}$  via

$$\boxed{pH = \log_{10} \left[ \frac{k_{ex}}{k_c} \right]}. \quad (3.3)$$

Effectively, this means that equation (3.3) enables to directly translate  $k_{ex}$  into pH if  $k_c$  has been calibrated. However, due to the intrinsically different exchange rates of amide and guanidyl protons (i.e. even at the same temperature each proton species has its own distinct  $k_c$ ), it is necessary to calculate pH via equation (3.3) separately for the amide and guanidyl signal. Consequently, up to two independent pH maps are obtained in this manner, one for the amide and one for the guanidyl signal, which in the following are referred to as  $pH_{amide}$  and  $pH_{gua}$ . Because  $k_c$  plays the central role in the presented pH mapping method, it is crucial to know its value as accurately as possible. Thus, also a stable and robust method to precisely calibrate  $k_c$  in vitro is introduced in the subsequent section 3.2.

In the following, all calculations are demonstrated for the generalized case of a pulsed presaturation (i.e. including the form factors  $c_1$  and  $c_2$ , as well as the duty cycle DC). In the case of a cw presaturation which, specifically, was used for all in vivo examinations within this thesis it holds true that  $DC = c_1 = c_2 = 1$ .

<sup>1</sup> Hence, the subscript  $c$  in  $k_c$  was chosen to indicate a constant temperature, i.e. following the style of  $a$  and  $b$  for acid-catalyzed ( $k_a$ ) and base-catalyzed ( $k_b$ ), respectively.

## 3.2 Calibration of the exchange rate characterizing constant $k_c$

For a proper and accurate pH mapping, it is essential to precisely know the value of  $k_c$  which, by definition, encompasses all temperature dependent variables. Therefore, to be able to correctly translate  $k_{ex}$  into pH, the calibration of  $k_c$  needs to be performed at the same temperature as the actual pH measurement. In principle, the calibration of  $k_c$  can be performed empirically in vitro by using model suspensions (or model solutions) with various, well-known, titrated pH values ( $pH_{titrated}$ , i.e. measured with a pH meter) and matching the pH values calculated from CEST-MRI via (3.3) to the known  $pH_{titrated}$  values. Interestingly, however, the calibration of  $k_c$  can also be determined analytically by examining  $MTR_{Rex}$  as a function of pH (again,  $MTR_{Rex}(pH)$  refers to either the amide or guanidyl CEST signal). It is well-known that  $MTR_{Rex}$  as a function of  $k_{ex}$  (i.e. equation (2.81)) increases, reaches a maximum and then decreases again [122–124]. The maximum of  $MTR_{Rex}(k_{ex})$  is given by [122–124]

$$k_{ex,max} = \frac{\omega_1}{c_2} = \frac{\gamma B_1}{c_2}. \quad (3.4)$$

Remarkably,  $k_{ex,max}$  only depends on the applied  $B_1$  as well as  $c_2$ , which are one of the few parameters that can be chosen by the experimenter. This means that for any given exchange rate  $k_{ex}$  there exists a corresponding  $B_1/c_2$  which yields the optimal (i.e. maximal possible) CEST signal, and vice versa. Using equation (3.3), the dependency of  $MTR_{Rex}$  on  $k_{ex}$  (equation (2.81)) can be directly translated into a dependency on pH given by

$$MTR_{Rex}(pH) = DC \cdot c_1 \cdot \frac{f_s \cdot k_c \cdot 10^{pH}}{R_{1w}} \cdot \frac{(\gamma B_1)^2}{\underbrace{(\gamma B_1)^2 + k_c \cdot 10^{pH} (k_c \cdot 10^{pH} + R_{2s}) \cdot c_2^2}_{\doteq \alpha}}. \quad (3.5)$$

Consequently,  $MTR_{Rex}(pH)$  has a maximum at position

$$pH_{max} = \log_{10} \left[ \frac{k_{ex,max}}{k_c} \right] = \log_{10} \left[ \frac{\gamma B_1}{c_2 k_c} \right]. \quad (3.6)$$

which is obtained by inserting equation (3.4) into equation (3.3) (Figure 3.1b). In analogy to  $k_{ex,max}$ ,  $pH_{max}$  also only depends on  $B_1$  and  $c_2$ , which both are given by the applied presaturation pulse parameters (Figure 3.1c). More importantly, the position of  $pH_{max}$  is

### 3 A novel model enabling quantitative CEST-based pH mapping

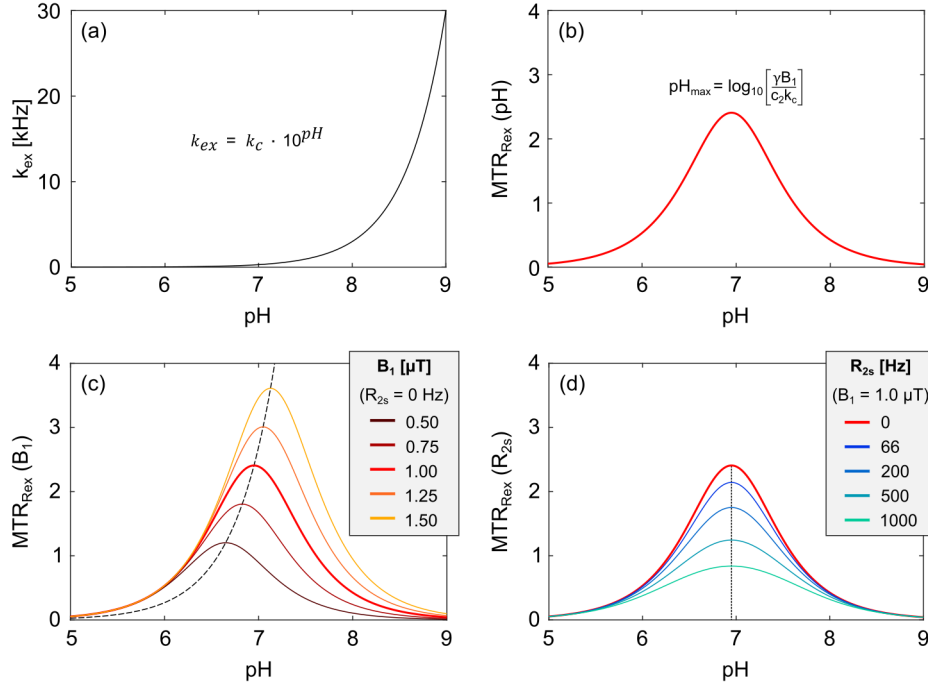


**Figure 3.1:** Simulated  $k_{ex}$  as a function of pH (a) and  $MTR_{Rex}$  as a function of pH,  $B_1$  and  $R_{2s}$  (b-d). (a) At a fixed Temperature (e.g. 37 °C in vivo), the dependency of  $k_{ex}$  on pH is fully characterized by only one rate constant  $k_c$ . (b) Remarkably,  $MTR_{Rex}(pH)$  is a symmetric function around position  $pH_{max}$  with a well-defined amplitude and FWHM (equation 3.9). The position of  $pH_{max}$  depends on the applied  $B_1$  (c, dashed line) and is independent of  $R_{2s}$  (d, dotted line). Simulations parameter are specified in Appendix A.3.

completely independent of tissue specific parameters, i.e. the proton fraction of the CEST pool  $f_s$ , the longitudinal relaxation rate of water  $R_{1w}$  and the transversal relaxation rate of the CEST pool  $R_{2s}$  (Figure 3.1d). By rearranging equation (3.6), the exchange rate characterizing constant  $k_c$  can be determined by

$$k_c = \frac{\gamma B_1}{c_2 \cdot 10^{pH_{max}}} \quad (3.7)$$

Thus, equation (3.7) enables to experimentally determine the value of  $k_c$  by finding the position of  $pH_{max}$  in model suspensions or solutions with various, well-known,  $pH_{titrated}$  values (i.e. by using a multi-pH phantom and fitting the position of the maximum  $MTR_{Rex}$  signal as a function of pH). In 2005, it has already been demonstrated by Woessner et al. [122] that the maximum of the CEST signal contains valuable information about the exchange rate  $k_{ex}$ . However, here in this work, their approach is extended which allows

for a complete characterization of the underlying exchange process ( $k_c$ ) by acquisition of only one  $MTR_{\text{Rex}}$  image of a single multi-pH phantom at one  $B_1$ . Furthermore, in comparison to *quantification of exchange rate using varying saturation power* (QUESP) [70, 71], the presented approach can be understood as an alternative and novel method to perform *quantification of exchange rate by variation of pH*.

### 3.3 Symmetry of $MTR_{\text{Rex}}$ as a function of pH

In addition, it is demonstrated in the following that  $MTR_{\text{Rex}}(\text{pH})$  is a symmetric function around position  $\text{pH}_{\text{max}}$  with a well-defined amplitude and FWHM. The symmetric shape of  $MTR_{\text{Rex}}(\text{pH})$  is a fundamental finding of the developed method and yields further insights into the nature of CEST. Also, the fact that  $MTR_{\text{Rex}}(\text{pH})$  is symmetric and that it has a nearly constant FWHM under a realistic<sup>2</sup> variation of  $B_1$  and  $R_{2s}$  allows for a stable, robust and easy to implement fitting procedure to precisely calibrate  $k_c$  in vitro.

By using the relation  $\text{pH}_{\text{max}} = \log_{10} \left[ \frac{\gamma B_1}{c_2 k_c} \right]$  found in (3.6), equation (3.5) can be rearranged to

$$MTR_{\text{Rex}}(\text{pH}) = DC \cdot \frac{c_1}{c_2} \cdot \frac{f_s \cdot \gamma B_1}{R_{1w}} \cdot \frac{1}{10^{\text{pH} - \text{pH}_{\text{max}}} + 10^{\text{pH}_{\text{max}} - \text{pH}} + \frac{c_2 R_{2s}}{\gamma B_1}}, \quad (3.8)$$

which, with respect to pH, is a symmetric function centered around position  $\text{pH}_{\text{max}}$ .

Alternatively,  $MTR_{\text{Rex}}(\text{pH})$  can also be expressed as a function with a well-defined amplitude  $A$  and FWHM  $\Gamma$  via

$$MTR_{\text{Rex}}(\text{pH}) = A \cdot \frac{10^{\Gamma/2} + 10^{-\Gamma/2} - 2}{10^{\text{pH} - \text{pH}_{\text{max}}} + 10^{\text{pH}_{\text{max}} - \text{pH}} + 10^{\Gamma/2} + 10^{-\Gamma/2} - 4}, \quad (3.9)$$

with

$$A := DC \cdot \frac{c_1}{c_2} \cdot \frac{f_s \cdot \gamma B_1}{R_{1w}} \cdot \left( 2 + \frac{c_2 R_{2s}}{\gamma B_1} \right)^{-1} \quad (3.10)$$

<sup>2</sup> Within the range of applicable  $B_1$  in vivo and typically estimated  $R_{2s}$  of CEST signals, i.e.  $B_1 = 0.4$  to  $1.6 \mu\text{T}$  (sections 5.1.1 and 5.2.1) and  $R_{2s} \simeq 25$  to  $120 \text{ Hz}$  [57, 61, 74, 90, 125, 126].

### 3 A novel model enabling quantitative CEST-based pH mapping

and

$$\Gamma := 2 \cdot \log_{10} \left[ \frac{\left( \frac{c_2 R_{2s}}{\gamma B_1} + 4 \right) + \sqrt{\left( \frac{c_2 R_{2s}}{\gamma B_1} + 4 \right)^2 - 4}}{2} \right]. \quad (3.11)$$

Using this notation, the tissue specific parameters  $f_s$  and  $R_{2s}$  can, in principle, be determined from a fit of multi-pH  $\text{MTR}_{\text{Rex}}$  data via

$$f_s = \frac{A}{DC \cdot \frac{c_1}{c_2} \cdot \frac{\gamma B_1}{R_{1w}}} \left( 10^{\Gamma/2} + 10^{-\Gamma/2} - 2 \right) \quad (3.12)$$

and

$$R_{2s} = \frac{\gamma B_1}{c_2} \left( 10^{\Gamma/2} + 10^{-\Gamma/2} - 4 \right). \quad (3.13)$$

Having performed the calibration of  $k_c$ , which enables translating  $k_{\text{ex}}$  into pH, the only remaining task is the actual measurement of  $k_{\text{ex}}$ , i.e. the extraction of  $k_{\text{ex}}$  from the amide and guanidyl CEST signals, respectively.

## 3.4 Extraction of exchange rates $k_{\text{ex}}$

The CEST effect intrinsically depends on the exchange rate  $k_{\text{ex}}$  and the relative concentration  $f_s$  of the investigated CEST pool via equation (2.81), i.e. in words: the signal strength depends on how fast, and respectively, how many magnetically labeled protons exchange with the water pool. Thus, Z-spectra can be used to obtain information about  $k_{\text{ex}}$  and, so far, various methods have already been proposed to extract  $k_{\text{ex}}$  [16, 59, 71, 79, 127–129]. In order to reliably extract  $k_{\text{ex}}$ , mainly two steps need to be fulfilled which are (i) the isolation of the pure CEST signal from the background of interfering signals and (ii) the compensation for  $f_s$  (essentially, i.e. independence of concentration<sup>3</sup>). To accomplish (i), the spillover- and relaxation-compensated inverse metric  $\text{MTR}_{\text{Rex}}$  is used. To achieve (ii), one well-established method is the power ratiometric approach (i.e. the  $\text{CEST}_{\text{ratio}}$ , subsection 3.4.1). However, to perform pH mapping as accurately as possible, one needs to extract  $k_{\text{ex}}$  from the Z-spectra as accurately as possible. Therefore,

<sup>3</sup> Note that, although  $\text{MTR}_{\text{Rex}}$  has a distinct dependency on pH (Figure 3.1b),  $k_{\text{ex}}$  and, thus, pH can not be determined from the value of  $\text{MTR}_{\text{Rex}}$  at only one  $B_1$  because the amplitude of  $\text{MTR}_{\text{Rex}}$  (equation (3.10)) is scaled by the tissue-specific value of  $f_s/R_{1w}$ .

in this thesis, the power ratiometric approach was extended by implementing a contrast- $B_1$ -correction fit model based on  $MTR_{Rex}$  theory (subsection 3.4.2) which increases the accuracy of extracting  $k_{ex}$ .

### 3.4.1 The power ratiometric approach ( $CEST_{ratio}$ )

In general, a ratiometric approach is based on the ratio of two arbitrary CEST signals. More specifically, the power ratiometric approach, which was developed by Longo, Sun, Aime et al. [59], uses the ratio of the same CEST signal at two different  $B_1$  amplitudes (i.e. the  $CEST_{ratio}$ , with  $B_{1,high} > B_{1,low}$ ). By definition, the  $CEST_{ratio}$  is independent of  $f_s$  and  $R_{1w}$  of the examined signal [59–61, 130]

$$\begin{aligned}
 CEST_{ratio}(k_{ex}) &:= \frac{MTR_{Rex}(B_{1,high})}{MTR_{Rex}(B_{1,low})} \\
 &= \frac{DC \cdot c_1 \cdot R_{1w} \cdot f_s \cdot k_{ex}}{DC \cdot c_1 \cdot R_{1w} \cdot f_s \cdot k_{ex}} \cdot \frac{\alpha(B_{1,high})}{\alpha(B_{1,low})} \\
 &\quad \underbrace{\hspace{10em}}_{=1} \\
 &= \left( \frac{B_{1,high}}{B_{1,low}} \right)^2 \cdot \frac{(\gamma B_{1,low})^2 + k_{ex}(k_{ex} + R_{2s}) \cdot c_2^2}{(\gamma B_{1,high})^2 + k_{ex}(k_{ex} + R_{2s}) \cdot c_2^2}. \tag{3.14}
 \end{aligned}$$

Here, as before,  $MTR_{Rex}$  refers to either the amide or the guanidyl CEST signal and  $\alpha$  to the labeling efficiency (equation (3.5)). Thus, the  $CEST_{ratio}$  represents a (i) spillover- and relaxation-compensated as well as, more particularly, (ii) concentration-independent metric with only two unknown parameters, i.e.  $k_{ex}$  and  $R_{2s}$ . Consequently, by using a fixed  $R_{2s}$ , the inherently concentration-independent  $CEST_{ratio}$  can be employed to experimentally determine  $k_{ex}$  from CEST data acquired at two different  $B_1$  amplitudes by rearranging equation (3.14) into

$$k_{ex} = -\frac{R_{2s}}{2} + \sqrt{\frac{R_{2s}^2}{4} + \left( \frac{(1 - CEST_{ratio}) \cdot (\gamma B_{1,low})^2}{CEST_{ratio} \cdot \left( \frac{B_{1,low}}{B_{1,high}} \right)^2 - 1} \right) \cdot \frac{1}{c_2^2}}. \tag{3.15}$$

By definition, the  $CEST_{ratio}$  represents the ratio of the labeling efficiency  $\alpha$  at high and low  $B_1$ , i.e.  $CEST_{ratio} = \frac{\alpha(B_{1,high})}{\alpha(B_{1,low})}$  (Figure 3.2). In a real CEST experiment, however, the  $B_1$  amplitude is not constant across the entire FOV due to  $B_1$  field inhomogeneities (i.e. the relative  $B_1$  can vary in each pixel). Consequently, to enable a quantitative pH mapping, the  $B_1$  field inhomogeneities need to be corrected by multiplying the nominal

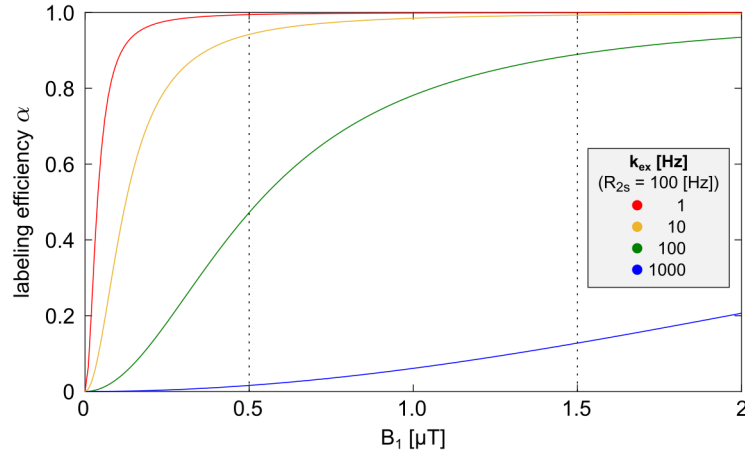


**Figure 3.2:** The labeling efficiency  $\alpha$  (colored lines) is shown as a function of  $B_1$  for various exchange rates  $k_{\text{ex}}$  (colors). The shape of  $\alpha(B_1)$  strongly depends on  $k_{\text{ex}}$ , which is why the  $\text{CEST}_{\text{ratio}} = \frac{\alpha(B_{1,\text{high}})}{\alpha(B_{1,\text{low}})}$  can be used to calculate  $k_{\text{ex}}$  for a fixed  $R_{2s}$  (equation (3.15)). Therefore,  $\text{MTR}_{\text{Rex}}$  data is acquired at two different  $B_1$  (e.g. at  $B_{1,\text{low}} = 0.5 \mu\text{T}$  and  $B_{1,\text{low}} = 1.5 \mu\text{T}$ , dotted vertical lines). In contrast, the  $\text{MTR}_{\text{Rex}}$ -based contrast- $B_1$ -correction enables to extract  $k_{\text{ex}}$  from data acquired at more than only two  $B_1$ .

values of  $B_{1,\text{high}}$  and  $B_{1,\text{low}}$  in equation (3.15) with the actual local relative  $B_1$  value in each pixel (by using a  $B_1$  field map, explained in detail in subsection 4.4.2.6). In this thesis, the  $\text{CEST}_{\text{ratio}}$  approach was extended by implementing a contrast- $B_1$ -correction fit model directly based on  $\text{MTR}_{\text{Rex}}$  theory which enables concentration-independent determination of  $k_{\text{ex}}$  from data acquired at more than only two  $B_1$ .

### 3.4.2 A robust $\text{MTR}_{\text{Rex}}$ -based contrast- $B_1$ -correction approach

In general, a common way to correct for  $B_1$  field inhomogeneities is the contrast- $B_1$ -correction method [131]. In the contrast- $B_1$ -correction method, the  $\text{MTR}_{\text{Rex}}$  contrast is acquired at multiple nominal  $B_1$  values but fitted at the actual local  $B_1$  values (typically, using a smoothing spline data interpolation fit and a  $B_1$  field map). This allows for calculation of  $B_1$ -corrected  $\text{MTR}_{\text{Rex}}$  contrasts at any desired nominal  $B_1$ . Contrary to the smoothing spline approach, in this thesis, an analytical contrast- $B_1$ -correction fit model

based on the  $MTR_{Rex}$  theory (equation (2.81) and (2.77)) was implemented, given by

$$MTR_{Rex}(B_1\text{-corrected}) := a \cdot b \cdot \frac{(\gamma B_1)^2}{\underbrace{(\gamma B_1)^2 + b \cdot (b + R_{2s}) \cdot c_2^2}_{\hat{=} \alpha}} \quad (3.16)$$

with the fit parameters  $a$  and  $b$ . Here, the fit parameter  $a$  represents a scaling factor, i.e.  $a \hat{=} DC \cdot c_1 \cdot f_s / R_{1w}$  in equation (2.81), which encompasses the maximal signal strength of  $MTR_{Rex}(B_1)$  and compensates for  $f_s$ . More importantly, the fit parameter  $b$  directly represents the exchange rate, i.e.  $b \hat{=} k_{ex}$  in equation (2.81), which encompasses the shape of  $MTR_{Rex}(B_1)$ , i.e. the labeling efficiency  $\alpha$  as a function of  $B_1$  (Figure 3.2). Consequently, equation (3.16) enables to directly extract  $k_{ex}$  from  $MTR_{Rex}$  data acquired at multiple  $B_1$  by a fit model approach. In principle, the extraction of  $k_{ex}$  from the fit parameter  $b$  in equation (3.16) is mathematically equivalent to calculating  $k_{ex}$  from the  $CEST_{ratio}$  via equation (3.15). However, using the fit model approach given by equation (3.16) allows for extraction of  $k_{ex}$  from CEST data acquired at more than two  $B_1$  [16, 59], in comparison to the  $CEST_{ratio}$  approach which only allows for extraction of  $k_{ex}$  from data acquired at two  $B_1$  (equation 3.15). In other words, the shape of the  $\alpha$  curve is essentially sampled at more than two  $B_1$  (i.e. more than two dotted vertical lines in Figure 3.2), which allows for a more robust determination of  $k_{ex}$ . The possibility of using more data for extraction of  $k_{ex}$  significantly increases the accuracy of  $k_{ex}$  which is especially important in the case of noisy data (e.g. in vivo). Accordingly, in this thesis, all acquired data was contrast- $B_1$ -corrected via equation (3.16) for all further data processing (see Figures 5.3 and 5.11b). Moreover, this fit model allows to reconstruct  $CEST_{ratio}$  data for any desired combination of  $B_{1,high}$  and  $B_{1,low}$ , since  $MTR_{Rex}$  data can be reconstructed at any nominal  $B_1$ .

Consequently, with a concentration-independent method for extracting  $k_{ex}$  at hand via equation (3.16) and a method for previous calibration of  $k_c$  in vitro via equation (3.7), CEST-based measurement of pH is feasible via  $pH = \log_{10} \left[ \frac{k_{ex}}{k_c} \right]$ , i.e. for each proton species separately yielding two individual pH maps, one for the amide and one for the guanidyl signal ( $pH_{amide}$  and  $pH_{gua}$ ). However, in reality,  $pH_{amide}$  and  $pH_{gua}$  exhibit intrinsically different ranges of pH sensitivity. For this reason, the pH sensitivity of CEST signals are analytically investigated in the following.

### 3.5 On the pH sensitivity of CEST signals

Although  $k_{ex}$  is more reliably extracted using the analytical  $MTR_{Rex}$ -based contrast- $B_1$ -correction fit model, it is still useful to investigate the behavior of the  $CEST_{ratio}$  as a function of pH. Accordingly, using equation (3.3), the dependency of the  $CEST_{ratio}$  on  $k_{ex}$  (equation (3.14)) can be reformulated as a dependency on pH given by

$$CEST_{ratio}(pH) = \left( \frac{B_{1,high}}{B_{1,low}} \right)^2 \cdot \frac{(\gamma B_{1,low})^2 + k_c \cdot 10^{pH} (k_c \cdot 10^{pH} + R_{2s}) \cdot c_2^2}{(\gamma B_{1,high})^2 + k_c \cdot 10^{pH} (k_c \cdot 10^{pH} + R_{2s}) \cdot c_2^2}. \quad (3.17)$$

Because the  $CEST_{ratio}$  has a distinct dependency on pH, it can be utilized to better understand the influence of various parameters on the pH sensitivity of CEST signals and to explore the experimental possibilities of tuning the pH sensitivity. For this purpose, the  $CEST_{ratio}(pH)$  (equation (3.17)) is in the following mathematically analyzed and simulated for various parameters. Most noticeable, the  $CEST_{ratio}(pH)$  approaches the limits

$$\lim_{pH \rightarrow -\infty} CEST_{ratio}(pH) = 1, \quad (3.18)$$

$$\lim_{pH \rightarrow \infty} CEST_{ratio}(pH) = \left( \frac{B_{1,high}}{B_{1,low}} \right)^2 \quad (3.19)$$

for low and high pH values, respectively (Figure 3.3a). For low pH (i.e. low  $k_{ex}$ ), the pH-limit of 1 is due to the fact that the pH-dependent terms in the right fraction of equation (3.17) approach zero. Accordingly, the remaining terms cancel each other to 1. More specifically, one can explain the low pH-limit of the  $CEST_{ratio}$  via the full-saturation limit (i.e.  $\alpha = 1$ ), which is fulfilled for both  $B_{1,high}$  and  $B_{1,low}$  at low pH (i.e.  $\alpha(B_{1,high}) \approx \alpha(B_{1,low}) \approx 1$ , e.g. Figure 3.2, red curve). In contrast, for high pH (i.e. high  $k_{ex}$ ), the right fraction in equation (3.17) is completely dominated by the pH-dependent terms and, thus, approaches 1. Accordingly, the remaining terms cancel each other to  $\left( \frac{B_{1,low}}{B_{1,high}} \right)^2$ . Importantly, the slope of the  $CEST_{ratio}(pH)$

$$\begin{aligned} \frac{\partial}{\partial pH} (CEST_{ratio}(pH)) &= c_2^2 \left( \frac{\gamma B_{1,high}}{B_{1,low}} \right)^2 \\ &\cdot \frac{k_c 10^{pH} \cdot \ln[10] \cdot (B_{1,high}^2 - B_{1,low}^2) \cdot (k_c \cdot 2^{pH+1} \cdot 5^{pH} + R_{2s})}{\left( (\gamma B_{1,high})^2 + c_2^2 \cdot k_c 10^{pH} (k_c 10^{pH} + R_{2s}) \right)^2} \end{aligned} \quad (3.20)$$

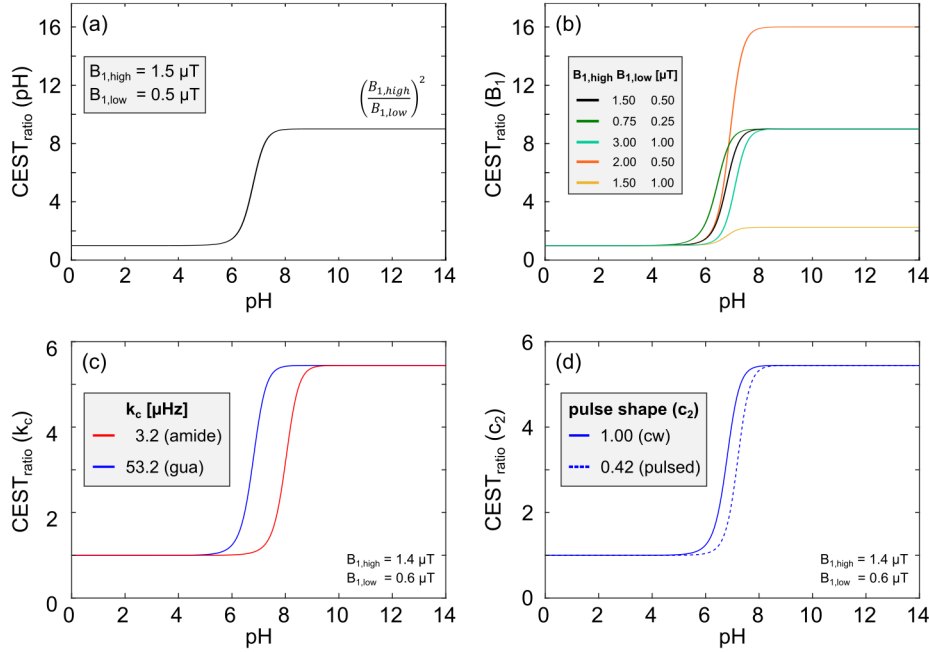


**Figure 3.3:** Simulated  $CEST_{ratio}$  as a function of pH and the influence of  $B_{1,high}$ ,  $B_{1,low}$ ,  $k_c$  and  $c_2$  on  $CEST_{ratio}(pH)$ . The  $CEST_{ratio}$  has as a distinct dependency on pH and approaches 1 and  $\left(\frac{B_{1,low}}{B_{1,high}}\right)^2$  for low and high pH, respectively (a). Variation of  $B_{1,high}$  and  $B_{1,low}$  enables to tune the position of the steepest slope (highest pH sensitivity) and range of the  $CEST_{ratio}$  (b). In contrast, the difference in the calibrated  $k_c$  values for amide and guanidyl protons (section 5.1.2) has the largest effect on the pH sensitivity (c). Remarkably, variation of the presaturation pulse shape enables shifting the pH sensitivity towards higher pH (d). If not explicitly specified,  $c_2 = 1.00$ ,  $k_c = 53.2 \mu Hz$  and  $R_{2s} = 100 Hz$ .

and its range are increased by maximizing the difference between  $B_{1,high}$  and  $B_{1,low}$  (Figure 3.3b, cf. orange and yellow curves). This is particularly interesting, as the slope of the  $CEST_{ratio}$  (equation (3.20)) can be interpreted as the pH sensitivity (cf. Figure 3.4a, where the normalized  $\frac{\partial}{\partial pH}(CEST_{ratio}(pH))$  is shown). Essentially, this is because a steeper slope of the  $CEST_{ratio}(pH)$  in combination with an increased range enables a more accurate and precise experimental determination of  $k_{ex}$  and, thus, pH. Consequently, the complete range of applicable  $B_1$  should be utilized for extraction of  $k_{ex}$  of the individual CEST signals (i.e. experimentally feasible  $B_1$  in the range of 0.6 to 1.4  $\mu T$  yielding measurable CEST signals, see sections 5.1.1 and 5.2.1).

Variation of  $B_{1,high}$  and  $B_{1,low}$  enables to shift the pH sensitivity of the  $CEST_{ratio}$  (Figure 3.3b). Thus, in principle, the range of highest pH sensitivity (steepest slope) can be

### 3 A novel model enabling quantitative CEST-based pH mapping

tuned along the pH scale by variation of  $B_{1,high}$  and  $B_{1,low}$  at a constant ratio (Figure 3.3b, cf. green, black and cyan curves). However, the tuning at a constant ratio of  $B_{1,high}$  and  $B_{1,low}$  is in conflict with the maximization of the pH sensitivity (maximizing the difference between  $B_{1,high}$  and  $B_{1,low}$  while allowing for a reliable signal extraction, i.e. using  $B_{1,high} = 1.4$  and  $B_{1,low} = 0.6$   $\mu\text{T}$ ). Also, in comparison to the ratiometric approach, the  $\text{MTR}_{\text{Rex}}$ -based contrast- $B_1$ -correction enables not only (i) an enhanced extraction of  $k_{\text{ex}}$  (section 3.4.2), but also (ii) an enhanced pH sensitivity over a broader range of pH values due to more utilized  $B_1$ .

Importantly, the value of  $k_c$  has, by far, the largest effect on the position of the steepest slope of  $\text{CEST}_{\text{ratio}}(\text{pH})$  (Figure 3.3c). This is particularly true, as the used  $k_c = 3.2$  and  $53.2$   $\mu\text{Hz}$  in Figure 3.3c correspond to the calibrated  $k_c$  of amide (red curve) and guanidyl protons (blue curve) determined in porcine brain lysates at  $37^\circ\text{C}$  (section 5.1.2). Accordingly, the range of highest pH sensitivity is dominated by the specific value of  $k_c$ . In fact, this allows to explain the significantly different pH sensitivities of amide and guanidyl protons observed in experiments, as each proton species has an intrinsically different  $k_c$ . Hence, the two individual  $\text{pH}_{\text{amide}}$  and  $\text{pH}_{\text{gua}}$  maps are combined by a weighted approach in order to enable a reliable pH mapping over a broader range of physiologically relevant pH values (subsequent section 3.6).

Remarkably, the shape of the presaturation pulse ( $c_2$ ) also enables shifting the position of the steepest slope of  $\text{CEST}_{\text{ratio}}(\text{pH})$  towards higher pH (Figure 3.3d). In principle, by shifting the pH sensitivity towards higher pH values for decreasing  $c_2$ , one should be able to shift the cw presaturation pH sensitivity of guanidyl protons (Figure 3.3c and d, solid blue curves) further into the physiologically relevant pH range by using a pulsed presaturation (Figure 3.3d, dashed blue curve). In addition, this effect is particularly interesting for the prospective examinations in humans where a pulsed presaturation is a prerequisite due to patient safety. The values  $B_{1,low} = 0.6$   $\mu\text{T}$  and  $B_{1,high} = 1.4$   $\mu\text{T}$  (Figure 3.3c and d) correspond to the maximized experimentally feasible range of  $B_1$  in porcine brain lysates and tumor-bearing mice (sections 5.1.1 and 5.2.1, respectively). The value  $c_2 = 0.42$  (Figure 3.3d) corresponds to the experimentally optimized  $c_2$  in creatine model solutions (section 5.3).

In summary, the following findings were obtained by analyzing the  $\text{CEST}_{\text{ratio}}(\text{pH})$ :

1. The  $\text{CEST}_{\text{ratio}}$  has a distinct dependency on pH (equation (3.17)).

### 3.6 Reliable pH mapping using a combination of the amide and guanidyl signals

2. The slope and range of the  $\text{CEST}_{\text{ratio}}(\text{pH})$  represent pH sensitivity (equation (3.20)).
3. The value of  $k_c$  dominates the position of highest pH sensitivity (Figure 3.3c).
4. Variation of  $B_{1,\text{high}}$  and  $B_{1,\text{low}}$  enables tuning the pH sensitivity (Figure 3.3b).
5. Variation of  $c_2$  enables shifting the pH sensitivity towards higher pH (Figure 3.3d).

All these insights are utilized in the following to enable a pH mapping with a broader total range of high pH sensitivity by combining  $\text{pH}_{\text{amide}}$  and  $\text{pH}_{\text{gua}}$  based on their individual pH sensitivities.

## 3.6 Reliable pH mapping using a combination of the amide and guanidyl signals

So far throughout this chapter, the amide and guanidyl CEST signals were only considered separately (sections 3.1 to 3.5). In principle, each of the two individually obtained  $\text{pH}_{\text{amide}}$  and  $\text{pH}_{\text{gua}}$  maps should contain the same information about pH and, therefore, yield identical pH values. Yet, due to the intrinsically different  $k_c$  of amide and guanidyl protons leading to significantly different pH sensitivities, it was experimentally observed that each proton species has a specific pH range in which it yields reliable pH values (cf. Figure 5.5). Interestingly, with the insights obtained by analyzing  $\frac{\partial}{\partial \text{pH}}(\text{CEST}_{\text{ratio}}(\text{pH}))$  (section 3.5), the different pH sensitivities of the amide and guanidyl signals can even be exploited to obtain a broader total range of high pH sensitivity. Accordingly, a more stable and reliable pH mapping over a broader range of physiological pH can be accomplished by using a weighted combination of the two individually obtained pH maps into a final pH map (i.e.  $\text{pH}_{\text{combi}}$ ) via

$$\begin{aligned} \text{pH}_{\text{combi}} &:= \frac{\sum_s (\text{pH}_s \cdot w_s(\text{pH}_s))}{\sum_s (w_s(\text{pH}_s))} \\ &= \frac{\text{pH}_{\text{amide}} \cdot w_{\text{amide}}(\text{pH}_{\text{amide}}) + \text{pH}_{\text{gua}} \cdot w_{\text{gua}}(\text{pH}_{\text{gua}})}{w_{\text{amide}}(\text{pH}_{\text{amide}}) + w_{\text{gua}}(\text{pH}_{\text{gua}})}. \end{aligned} \quad (3.21)$$

Here,  $w_s$  are the individual weightings of each CEST signal  $s = \text{amide}$  or  $\text{gua}$ . Importantly,  $w_{\text{amide}}$  and  $w_{\text{gua}}$  are functions of  $\text{pH}_{\text{amide}}$  and  $\text{pH}_{\text{gua}}$ , respectively. This is necessary in order to enable a reliable calculation of  $\text{pH}_{\text{combi}}$ , because the measured  $\text{pH}_{\text{amide}}$  and  $\text{pH}_{\text{gua}}$  should each be given more weighting in their respective range of highest pH sensitivity.

### 3 A novel model enabling quantitative CEST-based pH mapping

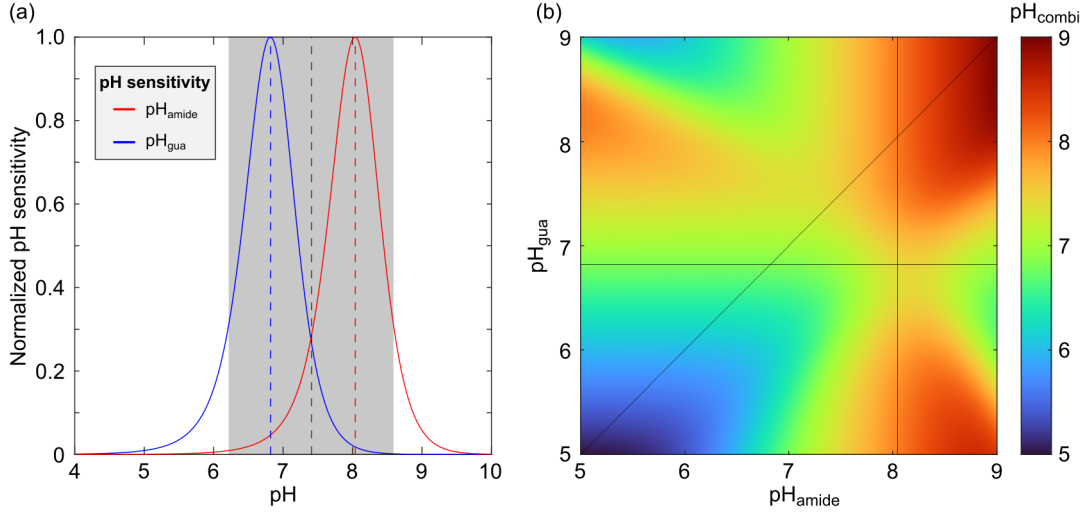


**Figure 3.4:** The theoretical pH sensitivities (a, normalized derivatives of Figure 3.3c) are used as weightings  $w_{amide}(pH_{amide})$  and  $w_{gua}(pH_{gua})$  for calculation of  $pH_{combi}$  (b, equation (3.21)). Remarkably, the range where either  $pH_{amide}$  or  $pH_{gua}$  have at least a pH sensitivity of 30% (a, gray shaded region) has a suitable transition at  $pH \approx 7.3$  (a, black dashed line). For each pair of  $pH_{amide}$  and  $pH_{gua}$  input values (b, axis of abscissa and ordinates, respectively), the corresponding  $pH_{combi}$  value is shown (b, color map). The vertical and horizontal line in (b) represent the pH value of highest pH sensitivity for  $pH_{amide}$  and  $pH_{gua}$ , respectively (cf. red and blue dashed lines in a). The diagonal line in (b) represents the  $pH_{combi}$  values with identical  $pH_{amide}$  and  $pH_{gua}$  input values. Simulation parameters are specified in Appendix A.3.

As determined in section 3.5, the slope of the  $CEST_{ratio}$  (equation (3.20)) can be defined as the pH sensitivity. Thus, one way to obtain suitable weightings is to use the measured  $pH_{amide}$  and  $pH_{gua}$  as an input to calculate their theoretical pH sensitivities via equation (3.20), i.e. by defining

$$w_s(pH_s) := \frac{\partial}{\partial pH} (CEST_{ratio,s}(pH_s)). \quad (3.22)$$

For calculation of  $w_{amide}(pH_{amide})$  and  $w_{gua}(pH_{gua})$  via equation (3.22), the calibrated values of  $k_c$  are used (section 5.1.2) in combination with the experimentally feasible maximal range of  $B_1$  (sections 5.1.1 and 5.2.1). Accordingly, the weightings (Figure 3.4a, red and blue curves, normalized to 1) reflect the different pH sensitivities of amide and guanidyl protons observed in experiments (cf. Figure 5.5). Most noticeable,  $pH_{amide}$  exhibits highest pH sensitivity at  $pH \approx 8$ , whereas  $pH_{gua}$  exhibits highest pH sensitivity at  $pH \approx 6.8$  (Figure 3.4a, red and blue dashed lines). Remarkably, the range where either  $pH_{amide}$  or

### 3.6 Reliable pH mapping using a combination of the amide and guanidyl signals

$\text{pH}_{\text{gua}}$  have at least a pH sensitivity of 30% (Figure 3.4a, gray shaded region) has transition at  $\text{pH} \approx 7.3$  (Figure 3.4a, black dashed line) which is an especially important pH range in vivo. Consequently, the suitable transition at this relevant pH value allows for an enhanced pH sensitivity of  $\text{pH}_{\text{combi}}$  over the complete physiologically relevant pH range (in principle, i.e. the envelope of the blue and red curve in Figure 3.4a). In fact, the  $\text{pH}_{\text{combi}}$  approach therefore also ensures a high pH sensitivity in pH regions where neither  $\text{pH}_{\text{amide}}$  nor  $\text{pH}_{\text{gua}}$  exhibit a particularly high pH sensitivity, i.e. at  $\text{pH} \approx 7.3$  (Figure 3.4a, black dashed line).

Having a method for obtaining suitable weightings for  $\text{pH}_{\text{amide}}$  and  $\text{pH}_{\text{gua}}$  at hand (equation (3.22)),  $\text{pH}_{\text{amide}}$  and  $\text{pH}_{\text{gua}}$  are used to calculate  $\text{pH}_{\text{combi}}$  via equation (3.21). Depending on the weightings (Figure 3.4a), the output value of  $\text{pH}_{\text{combi}}$  lies somewhere between the pair of  $\text{pH}_{\text{amide}}$  and  $\text{pH}_{\text{gua}}$  input values (Figure 3.4b). Accordingly, there is negligible variation of  $\text{pH}_{\text{combi}}$  in pH regions where  $\text{pH}_{\text{amide}}$  and  $\text{pH}_{\text{gua}}$  approximately agree (Figure 3.4b, regions close to the diagonal line). In contrast, there is more variation of  $\text{pH}_{\text{combi}}$  in pH regions where  $\text{pH}_{\text{amide}}$  and  $\text{pH}_{\text{gua}}$  disagree (Figure 3.4b, regions further away from the diagonal line). Importantly, in such a case  $\text{pH}_{\text{combi}}$  is dominated by the input value which is given stronger weighting (e.g. hot spots in Figure 3.4b). Regions where either  $\text{pH}_{\text{amide}}$  or  $\text{pH}_{\text{gua}}$  exhibit highest pH sensitivity are therefore dominated by either  $\text{pH}_{\text{amide}}$  or  $\text{pH}_{\text{gua}}$  (Figure 3.4b, vertical and horizontal line, respectively). All in all, compared to the individually obtained  $\text{pH}_{\text{amide}}$  and  $\text{pH}_{\text{gua}}$  measurements, the  $\text{pH}_{\text{combi}}$  approach allows for considerably more reliable pH measurements over a significantly broader range of pH (cf. bottom row of Figure 5.5 with Figure 5.8e) which is why all CEST-based  $\text{pH}_i$  measurements in vivo were performed using  $\text{pH}_{\text{combi}}$ .



## 4 Materials and Methods

In this chapter, the materials and methods used in this thesis are introduced. These include the utilized hardware, software, other equipment, settings and different data processing as well as evaluation techniques. Anatomical images were mapped onto the CEST images using the medical imaging interaction toolkit (MITK) [132] software package. All programming, simulations, fitting and post-processing was performed in MATLAB<sup>®</sup> (The MathWorks Inc., Natick, USA) version 9.7 (R2019b) using in-house and self-written code.

### 4.1 MR imaging system and experimental setup

#### 4.1.1 MR scanner

All measurements were performed on a 9.4 T small animal MR scanner (left side of Figure 4.1, BioSpec 94/20 USR, Bruker BioSpin MRI GmbH, Ettlingen, Germany), situated at the German Cancer Research Center (DKFZ, Heidelberg, Germany). The MR scanner has a static magnetic field strength of  $B_0 \approx 9.4033$  T resulting in a resonance frequency of  $\nu_0 \approx 400.3584$  MHz for  $^1\text{H}$ . The MR scanner was operated using ParaVision<sup>®</sup> version 360.1.1 (Bruker Corporation, Billerica, USA) which runs on TopSpin<sup>®</sup> (Bruker BioSpin).

#### 4.1.2 RF coils

Two different RF coils were used, depending on the type of performed measurements:

1. For examinations in vitro, a single resonant coil was used (Figure 4.1f, Bruker, 2-channel transmit/receive  $^1\text{H}$  volume resonator, diameter 40 mm).
2. For examinations in vivo, a double resonant coil was used (Bruker, 1-channel transmit/receive  $^{31}\text{P}/^1\text{H}$  volume resonator, diameter 40 mm).

The wobbling procedure was performed manually for each loading, i.e. RF coil tuning and

## 4 Materials and Methods

matching<sup>1</sup> (Figure 4.1g).  $B_0$  field distortions<sup>2</sup> were corrected by an integrated shimming procedure which was performed using an internally obtained  $B_0$  map and the *mapshim* setting in ParaVision<sup>®</sup>.

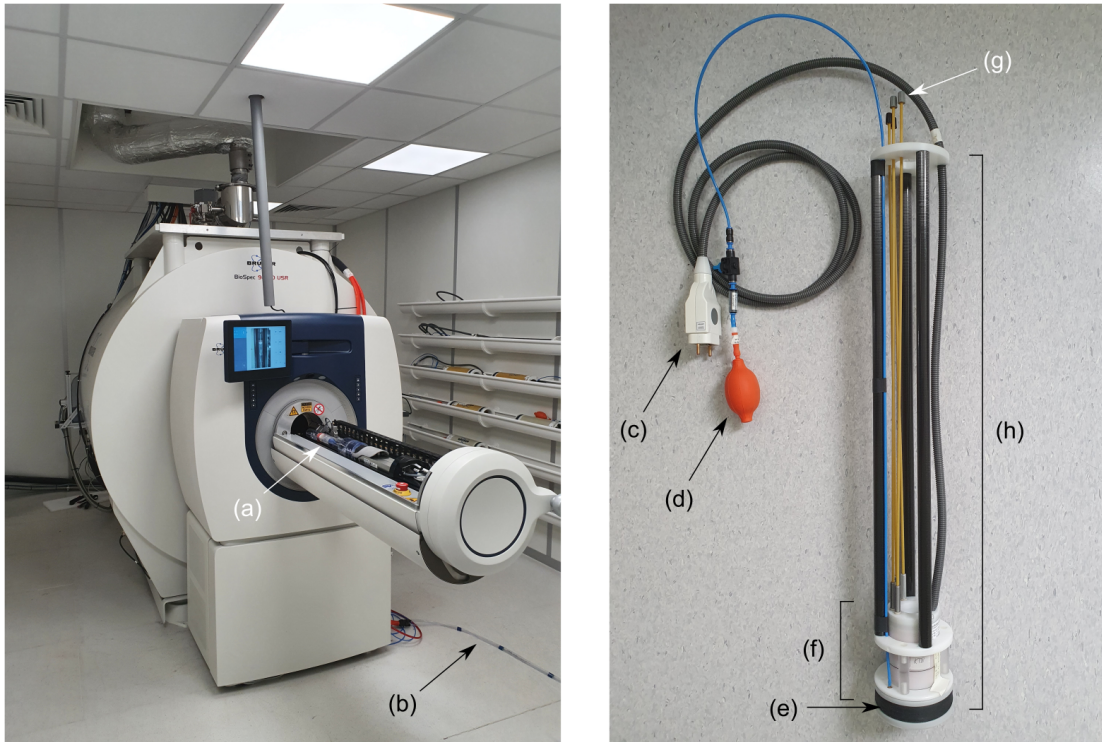


**Figure 4.1:** The used 9.4 T small animal MR scanner is situated at the German Cancer Research Center (DKFZ) in Heidelberg (left). From behind the scanner, the mounted RF coil (right, f) is inserted into the bore and positioned at the magnetic isocenter  $B_{0,iso}$  where it is used to transmit the  $B_1$  field and, in addition, to receive the MR signal. Imaging chamber (a), tube heating system (b), connection plug (c), pump device for coil fixation (d), inflatable rubber fixation ring (e), RF coil (f), tuning and matching knobs (g), mounting device (h).

### 4.1.3 Heating system

All measurements were performed and stabilized at a temperature of  $T_{subject} = 37 \pm 0.2^\circ\text{C}$ . In order to stabilize the temperature, a custom-built heating system was used. The heating system consisted of a water bath as heating device ( $T_{water\ bath} \approx 70^\circ\text{C}$ ) which is connected

<sup>1</sup> Modifications to the coil electronics and impedance in order to (i) adjust the resonance frequency to the loading (tuning) and (ii) to maximize the energy transfer between the coil and the loading (matching).

<sup>2</sup> Induced due to susceptibility effects of the sample.

to a first system of tubes filled with water (Figure 4.1b) which, in turn, exchanges heat with a second system of tubes filled with compressible air. The warm air was fed into the small animal imaging chamber (Figure 4.1a) with an airflow rate in the order of  $\sim 10 \frac{1}{\text{min}}$ . The temperature of the subject<sup>3</sup> was adjusted by regulating the airflow rate, which allowed for a fast response time and temperature control. Importantly, this heating system ensured maintaining a constant warming and homogeneous temperature profile without large temperature gradients across the subject. All temperature measurements were performed using a rectal temperature sensor (rectal temperature probe, SA instruments, Inc., NY, USA). For examinations in vitro, an identical rectal temperature sensor was installed inside the main chamber of the multi-chamber phantom to ensure reliable temperature measurements of the samples (Figure 4.2). To minimize heat loss, the gaps of the small animal imaging chamber plastic enclosure were sealed using adhesive tape.

#### 4.1.4 Preparation of examinations

For examinations in vivo, the handling of the tumor-bearing mice was performed by Stephanie Laier<sup>4</sup>, Melanie Müller<sup>5</sup> or Julia Förderer<sup>4</sup>. Prior to the actual examinations, several preparation steps were executed (steps in parentheses were only done for in vivo examinations):

- Preheat water bath to  $T_{water\ bath} \approx 70^\circ\text{C}$  and small animal chamber to  $T \approx 37^\circ\text{C}$  by use of warm air.
- Insert RF coil into the bore of the small animal scanner so that the center of the RF coil is at position  $z = B_{0,iso}$ , i.e. at the isocenter of the static magnetic field.
- (Connect respiratory sensor pad to the monitoring system).
- Place subject centered and straight in imaging chamber so that the desired region of interest (ROI), i.e. the tumor area or samples, will be imaged at position  $z = B_{0,iso}$ .
- (Reduce respiratory motion of tumor area using a respiratory cradle).
- (Insert rectal temperature sensor and check monitoring system, i.e. temperature and respiration).

---

<sup>3</sup> Depending on the type of examination, subject refers either to the mouse (in vivo) or the phantom (in vitro).

<sup>4</sup> From the Core Facility Tumor Models, Center for Preclinical Research at the DKFZ.

<sup>5</sup> From the Division of Medical Physics in Radiology at the DKFZ.

- Drive imaging chamber into the isocenter of the magnet.

## 4.2 Model systems

In this section, the used model systems are described. These include (i) *in vitro* model systems, i.e. porcine brain lysate model suspensions (subsection 4.2.1) and creatine model solutions (subsection 4.2.2) and (ii) *in vivo* model systems, i.e. tumor-bearing mice (subsection 4.2.3).

### In vitro sample production

In principle, the manufacturing procedure of the different *in vitro* model systems was the same for all samples. Highly concentrated stock solutions with concentration  $C_{stock,i}$  were prepared for all the required components  $i$  of the samples. For each sample, the desired final concentration of each component  $C_{final,i}$  was obtained by adding together certain volumes of the stock solutions  $V_{stock,i}$  to the total volume of all components  $V_{tot} = \sum_i V_{stock,i}$  via

$$V_{stock,i} = \frac{C_{final,i}}{C_{stock,i}} V_{tot}. \quad (4.1)$$

Calculation of concentrations were performed with the help of a MATLAB<sup>®</sup> script. To regulate and stabilize the  $\text{pH}_{\text{titrated}}$  values, phosphate-buffered saline (PBS)<sup>6</sup> was utilized as buffer with  $C_{\text{PBS}} = \frac{1}{15}$  M. If needed, final adjustments to match the measured  $\text{pH}_{\text{titrated}}$  to the target pH values were performed using small quantities<sup>7</sup> of hydrochloric acid (HCl,  $C_{\text{HCl}} = 1$  M) or sodium hydroxide (NaOH,  $C_{\text{NaOH}} = 1$  M). Measurements of  $\text{pH}_{\text{titrated}}$  were performed at  $T \approx 37^\circ\text{C}$  using a pH meter<sup>8</sup> (SevenGo<sup>®</sup> pH meter SG2, Mettler-Toledo GmbH, Gießen, Germany) which was calibrated directly before sample production. The error of  $\text{pH}_{\text{titrated}}$  was estimated from the variation of five consecutive pH meter measurements. For porcine brain lysates, the error of  $\text{pH}_{\text{titrated}}$  was  $\pm 0.02$  pH. For creatine model solutions, the error of  $\text{pH}_{\text{titrated}}$  was  $\pm 0.04$  pH.

<sup>6</sup> Potassium phosphate ( $\text{KH}_2\text{PO}_4$ ) and sodium phosphate ( $\text{Na}_2\text{HPO}_4$ ) with  $M_{\text{KH}_2\text{PO}_4} = 136.09 \frac{\text{g}}{\text{mol}}$  and  $M_{\text{Na}_2\text{HPO}_4} = 141.96 \frac{\text{g}}{\text{mol}}$ .

<sup>7</sup> In the order of  $\sim 10 \mu\text{l}$ .

<sup>8</sup> The pH meter internally corrects for temperature effects, thus, allowing for an accurate pH measurement even in the presence of temperature variations.

### Multi-chamber phantoms

All in vitro experiments were performed using small reaction tubes as sample containers. For porcine brain lysates, 2 ml Eppendorf<sup>®</sup> reaction tubes (Eppendorf SE, Hamburg, Germany) were used. For creatine model solutions, 120  $\mu$ l Rotilab<sup>®</sup> reaction tubes (Carl Roth GmbH + Co. KG, Karlsruhe, Germany) were used. Multiple of these smaller reaction tubes were placed inside a larger 50 ml Falcon<sup>®</sup> tube (Fisher Scientific GmbH, Schwerte, Germany), which served as a so-called multi-chamber phantom<sup>9</sup>. Using the self-made multi-chamber phantom, four samples were measured simultaneously in porcine brain lysate and eleven in creatine model solution experiments, respectively. For the actual measurements, the rest of the multi-chamber phantom was filled with regular tap water as good as possible while avoiding trapped air bubbles in order to increase the magnetic field homogeneity inside the phantom (i.e. by minimizing susceptibility effects). A rectal temperature sensor was installed inside the main chamber of the multi-chamber phantom to ensure reliable temperature measurements of the samples.

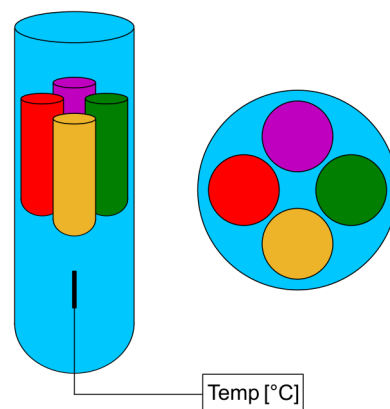


**Figure 4.2:** Illustration of the utilized multi-chamber phantom which enabled a simultaneous measurement of various samples (colors). A MR-safe temperature sensor was installed inside the main chamber which allowed for precise temperature monitoring during in vitro examinations (left). The surrounding water (blue) allows for a better magnetic field homogeneity across the entire FOV of the imaging slice (right).

<sup>9</sup> In MRI, a phantom refers to any sort of specially designed imaging object (typically plastic containers filled with samples of e.g. various materials) which is used to evaluate, analyze, optimize etc. the experiment without needing a living subject.

### 4.2.1 Porcine brain lysates

Porcine brain lysates are tissue homogenates produced from pig brains. A tissue homogenate is obtained by mechanically disrupting the cell membranes of fresh biological tissue. Importantly, the disruption only mechanically permeabilizes the cell membranes while simultaneously leaving all cell organelles intact (e.g. the nucleus or mitochondria). In this thesis, therefore, a distinction is made between pH-values measured via the endogenous amide and guanidyl signals in porcine brain lysates (simply referred to as pH) and in vivo (referred to as intracellular pH ( $\text{pH}_i$ )). The procedure of tissue homogenization allows for fine adjustments of e.g. pH-values in an in vivo-like model suspension which then can be used as in vitro experiments in a controlled manner.



**Figure 4.3:** Dounce homogenizer used for sample preparation of porcine brain lysates. Tissue is forced through the small gap between the glass vessel (left) and the glass pestle (right) which mechanically disrupts cell membranes while leaving cell organelles intact.

#### Sample preparation

Before preparation of porcine brain lysates, the pig brains were freshly obtained from a local butchery while continuously being cooled using ice. Samples were prepared at various  $\text{pH}_{\text{titrated}}$  and tissue concentrations ( $C_{\text{tissue}}$ ) from a mixture<sup>10</sup> of gray and white matter

<sup>10</sup> Approximately 50% gray matter and 50% white matter.

according to a previously established procedure [133–135]. The pH series (in the range of  $\text{pH}_{\text{titrated}} = 5.5$  to 8.0, Table 4.1) was prepared at a constant tissue concentration of  $C_{\text{tissue}} = 33.3\%$  [w/v]<sup>11</sup>. The concentration series (in the range of  $C_{\text{tissue}} = 16.7$  to 33.3% [w/v], Table 4.2) was prepared with a constant  $\text{pH}_{\text{titrated}} = 7.0$ . The final  $\text{pH}_{\text{titrated}}$  values ( $\text{pH}_{\text{titrated}}(\text{final})$ ) marginally differed from the target pH ( $\text{pH}_{\text{titrated}}(\text{target})$ ), see Tables 4.1 and 4.2. In order to preserve the proteome as good as possible<sup>12</sup>, the samples were chilled using ice during production when ever possible. Mechanical disruption of the cell membranes was performed using a Dounce homogenizer<sup>13</sup> (Figure 4.3). Tissue homogenization was performed in two steps with different gap sizes between the glass pestle and the surrounding glass vessel. In the first step, a gap size of  $\sim 115 \mu\text{m}$  was used to grind the brain tissue into a manageable size for the second step. In the second step, a gap size of  $\sim 50 \mu\text{m}$  was used to fully disrupt the cell membranes while sparing the organelles.

**Table 4.1:** pH series of porcine brain lysate model suspensions (varying  $\text{pH}_{\text{titrated}}$  values at constant tissue concentration of  $C_{\text{tissue}} = 33.3\%$ [w/v]). The error of  $\text{pH}_{\text{titrated}}$  was  $\pm 0.02$  pH.

<b><math>\text{pH}_{\text{titrated}}</math> (target)</b>	<b>5.50</b>	<b>6.00</b>	<b>6.00</b>	<b>6.20</b>	<b>6.40</b>	<b>6.40</b>	<b>6.50</b>	<b>6.60</b>	<b>6.70</b>	<b>6.80</b>
$\text{pH}_{\text{titrated}}$ (final)	5.47	5.99	6.01	6.21	6.40	6.41	6.51	6.59	6.69	6.80
Session / examination	2/1	1/1	2/1	3/1	2/1	3/1	1/1	3/1	2/1	3/1
<b><math>\text{pH}_{\text{titrated}}</math> (target)</b>	<b>7.00</b>	<b>7.00</b>	<b>7.00</b>	<b>7.20</b>	<b>7.30</b>	<b>7.40</b>	<b>7.50</b>	<b>7.60</b>	<b>7.60</b>	<b>8.00</b>
$\text{pH}_{\text{titrated}}$ (final)	7.01	6.98	7.02	7.20	7.33	7.41	7.52	7.61	7.60	8.02
Session / examination	1/1	2/2	3/2	3/2	2/2	3/2	1/1	2/2	3/2	2/2

The samples were produced in three sessions (each on a separate day) and were freshly prepared directly before MRI examination (see Tables 4.1 and 4.2). In each session, data was acquired from the respective samples in two separate MRI examinations as a maximum of four samples could be examined simultaneously. To allow for a better comparison of the acquired CEST data between the different sessions, some samples of the pH series were manufactured at similar  $\text{pH}_{\text{titrated}}$  values (e.g. with  $\text{pH}_{\text{titrated}} = 7$ , beginning of fourth

<sup>11</sup> Weight per volume.

<sup>12</sup> To inhibit the denaturation of proteins and metabolites, thus ensuring in vivo-like characteristics.

<sup>13</sup> Named after Alexander Dounce.

**Table 4.2:** Concentration series of porcine brain lysate model suspensions (varying tissue concentrations at constant  $\text{pH}_{\text{titrated}} = 7.0$ ). The error of  $\text{pH}_{\text{titrated}}$  was  $\pm 0.02$  pH.

$C_{\text{tissue}}$ [% w/v]	16.7	22.2	27.8	33.3	16.7	22.2	27.8	33.3
$\text{pH}_{\text{titrated}}$ (target)	7.00	7.00	7.00	7.00	7.00	7.00	7.00	7.00
$\text{pH}_{\text{titrated}}$ (final)	7.01	7.01	7.01	7.01	7.01	7.00	7.01	7.01
Session / examination	1/2	1/2	1/2	1/2	3/2	3/2	3/2	3/2

row in Table 4.1) which were used to exclude any potential systematic biases.

#### 4.2.2 Creatine model solutions

Creatine is an organic compound ( $\text{C}_4\text{H}_9\text{N}_3\text{O}_2$ ,  $M_{\text{C}_4\text{H}_9\text{N}_3\text{O}_2} = 131.13 \frac{\text{g}}{\text{mol}}$ ) which is found in vertebrates where it plays an important role in the energy metabolism and is primarily present in muscle and brain tissue. The tissue metabolite creatine has a guanidinium group ( $(\text{NH}_2)_2$ ) and only exhibits one clear CEST resonance, i.e. the guanidyl proton resonance at  $\Delta\omega_{\text{gua}} = 2.0$  ppm. As creatine is soluble in water and relatively stable at in vivo temperatures, aqueous creatine solutions are commonly used as a simple two-pool model system for CEST experiments. Creatine (Sigma-Aldrich Chemie GmbH, Taufkirchen, Germany) samples were prepared at eleven different pH values in the range of  $\text{pH}_{\text{titrated}} = 6.0$  to 8.2 and a constant concentration of  $C_{\text{creatin}} = 50$  mM (Table 4.3). All samples were produced with the help of Lilli Diederichs<sup>14</sup>. In order to adjust the relaxation time to  $T_1 \approx 2.6$  s, gadolinium (Gd) was used in form of gadoteric acid (Gd-DOTA, Dotarem<sup>®</sup>, Guerbet GmbH, Sulzbach, Germany) with a concentration of  $C_{\text{Gd-DOTA}} = 45$   $\mu\text{M}$ , as determined by [137] and refined by [136].

**Table 4.3:** pH series of creatine model solutions with a constant concentration of  $C_{\text{creatin}} = 50$  mM. The error of  $\text{pH}_{\text{titrated}}$  was  $\pm 0.04$  pH.

$\text{pH}_{\text{titrated}}$ (target)	6.0	6.2	6.4	6.6	6.8	7.0	7.2	7.4	7.6	7.8	8.0
$\text{pH}_{\text{titrated}}$ (final)	5.98	6.16	6.39	6.56	6.78	6.97	7.20	7.40	7.64	7.91	8.20

<sup>14</sup> Within the framework of her bachelor thesis [136], where further details are provided.

### 4.2.3 Tumor-bearing mice

Animal care and all animal experiments were performed according to the national guidelines and, firstly, were approved by an institutional review board and animal welfare committee headed by the local animal welfare officer at the German Cancer Research Center (DKFZ) in Heidelberg, Germany. In addition, all experiments were approved by the responsible national authority under license G284-15, i.e. by the local Governmental Committee for Animal Experimentation (Regierungspräsidium Karlsruhe) in Karlsruhe, Germany, and were performed accordingly. Mice examinations were carried out with the help of PD Dr. Karin Müller-Decker<sup>15</sup>, Stephanie Laier<sup>15</sup>, Julia Förderer<sup>15</sup> and Melanie Müller<sup>16</sup>. The culturing of the tumor cells was performed by Dr. Andrey Glinka<sup>17</sup> and Renate Bangert<sup>16</sup>.

#### Animal tumor preparation and monitoring

Five to six-week-old nude mice ( $n = 14$ , female NMRI Nude, Janvier Labs, Le Genest-Saint-Isle, France) were xenografted with DLD1 cancer cells (human colon cancer cell line). Under isoflurane anesthesia,  $2 \cdot 10^6$  DLD1 cells re-suspended in 100  $\mu$ l PBS were injected subcutaneously into the right flank. Once the tumor diameter reached 3.5 mm (i.e. day zero, d0), in vivo MRI examinations of DLD1 xenografted nude mice were performed as described below using the 9.4 T small animal scanner described in subsection 4.1.1. Weight of the mice was determined three times in the first week, and afterwards, if stable, once per week. Tumor volume was measured three times per week and, in addition, directly before MRI examination and post-mortem. According to GV-SOLAS criteria (Gesellschaft für Versuchstierkunde, Society for Laboratory Animal Science, Freiburg, Germany), experiments were terminated if either (i) weight loss of mice was more than or equal to 20%, (ii) tumor lesions bled or ulcerated, (iii) tumor lesions reached more than or equal to 1.5 cm in diameter in one dimension, or (iv) mice suffered from diarrhea. Post-mortem, tumors were investigated and checked for necrosis by means of routine hematoxylin/eosin staining.

---

<sup>15</sup> From the Core Facility Tumor Models, Center for Preclinical Research at the DKFZ.

<sup>16</sup> From the Division of Medical Physics in Radiology at the DKFZ.

<sup>17</sup> From the Division of Molecular Embryology at the DKFZ.

### **In vivo pH<sub>i</sub> measurements in tumor lesions of different sizes**

Tumor lesions of different sizes were examined by performing in vivo MRI examinations as described below on days d0, d3 and d10 ( $n = 6$  mice), on days d0, d3, d7 and d10 ( $n = 6$  mice, i.e. treated and control mice, see subsequent subsection), on day d3 ( $n = 1$  mouse) and on day d10 ( $n = 1$  mouse)<sup>18</sup>. Treated mice were excluded in the evaluation of pH<sub>i</sub> measurements with tumor lesions of different sizes.

### **In vivo pH<sub>i</sub> measurements in tumor lesions of treated and control mice**

$n = 6$  mice were randomized into two cohorts, i.e. treatment and control ( $n = 3$  mice in each group). Five days after transplantation, once the tumor reached a diameter of 3.5 mm in one dimension, treatment started (i.e. day zero, d0). Treatment mice orally received 10 mg/kg Monensin, 500 mg/kg Fenofibrat via diet and 40 mg/kg Metformin via drinking water. Control mice received Kliba diet 3437 (KLIBA NAFAG, Kaiseraugust, Switzerland) and normal drinking water. For treatment and control mice, in vivo MRI examinations were performed on days d0, d3, d7 and d10 as described below. Control mice were included in the evaluation of pH<sub>i</sub> measurements with tumor lesions of different sizes.

### **In vivo MRI examination preparation and procedure**

MRI examinations were performed under sevoflurane anesthesia. During anesthesia, the mice were kept at a constant body temperature<sup>19</sup> of  $T_{mouse} = 37 \pm 0.2^\circ\text{C}$  by use of the heating system described in subsection 4.1.3 (i.e. warm air blown into the small animal imaging chamber). Eye cream was applied during anesthesia and examination to avoid eye drying. During MRI examination, an optimized positioning of a respiratory small animal cradle (SA instruments, Inc., NY, USA) was utilized to suppress breathing-induced motion artifacts in the tumor region. The respiratory cradle was positioned around the abdomen of the mouse so that the tumor lesion was completely covered. Subsequently, the respiratory cradle was adjusted so that the breathing-induced motion was mainly restricted to the thorax region (i.e. mitigating abdominal respiratory motion). Simultaneous suppression of surrounding healthy tissue could not be achieved. A respiratory sensor (breathing surface pad connected to a pressure transducer) was placed under the mouse

<sup>18</sup> Note that in the journal article [121] a misleading terminology was used stating  $n = 19$  mice (wrong) instead of  $n = 19$  measurements performed in tumor lesions of  $n = 11$  mice (correct).

<sup>19</sup> As detected by a rectal temperature probe.

and used to monitor animal respiration.

## 4.3 Data acquisition

In this section, the data acquisition is described. This MR data acquisition protocols, parameters and settings.

### 4.3.1 The CEST pulse sequence, mean $B_1$ and the presaturation pulse shape $c_2$

Within the scope of this thesis, a custom-built CEST pulse sequence was implemented on the 9.4 T small animal MR scanner which was used to perform all measurements. The implementation was realized with the help of Dr. Steffen Görke<sup>20</sup> who performed the sequence programming<sup>21</sup>. The CEST pulse sequence is described in subsection 2.4.4.

Prior to the presaturation block (Figure 2.9, green), a recovery time  $t_{rec}$  can be added. This was used in order to acquire the fully relaxed  $M_0$  images at the beginning and end of each CEST scan. For acquisition of all other images  $M(\Delta\omega)$ ,  $t_{rec} = 0$ . In case of a pulsed presaturation,  $\overline{B_1}$  (mean  $B_1$ ) was calculated via

$$\overline{B_1} = \frac{1}{t_p} \int_0^{t_p} B_1(t) dt, \quad (4.2)$$

which allows for comparison of  $B_1$  between cw and pulsed CEST experiments. For the utilized Gaussian-shaped presaturation pulses, the form factor value ( $c_2$ ) which also encompasses the shape of the presaturation pulse (Figure 4.4) was numerically calculated via [138, 139]

$$c_2 = \frac{\left( \int_0^{t_p} B_1(t) dt \right)^2}{t_p \int_0^{t_p} B_1^2(t) dt}. \quad (4.3)$$

<sup>20</sup> From the Division of Medical Physics in Radiology at the DKFZ.

<sup>21</sup> In ParaVision® version 360.1.1 (Bruker Corporation, Billerica, USA).

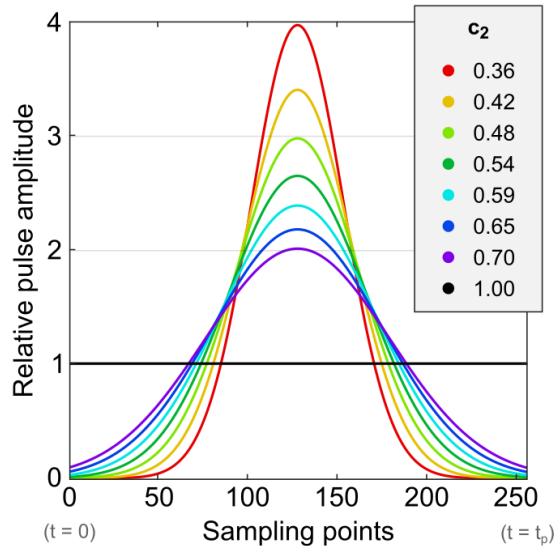


**Figure 4.4:** Illustration of the various presaturation pulse shapes ( $c_2$ ) used for the pulsed CEST experiments with creatine model solutions. The area under the curve is equal for each  $c_2$ .

### 4.3.2 The CEST-MRI data set

A CEST-MRI data set consists of several individually acquired MR images, each of which is acquired with a presaturation at a different frequency offset  $\Delta\omega$  (Figure 2.7). For this reason, the combined CEST-MRI data has a spatial dimension (MR images) and a spectral dimension ( $\Delta\omega$ ). Accordingly, each frequency offset  $\Delta\omega$  corresponds to a complete image ( $M(\Delta\omega)$ ) and, vice versa, each pixel ( $x, y$ ) in the image<sup>22</sup> corresponds to an individual  $Z(x, y)$ -spectrum. In addition, CEST-MRI data is also acquired at several RF amplitudes  $B_1$ , which adds another dimension ( $B_1$ ) to the data set.

### 4.3.3 Image readout

In order to detect the decaying CEST contrast, the modified water signal needs to be measured fast and immediately after presaturation (Figure 2.9, blue). Two different types of fast image acquisition were used, depending on the type of performed measurements:

- (i) A rapid acquisition with relaxation enhancement (RARE) image acquisition was

<sup>22</sup> In the case of a 3D image acquisition, each voxel ( $x, y, z$ ) corresponds to an individual  $Z(x, y, z)$ -spectrum and vice versa.

used for examinations in vivo and in porcine brain lysates (SE-based imaging sequence).

- (ii) A fast imaging with steady state precession (FISP) image acquisition was used for examinations in creatine model solutions (GRE-based imaging sequence).

Importantly, the type of used image readout does not influence the CEST effect<sup>23</sup>, as it is only used for image acquisition (i.e. to acquire the modified water signal). However, each type of image readout exhibits certain differing basic imaging properties, such as a different SNR or a different image contrast<sup>24</sup>. In general, all types of image readout are characterized by image acquisition parameters. The most important imaging parameters are: The field of view (FOV), the matrix size (i.e. number of pixels for 2D or voxels for 3D images), the resolution, the slice thickness ( $d_s$ ), the flip angle (FA), the echo time (TE), the repetition time (TR), the excitation bandwidth (exBW) and the acquisition bandwidth (acBW). The image readout parameters were optimized for each type of examination and are presented in Table 4.4.

**Table 4.4:** Optimized MRI readout parameters utilized in this thesis.

Parameter	Unit	Porcine brain lysates	Tumor-bearing mice	Creatine model solutions
Sequence	—	RARE	RARE	FISP
FOV	[mm]	$30 \times 30$	$30 \times 30$	$30 \times 30$
Matrix	—	$60 \times 60$	$40 \times 40$	$60 \times 60$
Resolution	mm	$0.5 \times 0.5$	$0.75 \times 0.75$	$0.5 \times 0.5$
$d_s$	mm	2	2	2
FA	[°]	180	180	15
TE	[ms]	4.628	4.628	1.887
TR	[ms]	281.126	188.57	3.774
PF	—	off	off	off
Encoding	—	centric	centric	centric
PE direction	—	left-right (columns)	left-right (columns)	left-right (columns)
RARE factor	—	60 (single shot)	40 (single shot)	—
exBW	[kHz]	20	20	25
acBW	[kHz]	50 (833.3 [Hz/pix])	50 (1250 [Hz/pix])	20 (333.3 [Hz/pix])

<sup>23</sup> Provided that steady-state ( $Z^{ss}$ ) is reached (section 2.5), which is given within the scope of this thesis.

<sup>24</sup> For example, a  $T_1$ -weighted,  $T_2$ -weighted, or proton density-weighted image contrast.

### 4.3.4 MR data acquisition protocol

The CEST scan parameters are presented in Table 4.5. For Z-spectra normalization, two  $M_0$  images were acquired at -300 ppm (i.e. one at the beginning and one at the end of each CEST scan). For acquisition of  $M_0$  images, an additional recovery time interval was added to ensure complete relaxation of the water magnetization (i.e. complete recovery towards the equilibrium magnetization). The WASABI scans (subsection 4.4.1) were realized by a rectangular cw presaturation pulse of amplitude  $B_1 = 5 \mu\text{T}$  and duration  $t_p = 3.7 \text{ ms}$  at 25 frequency offsets in equal steps between  $\pm 1.2 \text{ ppm}$ . For the WASABI scans an additional recovery interval of  $t_{rec} = 3 \text{ s}$  was included between each frequency offset for signal recovery. In addition, for examinations in vivo an anatomical high-resolution 3D image was acquired using a  $T_{2w}$ -RARE sequence<sup>25</sup>. The acquisition protocol consisted of several steps:

1. **Localizer:** Rapid acquisition of a 3D localizer image (Figure 4.5, b). Check positioning of mouse or phantom and coil sensitivity profile, if needed correct positioning. For phantom experiments: check for interfering air bubbles.
2. **Adjustments:** Manually set RF reference power and receiver gain (in a slice positioned approximately within later FOV), and obtain internal  $B_0$  map (needed for shimming).
3. **Wobble:** Manually tune and match RF coils (Figure 4.1g).
4. **Anatomical image:** Acquisition of high-resolution 3D anatomical image (in vivo only).
5. **Positioning of FOV:** Define the CEST imaging slice (Figure 4.5, gray boxes) with help of the anatomical image (in plane) and localizer (out of plane).
6. **Shimming:** For in vivo examinations: Define the adjustment volume with help of the anatomical image (in plane, Figure 4.5a) and localizer (out of plane, Figure 4.5c, d), i.e. tumor ROI including back muscles and  $B_0$  isocenter if simultaneously possible, no air (Figure 4.5, green ellipsoids). For in phantom measurements: Define adjustment volume using the localizer (entire phantom cross section in FOV, no air). Start iterative shimming procedure.

<sup>25</sup> FOV =  $30 \times 30 \times 16 \text{ mm}^3$ , matrix =  $240 \times 240 \times 16$ , resolution =  $0.125 \times 0.125 \times 1 \text{ mm}^3$  with an acquisition time of 6:06 min.

7. **WASABI:** Acquisition of one WASABI scan (needed for  $B_0$  and  $B_1$  field mapping).
8. **CEST:** Acquisition of multiple CEST scans at various nominal  $B_1$  (Details are provided in Table 4.5).

**Table 4.5:** Optimized acquisition parameters of the CEST scans. The complete lists of frequency offsets  $\Delta\omega$  for sampling of Z-spectra are provided in Appendix A.2. The three different data acquisition sessions of porcine brain lysates are labeled S1, S2 and S3, respectively. Acquisition time ( $t_{acq}$ ).

Parameter	Unit	Porcine brain lysates	Tumor-bearing mice	Creatine model solutions
Presaturation	—	cw	cw	pulsed <sup>26</sup> (7 different $c_2$ ) & cw
$t_{sat}$	[s]	10	6	12
$n_p$	[#]	1	1	pulsed: 118 <sup>27</sup> cw: 2 <sup>28</sup>
$\Delta\omega$	[#]	92 (S1) 48 (S2) 58 (S3)	42	82
$B_1$	[μT]	0.5, 0.75, 1.0, 1.5, 2.0, 2.5 (S1) 0.5, 0.75, 1.0, 1.5, 2.0, 2.5 (S2) 0.6, 1.0, 1.4, 2.0 (S3)	0.6, 1.0, 1.4	0.6, 1.0, 1.4
$t_{rec}(M_0)$	[s]	20	12	20
$t_{acq}$	[min/ $B_1$ ]	16:47	4:56	17:56

## 4.4 Data processing and evaluation

In this section, the data processing and evaluation procedures are described. All acquired MR raw data was reconstructed by the scanner using a magnitude-based reconstruction (yielding intensity-based images) and exported using the digital imaging and communications in medicine (DICOM) file format. Anatomical images were mapped onto the CEST images using the MITK [132] software package. All further data processing and evaluation was performed using in-house and self-written code in MATLAB<sup>®</sup>.

<sup>26</sup> With  $c_2 = 0.36, 0.42, 0.48, 0.54, 0.59, 0.65$  and  $0.70$ , as illustrated in Figure 4.4.

<sup>27</sup> With  $t_p = 100$  ms and  $t_d = 2$  ms, thus resulting in  $t_{sat} = 12.036$  s.

<sup>28</sup> Two rectangular cw pulses with  $t_p = 6$  s each were necessary for  $t_{sat} = 12$  s, as  $t_{p, max} = 10$  s.

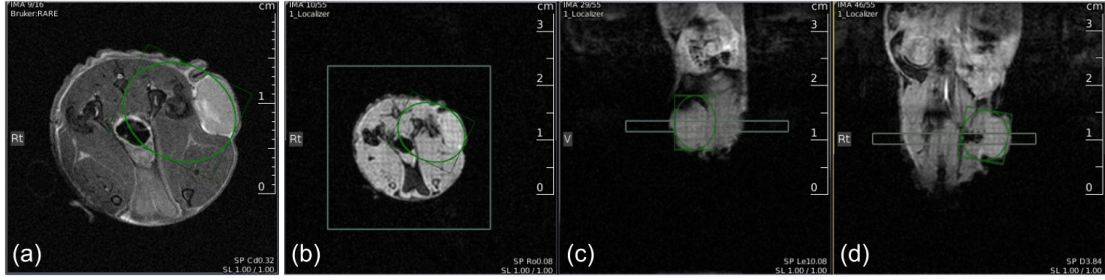


**Figure 4.5:** Screenshots of the anatomical image (a) and localizer (b-d) showing the positioning procedure of the FOV (b-d, gray boxes) and the adjustment volume (green ellipsoids). The image slice is positioned centrally within the tumor (c, d). For an optimized shimming procedure of the tumor area, the adjustment volume should cover the entire tumor, include some muscle tissue as well as, if possible, the  $B_0$  isocenter and, importantly, avoid including any surrounding air.

#### 4.4.1 $B_0$ and $B_1$ field mapping

In order to achieve a pixel-by-pixel mapping of the static magnetic field ( $B_0$ ) and the RF excitation field ( $B_1$ ), the water shift and  $B_1$  mapping (WASABI) method [140] was utilized. The WASABI method simultaneously enables both  $B_0$  and  $B_1$  field mapping, i.e. the mapping of magnetic field inhomogeneities ( $\Delta B_0$  and  $\Delta B_1$ ). Effectively, Rabi oscillations are induced by applying an off-resonant, short, rectangular presaturation pulse<sup>29</sup>, which results in a sinc-like Z-spectrum in the  $\Delta\omega$  offset dimension (WASABI-spectrum). The WASABI-spectrum is acquired using the CEST imaging sequence<sup>30</sup>, by sampling  $Z(\Delta\omega)$  at several offsets between the water frequency (e.g. 25 regularly spaced offsets between  $\pm 1.2$  ppm). The symmetry axis of the WASABI-spectrum is used to determine  $B_0$  while the oscillation frequency of the WASABI-spectrum is used to determine  $B_1$  via [140]

$$Z(\Delta\omega) = \left\| \left| c - d \cdot \sin^2 \left( \tan^{-1} \left( \frac{\gamma \cdot B_1}{\Delta\omega - \delta\omega_w} \right) \right) \cdot \sin^2 \left( \sqrt{(\gamma \cdot B_1)^2 + (\Delta\omega - \delta\omega_w)^2} \cdot \frac{t_p}{2} \right) \right\|. \quad (4.4)$$

<sup>29</sup> With a pulse amplitude and a pulse duration in the order of  $B_1 \sim 5 \mu\text{T}$  and  $t_p \sim 3.7$  ms, respectively.

<sup>30</sup> Using the same image acquisition for the field mapping as for the actual CEST imaging (only the presaturation block is changed, while the imaging block remains identical) considerably simplifies the entire post-processing procedure.

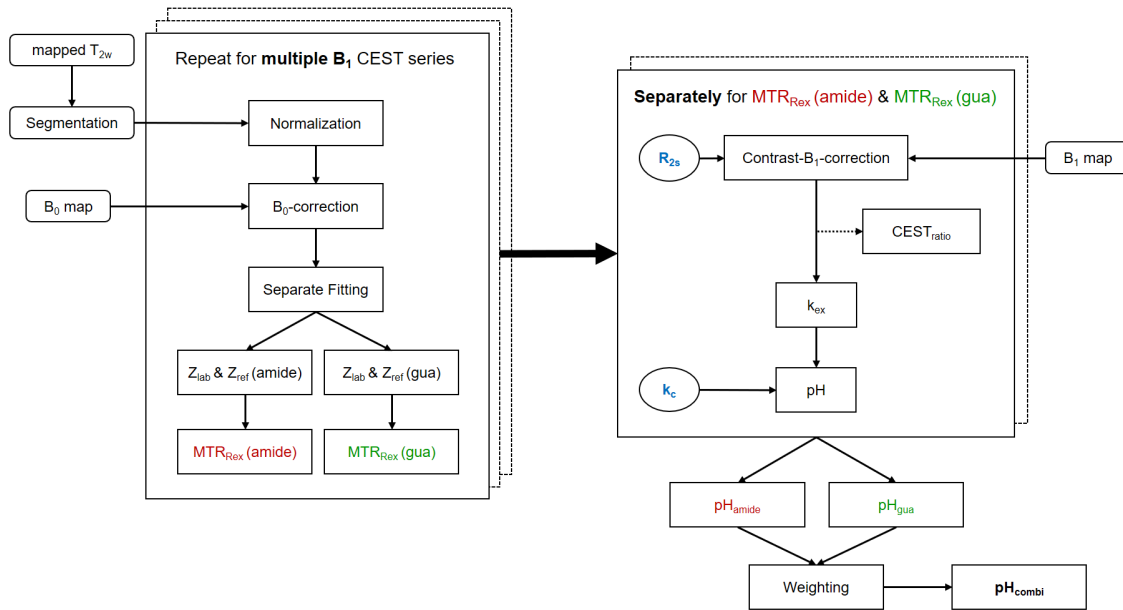


**Figure 4.6:** The CEST data post-processing and pH mapping workflow consisted of several consecutively performed steps. Post-processing was performed on a pixel-by-pixel basis (except for the segmentation).

Here, the free parameters  $c$  and  $d$  describe the amplitude modulation (not of interest),  $B_1$  describes the changes in periodicity and the water frequency shift  $\delta\omega_w$  describes the symmetry axis of  $Z(\Delta\omega)$ . By fitting the WASABI-spectrum, the  $B_0$  shift is calculated via  $\Delta B_0 = \gamma \cdot \delta\omega_w$  while the relative  $\Delta B_1$  values are directly determined by the fit. Representative  $B_0$  and  $B_1$  maps of porcine brain lysates and a tumor-bearing mouse are shown in Figures 5.1d, e, and 5.10d, e, respectively.

#### 4.4.2 CEST data post-processing and pH mapping workflow

This section describes the post-processing workflow of the acquired CEST data. All post-processing was performed on a pixel-by-pixel basis, except for the segmentation. As an overview, the entire post-processing workflow is illustrated in Figure 4.6.

##### 4.4.2.1 Segmentation

In a first step, the acquired CEST images were semi-automatically segmented. Therefore, the images were partitioned into two regions which are (i) the actual imaged object of interest (i.e. the segment containing the mouse or phantom) and (ii) the rest outside of this region. For in vitro examinations, the segmentation was performed on the first  $M_0$

## 4 Materials and Methods

image of the first CEST- $B_1$ -series. In contrast, for in vivo examinations, the segmentation was performed on the mapped anatomical image. The mapped anatomical image was obtained by mapping the additionally acquired anatomical image onto the CEST images using the MITK [132] software package. In short, this was accomplished by scaling down the resolution of the highly-resolved anatomical image to match the resolution of the CEST images (i.e. by binning pixels together).

### 4.4.2.2 Normalization

In a second step, the acquired CEST data was normalized according to  $Z(\Delta\omega) = \frac{M_{sat}^{ss}(\Delta\omega)}{M_0(\Delta\omega)}$  (section 2.4.2). The normalization of Z-spectra was performed by linearly interpolating between the two acquired  $M_0$  images of the corresponding CEST- $B_1$ -series (one  $M_0$  image was acquired at the beginning and one at the end of each CEST scan). The linear interpolation over the frequency offset index (i.e. along the spectral dimension  $\Delta\omega$ ) enabled to obtain an individual  $M_0$  image for each separate  $M_{sat}^{ss}(\Delta\omega)$ .

### 4.4.2.3 $B_0$ correction

In a next step, the Z-spectra were corrected for inhomogeneities in the static magnetic field  $B_0$ . This was necessary because unavoidable  $B_0$  field inhomogeneities remain even after shimming the FOV.  $B_0$  inhomogeneities lead to a spectral shift of each acquired Z-spectrum as a whole, which is especially noticeable at the DS of the water frequency offset (i.e.  $\Delta\omega_{water}$  is not exactly at 0 ppm). In order to correct for  $B_0$  inhomogeneities, the acquired  $Z(\Delta\omega_{uncorrected})$ -spectra were shifted along the frequency dimension (i.e. the  $\Delta\omega$ -axis) according to the local  $\Delta B_0$  in each pixel which is given by the  $B_0$  map obtained from the WASABI measurement (subsection 4.4.1). The  $B_0$  correction was performed for each Z-spectrum separately (i.e. for each pixel and CEST- $B_1$ -series, respectively) by the following procedure:

1. A smoothing spline fit with a smoothing parameter of 0.999<sup>31</sup> was used to interpolate the  $Z(\Delta\omega_{uncorrected})$ -spectrum.
2. Each frequency offset  $\Delta\omega_{uncorrected}$  of the  $Z(\Delta\omega_{uncorrected})$ -spectrum was mapped onto the smoothing spline, i.e. shifted along the Z-axis according to the Z-value of the interpolated  $Z(\Delta\omega_{uncorrected})$ -spectrum.

---

<sup>31</sup> Very little smoothing, as the smoothing parameter  $\in [0,1]$  where 0 represents a linear interpolation between the Z-values of the first and last frequency offset index and 1 represents no smoothing at all. For examinations in creatine model solutions, a smoothing parameter of 1 was used.

3. The smoothed and interpolated  $Z(\Delta\omega_{uncorrected})$ -spectrum was shifted along the  $\Delta\omega$ -axis according to its local  $\Delta B_0$ , i.e. via  $\Delta\omega = \Delta\omega_{uncorrected} + \Delta B_0$ , yielding the final  $B_0$ -corrected  $Z$ -spectrum.

A representative  $B_0$  map of porcine brain lysates is shown in Figure 5.1d.

#### 4.4.2.4 Determination of $Z_{lab}$ and $Z_{ref}$

Subsequently, the  $B_0$ -corrected  $Z$ -spectra were used to pixel-wise determine the labeled  $Z$ -spectrum ( $Z_{lab}$ ) and the reference  $Z$ -spectrum ( $Z_{ref}$ ).  $Z_{lab}$  and  $Z_{ref}$  are needed for CEST signal extraction and to isolate the signals from interfering concomitant effects.  $Z_{lab}$  represents the acquired data points in the measured  $Z$ -spectrum (including all CEST pools). In contrast,  $Z_{ref}$  corresponds to the theoretical  $Z$ -spectrum without the specific CEST pool of interest (all other pools except for the pool of interest, i.e. the background).  $Z_{lab}(\Delta\omega_s)$  corresponds to the measured  $Z$ -value of the label pool  $s$  at position  $\Delta\omega_s$ , whereas  $Z_{ref}(\Delta\omega_s)$  represents the reference  $Z$ -value of  $s$  at position  $\Delta\omega_s$ . Importantly,  $Z_{lab}$  is simply obtained via measurement whereas  $Z_{ref}$ , however, can not be directly measured. Therefore, several approaches exist in order to extract CEST signals from the background, such as the asymmetry approach, the multiple Lorentzian fitting approach or the polynomial and Lorentzian fitting approach. In this thesis, two different approaches were used to obtain  $Z_{ref}$ :

- (i) The asymmetry approach was used (paragraph in 4.4.2.4) for creatine model solution experiments (section 5.3).
- (ii) A first order polynomial and Lorentzian fitting approach was used (paragraph in 4.4.2.4) for all other experiments (porcine brain lysates and tumor-bearing mice, section 5.1 and 5.2, respectively).

**Asymmetry approach** The simplest way to determine  $Z_{ref}$  is the asymmetry approach [46]. The asymmetry approach uses the measured  $Z$ -value at the exact opposite side of the  $Z$ -spectrum to obtain  $Z_{ref}$  via

$$Z_{ref}(\Delta\omega) = Z_{lab}(-\Delta\omega). \quad (4.5)$$

Importantly, this approach only yields reliable and quantitative  $Z_{\text{ref}}$ -values under the assumption of a simple two-pool model<sup>32</sup>. Therefore, the asymmetry approach can not be used for a reliable and quantitative  $Z_{\text{ref}}$  determination of in vivo-like Z-spectra. However, this assumption certainly holds true for simple creatine model solutions.

**Multiple Lorentzian fitting approach** Another common way to determine  $Z_{\text{ref}}$  is the (multiple) Lorentzian fitting approach [141, 142]. The multiple Lorentzian fitting approach is based on the assumption that the resonances of all signals contributing to the Z-spectrum can be described by a single Lorentzian-shaped function. For a CEST pool  $s$ , the Lorentzian function<sup>33</sup> centered around position  $x_s$  is given by

$$\mathcal{L}_s = \mathcal{A}_s \cdot \frac{\left(\frac{\Gamma_s}{2}\right)^2}{x_s^2 + \left(\frac{\Gamma_s}{2}\right)^2}, \quad (4.6)$$

where  $\mathcal{A}_s$  is the amplitude and  $\Gamma_s$  the FWHM of the Lorentzian. For each pool  $s$ , the position  $x_s$  of the corresponding Lorentzian is shifted according to its specific resonance frequency offset  $\delta\omega_s$  via

$$x_s = \Delta\omega - \delta\omega_s. \quad (4.7)$$

Therefore, the complete Z-spectrum is fitted by a superposition of Lorentzians via

$$Z_{\text{fitted}} = Z_{\text{max}} - (\mathcal{L}_{DS} - \mathcal{L}_{MTC} - \mathcal{L}_{rNOE} - \mathcal{L}_{amide} - \mathcal{L}_{gua} - \mathcal{L}_{amine}), \quad (4.8)$$

i.e. one Lorentzian for each pool<sup>34</sup> contributing to the Z-spectrum. In equation (4.8),  $Z_{\text{max}}$  represents a constant offset to the Z-spectrum<sup>35</sup> which is added to the fit function in order to account for potentially occurring incomplete relaxation of the water signal. Accordingly, the reference value of any desired pool  $s$  is calculated via [143]

$$Z_{\text{ref},s} = Z_{\text{max}} - \sum_{i \neq s} (\mathcal{L}_i) = Z_{\text{fitted}} + \mathcal{L}_s, \quad (4.9)$$

<sup>32</sup> If no other interfering concomitant effects are present in the Z-spectra and the frequency offset of the CEST signal of interest is far enough from the water resonance, i.e.  $\delta\omega_s \gg \omega_1$ .

<sup>33</sup> In this thesis, a function with a Lorentzian line shape is also simply referred to as Lorentzian.

<sup>34</sup> Direct water saturation (DS), semi-solid MT (MTC), exchange-relayed NOE (rNOE) and CEST signals of amide, guanidyl and amine protons.

<sup>35</sup> If the maximum of the Z-spectrum at large frequency offsets is not exactly at  $Z = 1$ .

i.e. by summing up all pools except for the pool of interest.

**Polynomial and Lorentzian fitting approach** Another common approach to obtain  $Z_{\text{ref}}$  is the polynomial and Lorentzian fitting approach [41, 54, 144]. By definition, the reference value  $Z_{\text{ref}}(\Delta\omega)$  of a pool  $s$  represents the background consisting of all other pools. In principle, this background can be approximated by any appropriate function. The polynomial and Lorentzian fitting approach utilizes polynomial functions of  $n^{\text{th}}$  order to describe the background and a Lorentzian function to describe the pool of interest. In this thesis, Z-spectra were fitted pixel-by-pixel using a first order polynomial and Lorentzian fit model (i.e. a linear and Lorentzian fit). The amide and guanidyl CEST signals ( $s$ ) were extracted separately from the background by an individual linear and Lorentzian fit given by

$$Z_{\text{fitted},s}(\Delta\omega_s) = \underbrace{m_s \cdot (\Delta\omega_{\text{RF}} - \delta\omega_{\text{poly},s}) + c_s}_{\text{background}} - \mathcal{L}_s, \quad (4.10)$$

where  $c_s$  and  $m_s$  represent the coefficients of the linear function (i.e. the intercept and slope, respectively) and  $\delta\omega_{\text{poly},s}$  represents the frequency offset position of the linear function with  $\delta\omega_{\text{amide}} = 3.6$  and  $\delta\omega_{\text{gua}} = 2.0$  ppm, respectively. Importantly, the separate fitting of the amide and guanidyl CEST signals was performed by including only spectral data points close to each respective resonance frequency (with approximately  $\pm 0.5$  ppm, see Table 4.6 and 4.7 for details). The Z-spectra fitted via equation (4.10) were then used to calculate  $Z_{\text{lab}}$  and  $Z_{\text{ref}}$  according to [143] via

$$Z_{\text{lab},s} = Z_{\text{fitted},s}, \quad (4.11)$$

and

$$Z_{\text{ref},s} = Z_{\text{fitted},s} + \mathcal{L}_s. \quad (4.12)$$

The fit model given by equation (4.10) was utilized for determination of  $Z_{\text{lab}}$  and  $Z_{\text{ref}}$  in Z-spectra of porcine brain lysates (Figure 5.2) and tumor-bearing mice (Figure 5.11). The optimized fit parameters are provided in Tables 4.6 and 4.7 (i.e. the offsets which actually were fitted along with the starting values and boundaries of the fit model parameters used for the separate amide and guanidyl CEST signal extraction at each applied  $B_1$ ). For each acquired nominal  $B_1$ , the offset ranges for the fitting procedure were slightly adjusted and optimized to the respective Z-spectra at each different  $B_1$  ( $\Delta\omega_{\text{fitted}}$  in Table 4.6 and 4.7).

#### 4 Materials and Methods

This was performed in order to account for the peak broadening of CEST signals with increasing  $B_1$  [58]. Also, the available reasonable offset ranges were limited by the amine signal at  $\delta\omega_{amine} \approx 2.7$  and the curvature of the DS.

**Table 4.6:** Z-spectrum fit parameters used for extraction of  $Z_{lab}$  and  $Z_{ref}$  in porcine brain lysates. Fitted offsets ( $\Delta\omega_{fitted}$ ), intercept of linear function with  $Z(\Delta\omega = 0)$  ( $c_s$ ), slope of linear function ( $m_s$ ), point of reference of linear function ( $\delta\omega_{poly}$ ), amplitude of Lorentzian ( $\mathcal{A}_s$ ), FWHM of Lorentzian ( $\Gamma_s$ ) and position of Lorentzian ( $\delta\omega_s$ ). Fitting of Z-spectra acquired at  $B_1 = 2.0$  and  $2.5 \mu\text{T}$  was not stable due to the increased peak broadening at higher  $B_1$ . The parameters are presented in the following order: lower boundary | starting value | upper boundary.

Parameter	Unit	Amide		
<b><math>B_1</math></b>	<b><math>[\mu\text{T}]</math></b>	<b>0.5, 0.6, 0.75</b>	<b>1.0</b>	<b>1.4, 1.5</b>
$\Delta\omega_{fitted}$	[ppm]	4.0 to 2.9	4.4 to 2.9	4.6 to 2.9
$c_{amide}$	[Z-value]	0   0.95   1	0   0.8   1	0   0.7   1
$m_{amide}$	$[\frac{\text{Z-value}}{\text{ppm}}]$	0   0.01   0.2	0   0.02   0.2	0   0.03   0.2
$\delta\omega_{poly}$	[ppm]	3.45   3.55   3.65	3.45   3.55   3.65	3.45   3.55   3.65
$\mathcal{A}_{amide}$	[Z-value]	0.0001   0.001   0.2	0.0001   0.001   0.2	0.0001   0.001   0.2
$\Gamma_{amide}$	[ppm]	0.001   0.4   0.7	0.001   0.4   0.7	0.001   0.4   0.8
$\delta\omega_{amide}$	[ppm]	3.55 (fixed)	3.55 (fixed)	3.55 (fixed)
Parameter	Unit	Guanidyl		
<b><math>B_1</math></b>	<b><math>[\mu\text{T}]</math></b>	<b>0.5, 0.6, 0.75</b>	<b>1.0</b>	<b>1.4, 1.5</b>
$\Delta\omega_{fitted}$	[ppm]	2.5 to 1.5	2.5 to 1.5	2.5 to 1.5
$c_{gua}$	[Z-value]	0   0.9   1	0   0.75   1	0   0.65   1
$m_{gua}$	$[\frac{\text{Z-value}}{\text{ppm}}]$	0   0.01   0.2	0   0.02   0.2	0   0.03   0.2
$\delta\omega_{poly}$	[ppm]	1.92   2.02   2.12	1.92   2.02   2.12	1.92   2.02   2.12
$\mathcal{A}_{gua}$	[Z-value]	0.0001   0.001   0.2	0.0001   0.001   0.2	0.0001   0.001   0.2
$\Gamma_{gua}$	[ppm]	0.001   0.2   0.5	0.001   0.3   0.5	0.001   0.35   0.55
$\delta\omega_{gua}$	[ppm]	2.02 (fixed)	2.02 (fixed)	2.02 (fixed)

**Table 4.7:** Z-spectrum fit parameters used for extraction of  $Z_{\text{lab}}$  and  $Z_{\text{ref}}$  in tumor-bearing mice. Fitted offsets ( $\Delta\omega_{\text{fitted}}$ ), intercept of linear function with  $Z(\Delta\omega = 0)$  ( $c_s$ ), slope of linear function ( $m_s$ ), point of reference of linear function ( $\delta\omega_{\text{poly}}$ ), amplitude of Lorentzian ( $\mathcal{A}_s$ ), FWHM of Lorentzian ( $\Gamma_s$ ) and position of Lorentzian ( $\delta\omega_s$ ). The parameters are presented in the following order: lower boundary | starting value | upper boundary.

Parameter	Unit	Amide		
<b>B<sub>1</sub></b>	<b>[<math>\mu\text{T}</math>]</b>	<b>0.6</b>	<b>1.0</b>	<b>1.4</b>
$\Delta\omega_{\text{fitted}}$	[ppm]	4.1 to 3.1	4.3 to 2.9	4.6 to 2.9
$c_{\text{amide}}$	[Z-value]	0   0.95   1	0   0.8   1	0   0.7   1
$m_{\text{amide}}$	[ $\frac{\text{Z-value}}{\text{ppm}}$ ]	0   0.01   0.2	0   0.02   0.2	0   0.03   0.2
$\delta\omega_{\text{poly}}$	[ppm]	3.45   3.55   3.65	3.45   3.55   3.65	3.45   3.55   3.65
$\mathcal{A}_{\text{amide}}$	[Z-value]	0.0001   0.001   0.2	0.0001   0.001   0.2	0.0001   0.001   0.2
$\Gamma_{\text{amide}}$	[ppm]	0.001   0.4   0.7	0.001   0.4   0.7	0.001   0.4   0.8
$\delta\omega_{\text{amide}}$	[ppm]	3.45   3.55   3.65	3.45   3.55   3.65	3.45   3.55   3.65
Parameter	Unit	Guanidyl		
<b>B<sub>1</sub></b>	<b>[<math>\mu\text{T}</math>]</b>	<b>0.6</b>	<b>1.0</b>	<b>1.4</b>
$\Delta\omega_{\text{fitted}}$	[ppm]	2.5 to 1.5	2.5 to 1.6	2.5 to 1.6
$c_{\text{gua}}$	[Z-value]	0   0.9   1	0   0.75   1	0   0.65   1
$m_{\text{gua}}$	[ $\frac{\text{Z-value}}{\text{ppm}}$ ]	0   0.01   0.2	0   0.02   0.2	0   0.03   0.2
$\delta\omega_{\text{poly}}$	[ppm]	1.92   2.02   2.12	1.92   2.02   2.12	1.92   2.02   2.12
$\mathcal{A}_{\text{gua}}$	[Z-value]	0.0001   0.001   0.2	0.0001   0.001   0.2	0.0001   0.001   0.2
$\Gamma_{\text{gua}}$	[ppm]	0.001   0.2   0.5	0.001   0.3   0.5	0.001   0.35   0.55
$\delta\omega_{\text{gua}}$	[ppm]	1.92   2.02   2.12	1.92   2.02   2.12	1.92   2.02   2.12

#### 4.4.2.5 Calculation of contrast metric

Next, the separately fitted  $Z_{\text{lab}}$  and  $Z_{\text{ref}}$  values of the amide and guanidyl signals were used to calculate the inverse contrast metric  $\text{MTR}_{\text{Rex}}$  (to obtain the isolated CEST contrast, i.e. spillover- and relaxation-compensated, see section 2.5.4) according to equation (2.81). In doing so,  $\text{MTR}_{\text{Rex}}(\text{amide})$  and  $\text{MTR}_{\text{Rex}}(\text{gua})$  were calculated separately for each  $B_1$ . Calculation of  $Z_{\text{lab}}$  and  $Z_{\text{ref}}$  in creatine model solutions was performed by the asymmetry approach (see section 2.5.4) according to equation (4.5).

#### 4.4.2.6 B<sub>1</sub> correction

Thereafter, the calculated  $MTR_{\text{Rex}}$  contrasts were corrected for B<sub>1</sub> field inhomogeneities. A correction for B<sub>1</sub> field inhomogeneities was necessary<sup>36</sup> as the CEST effect strongly depends on the saturation amplitude B<sub>1</sub>. This is especially relevant at UHF, where the high B<sub>0</sub> inevitably leads to increased B<sub>1</sub> inhomogeneities due to  $B_0 \propto \nu_0 \propto \lambda^{-1}$  (i.e. shorter RF wavelengths leading to larger inhomogeneities across the FOV). Consequently, B<sub>1</sub> inhomogeneities across the imaged volume lead to a change in the CEST contrast of different pixels, i.e. even if the pixels should theoretically yield the identical CEST contrast. Therefore, the contrast-B<sub>1</sub>-correction method [145] was utilized to separately correct  $MTR_{\text{Rex}}(\text{amide}, B_1)$  and  $MTR_{\text{Rex}}(\text{gua}, B_1)$ . For the contrast-B<sub>1</sub>-correction, the fit model defined in equation (3.16) was used (i.e. conforming to  $MTR_{\text{Rex}}$  theory) with a fixed  $R_{2s}(\text{amide}) = R_{2s}(\text{gua}) = 100$  Hz (subsection 3.4.2). The optimized fit parameters (i.e. starting values and boundaries) are provided in Table 4.8.

**Table 4.8:** Optimized fit parameters of the contrast-B<sub>1</sub>-correction fit model according to  $MTR_{\text{Rex}}$  theory.  $MTR_{\text{Rex}}(\text{amide}, B_1)$  and  $MTR_{\text{Rex}}(\text{gua}, B_1)$  were corrected separately. In either case, a fixed  $R_{2s}(\text{amide}) = R_{2s}(\text{gua}) = 100$  Hz was used.

Parameter	Unit	Lower boundary	Starting value	Upper boundary
<b>a</b>	[s]	0	0.1	100
<b>b</b>	[Hz]	0.1	100	10000

The contrast-B<sub>1</sub>-correction was performed pixel-by-pixel by the following procedure:

1. The calculated values of  $MTR_{\text{Rex}}(B_1)$  acquired at multiple nominal B<sub>1</sub> amplitudes ( $B_{1,nom}$ , as set in the acquisition protocol settings) were assigned to their actual local B<sub>1</sub> amplitude ( $B_{1,loc}$ ), i.e. shifted along the B<sub>1</sub>-dimension via  $B_{1,loc} = B_{1,nom} \cdot B_{1,rel}$ . Here,  $B_{1,rel}$  is the local relative  $\Delta B_1$  amplitude which is given by the B<sub>1</sub> map obtained from the WASABI measurement (subsection 4.4.1).
2. The B<sub>1</sub>-corrected values of  $MTR_{\text{Rex}}(B_1)$  were fitted according to equation (3.16) with the two fit parameters  $a$  and  $b$  (i.e. conforming to  $MTR_{\text{Rex}}$  theory).
3. The fit results of  $a$  and  $b$  were used to calculate B<sub>1</sub>-corrected values of  $MTR_{\text{Rex}}$  for any desired  $B_{1,nom}$ .

<sup>36</sup> Besides the fact that, in this thesis, the contrast-B<sub>1</sub>-correction is also used to extract  $k_{\text{ex}}$ .

All further data processing was performed using contrast- $B_1$ -corrected data. A representative  $B_1$  map of the porcine brain lysates is shown in Figure 5.1e. An example of the contrast- $B_1$ -correction for  $MTR_{\text{Rex}}(\text{amide}, B_{1,\text{nom}})$  and  $MTR_{\text{Rex}}(\text{gua}, B_{1,\text{nom}})$  is provided in Figure 5.3, i.e. stars and squares, respectively. In this manner, it was possible to also obtain  $\text{CEST}_{\text{ratio}}$  values, for instance, with any desired combination of  $B_{1,\text{high}}$  and  $B_{1,\text{low}}$ , although only distinct  $B_{1,\text{nom}}$  data was acquired. Importantly, the fit result of  $b$  was used to extract  $k_{\text{ex}}$ , as explained in section 3.4.2.

### 4.4.2.7 Extraction of $k_{\text{ex}}$

For extraction of  $k_{\text{ex}}$ , the fit results of the fit parameter  $b$  obtained from the contrast- $B_1$ -correction were used. This was possible, as  $b \hat{=} k_{\text{ex}}$  (compare equation (3.16) with equation (2.81)). Extraction of  $k_{\text{ex}}(\text{amide})$  and  $k_{\text{ex}}(\text{gua})$  was performed separately using the fit parameter  $b$  from the contrast- $B_1$ -correction of  $MTR_{\text{Rex}}(\text{amide})$  and  $MTR_{\text{Rex}}(\text{gua})$ , respectively .

### 4.4.2.8 $\text{pH}_{\text{amide}}$ and $\text{pH}_{\text{gua}}$ mapping

In order to obtain pH values, the extracted values of  $k_{\text{ex}}(\text{amide})$  and  $k_{\text{ex}}(\text{gua})$  were used for separate calculation of  $\text{pH}_{\text{amide}}$  and  $\text{pH}_{\text{gua}}$  according to equation (3.3). For determination of  $\text{pH}_{\text{amide}}$  and  $\text{pH}_{\text{gua}}$ , the calibrated values of the exchange rate determining constants  $k_{\text{c}}(\text{amide})$  and  $k_{\text{c}}(\text{gua})$  were used (section 5.1.2). Consequently, the value of  $k_{\text{c}}(\text{amide}) = 3.2 \mu\text{Hz}$  was used for calculation of  $\text{pH}_{\text{amide}}$ , while the value of  $k_{\text{c}}(\text{gua}) = 53.2 \mu\text{Hz}$  was used for calculation of  $\text{pH}_{\text{gua}}$ .

### 4.4.2.9 $\text{pH}_{\text{combi}}$ mapping

Finally, the determined values of  $\text{pH}_{\text{amide}}$  and  $\text{pH}_{\text{gua}}$  were used for calculation of  $\text{pH}_{\text{combi}}$  according to equation (3.21). Calculation of the weightings  $w_{\text{amide}}$  and  $w_{\text{gua}}$  was accomplished via equation (3.20) using  $k_{\text{c}}(\text{amide}) = 3.2 \mu\text{Hz}$ ,  $k_{\text{c}}(\text{gua}) = 53.2 \mu\text{Hz}$ ,  $B_{1,\text{high}}(\text{amide}) = B_{1,\text{high}}(\text{gua}) = 1.4 \mu\text{T}$ ,  $B_{1,\text{low}}(\text{amide}) = B_{1,\text{low}}(\text{gua}) = 0.6 \mu\text{T}$  and  $R_{2s}(\text{amide}) = R_{2s}(\text{gua}) = 100 \text{ Hz}$ . Weightings were normalized to 1.

## Correlation of $\text{pH}_{\text{titrated}}$ and pH measured via CEST-MRI

To quantify the correlation between the pH values measured with the pH meter ( $\text{pH}_{\text{titrated}}$ ) and the pH values determined by the developed method ( $\text{pH}_{\text{amide}}$ ,  $\text{pH}_{\text{gua}}$ , and  $\text{pH}_{\text{combi}}$ , respectively), the Pearson correlation coefficient (PCC, hereafter simply referred to as  $r$ )

## 4 Materials and Methods

was calculated. The  $r$ -value ( $r \in [-1, 1]$ ) is a measure to assess the linear correlation of two datasets  $X, Y$  (e.g.  $\text{pH}_{\text{titrated}}$  and  $\text{pH}_{\text{combi}}$ ), where (i)  $r = 1$  represents a complete positive linear correlation, (ii)  $r = 0$  represents no linear correlation at all and (iii)  $r = -1$  represents a complete negative correlation. The statistical significance of the  $r$ -value is given by its corresponding  $p$ -value ( $p \in [0, 1]$ ) which, very briefly summarized, represents the probability of obtaining the  $r$ -value simply by chance. Typically, the calculated  $r$ -value is considered to be statistically significant if  $p < 0.0001$ .

### 4.4.3 Calibration of $k_c$

For the calibration of  $k_c$ , the isolated and  $B_1$ -corrected  $\text{MTR}_{\text{Rex}}$  data with various well-defined  $\text{pH}_{\text{titrated}}$  values were used. A ROI was defined in the  $\text{MTR}_{\text{Rex}}$  images for each of the different  $\text{pH}_{\text{titrated}}$  samples. For each  $B_1$  individually, the mean  $\text{MTR}_{\text{Rex}}$  ROI values of each  $\text{pH}_{\text{titrated}}$  sample were fitted to the symmetric function given by equation (3.9) (i.e. fitted as a function of  $\text{pH}$ ). The fit function was used to determine the peak position  $\text{pH}_{\text{max}}$ . Finally,  $\text{pH}_{\text{max}}$  was used to calculate  $k_c$  via equation (3.7). The error of  $k_c$  was obtained from the 95% confidence interval of the fit. The calibration of  $k_c$  was performed at  $T = 37 \pm 0.2^\circ\text{C}$ .

### Porcine brain lysates

For each  $B_1$  in the range of  $B_1 = 0.6$  to  $1.4 \mu\text{T}$  (with a step size of  $0.1 \mu\text{T}$ ), calibration of  $k_c$  for amide and guanidyl protons was performed separately using  $\text{MTR}_{\text{Rex}}(\text{amide})$  and  $\text{MTR}_{\text{Rex}}(\text{gua})$  data in the range of  $\text{pH}_{\text{titrated}} = 5.5$  to  $8.0$  (i.e. the 12 different  $\text{pH}_{\text{titrated}}$  samples from session 1 and 2, Table 4.1). To ensure a robust fitting procedure, the samples from the third session (see Table 4.1) were excluded in the experimental determination of  $k_c$  because they exhibited a slightly different tissue concentration (i.e.  $f_s$ ) which resulted in slightly different  $\text{MTR}_{\text{Rex}}$  values (i.e. scaling along the  $\text{MTR}_{\text{Rex}}$ -axis, data not shown). The optimized fit parameters (i.e. starting values and boundaries) are provided in Table 4.9.

**Table 4.9:** Optimized fit parameters for the calibration of  $k_c$  in porcine brain lysates (amide and guanidyl) and creatine model solutions (guanidyl). The parameters are presented in the following order: lower boundary | starting value | upper boundary.

Pool	A [a.u.]	$\Gamma$ [pH]	$\text{pH}_{\text{max}}$ [pH]
Amide	0   0.1   100	0   1   3	6   8   10
Guanidyl	0   0.1   100	0   1   3	5   6.5   8

### Creatine model solutions

For each  $B_1$  in the range of  $B_1 = 0.6$  to  $1.4 \mu\text{T}$  (with a step size of  $0.1 \mu\text{T}$ ) and each of the eight different  $c_2$  in the range of  $c_2 = 0.36$  to  $1.00$ , calibration of  $k_c(\text{gua})$  was performed using  $\text{MTR}_{\text{Rex}}(\text{gua})$  data in the range of  $\text{pH}_{\text{titrated}} = 6.0$  to  $8.2$  (i.e. the 11 different  $\text{pH}_{\text{titrated}}$  samples). Since calibration of  $k_c(\text{gua})$  in creatine model solutions was performed using the same fit parameters as for calibration of  $k_c(\text{gua})$  in porcine brain lysates, the optimized fit parameters (i.e. starting values and boundaries) are provided in the bottom row of Table 4.9.



## 5 Results

Within the scope of this thesis, a novel method for non-invasive, high-resolution, quantitative mapping of  $\text{pH}_i$  was developed which is applicable for cancer imaging *in vivo*. To accomplish this, firstly, a novel model was developed which enabled, for the first time, quantitative  $\text{pH}_i$  mapping using the endogenous amide and guanidyl CEST signals *in vivo*. The underlying theoretical framework explaining the principle of the developed method was introduced in chapter 3. In this chapter, first of all, the developed method was validated *in vitro* using porcine brain lysates for calibration of  $k_c$  and to demonstrate the feasibility of concentration-independent  $\text{pH}$  measurements across a broad range of physiologically relevant  $\text{pH}$  values (section 5.1). Further, using the insights and calibration obtained from porcine brain lysates, applicability for examinations *in vivo* was demonstrated in the lesions of tumor-bearing mice, showing a physiologically plausible median  $\text{pH}_i$  of approximately 7.2, independent of tumor size (section 5.2). In addition, creatine model solutions were investigated using a pulsed presaturation scheme, demonstrating the possibility of tuning the  $\text{pH}$  sensitivity by variation of the presaturation pulse shape (section 5.3). Parts of this chapter have already been published in [121, 146].

### 5.1 *In vitro* validation using porcine brain lysates

In order to demonstrate the applicability of the developed method, porcine brain lysates were investigated. Porcine brain lysates were chosen as *in vivo*-like model suspensions to mimic, as far as possible, the *in vivo* composition of proteins and peptides as well as the *in vivo*  $Z$ -spectrum. In the  $Z$ -spectra, extraction of the amide and guanidyl signals from the background was achieved using separate first order polynomial and Lorentzian fits which were stable over a broad range of  $\text{pH}$  and  $B_1$  (subsection 5.1.1). Using the extracted signals at different  $\text{pH}$  and  $B_1$ , the calibration of  $k_c$  yielded a value of  $3.2 \pm 0.5$  and  $53.2 \pm 3.7$   $\mu\text{Hz}$  for the amide and the guanidyl signal, respectively (subsection 5.1.2). Having performed the calibration of the amide and guanidyl signals,  $\text{pH}$  mapping was accomplished by determination of  $k_{\text{ex}}$  from the  $\text{MTR}_{\text{Rex}}$ -based contrast- $B_1$ -correction. Using the weighted combination of  $\text{pH}_{\text{amide}}$  and  $\text{pH}_{\text{gua}}$ , a reliable  $\text{pH}_{\text{combi}}$  mapping was

## 5 Results

feasible in the physiologically relevant pH range of 6.2 to 8.0 with an average variation of around  $\pm 0.2$  (subsection 5.1.3).

### Assessment of in vivo-like Z-spectra

In vivo, the most prominent features of Z-spectra are the vertical offset due to the broad MTC, as well as, the amide and the guanidyl resonances at around  $\Delta\omega \approx 3.6$  and 2.0 ppm, respectively. Therefore, in a first step, the Z-spectra of the porcine brain lysates were assessed in order to verify the vivo-like conditions. More specifically, porcine brain lysates were examined with (i) varying  $\text{pH}_{\text{titrated}}$  at a fixed tissue concentration of 33.3%(w/v) and (ii) varying tissue concentration at a fixed  $\text{pH}_{\text{titrated}}$  of 7. Examination of Z-spectra of the porcine brain lysates showed typical signals comparable to in vivo examinations, i.e. comparatively small CEST signals and large MTC (Figure 5.1a and b, representative single-pixel Z-spectra acquired with  $B_1 = 1 \mu\text{T}$ ).

For the  $\text{pH}_{\text{titrated}}$  series (Figure 5.1a), the characteristic and, in particular, pH-dependent resonances arising from amide and guanidyl protons were observed at  $\Delta\omega \approx 3.6$  and 2.0 ppm, respectively. Furthermore, a broad and, most notably, pH-independent offset due to the MTC background was detected. This is especially apparent off-resonant from the amide and guanidyl signals, where the Z-values are approximately the same, independent of pH (Figure 5.1a, same Z-value of different colors at  $\Delta\omega \approx 1$  and 5 ppm). The corresponding pixels of the single-pixel Z-spectra in Figure 5.1a with  $\text{pH}_{\text{titrated}} = 6.0$  (red), 6.5 (yellow), 7.0 (green) and 7.5 (blue) are illustrated in the associated  $M_0$  image (Figure 5.1c, same colors as in a).

For the concentration series (Figure 5.1b), a strong dependency of the MTC on tissue concentration was observed (i.e. the significantly different vertical offsets for varying tissue concentration, even at the same  $B_1 = 1 \mu\text{T}$ ). In contrast to the tissue concentration-dependent MTC, the relative signal strength of the amide resonance compared to the guanidyl resonance did not change with varying tissue concentration (Figure 5.1b, cf resonances at  $\Delta\omega \approx 3.6$  and 2.0 ppm within the different shades of green).

Altogether, the presence of the comparatively small and pH-dependent amide and guanidyl signals along with the broad and large concentration-dependent MTC validate the assumption that porcine brain lysates allow for in vivo-like model suspensions. Also, smooth  $B_0$  and  $B_1$  maps were observed showing only minor field inhomogeneities across all samples

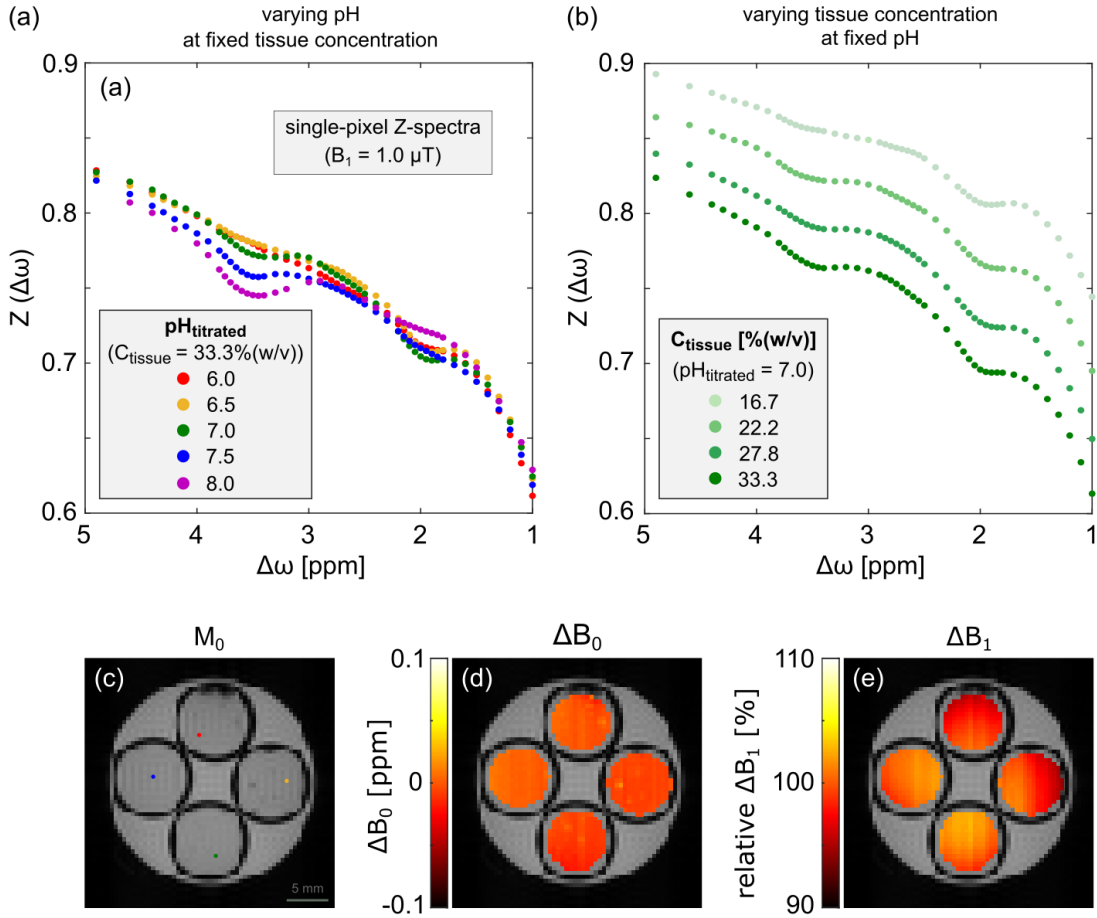


**Figure 5.1:** Representative single-pixel Z-spectra of porcine brain lysates at various  $\text{pH}_{\text{titrated}}$  (a, at a fixed tissue concentration) and various tissue concentrations (b, at a fixed  $\text{pH}_{\text{titrated}}$ ). The Z-spectra (acquired with  $B_1 = 1 \mu\text{T}$ ,  $B_0$ -corrected) exhibited typical signals comparable to in vivo Z-spectra, i.e. comparatively small amide and guanidyl signals ( $\Delta\omega = 3.6$  and  $2.0$  ppm, respectively) along with a broad and large vertical offset due to the MTC (background). a, Variation of  $\text{pH}_{\text{titrated}}$  has a strong effect on the pH-dependent resonances of amide and guanidyl protons, but no effect on the pH-independent MTC (pixels corresponding to Z-spectra are indicated in c). b, In contrast, variation of tissue concentration has a strong effect on the MTC, but no effect on the relative amplitudes of the amide and guanidyl signals. The  $B_0$  and  $B_1$  field maps showed very good homogeneity of  $\Delta B_0 < 0.03$  ppm and  $\Delta B_1 < 5\%$ , respectively (d and e, respectively). Note, that the  $\text{pH}_{\text{titrated}} = 8$  sample was acquired in a different session and with slightly different frequency offsets  $\Delta\omega$ . The gray scale bar in panel (c) represents 5 mm. Subfigures a and b were adapted from Figure 3 in [121].

## 5 Results

with mean ROI values of  $\Delta B_0 < 0.03$  ppm and  $\Delta B_1 < 5\%$ , respectively (Figure 5.1d and e, respectively).

### 5.1.1 Extraction of pH-dependent signals from background

In order to reliably isolate only the pH-dependent information from the Z-spectra (ultimately, i.e.  $k_{ex}$ ), the extraction of the pH-dependent amide and guanidyl signals from the background of concomitant effects was investigated.

#### Determination of pH and $B_1$ range allowing for reliable extraction of $Z_{ref}$ and $Z_{lab}$

To isolate the pH-dependent signals from the Z-spectra, in a first step, the fit model given by equation (4.10) was used to extract the amide and guanidyl signals pixel-by-pixel (subsection 4.4.2). In particular, to determine the pH and  $B_1$  range in which the linear and Lorentzian fit model is able to reliably extract  $Z_{ref}$  and  $Z_{lab}$  from the acquired Z-spectra, the separate amide and guanidyl signal extraction was investigated at various pH and  $B_1$  (Figure 5.2).

Most notably, and independent of pH, lower Z-spectra were observed for increasing  $B_1$  (Figure 5.2, cf.  $B_1 = 0.5, 1.0$  and  $1.5$   $\mu\text{T}$ , i.e. squares, discs and stars, respectively). Thus, to ensure a robust fitting procedure over a broad range of  $B_1$ , different fit parameters were used for signal extraction of the amide and guanidyl signals at different  $B_1$  amplitudes (i.e. including different start values and boundaries of the fitting procedure, see Table 4.6). In general, due to the higher labeling efficiency  $\alpha$  at higher  $B_1$ , an increased CEST effect was observed for increasing  $B_1$  (Figure 5.2, cf. the smaller amplitudes of amide or guanidyl signals at  $B_1 = 0.5$   $\mu\text{T}$  with the larger amplitudes at  $B_1 = 1.5$   $\mu\text{T}$ , i.e. squares and stars, respectively). However, the general signal strength of either (i) the amide signal at lower pH ( $\text{pH}_{\text{titrated}} = 6.0$ ) or (ii) the guanidyl signal at higher pH ( $\text{pH}_{\text{titrated}} = 8.0$ ) is too weak to resolve any further signal increase with increasing  $B_1$  (e.g. Figure 5.2a and e, respectively, i.e. red and purple). In fact, just from observing the Z-spectra at different pH, the significantly different pH dependencies of amide and guanidyl protons become apparent.

More specifically, at lower pH values ( $\text{pH}_{\text{titrated}} = 6.0$ ), the guanidyl signal was clearly visible whereas practically no amide signal was observed (Figure 5.2a, red). In contrast, the opposite effect occurs at higher pH values ( $\text{pH}_{\text{titrated}} = 8.0$ ), where the amide sig-

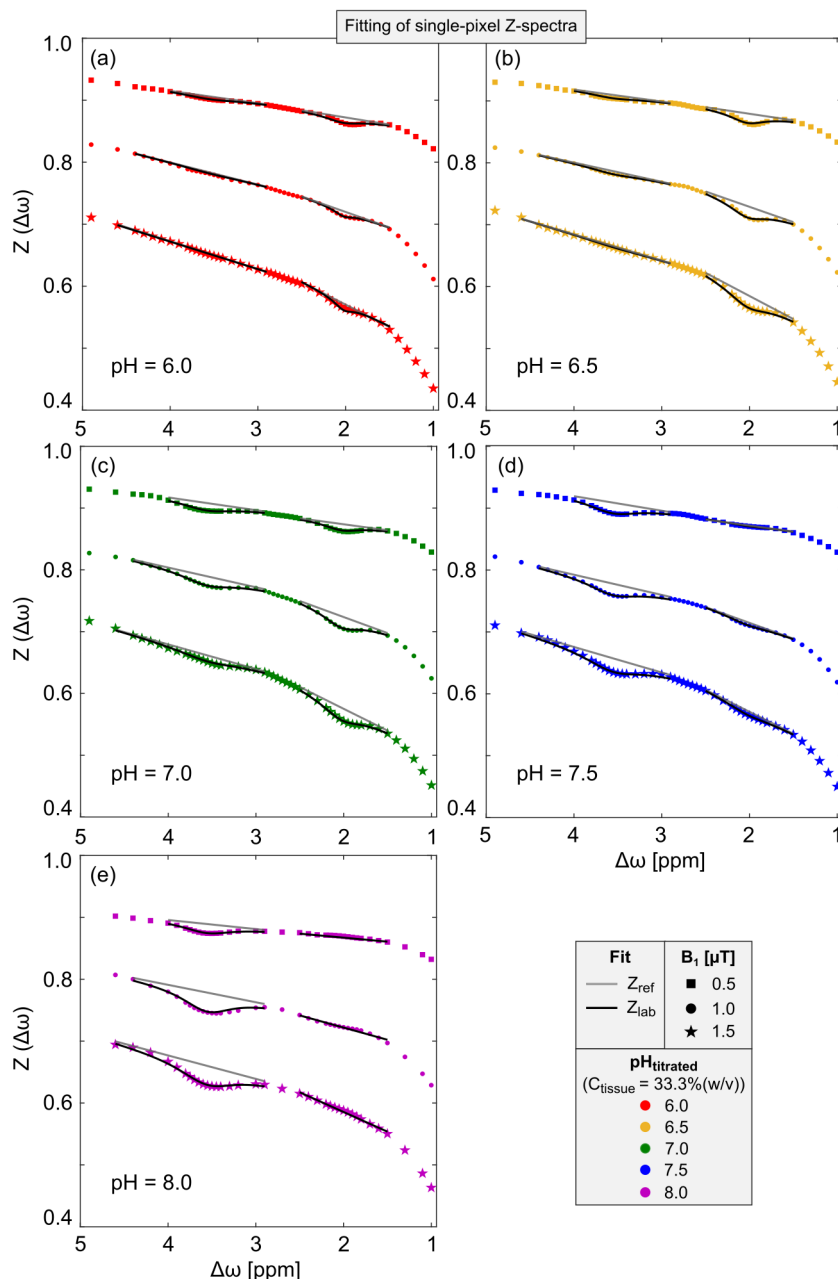


**Figure 5.2:** Fitting procedure to extract the amide and guanidyl signals pixel-by-pixel from Z-spectra of porcine brain lysates at various pH and  $B_1$ . The amide and guanidyl signals were extracted separately from the background of concomitant MTC by linear and Lorentzian fits (gray and black lines, i.e.  $Z_{ref}$  and  $Z_{lab}$ , respectively). At pH = 6.0 (a), only the guanidyl signal is detectable ( $\Delta\omega = 2.0$ ). Conversely, at pH = 8.0 (e), only the amide signal is detectable ( $\Delta\omega = 3.6$ ). For  $6.5 \leq \text{pH} \leq 7.5$  (b-d), both signals are detectable. Extraction of the amide and guanidyl signals was stable over a broad range of pH as well as  $B_1$  (different colors and symbols, respectively). Each fit is only displayed within its respective range of offsets which were used for the actual fitting procedure. Single-pixel Z-spectra were obtained from the same pixels as shown in Figure 5.1. Note, that the  $pH_{titrated}=8.0$  sample was acquired with slightly different frequency offsets. Only excerpts containing the amide and guanidyl signals of the acquired Z-spectra are shown.

## 5 Results

nal was clearly visible while effectively no guanidyl signal was detected (Figure 5.2e, purple). Importantly, the separate extraction of  $Z_{\text{ref}}$  and  $Z_{\text{lab}}$  for the amide and guanidyl signals from the background (Figure 5.2, gray and black lines, respectively), was stable over a broad range of pH as well as  $B_1$  (Figure 5.2, different colors and symbols, respectively). A reliable extraction of  $Z_{\text{ref}}$  and  $Z_{\text{lab}}$  is particularly important, as these values were used to calculate the isolated  $\text{MTR}_{\text{Rex}}$  contrast for the amide and guanidyl signals (subsection 4.4.2).

Regarding pH, a robust extraction of the amide signal was feasible in the range of  $\text{pH} \geq 7.0$  (Figure 5.2c,d and e, i.e. green, blue and purple). In contrast, a robust extraction of the guanidyl signal was feasible in the range of  $6.0 \leq \text{pH} \leq 7.3$  (Figure 5.2a, b and c, i.e. red, yellow and green).

Regarding  $B_1$ , a robust and reliable extraction of the amide and guanidyl signal was feasible in the range of  $0.5 \leq B_1 \leq 1.5 \mu\text{T}$  (Figure 5.2, in between squares and stars). Outside of this region, for  $B_1 < 0.5 \mu\text{T}$ , the amide and guanidyl signals were not pronounced enough for a robust and reliable signal extraction. In contrast, for  $B_1 > 1.5 \mu\text{T}$ , the signals were too broad, thus, also compromising signal extraction. In principle, depending on the specific pH value, also a reliable signal extraction of either only the amide or, conversely, only the guanidyl signal was possible for slightly lower or higher  $B_1$  (e.g. for amide at  $\text{pH} = 8.0$  with  $B_1 > 1.5$ ). However, as the ultimate goal was to enable a robust and reliable  $\text{pH}_i$  mapping in vivo (where, a priori, the  $\text{pH}_i$  value is unknown), it was determined that the range of  $0.5 \leq B_1 \leq 1.5 \mu\text{T}$  can be used for reliable extraction of  $Z_{\text{ref}}$  and  $Z_{\text{lab}}$  for both the amide and guanidyl signals.

### **$\text{MTR}_{\text{Rex}}$ -based contrast- $B_1$ -correction for reliable extraction of $k_{\text{ex}}$**

In order to correct the separately extracted, isolated  $\text{MTR}_{\text{Rex}}$  contrasts of the amide and guanidyl signals obtained at various nominal  $B_1$  for  $B_1$ -field inhomogeneities, in a next step, the contrast- $B_1$ -correction fit model based on  $\text{MTR}_{\text{Rex}}$  theory was utilized (equation (3.16)). Importantly, as this fitting procedure was not only utilized to correct  $\text{MTR}_{\text{Rex}}(B_1)$  for  $B_1$ -field inhomogeneities, but crucially, also to extract the exchange rates  $k_{\text{ex}}$  (subsection 3.4.2), the reliability of the pixel-by-pixel contrast- $B_1$ -correction was assessed by investigating  $\text{MTR}_{\text{Rex}}(\text{amide})$  and  $\text{MTR}_{\text{Rex}}(\text{gua})$  at various pH (Figure 5.3).

Most notably, as it already was the case for Z-spectra at different pH (Figure 5.2), the

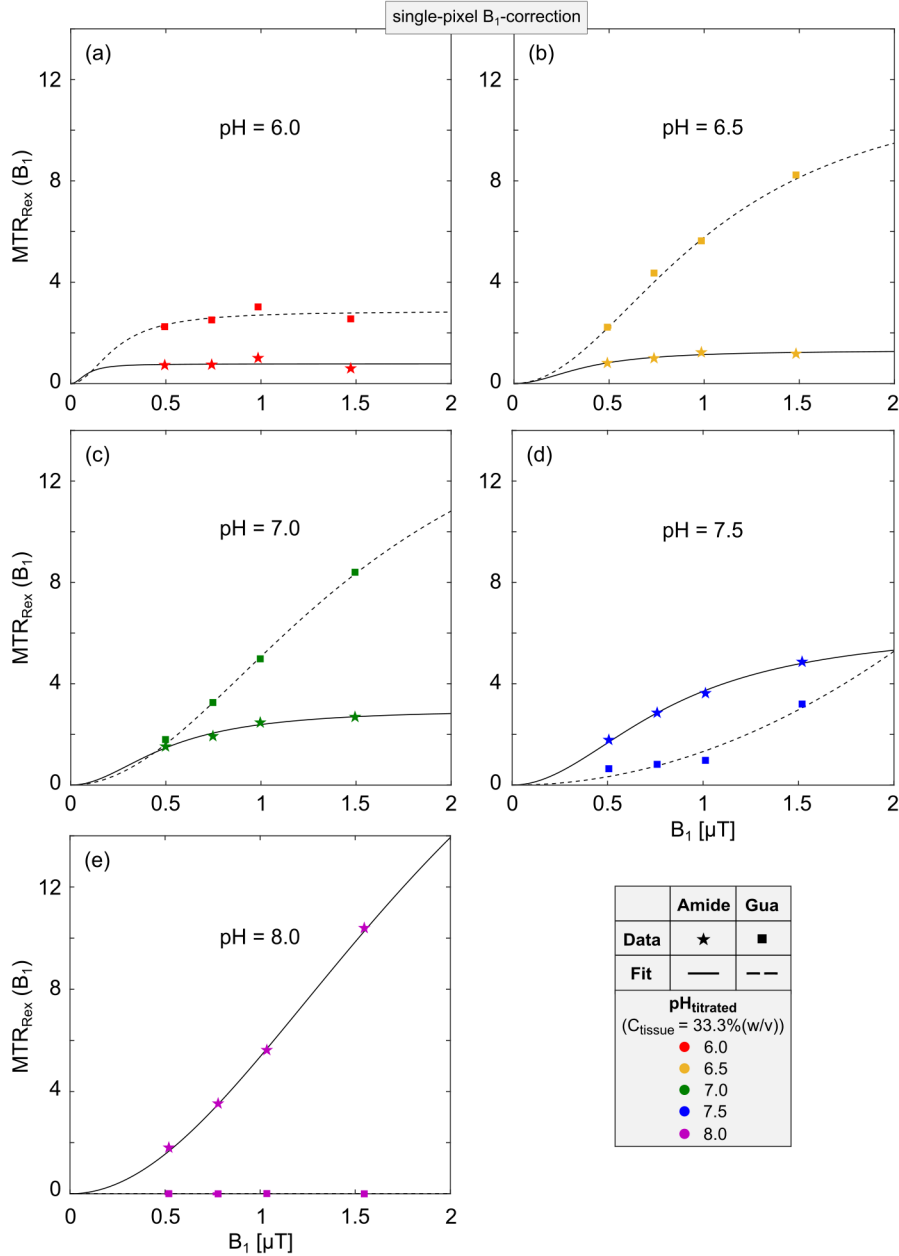


**Figure 5.3:** Fitting procedure of the pixel-by-pixel  $MTR_{\text{Rex}}$ -based contrast- $B_1$ -correction for the amide and guanidyl signals extracted from porcine brain lysates at various pH and  $B_1$ . The  $MTR_{\text{Rex}}(\text{amide})$  and  $MTR_{\text{Rex}}(\text{gua})$  contrasts were calculated separately from the fitted Z-spectra acquired at each nominal  $B_1$  (cf. Figure 5.2,  $Z_{\text{lab}}$  and  $Z_{\text{ref}}$ ). Using the  $B_1$  map (Figure 5.1e), the  $MTR_{\text{Rex}}(B_1)$  values of the amide and guanidyl signals were shifted along the  $B_1$  dimension according to the local relative  $B_1$  amplitude (i.e. stars and squares, respectively). A model based on  $MTR_{\text{Rex}}$  theory was used to fit the  $B_1$ -corrected  $MTR_{\text{Rex}}$  values and to reconstruct the  $MTR_{\text{Rex}}(\text{amide})$  as well as  $MTR_{\text{Rex}}(\text{gua})$  contrast at any desired  $B_1$  (i.e. solid and dashed lines, respectively). The  $MTR_{\text{Rex}}$ -based contrast- $B_1$ -correction was stable over a broad range of pH (different colors). Fits are illustrated for the same single-pixel Z-spectra as shown in Figure 5.1a and 5.2, respectively.

## 5 Results

significantly different pH dependencies of amide and guanidyl protons were clearly visible just from examining  $MTR_{\text{Rex}}(\text{amide})$  and  $MTR_{\text{Rex}}(\text{gua})$ , respectively, at different  $\text{pH}_{\text{titrated}}$  (Figure 5.3, stars and squares, respectively, cf different colors). For pH values with approximately  $\text{pH}_{\text{titrated}} < 7.3$ , a higher  $MTR_{\text{Rex}}$  signal was observed for guanidyl compared to amide protons, i.e.  $MTR_{\text{Rex}}(\text{amide}) < MTR_{\text{Rex}}(\text{gua})$  (Figure 5.3a, b and c, i.e. red, yellow and green squares above stars). Conversely, the opposite effect was found for pH values with approximately  $\text{pH}_{\text{titrated}} > 7.3$ , where a higher  $MTR_{\text{Rex}}$  signal was observed for amide compared to guanidyl protons, i.e.  $MTR_{\text{Rex}}(\text{amide}) > MTR_{\text{Rex}}(\text{gua})$  (Figure 5.3d and e, i.e. blue and green squares below stars). In general, an increase of  $MTR_{\text{Rex}}(B_1)$  was observed for increasing  $B_1$  which is due to the higher  $B_1$  leading to a higher labeling efficiency (i.e.  $\lim_{B_1 \rightarrow \infty} \alpha(B_1) = 1$ ), in coherence with  $MTR_{\text{Rex}}$  theory.

However, at lower pH values (i.e.  $\text{pH}_{\text{titrated}} = 6.0$ ), no such increase of  $MTR_{\text{Rex}}(B_1)$  was observed for increasing  $B_1$  especially for the amide signal but also for the guanidyl signal (Figure 5.3a, red stars and squares). Essentially, this is because the labeling efficiency  $\alpha$  is very close to 1 at lower pH, i.e. at low  $k_{\text{ex}}$ , where the full saturation limit ( $\alpha = 1$ ) holds true even for a low  $B_1$  of 0.5  $\mu\text{T}$  (cf with the red curve in Figure 3.2). Consequently, no further increase of  $MTR_{\text{Rex}}(\text{amide})$  and  $MTR_{\text{Rex}}(\text{gua})$  was detected for increasing  $B_1$  at  $\text{pH}_{\text{titrated}} = 6.0$  (Figure 5.3a, red stars and squares). In contrast, at higher pH values (i.e.  $\text{pH}_{\text{titrated}} = 8.0$ ), the signal strength of  $MTR_{\text{Rex}}(\text{gua})$  was clearly too weak to resolve any signal increase for increasing  $B_1$  (Figure 5.3e, purple squares), whereas for  $MTR_{\text{Rex}}(\text{amide})$  a distinct signal increase was found for increasing  $B_1$  (Figure 5.3e, purple stars). The minuscule values of  $MTR_{\text{Rex}}(\text{gua})$  at  $\text{pH}_{\text{titrated}} = 8.0$  are a direct consequence of the minuscule guanidyl signals in Z-spectra at  $\text{pH}_{\text{titrated}} = 8.0$  (Figure 5.2e,  $\Delta\omega = 2.0$  ppm).

Importantly, the  $MTR_{\text{Rex}}$ -based contrast- $B_1$ -correction fit was stable over a broad range of pH, for  $MTR_{\text{Rex}}(\text{amide})$  and  $MTR_{\text{Rex}}(\text{gua})$ , respectively (Figure 5.3, solid and dashed lines, respectively). A reliable contrast- $B_1$ -correction is particularly important, as the value of the fit parameter  $b$  (equation (3.16)) was directly used to extract the exchange rates  $k_{\text{ex}}$  (subsection 3.4.2).

### 5.1.2 Calibration of $k_c$ for the amide and guanidyl signal

In order to ensure a calibration of the pH dependency of the amide and guanidyl CEST signals under in vivo-like conditions (i.e. comparatively small CEST signals and large

## 5.1 In vitro validation using porcine brain lysates

MTC), model suspensions made from porcine brain lysates were investigated at  $T = 37^\circ\text{C}$  to determine  $k_c$ . For calibration of  $k_c$ , the isolated and  $B_1$ -corrected  $MTR_{\text{Rex}}$  signals from amide and guanidyl protons between  $\text{pH} = 5.5$  and  $8.0$  were included and examined separately as a function of  $\text{pH}$  for  $B_1$  values between  $0.6$  and  $1.4 \mu\text{T}$  (Figure 5.4a and b, different colors).

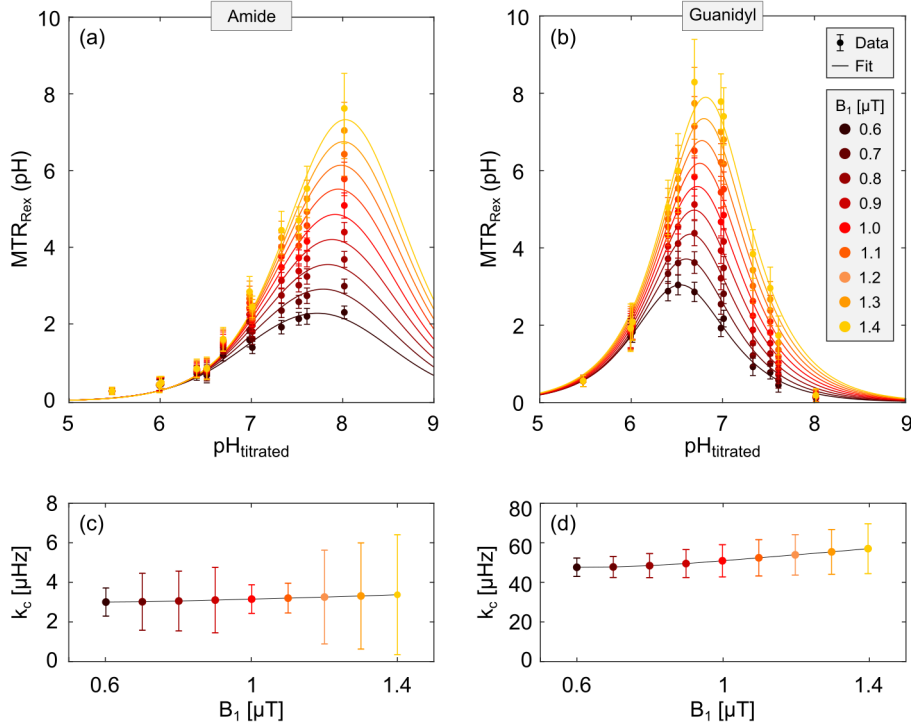


**Figure 5.4:** Calibration of  $k_c$  for amide (a, c) and guanidyl protons (b, d) in porcine brain lysates at various  $\text{pH}_{\text{titrated}}$  and  $B_1$ . In coherence with theory (cf. Figure 3.1c),  $MTR_{\text{Rex}}$  showed the expected symmetric shape as a function of  $\text{pH}$  for amide and guanidyl protons, respectively (a and b, respectively). c, d: For the amide and guanidyl signal separately, the  $B_1$ -corrected  $MTR_{\text{Rex}}$  values were used to experimentally determine  $\text{pH}_{\text{max}}$  by an individual fit for each  $B_1$  via equation (3.7). An average  $k_c$  of  $3.2 \pm 0.5$  and  $53.2 \pm 3.7 \mu\text{Hz}$  was found for the amide and guanidyl protons, respectively (c, d). All values are mean ROI values  $\pm$  STD (a, b). Error bars for  $k_c$  were obtained from the 95% confidence interval of the fit (c, d). Figure was adapted from Figure 4 in [121].

Most notably, and in coherence with theory (cf. Figure 3.1b), the expected  $\text{pH}$  dependency of the isolated  $MTR_{\text{Rex}}$  contrast was observed for  $MTR(\text{amide})$  and  $MTR(\text{gua})$ , respectively, i.e. the symmetric shape of  $MTR_{\text{Rex}}$  as a function of  $\text{pH}$  (Figure 5.4a and b, respectively). Remarkably, the found symmetric shape of  $MTR_{\text{Rex}}(\text{pH})$  supported the

## 5 Results

underlying assumption of describing a single CEST pool by only one  $k_c$  and, in addition, enabled a stable and robust fitting procedure, thus, allowing for an accurate determination of  $\text{pH}_{\text{max}}$ . Importantly, with increasing  $B_1$  the expected shift of  $\text{pH}_{\text{max}}$  towards higher pH also was observed (cf. Figure 5.4a and b with Figure 3.1c). As demonstrated in the theory section 3.1, experimental determination of  $\text{pH}_{\text{max}}$  allows calculation of  $k_c$  (equation (3.7)) which, in turn, enables calibration of the entire pH dependency of the amide and guanidyl CEST signal at a fixed temperature (Table 5.1).

**Table 5.1:** Calibrated values of  $k_c$  for amide and guanidyl protons in porcine brain lysates at  $T = 37 \pm 0.2^\circ\text{C}$ .

	Amide	Guanidyl
$k_c$ [ $\mu\text{Hz}$ ]	$3.2 \pm 0.5$	$53.2 \pm 3.7$

By fitting the well-defined symmetric function given by equation (3.9) separately to each  $B_1$  data, measurement of  $\text{pH}_{\text{max}}$  led to an average  $k_c$  of  $3.2 \pm 0.5$  and  $53.2 \pm 3.7$   $\mu\text{Hz}$  for the amide and guanidyl signal, respectively (Figure 5.4c and d). For the  $k_c$  values, a slight dependency on  $B_1$  was observed, which however, was within the observed variation of  $k_c$  as a function of  $B_1$ . Also, the  $\text{MTR}_{\text{Rex}}(\text{gua})$  values at  $\text{pH}_{\text{titrated}} > 7.5$  were underestimated (Figure 5.4b), as already observed in the Z-fits and contrast- $B_1$ -correction of guanidyl protons at  $\text{pH}_{\text{titrated}} > 7.5$ , respectively (Figure 5.2e,  $\Delta\omega = 2.0$  ppm and Figure 5.3e, purple squares, respectively).

### 5.1.3 pH mapping

Having performed the calibration of  $k_c$  for the amide and guanidyl signals, quantitative pH mapping was realized by determining  $k_{\text{ex}}$  pixel-by-pixel directly from the fit parameter  $b$  of the  $\text{MTR}_{\text{Rex}}$ -based contrast- $B_1$ -correction (equation (3.16)). Because amide and guanidyl protons have significantly different pH dependencies (i.e. different  $k_c$ ), the pH range in which each proton species yields a reliable pH mapping was experimentally investigated.

#### Separate pH mapping for the amide and guanidyl signal

As established in section 3.5, the slope and range of the  $\text{CEST}_{\text{ratio}}$  represent the pH sensitivity which is maximized by increasing the difference between  $B_{1,\text{high}}$  and  $B_{1,\text{low}}$

(cf. Figure 3.3b). Thus, the measured  $\text{CEST}_{\text{ratio}}(\text{amide})$  and  $\text{CEST}_{\text{ratio}}(\text{gua})$  values obtained with the maximized range of experimentally feasible  $B_1$ , i.e.  $B_{1,\text{low}} = 0.6 \mu\text{T}$  and  $B_{1,\text{high}} = 1.4 \mu\text{T}$ , were investigated as a function of pH (Figure 5.5a and b, blue data points).

In general and in coherence with theory (cf. Figure 3.3c), the expected distinct pH dependency of  $\text{CEST}_{\text{ratio}}$  was observed within the respective range of appropriate pH sensitivity, i.e.  $\text{pH}_{\text{titrated}} = 7.3$  to  $8.0$  and  $6.2$  to  $7.3$ , respectively, for amide and guanidyl protons, respectively (Figure 5.5a and b, gray shaded regions). In addition, for lower pH values outside of the gray shaded regions (i.e.  $\text{pH}_{\text{titrated}} < 7.3$  for  $\text{CEST}_{\text{ratio}}(\text{amide})$  and  $\text{pH}_{\text{titrated}} < 6.2$  for  $\text{CEST}_{\text{ratio}}(\text{gua})$ , respectively), the theoretically expected and experimentally found  $\text{CEST}_{\text{ratio}}$  values approximately agreed within the observed STD of mean ROI values (Figure 5.5a and b, cf. error bars with black lines). Conversely, for higher pH values outside of the gray shaded regions (i.e.  $\text{pH}_{\text{titrated}} > 7.3$  for  $\text{CEST}_{\text{ratio}}(\text{gua})$  only), an increasing discrepancy was observed between the expected and measured  $\text{CEST}_{\text{ratio}}(\text{gua})$  values for increasing pH (Figure 5.5b). This is explained by the underestimated  $\text{MTR}_{\text{Rex}}(\text{gua})$  values at  $\text{pH}_{\text{titrated}} > 7.5$ , in particular, at higher  $B_1$  (Figure 5.4b) which leads to significantly underestimated  $\text{CEST}_{\text{ratio}}(\text{gua})$  values at  $\text{pH}_{\text{titrated}} > 7.5$ . Similarly, a reliable extraction of exchange rates  $k_{\text{ex}}$  for amide and guanidyl protons was only feasible in the aforementioned specific pH regions (Figure 5.5c and d, gray shaded regions, note the different scaling of the  $k_{\text{ex}}$ -axes).

In order to experimentally evaluate the pH sensitivity of  $\text{pH}_{\text{amide}}$  and  $\text{pH}_{\text{gua}}$ , the measured pH values were correlated to the titrated pH values, i.e.  $\text{pH}_{\text{titrated}}$  (Figure 5.5e and f). Most notably and in good coherence with theory (cf. Figure 3.4a), an acceptable signal correlation was observed for  $\text{pH}_{\text{amide}}$  ( $r = 0.6912$ ,  $p = 0.129$ ) and a very good signal correlation was observed for  $\text{pH}_{\text{gua}}$  ( $r = 0.9250$ ,  $p < 0.0001$ ) in the range of  $\text{pH}_{\text{titrated}} = 7.3$  to  $8.0$  and  $6.2$  to  $7.3$ , respectively (Figure 5.5e and f, gray shaded regions). Outside of the gray shaded regions, the pH sensitivity of either  $\text{pH}_{\text{amide}}$  or  $\text{pH}_{\text{gua}}$  was too weak for a reliable pH mapping. Apparently, the  $\text{pH}_{\text{amide}}$  seemed to have a good correlation between a  $\text{pH}_{\text{titrated}}$  of  $5.5$  and  $6.8$  ( $r = 0.9119$ ,  $p = 0.0003$ , Figure 5.5e). However, at  $\text{pH}_{\text{titrated}} < 6.8$ , the deviations of  $\text{pH}_{\text{amide}}$  were too severe for reliable pH measurements (i.e. error bars in Figure 5.5e, obtained from the STD of mean ROI values) which was also visible in the  $\text{pH}_{\text{amide}}$  maps (cf. Figure 5.6, c, top and right sample). Importantly, the observed ranges in which each proton species yields reliable pH measurements verified the approach of a

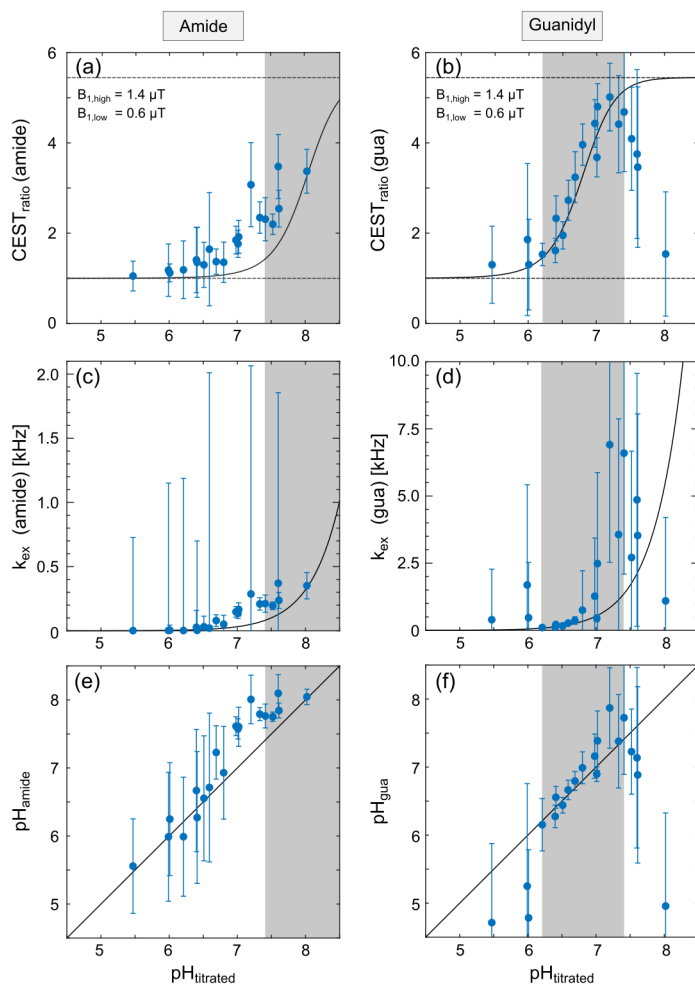


**Figure 5.5:** Experimentally determined  $\text{CEST}_{\text{ratio}}$  (top row),  $k_{\text{ex}}$  (middle row) and pH (bottom row) of the amide and guanidyl signals in porcine brain lysates (left and right column, respectively). In coherence with theory, the  $\text{CEST}_{\text{ratio}}$  ( $B_{1,\text{high}} = 1.4 \mu\text{T}$ ,  $B_{1,\text{low}} = 0.6 \mu\text{T}$ ) of the amide (a) and guanidyl signals (b) showed the distinct dependency on pH (black lines) within the range of their respective pH sensitivity, i.e. 7.3 to 8.0 and 6.2 to 7.3 for amide and guanidyl protons, respectively (gray shaded regions, cf. Figure 3.4a). A reliable extraction of  $k_{\text{ex}}(\text{amide})$  (c) and  $k_{\text{ex}}(\text{gua})$  (d) was only feasible in the gray shaded regions, in which a good signal correlation was observed for  $\text{pH}_{\text{amide}}$  (e,  $r = 0.6912$ ,  $p = 0.129$ ) and  $\text{pH}_{\text{gua}}$  (f,  $r = 0.9250$ ,  $p < 0.0001$ ). Outside of the gray shaded regions, deviations were stronger impeding reliable pH measurements. All values are mean ROI values  $\pm$  STD. Simulation parameters (a-d, black lines) are specified in Appendix A.3. Subfigures a, b, e and f were adapted from Figure 5 in [121].

## 5.1 In vitro validation using porcine brain lysates

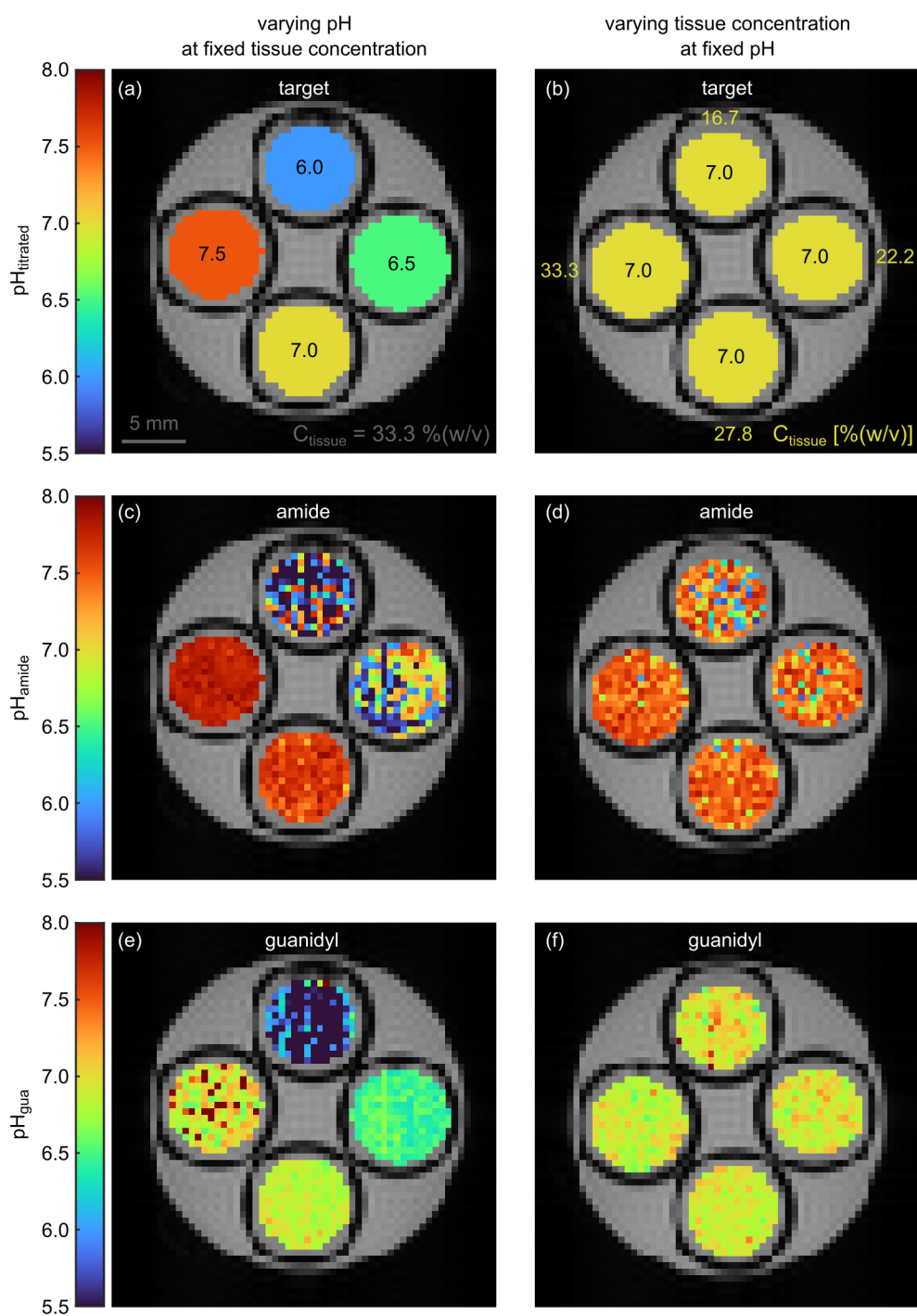


**Figure 5.6:** Experimentally determined  $\text{pH}_{\text{amide}}$  and  $\text{pH}_{\text{gua}}$  maps in porcine brain lysates (middle and bottom row, respectively) at varying pH values (left column) and varying tissue concentrations (right column). In coherence with theory (cf. Figure 3.4a), it was observed that  $\text{pH}_{\text{amide}}$  is more reliable at  $\text{pH}_{\text{titrated}} > 7.3$  (c) whereas  $\text{pH}_{\text{gua}}$  at  $\text{pH}_{\text{titrated}} < 7.3$  (e). Under variation of tissue concentration, no significant change of measured pH was observed in the  $\text{pH}_{\text{amide}}$  (d) or  $\text{pH}_{\text{gua}}$  maps (f), thus, verifying concentration independence. To provide a visual reference, the top row illustrates the computer generated target  $\text{pH}_{\text{titrated}}$  maps (a and b).

## 5 Results

weighted combination of the two individually obtained  $\text{pH}_{\text{amide}}$  and  $\text{pH}_{\text{gua}}$  values to enable a reliable  $\text{pH}_{\text{combi}}$  mapping over a broader range of pH values.

To assess whether the developed pH mapping method is independent of changes in concentration (essentially, i.e. independent of  $f_s$ ), the  $\text{pH}_{\text{amide}}$  and  $\text{pH}_{\text{gua}}$  maps were also investigated under variation of tissue concentration (Figure 5.6, right column). Under variation of tissue concentration, no significant variation of measured pH was found for  $\text{pH}_{\text{amide}}$  and  $\text{pH}_{\text{gua}}$ , respectively (Figure 5.6d and f, respectively), thus, verifying the concentration independence of the developed pH mapping method.

### Combined pH mapping

In order to enable a reliable pH mapping over a broader range of physiologically relevant pH values, the  $\text{pH}_{\text{amide}}$  and  $\text{pH}_{\text{gua}}$  maps were combined into  $\text{pH}_{\text{combi}}$ . To calculate  $\text{pH}_{\text{combi}}$ , the  $\text{pH}_{\text{amide}}$  and  $\text{pH}_{\text{gua}}$  maps were combined pixel-by-pixel using a weighted combination approach based on their individual pH sensitivities (section 3.6). To ensure a reliable pH mapping, effectively, the weightings need to combine both pH signals so that each signal is given stronger weighting within its respective region of high pH sensitivity. A reliable  $\text{pH}_{\text{combi}}$  is especially important in the transition region where both,  $\text{pH}_{\text{amide}}$  as well as  $\text{pH}_{\text{gua}}$ , exhibit merely a moderate pH sensitivity ( $\text{pH} \simeq 7.3$ , Figure 5.5e and f, cf. Figure 3.4a). Therefore, the weightings of  $\text{pH}_{\text{amide}}$  and  $\text{pH}_{\text{gua}}$ , respectively, ( $w_{\text{amide}}$  and  $w_{\text{gua}}$ , respectively) were investigated under variation of pH and tissue concentration (Figure 5.7).

Under variation of pH (Figure 5.7, left column) and in coherence with theory (cf. Figure 3.4a), it was found that  $\text{pH}_{\text{amide}}$  is given a stronger weighting of  $w_{\text{amide}} > 0.7$  for  $\text{pH}_{\text{titrated}} > 7.3$  (Figure 5.7a, left sample) whereas  $\text{pH}_{\text{gua}}$  is given a stronger weighting of  $w_{\text{gua}} > 0.7$  for  $\text{pH}_{\text{titrated}} < 7.3$  (Figure 5.7c, bottom and right sample). Equally important, under variation of tissue concentration (Figure 5.7, right column), no significant change was observed for  $w_{\text{amide}}$  and  $w_{\text{gua}}$ , respectively, thus allowing for a concentration-independent weighted combination approach (cf. approximately constant weightings in Figure 5.7b and d, respectively).

To assess the reliability of the weighted combination approach, the final  $\text{pH}_{\text{combi}}$  maps were examined under variation of pH and tissue concentration (Figure 5.8). Most noticeable, compared to the individually obtained  $\text{pH}_{\text{amide}}$  and  $\text{pH}_{\text{gua}}$  maps at varying pH with

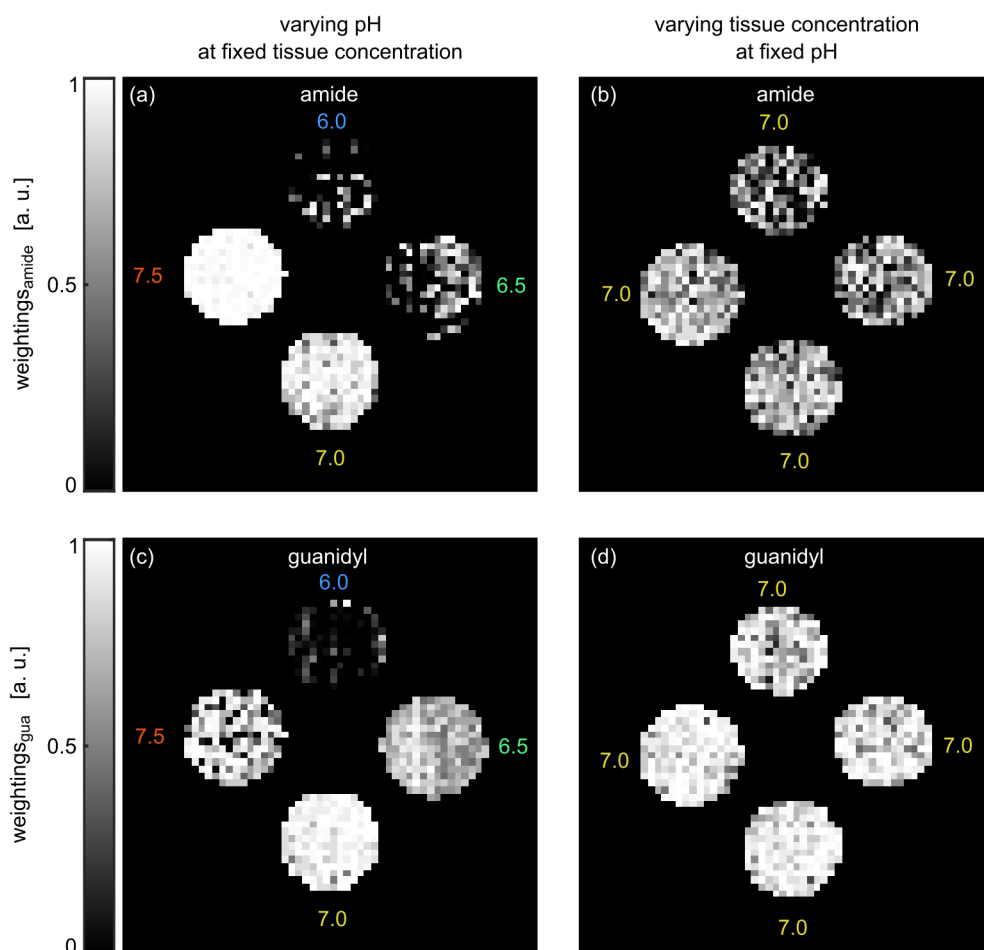


**Figure 5.7:** Normalized weightings of  $\text{pH}_{amide}$  ( $w_{amide}$ , top row) and  $\text{pH}_{gua}$  ( $w_{gua}$ , bottom row) at various pH (left column) and tissue concentration (right column) used for calculation of  $\text{pH}_{combi}$  in porcine brain lysates. In coherence with theory (cf. Figure 3.4a),  $\text{pH}_{amide}$  is given stronger weighting at  $\text{pH}_{titrated} > 7.3$  (a, left sample), whereas  $\text{pH}_{gua}$  is given stronger weighting at  $\text{pH}_{titrated} < 7.3$  (c, bottom and right samples). Under variation of tissue concentration, no significant changes were observed for  $w_{amide}$  and  $w_{gua}$ , respectively (c and d, respectively). The value of  $\text{pH}_{titrated}$  is indicated by the colored numbers (same coloring as in Figure 5.6).

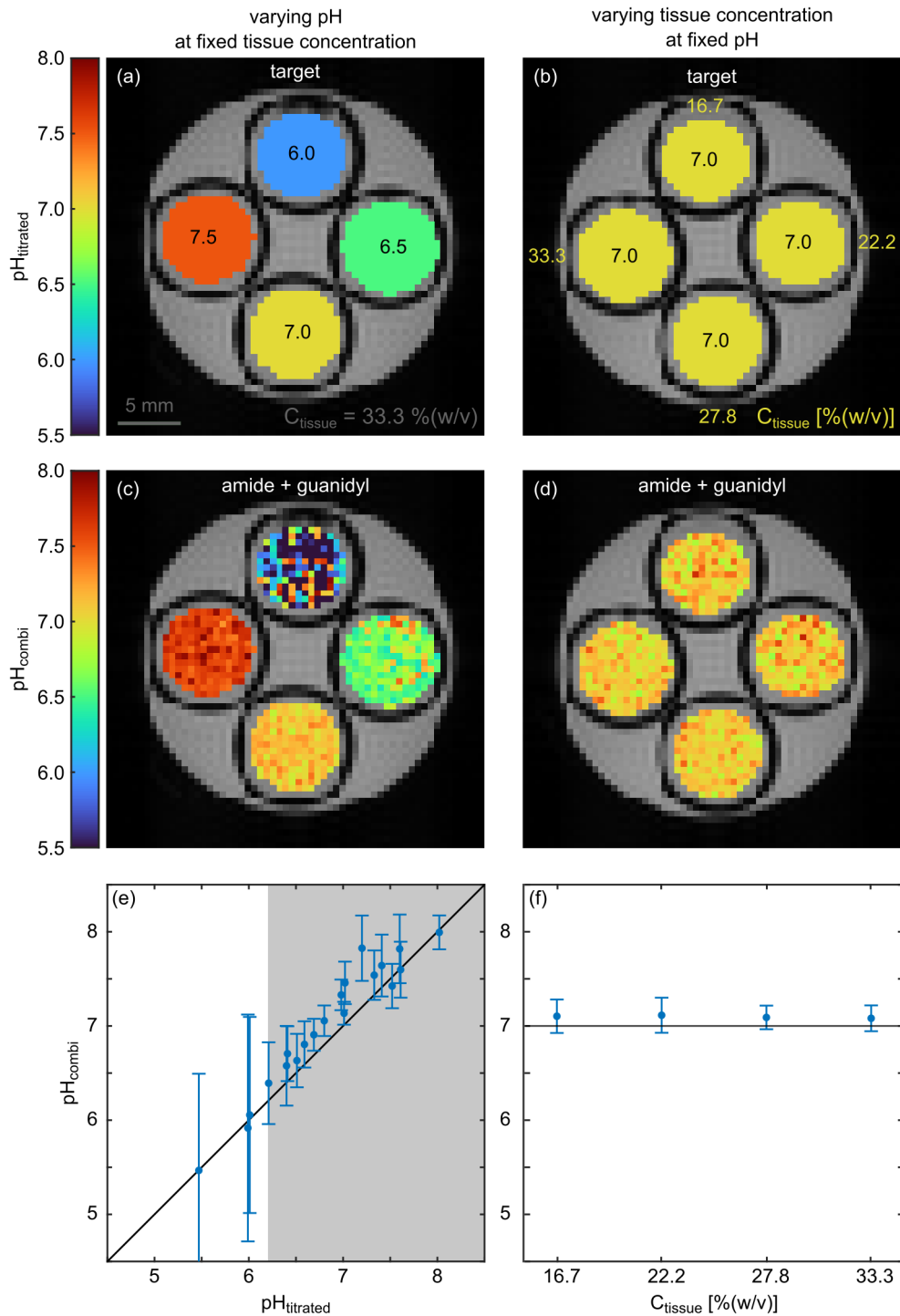


**Figure 5.8:** Experimentally determined final pH<sub>combi</sub> maps in porcine brain lysates at varying pH (left column) and varying tissue concentration (right column) obtained from the weighted combination of pH<sub>amide</sub> and pH<sub>gua</sub>. In comparison to the individual pH<sub>amide</sub> and pH<sub>gua</sub> maps (cf. Figure 5.6), a significantly enhanced correlation ( $r = 0.9430$ ,  $p < 0.0001$ ) was observed for pH<sub>combi</sub> maps over a broader range of pH<sub>titrated</sub> values from 6.2 to 8.0 (e, gray shaded region). Under variation of tissue concentration, no significant change was observed in the pH<sub>combi</sub> maps (d and f), thus, also verifying concentration independence of the pH<sub>combi</sub> approach. For pH<sub>titrated</sub> < 6.2, deviations were stronger impeding reliable pH measurements (e, larger error bars outside of the gray shaded region) which was also visible in the pH<sub>combi</sub> maps (c, top sample with pH<sub>titrated</sub> = 6.0). All values are mean ROI values  $\pm$  STD (e, f). Subfigures c-f were adapted from Figure 6 in [121].

a fixed tissue concentration (Figure 5.6c and e), the pH values obtained from the  $\text{pH}_{\text{combi}}$  maps were significantly more reliable, in particular, in the transition range where amide and guanidyl protons both exhibit a pH sensitivity of only 30%, i.e. at around  $\text{pH} \simeq 7.3$  (Figure 5.8c and e). In the range of  $\text{pH}_{\text{titrated}} = 6.2$  to 8.0 (Figure 5.8e, gray shaded region), the  $\text{pH}_{\text{combi}}$  values showed a very good correlation ( $r = 0.9430$ ,  $p < 0.0001$ ). Also within this range of  $6.2 \leq \text{pH}_{\text{titrated}} \leq 8.0$ , a homogeneous appearance with an average variation of around  $\pm 0.2$  was observed in the  $\text{pH}_{\text{combi}}$  maps (Figure 5.8c, all samples except top sample). For  $\text{pH}_{\text{titrated}} < 6.2$ , deviations of  $\text{pH}_{\text{combi}}$  from  $\text{pH}_{\text{titrated}}$  were significantly larger (Figure 5.8e, larger error bars outside of the gray shaded region). As established in section 3.5, this is attributed to the intrinsically lower pH sensitivity of amide and guanidyl CEST signals at  $\text{pH} < 6.2$ , which prevented a reliable pH measurement in the range of  $\text{pH}_{\text{titrated}} < 6.2$ . In pH regions where either  $\text{pH}_{\text{amide}}$  or  $\text{pH}_{\text{gua}}$  reliably measured pH ( $\text{pH}_{\text{titrated}} > 7.5$  and  $6.2 \leq \text{pH}_{\text{titrated}} \leq 7.0$ , respectively), it was found that  $\text{pH}_{\text{combi}}$  also reliably measures pH.

Remarkably, the  $\text{pH}_{\text{combi}}$  approach, in addition, even enabled reliable measurement of pH in regions where neither  $\text{pH}_{\text{amide}}$ , nor  $\text{pH}_{\text{gua}}$  could reliably measure pH. In particular, this effect was apparent in the transition range at around  $\text{pH}_{\text{titrated}} = 7.3$  (Figure 5.8 e), which is an especially important pH range as it is relevant in vivo. The fact that  $\text{pH}_{\text{combi}}$  is reliable even in this pH range can be attributed to the well functioning weighted combination approach, i.e. with efficiently working  $w_{\text{amide}}$  and  $w_{\text{gua}}$  (cf. Figure 5.7). For example, at  $\text{pH}_{\text{titrated}} = 7.5$ ,  $\text{pH}_{\text{amide}}$  yields higher and  $\text{pH}_{\text{gua}}$  yields lower pH values than  $\text{pH}_{\text{titrated}}$  (Figure 5.6c and e, left samples). However,  $\text{pH}_{\text{amide}}$  and  $\text{pH}_{\text{gua}}$  were weighted accurately so that  $\text{pH}_{\text{combi}} \approx \text{pH}_{\text{titrated}} = 7.5$  (Figure 5.8c, left sample).

Importantly, under variation of tissue concentration, no significant change of measured pH was found in the  $\text{pH}_{\text{combi}}$  maps (Figure 5.8d and f), thus allowing a reliable and, in particular, concentration-independent pH measurement using the  $\text{pH}_{\text{combi}}$  approach.

## 5.2 In vivo application

In order to demonstrate the applicability of the developed pH mapping method in vivo, a total of  $n = 14$  tumor-bearing mice were investigated. Therefore, the in vitro calibrated  $k_c$  (subsection 5.1.2) and theoretically derived weighting parameters for a reliable  $\text{pH}_{\text{combi}}$

## 5 Results

mapping in porcine brain lysates (subsection 5.1.3) were used for  $\text{pH}_{\text{combi}}$  measurements in vivo. In addition, the in vitro optimized acquisition protocol and fitting parameters (fitting of Z-spectra and contrast- $B_1$ -correction, subsection 5.1.1) were used as a starting point to optimize the experimental setup, the acquisition protocol and the fitting procedure for application in vivo (subsection 5.2.1). Using the optimized setup,  $n = 19$   $\text{pH}_{\text{combi}}$  measurements were performed in tumor lesions of different sizes (i.e. in  $n = 11$  tumor-bearing mice at different days of tumor growth) yielding a physiologically plausible median  $\text{pH}_i$  of approximately 7.2, independent of tumor size (subsection 5.2.2). In addition, in order to detect a change of  $\text{pH}_i$ , it was attempted to medicinally induce a drop of  $\text{pH}_i$  in tumor lesions of  $n = 3$  mice. The used treatment was not effective, i.e. did not lead to an intracellular acidification, clearly indicated by the approximately same tumor growth of the treatment and control group. Interestingly, in coherence with the failed treatment, the  $\text{pH}_{\text{combi}}$  tumor region of interest (ROI) analysis detected no significant changes in  $\text{pH}_i$  (subsection 5.2.2).

### 5.2.1 Prerequisites for a robust and reliable $\text{pH}_i$ mapping in vivo

To enable a robust and reliable  $\text{pH}_i$  mapping in vivo, firstly, the experimental prerequisites were investigated.

#### Experimental setup and parameter optimization

To reliably utilize the relaxation-compensated inverse metric  $\text{MTR}_{\text{REX}}$ , it is a prerequisite to acquire the Z-spectra in steady-state (section 2.5). Therefore, it was assessed which saturation time  $t_{\text{sat}}$  is required to meet the steady-state condition in vivo, by experimentally investigating the  $t_{\text{sat}}$  dependency of Z-spectra in a tumor lesion of one mouse. More specifically, Z-values acquired with  $B_1 = 1 \mu\text{T}$  were examined at the spectral position of the amide signal, i.e.  $\Delta\omega = 3.6 \text{ ppm}$  (Figure 5.9).

It was found that a saturation duration of  $t_{\text{sat}} = 6 \text{ s}$  (Figure 5.9, red data point) is above 95% of the steady-state (Figure 5.9b, dashed horizontal line). As  $t_{\text{sat}} = 6 \text{ s}$  was sufficient to approximately reach the steady-state condition in the tumor lesions, this  $t_{\text{sat}}$  was utilized in the in vivo CEST acquisition protocol to minimize the total acquisition time while still ensuring a quantitative  $\text{MTR}_{\text{REX}}$  analysis which is a prerequisite of the developed pH mapping method.

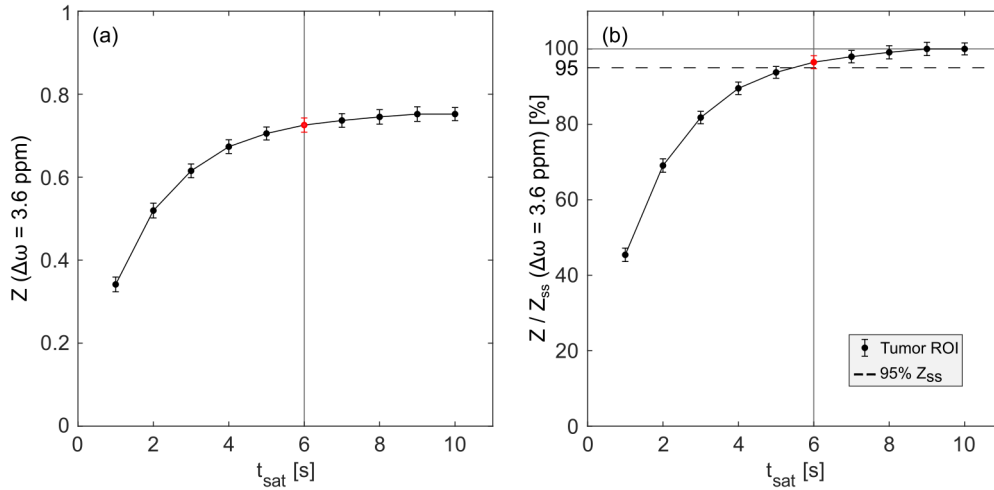


**Figure 5.9:** Measured (a) and relative (b) Z-values of a representative in vivo tumor lesion as a function of the saturation duration  $t_{sat}$  at the spectral position of the amide signal ( $\Delta\omega = 3.6$  ppm,  $B_1 = 1$   $\mu$ T, average of 10 measurements). With increasing  $t_{sat}$ , the measured Z-values approach the steady-state condition (a). For  $t_{sat} = 6$  (red data point, utilized in the vivo acquisition protocol), the relative Z-value is above 95% of the steady-state condition (b). The dashed horizontal line illustrated the border of having reached 95% of the steady-state. All values are mean ROI values  $\pm$  STD.

To optimize the SNR, already for the in vitro examinations a single-shot 2D-RARE image readout was used which allows for a fast image acquisition with the maximally available MR signal (maximal transversal magnetization due to RF excitation pulses with  $FA = 90^\circ$ ). Compared to the in vitro image readout with a resolution of  $0.5 \times 0.5$  mm<sup>2</sup> and a matrix size of  $60 \times 60$ , a larger pixel size was used for the in vivo image readout with a resolution of  $0.75 \times 0.75$  mm<sup>2</sup> and a matrix size of  $40 \times 40$  while maintaining the same FOV of  $30 \times 30$  mm<sup>2</sup>. This allowed for acquisition of Z-spectra with sufficient SNR while simultaneously minimizing the readout time to additionally mitigate breathing-induced artifacts.

Moreover, as the dependency of  $k_{ex}$  on temperature is exponential, it was essential to stabilize the temperature of the mouse at  $T = 37^\circ\text{C}$  as good as experimentally feasible. It was found that maintaining the temperature by use of warm air is far superior compared to using a water-heated warming pad. By using warm air blown into the small animal imaging chamber, less temperature gradients occurred in comparison to using a heating pad, thus allowing for a homogeneous temperature profile across the tumor lesions. In

## 5 Results

addition, the setup with warm air allowed for a fast temperature regulation of the mice with a response time of under a minute, thus, enabling to maintain a rectal temperature of  $T = 37 \pm 0.2^\circ\text{C}$  during all in vivo examinations.

For the used tumor model (with tumor cells injected subcutaneously into the right flank), it was observed that inevitable abdominal motion due to breathing of the mice led to significant artifacts in the acquired Z-spectra. Interestingly, in Z-spectra acquired under sevoflurane anesthesia significantly less breathing-induced motion artifacts were observed in comparison to Z-spectra acquired under isoflurane anesthesia, which is why sevoflurane was used. In the tumor lesions, remaining breathing-induced motion artifacts could be further suppressed by using an optimized positioning of a respiratory cradle (see section 4.2.3) which enabled acquisition of Z-spectra with sufficient spectral SNR for a reliable extraction of the amide and guanidyl signals (cf. Figure 5.11a). Simultaneous mitigation of breathing-induced motion outside of the tumor lesions was not adequate for a reliable signal extraction of surrounding healthy tissues.

Regarding the size of the tumor lesions, it was only possible to reliably evaluate tumor lesions within a certain range of sizes. More specifically, tumor lesions with a diameter smaller than approximately 0.5 cm could not be spatially resolved well enough for a reliable ROI analysis, as only a few pixels actually contained tumorous tissue. Out of those few pixels, additionally, most could not be reliably evaluated due to interfering partial volume artifacts from neighboring tissue. Conversely, tumors with a diameter of larger than approximately 1 cm tended to develop necrotic tissue which, for the used tumor model, in some cases did not yield sufficient CEST signals.

Also, it was found that the shimming of the tumor lesions is extremely important. For an optimized shimming procedure of the tumor area, the adjustment volume should cover the entire tumor, include some muscle tissue and, importantly, avoid including any surrounding air. The shimming of the tumor area could be optimized by using a shimming volume which included the  $B_0$  isocenter and maximized the immobile regions of the mouse (back muscles and spine), while simultaneously minimizing the shimming volume containing other abdominal regions and, in particular, avoiding surrounding air (see section 4.3.4 and Figure 4.5). Yet, in some tumor lesions a sufficient shimming could not be achieved, thus, preventing a reliable evaluation.

In summary, tumor lesions were systematically excluded from further evaluations if at least one of the following criteria occurred:

- (i) Relative  $\Delta B_1 < 60\%$  of the nominal  $B_1$ ,
- (ii)  $|\Delta B_0| > 0.5$  ppm,
- (iii) tumor lesion diameter  $< 0.5$  cm (in FOV), or
- (iv) no detectable CEST signals.

### Signal extraction and pH mapping

In a next step, the in vivo post processing and fitting procedure was optimized. For the application in vivo, an additionally acquired high-resolution anatomical image was used to accurately identify the tumor region for further ROI analysis ( $T_{2w}$ , Figure 5.10a). Accordingly, the tumor ROI was defined on the anatomical image (Figure 5.10a, white line) and scaled down (Figure 5.10b, white line) to match the nominal resolution of the acquired CEST images (Figure 5.10c, white line shown on an  $M_0$ , i.e. unsaturated image). Importantly, the  $B_0$  and  $B_1$  field maps (Figure 5.10d and e, respectively) were not only used (i) to correct the  $Z$ -spectra and the  $MTR_{\text{Rex}}$  contrasts for  $B_0$ - and  $B_1$ -field inhomogeneities, respectively (Figure 5.11a and b, respectively) but also (ii) to systematically exclude tumor lesions as established in the previous subsection.

In analogy to the assessment performed in porcine brain lysates, the in vivo  $Z$ -spectra and contrast- $B_1$ -correction were investigated to assess the experimentally feasible range of  $B_1$  values allowing for a robust and reliable amide and guanidyl signal extraction. In vivo, a robust extraction of  $Z_{\text{ref}}$  and  $Z_{\text{lab}}$  for the amide and guanidyl signal was feasible for  $0.6 \leq B_1 \leq 1.4$   $\mu\text{T}$  (Figure 5.11a). For  $B_1 < 0.6$   $\mu\text{T}$ , the amide and guanidyl signals were not pronounced enough for a robust and reliable signal extraction. In contrast, for  $B_1 > 1.4$   $\mu\text{T}$ , the signals were too broad, thus, also compromising signal extraction. To minimize the total acquisition time of the in vivo acquisition protocol compared to the in vitro acquisition protocol, (i) the number of acquired  $B_1$  was reduced to three, i.e.  $B_1 = 0.6, 1.0$  and  $1.4$   $\mu\text{T}$  (Figure 5.11a and b) and (ii) the number of acquired offsets  $\Delta\omega$  was reduced to 42 (a complete list is provided in A.2).

Most importantly, for the in vivo tumor lesions, the starting values and boundaries of the fits were changed slightly in comparison to the in vitro case (cf. Tables 4.6 and 4.7).

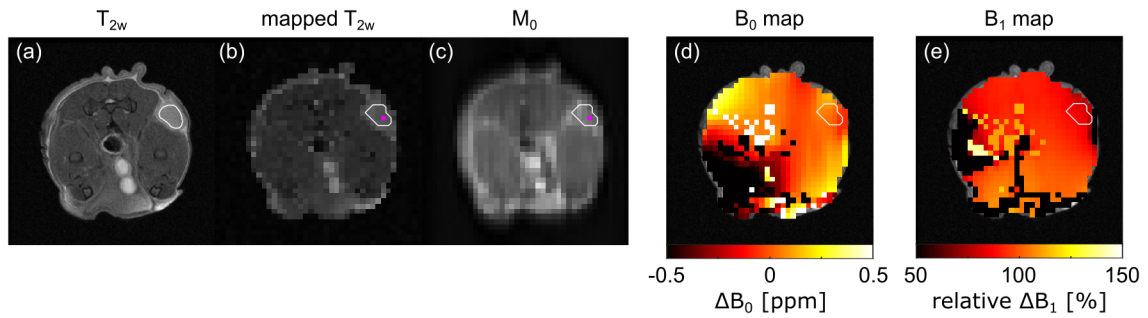


**Figure 5.10:** For an optimized in vivo post-processing, the tumor ROI was defined on the high-resolution  $T_{2w}$  anatomical image (a, white line) and scaled down (b, white line) to match the nominal resolution of the acquired CEST images (c). The  $B_0$  and  $B_1$  maps were used to correct for  $B_0$  and  $B_1$  field inhomogeneities (d and e, respectively, cf. Figure 5.11a and b). In addition, the  $B_0$  and  $B_1$  field maps were also used to systematically exclude tumor lesions with either a  $B_1 < 60\%$  of the nominal applied  $B_1$  or a  $|\Delta B_0| > 0.5$  ppm. The magenta dot (b and c) illustrates the pixel corresponding to the Z-spectra, contrast- $B_1$ -corrections and highlighted pixel in the  $\text{pH}_{\text{combi}}$  map shown in Figure 5.11a, b and d, respectively.

With these minuscule changes, the used linear and Lorentzian fit model also enabled a stable separate extraction of the amide and guanidyl signal from the background of concomitant effects, equally well as was the case for the in vitro porcine brain lysates (cf. Figures 5.2 and 5.11a). Similarly, the  $B_1$  correction was found to also reliably work in vivo (cf. Figures 5.3 and 5.11b). Using the experimentally determined  $k_c$  of amide and guanidyl protons calibrated in porcine brain lysates, the  $\text{pH}_{\text{amide}}$  and  $\text{pH}_{\text{gua}}$  maps were calculated separately and combined into  $\text{pH}_{\text{combi}}$  using the weighting parameters optimized in vitro (Figure 5.11c and d). Outside of the tumor lesions, quantitative  $\text{pH}_i$  mapping of surrounding healthy tissue was compromised by breathing-induced motion artifacts (cf. Figures 5.11c and d).

### 5.2.2 $\text{pH}_i$ mapping in tumor-bearing mice

With the optimized experimental and post-processing setup at hand,  $\text{pH}_{\text{combi}}$  measurements were performed in lesions of tumor-bearing mice. Assuming transferability of the in porcine brain lysates calibrated  $k_c$  of amide and guanidyl protons for examinations in vivo, the in vivo applicability of the  $\text{pH}_{\text{combi}}$  method was assessed by measuring  $\text{pH}_i$  in tumor lesions of different sizes and by comparing treated and control mice.

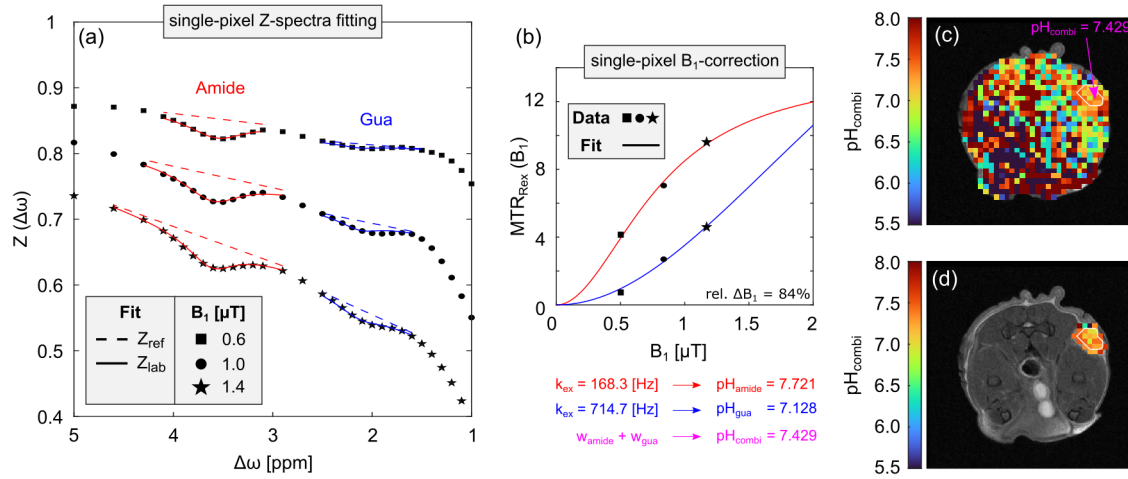


**Figure 5.11:** Representative single-pixel Z-spectra fits (a), contrast-B<sub>1</sub>-corrections (b) and pH<sub>combi</sub> maps (c and d) in a tumor-bearing mouse. In the tumor regions, extraction of Z<sub>ref</sub> and Z<sub>lab</sub> (a, dashed and solid lines) for the amide and guanidyl signals (a, red and blue) was stable for the acquired nominal B<sub>1</sub> = 0.6, 1.0 and 1.4 μT (a, squares, discs and stars) using the optimized linear and Lorentzian fits. The contrast-B<sub>1</sub>-correction of the amide and guanidyl signal (b, red and blue curves) was also stable in the tumor lesions. Outside of the tumor lesions, quantitative pH<sub>i</sub> mapping of surrounding healthy tissue was compromised by breathing-induced motion artifacts (cf. c and d). Z-spectra fits are only illustrated within their respective range of offsets which were used for the actual fitting procedure. Z-spectra and contrast-B<sub>1</sub>-correction (a and b) are shown for the pixel illustrated in (c) and in Figure 5.10b and c as magenta dot.

### pH<sub>i</sub> mapping in tumor lesions of different sizes

To assess the robustness and reliability of pH<sub>combi</sub>, firstly, pH<sub>combi</sub> measurements were performed in tumor lesions of different sizes ranging from diameters of 3 to 15 mm (Figure 5.12). Therefore, the sizes of  $n = 19$  tumor lesions<sup>1</sup> were sorted into three groups with small (i.e. 3 – 7 mm,  $n = 9$ ), medium (i.e. 8 – 11 mm,  $n = 6$ ), and large (i.e. 12 – 15 mm,  $n = 4$ ) diameters (Figure 5.12a, b and c, respectively).

Most noticeable and independent of tumor size, plausible pH<sub>i</sub> values of approximately 7.2 were detected in the tumor lesions (Figure 5.12d, dashed horizontal line). More specifically, median pH<sub>i</sub> values of 7.15, 7.29 and 7.28 were found for small, medium and large tumors, respectively (Figure 5.12d, red, blue and green box plots<sup>2</sup>, respectively, and Table

<sup>1</sup> Tumor lesions of different sizes were examined by performing in vivo MRI examinations on different days after implantation, see section 4.2.3.

<sup>2</sup> Note that in Figure 7E of the journal article [121] the box plots of medium and large tumors were

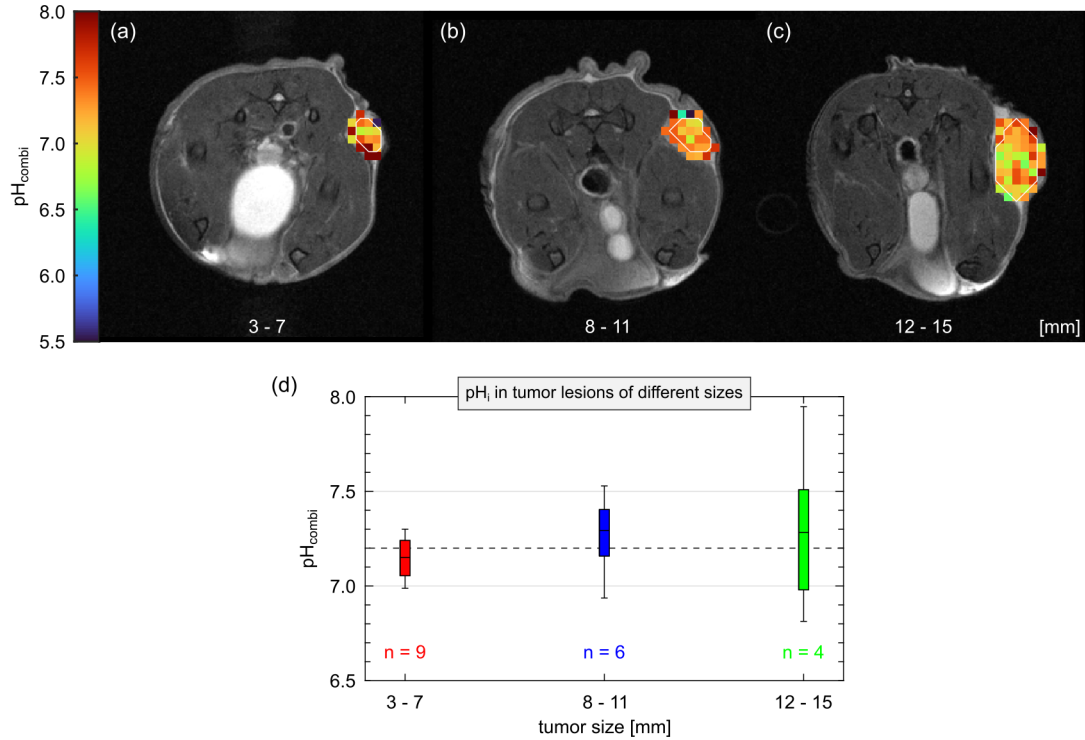


**Figure 5.12:** In vivo application of the developed  $\text{pH}_{\text{combi}}$  mapping method in tumor-bearing mice with different sizes of tumor lesions. Representative mice are shown for each group of tumor lesions measured with diameters of 3 – 7 (a,  $n = 9$ ), 8 – 11 (b,  $n = 6$ ) and 12 – 15 mm (c,  $n = 4$ ). In the  $\text{pH}_{\text{combi}}$  maps, a modest heterogeneity was observed especially across larger tumor lesions which showed an increased  $\text{pH}_i > 7.0$  only in some regions (c). A ROI analysis demonstrated physiologically plausible  $\text{pH}_i$  values of around 7.2 (d, dashed line) with median  $\text{pH}_i$  values of 7.15, 7.29 and 7.28 for small, medium and large tumors, respectively (d). For the ROI analysis, only pixels completely within the tumor lesions were selected (white lines in a-c). For the box plots, mean ROI values were used as input. Outside of the tumor lesions, quantitative  $\text{pH}_i$  mapping of surrounding healthy tissue was compromised by breathing-induced motion artifacts. Figure was adapted from Figure 7 in [121].

5.2) which agreed well within the observed variation of  $\text{pH}_{\text{combi}}$  measurements in different tumor sizes (Figure 5.12d), thus indicating robust  $\text{pH}_{\text{combi}}$  measurements in vivo. However, in the  $\text{pH}_{\text{combi}}$  maps, a heterogeneity was observed across the tumors lesions, in particular, for larger tumor lesions where an increased  $\text{pH}_i > 7.0$  was detected only in some regions (Figure 5.12c). The heterogeneity of the larger tumor lesions was verified by means of post mortem biopsy which, typically, revealed necrotic tissue in the center and vital tissue mostly in the periphery of the tumors.

**Table 5.2:** Experimentally determined  $\text{pH}_i$  in  $n = 19$  tumor lesions of different sizes. The  $\text{pH}_{\text{combi}}$  values are presented in the manner of median (lower quartile, upper quartile).

Tumor diameter [mm]	3 – 7 ( $n = 9$ )	8 – 11 ( $n = 6$ )	12 – 15 ( $n = 4$ )
$\text{pH}_{\text{combi}}$	7.15 (7.05, 7.24)	7.29 (7.16, 7.40)	7.28 (6.98, 7.51)

Most importantly, the plausible  $\text{pH}_i$  values found in tumor lesions indicated transferability of the in porcine brain lysates calibrated  $k_c$  of amide and guanidyl protons for examinations in vivo.

### **$\text{pH}_i$ mapping in tumor lesions of treated and control mice**

To assess, whether the developed  $\text{pH}_{\text{combi}}$  mapping method can detect a change of  $\text{pH}_i$  in vivo under treatment, the tumor lesions of  $n = 3$  treated and  $n = 3$  control mice were measured on four different days, i.e. d0, d3, d7 and d10. The idea of the treatment was to stop tumor growth by specifically inducing a significant decrease of  $\text{pH}_i$  in the tumor cells in the order of  $\sim 1$  pH unit which, in principle, should be detectable via  $\text{pH}_{\text{combi}}$  measurements (cf. error bars in gray shaded region of Figure 5.8e, with an average variation of  $\pm 0.2$  pH units). However, the used treatment was not effective which was clearly indicated by the approximately same tumor growth of the treatment and control group, respectively (Figure 5.13b, green and blue data points).

To evaluate the ROI analysis in those mice as reliable as possible, all  $\text{pH}_{\text{combi}}$  measurements in the tumor lesions on day d0 (Figure 5.13a and b, red shaded regions) and, in addition, some  $\text{pH}_{\text{combi}}$  measurements in tumor lesions on days d3, d7 and d10 were systematically excluded (Figure 5.13a, data points with  $n < 3$ ) due to the findings established

---

swapped. However, the main message – here as well as in [121] – was that the plausible  $\text{pH}_i$  values of approximately 7.2 found in tumor lesions are independent of tumor size.

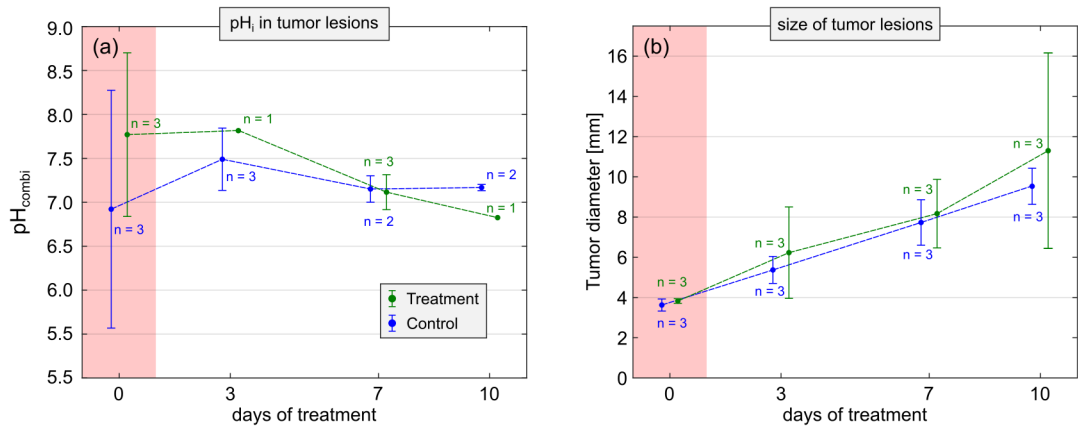


**Figure 5.13:** Treatment course of  $\text{pH}_i$  in tumor lesions measured via  $\text{pH}_{\text{combi}}$  (a) and growth of tumor lesions (b) in treated ( $n = 3$ , green) and control mice ( $n = 3$ , blue). For the treated and control mice, no significant difference of  $\text{pH}_i$  was detected (a) which was in coherence with the observed approximately same tumor growth of the treatment and control group (b). Tumor lesions on day d0 (red shaded regions) were too small, thus, preventing a reliable ROI analysis (larger errors, cf. Figure 5.14, left column). Some tumor lesions on days d3, d7 and d10 were also systematically excluded as established in subsection 5.2.1 (data points with  $n < 3$ ). For the ROI analysis, only pixels completely within the tumor lesions were selected (cf. magenta lines in Figure 5.14a-d). Due to the small sample sizes (a,  $n \leq 3$ ), median ROI  $\text{pH}_{\text{combi}}$  values were used as input for each shown data point (a, mean  $\pm$  STD). Values in (b) represent mean  $\pm$  STD diameters of the tumor lesions (largest diameter in one dimension).

in subsection 5.2.1. In particular, tumor lesions on day d0 were too small, thus, preventing a reliable ROI analysis (Figure 5.14). Due to the small sample sizes (a,  $n \leq 3$ ), the median  $\text{pH}_{\text{combi}}$  value of each remaining evaluable tumor ROI was used as input for each group and measurement day, respectively (Figure 5.13a, data points displayed as mean  $\pm$  STD). Considering the small sample size, no significant change of  $\text{pH}_i$  was detected in the  $\text{pH}_{\text{combi}}$  ROI analysis which, however, was in coherence with the approximately same tumor growth of the treatment and control group, respectively (Figure 5.13b, green and blue data points).

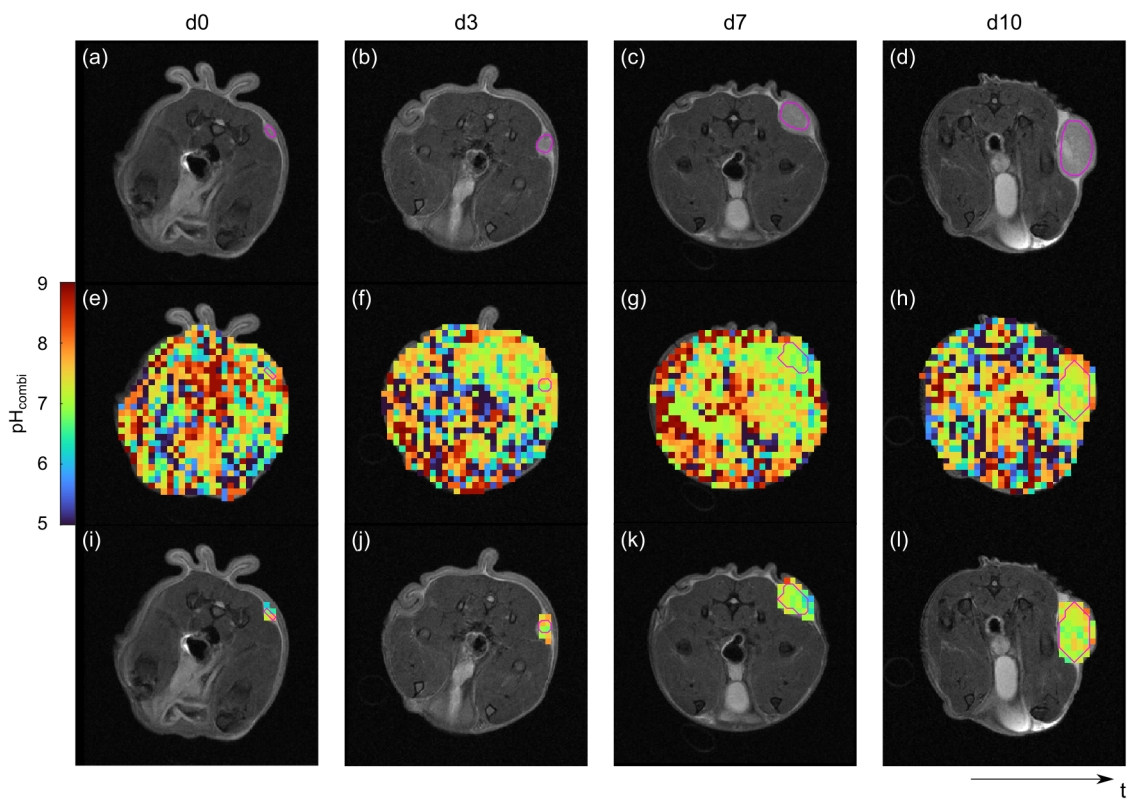


**Figure 5.14:** Time course showing representative  $\text{pH}_i$  maps (middle and bottom row) of control mice for each measurement day, i.e. d0, d3, d7 and d10 (columns). Tumor lesions on day d0 (left column) were too small for a reliable ROI analysis (cf. Figure 5.13, red shaded region). Outside of the tumor lesions, quantitative  $\text{pH}_i$  mapping of surrounding healthy tissue was compromised by breathing-induced motion artifacts.

### 5.3 Transfer to pulsed CEST

Until now, only the simple case of cw presaturation was used, i.e.  $DC = c_2 = c_1 = 1$ . In an effort to translate the developed method for examinations in humans<sup>3</sup>, a pulsed presaturation was investigated using simple creatine model solutions at various  $\text{pH}_{\text{titrated}}$  as a model system for the guanidyl signal. The pulsed presaturation experiments were realized with the help of Lilli Diederichs, i.e. within the framework of her bachelor thesis [136]. Parts of this section have already been published in [146].

Most notably, in the Z-spectra of creatine model solutions a clear guanidyl proton resonance at around  $\Delta\omega \approx 2.0$  ppm was observed which strongly depended on pH, i.e. peak amplitude and width (Figure 5.15a), in coherence with theory (equation (2.75)). In contrast, as a function of the presaturation pulse shape  $c_2$ , no relevant peak broadening of the guanidyl signal was observed in the Z-spectra of creatine model solutions (Figure 5.15b). However, a slight peak broadening of the guanidyl signal was found for decreasing  $c_2$ , i.e. for sharper presaturation pulses (Figure 5.15b, small panel).

In coherence with theory (equation (3.9)), the pH dependency of  $\text{MTR}_{\text{Rex}}(\text{pH})$  showed the expected symmetric shape also for pulsed presaturations (Figure 5.16a). Remarkably, the shift of  $\text{pH}_{\text{max}}$  towards higher pH not only was experimentally observed for higher  $\overline{B_1}$  (Figure 5.16a, cf. solid and dashed black lines) but also for decreasing  $c_2$ , i.e. sharper pulses, as expected from theory (Figure 5.16a, colored lines, cf. Figure 3.3d).

Experimental determination of  $\text{pH}_{\text{max}}$  enabled calculating a mean  $k_c(c_2)$  of  $89 \pm 3$   $\mu\text{Hz}$  (Figure 5.16b). For  $k_c(c_2)$ , a trend towards decreasing  $k_c$  was observed for increasing  $c_2$  which, however, was smaller than the  $\overline{B_1}$  dispersion of  $k_c$  for each  $c_2$  (error bars in Figure 5.16b). Also, the cw case was observed to deviate. Accordingly, for each  $c_2$  calculation of  $\text{pH}_{\text{gua}}$  was performed using the corresponding  $k_c$ .

Also in coherence with theory, it was observed that the position of the steepest slope of the  $\text{CEST}_{\text{ratio}}$  as a function of  $c_2$  is shifted towards higher pH values for decreasing  $c_2$  (Figure 5.16c,  $B_{1,\text{low}} = 0.6$   $\mu\text{T}$ ,  $B_{1,\text{high}} = 1.4$   $\mu\text{T}$ , cf. Figure 3.3d). The experimentally observed shift of the steepest slope of the  $\text{CEST}_{\text{ratio}}$  indicated the ability to shift the pH sensitivity towards higher pH by tuning the shape of the presaturation pulse. Remarkably,

<sup>3</sup> Where a pulsed presaturation is a prerequisite due to patient safety and hardware limitations.

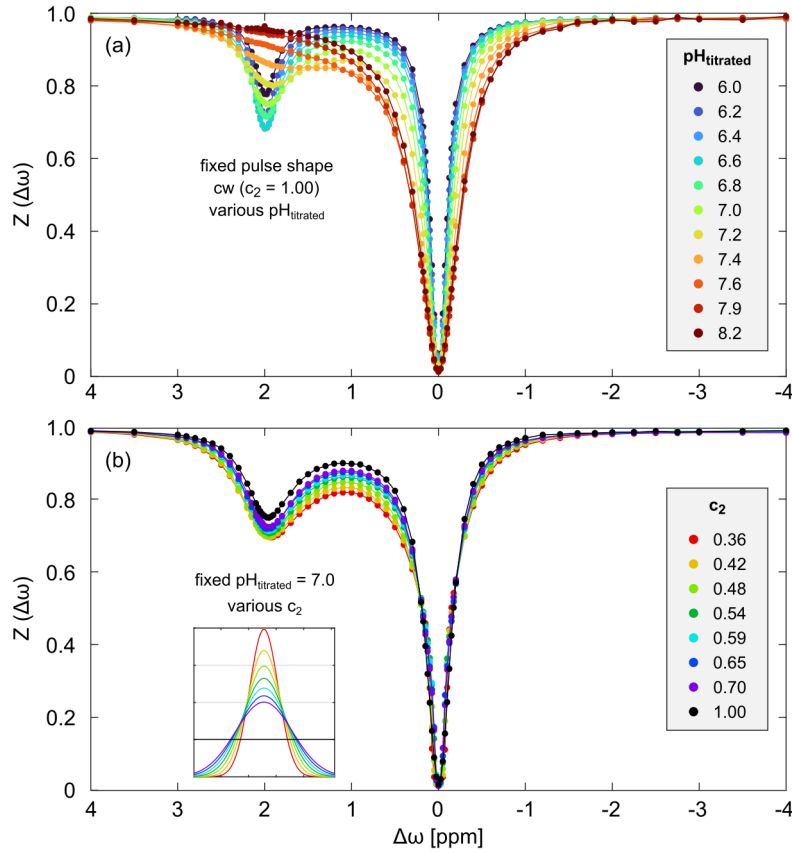


**Figure 5.15:** Z-spectra of creatine model solutions as a function of pH (a) and presaturation pulse shape  $c_2$  (b) acquired with  $\overline{B}_1 = 1 \mu\text{T}$ . Using a cw presaturation pulse, the acquisition of Z-spectra at various  $\text{pH}_{\text{titrated}}$  showed the expected strong pH dependency of the guanidyl signal at  $\Delta\omega = 2.0 \text{ ppm}$  and peak broadening with increasing pH (a, various colors). In contrast, in Z-spectra acquired with different presaturation pulse shapes at a fixed pH of  $\text{pH}_{\text{titrated}} = 7$ , no relevant peak broadening of the guanidyl signal was observed as a function of  $c_2$ . The used presaturation pulse shapes are illustrated in the small panel in (b), see Figure 4.4 for the larger version. All Z-spectra are mean ROI Z-spectra (ROIs are indicated in Figure 5.17a-c).

## 5 Results

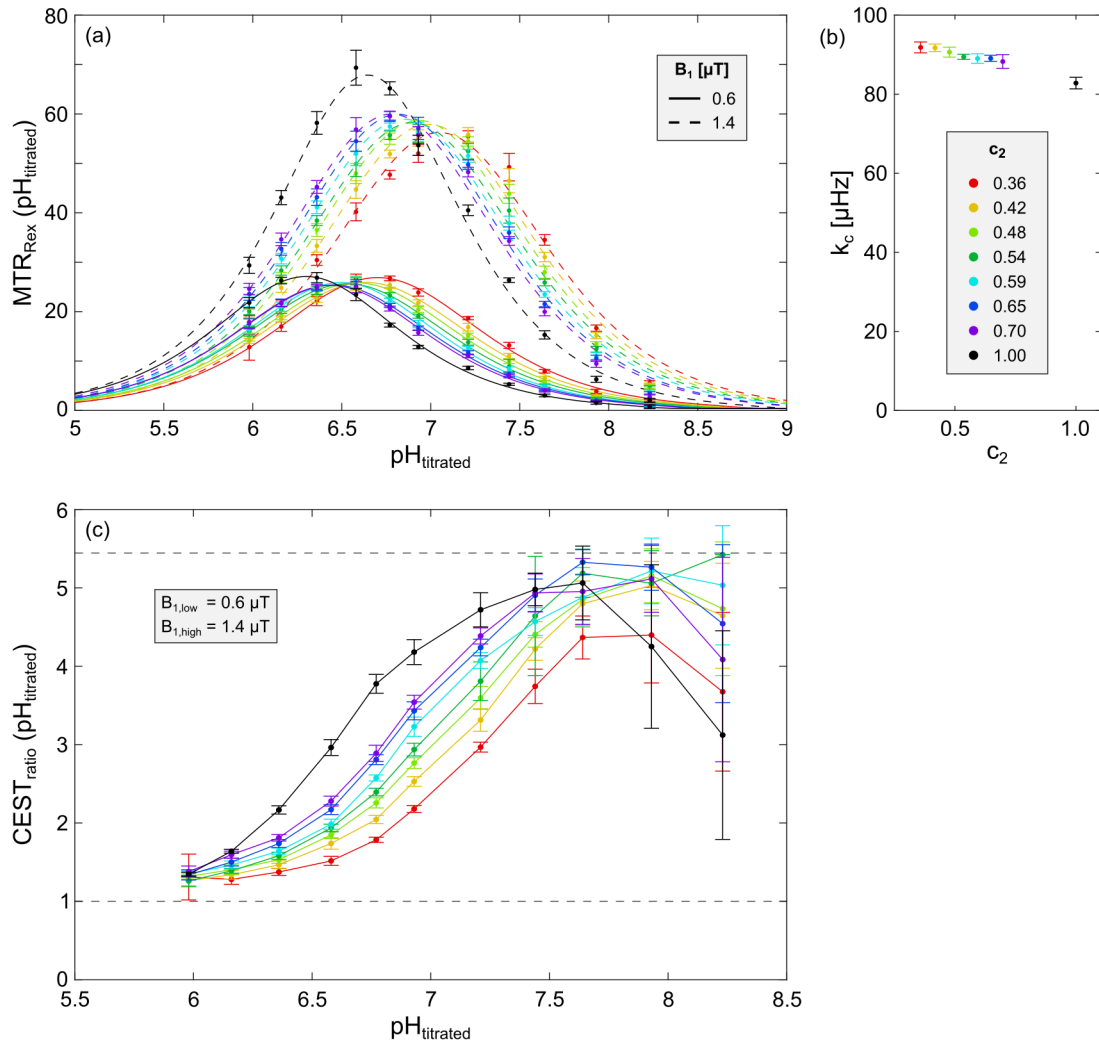


**Figure 5.16:** Effect of the presaturation pulse shape  $c_2$  on  $MTR_{\text{Rex}}$  (a),  $k_c$  (b) and the  $\text{CEST}_{\text{ratio}}$  (c) in creatine model solutions. In coherence with theory,  $MTR_{\text{Rex}}$  showed the expected symmetric shape also for pulsed presaturations (a, cf. Figure 3.1b). Remarkably, the shift of  $\text{pH}_{\text{max}}$  towards higher pH not only occurs for higher  $B_1$  (a, cf. solid and dashed black lines) but also for decreasing  $c_2$  (a, different colors), i.e. for sharper pulses. For  $k_c$  as a function of  $c_2$ , a trend towards smaller  $k_c$  values was observed for increasing  $c_2$  (b). In coherence with theory, the  $\text{CEST}_{\text{ratio}}$  exhibited a shift towards higher pH for decreasing  $c_2$  (c, cf. Figure 3.3d), thus, verifying the possibility of shifting the highest pH sensitivity of  $\text{pH}_{\text{gua}}$  above  $\text{pH}_{\text{titrated}} = 7.0$ .

using  $c_2 = 0.42$ , the range of highest  $\text{pH}_{\text{gua}}$  sensitivity was shifted to the physiologically relevant range of  $\text{pH} = 7.0$  to  $7.5$  (Figure 5.16c, yellow data points).

Having found the optimal  $c_2$  in creatine model solutions,  $\text{pH}_{\text{gua}}$  maps for a cw and  $c_2 = 0.42$  presaturation were calculated (Figure 5.17a and b). For both cw and  $c_2 = 0.42$ , respectively, a very good correlation of  $\text{pH}_{\text{gua}}$  and  $\text{pH}_{\text{titrated}}$  was observed in the  $\text{pH}$  range of  $\text{pH}_{\text{titrated}} = 6.5$  to  $7.5$  with  $r = 0.9922$ ,  $p < 0.0001$  for cw and  $r = 0.9953$ ,  $p < 0.0001$  for  $c_2 = 0.42$ , respectively (Figure 5.17d and e, gray shaded regions). However, for the optimized presaturation pulse shape  $c_2 = 0.42$ , significantly smaller fluctuations were detected in the  $\text{pH}_{\text{gua}}$  values in comparison to using the cw presaturation, thus demonstrating the improved sensitivity of  $\text{pH}_{\text{gua}}$  above  $\text{pH} = 7.0$  using  $c_2 = 0.42$  (cf. STD error bars in Figure 5.17d and e). In addition, the inverse of the RMS was used as a measure to assess the  $\text{pH}$  specificity (i.e. the RMS of all single-pixel  $\text{pH}_{\text{gua}}$  values within each ROI with respect to the  $\text{pH}_{\text{titrated}}$  value of each corresponding ROI). Accordingly, a clear improvement of the  $\text{pH}$  specificity was found for  $c_2 = 0.42$  in the range of  $\text{pH}_{\text{titrated}} = 6.5$  to  $7.5$  (Figure 5.17e).

## 5 Results

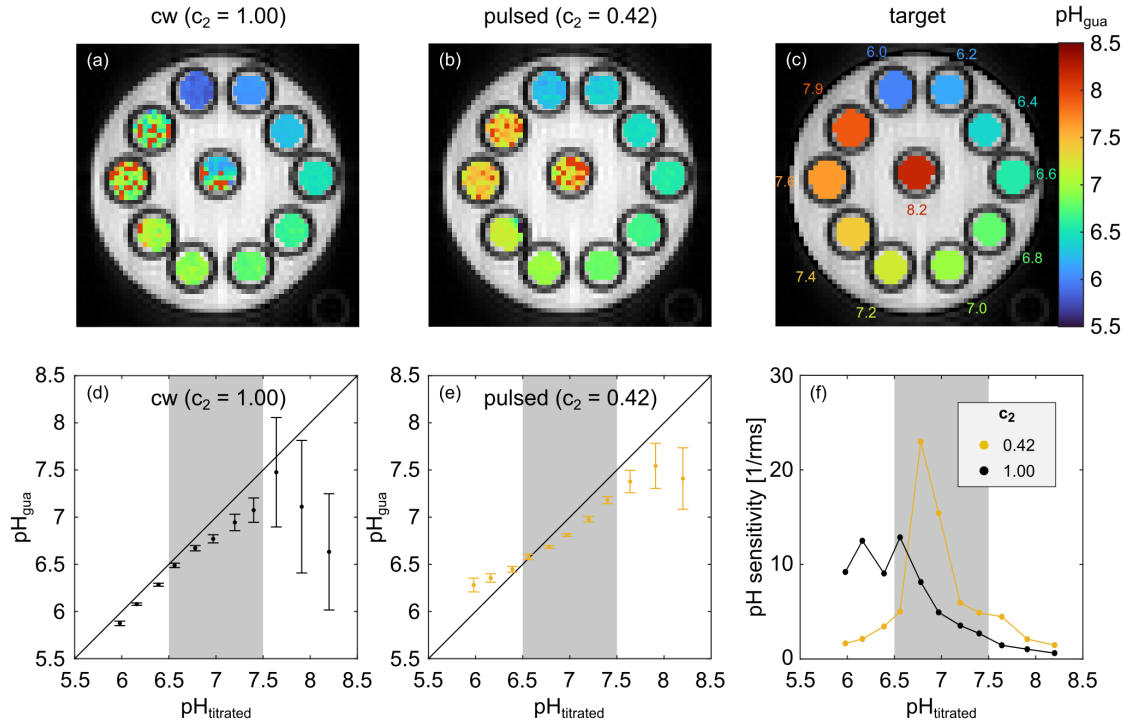


**Figure 5.17:** Correlation of  $\text{pH}_{\text{gua}}$  and  $\text{pH}_{\text{titrated}}$  for a cw (a, d) and pulsed presaturation using  $c_2 = 0.42$  (b, e) in creatine model solutions and shift of pH sensitivity (f). In the range of  $\text{pH}_{\text{titrated}} = 6.5$  to  $7.5$  (gray shaded regions), a very good correlation was observed for both the cw and the pulsed presaturation using  $c_2 = 0.42$  with  $r = 0.9922$  and  $r = 0.9953$ , respectively (d and e, respectively). However, for the pulsed presaturation significantly smaller fluctuations were observed for pH values above  $\text{pH}_{\text{titrated}} > 7.0$  (i.e. smaller STD, cf. error bars in d and e), thus, indicating the improved pH sensitivity using  $c_2 = 0.42$ . In the physiologically relevant range, the improved pH specificity of the optimized presaturation pulse compared to cw was illustrated by means of 1/RMS of the single-pixel  $\text{pH}_{\text{gua}}$  values within each ROI (f). To provide a visual reference, the computer generated target  $\text{pH}_{\text{titrated}}$  maps are illustrated in (c). All values in (d, e) are mean ROI values. ROI are indicated in (a-c).

## 6 Discussion

In tumorous tissues,  $\text{pH}_i$  is known to be typically increased and, thus, has been established as a particularly valuable biomarker for the assessment of cancer. Therefore, a method allowing for non-invasive  $\text{pH}_i$  mapping of tumors in vivo would enable to assess the potential of  $\text{pH}_i$  as a valuable imaging biomarker for cancer diagnosis, treatment planning and monitoring. So far, however, application of CEST-based approaches for quantitative  $\text{pH}_i$  mapping in cancer were prevented due to several simultaneously occurring effects on endogenous CEST signals in tumor tissues, such as concentration changes, other superimposing CEST signals, magnetization transfer contrast (MTC), and spillover dilution (SD). Therefore, in this thesis, a novel method was developed based on the CEST signal of amide and guanidyl protons, i.e. using endogenous CEST signals primarily associated with mobile proteins and peptides within cells, which simultaneously compensates for all aforementioned concomitant effects, thus, enabling for the first time non-invasive, high-resolution, quantitative  $\text{pH}_i$  mapping of tumors in vivo.

### 6.1 Isolation of pH-dependent signal contributions from concomitant effects

All measurements in this thesis were performed using a static magnetic field strength of  $B_0 = 9.4$  T which allows for acquisition of Z-spectra with a high spectral selectivity. This means that the amide and guanidyl CEST signals resonating at frequency offsets of  $\Delta\omega_{amide} \approx 3.6$  and  $\Delta\omega_{gua} \approx 2.0$  ppm relative to the water signal can be distinguished. This spectral separation allows for the extraction of both signals from the background of other magnetization transfer contributions within the acquired Z-spectra.

In order to isolate the pH-dependency of CEST signals from some of the aforementioned concomitant effects, several CEST-MRI-based approaches, e.g. the  $\text{CEST}_{\text{ratio}}$  approach, have already been presented [16, 59–87] which, however, do not enable simultaneous compensation of all effects on CEST signals in cancerous tissues (see listing in chapter 1).

In contrast, the developed method is applicable for mapping  $\text{pH}_i$  of tumors in vivo due to the simultaneous compensation of all aforementioned concomitant effects which was achieved by using a combination of:

1. The spillover-corrected and relaxation-compensated CEST signal, i.e. the inverse magnetization transfer ratio  $\text{MTR}_{\text{Rex}}$  [57, 58, 90, 119], of amide and guanidyl protons (subsection 2.5.4).
2. A linear and Lorentzian fit for separate amide and guanidyl signal extraction from the Z-spectra (subsection 4.4.2).
3. A  $\text{MTR}_{\text{Rex}}$ -based contrast- $B_1$ -correction enabling concentration-independent extraction of exchange rates  $k_{\text{ex}}$ , and thus, pH (subsection 3.4.2).

The  $\text{MTR}_{\text{Rex}}$  contrast metric is a well-established approach which enables to compensate for relaxation properties of the water signal (SD) but also for other magnetization transfer contributions. Therefore, in the following, the compensation of the remaining concomitant effects is discussed.

### 6.1.1 Extraction of pH-dependent signals from Z-spectra

For a quantitative assessment of CEST experiments, the signal extraction from the acquired Z-spectra is the most critical step. In particular, for pH mapping, as the extraction of the pH-dependent amide and guanidyl signals from the Z-spectra depends on the exact values of  $Z_{\text{ref}}$  and  $Z_{\text{lab}}$  determined by the fitting procedure (subsection 4.4.2). Ideally, a perfect fit model would always be able to only extract the pH-dependent CE information from confounding contributions within the Z-spectra (i.e. DS, MTC, rNOE).

In particular, the specific challenge for pH mapping is that the fit model needs to accurately extract the signal over a broad range of pH as well as  $B_1$  values. In this thesis, the reliable extraction of the amide and guanidyl CEST signal was achieved using first order polynomial (i.e. linear) and Lorentzian fits [41, 54, 144]. More specifically, for each the amide and the guanidyl signal, respectively, a separate linear and Lorentzian fit was utilized for signal extraction (subsection 4.4.2 and Figure 5.2). To assess the pH specificity of the extracted signals, the resulting values of  $\text{MTR}_{\text{Rex}}$  were investigated as a function of pH. In lack of a true ground truth of the  $\text{MTR}_{\text{Rex}}$  values, the  $\text{MTR}_{\text{Rex}}(\text{pH})$  curves were used as a kind of ground truth. Remarkably, it was found that the relatively simple fit model reliably extracts the signals across the necessary broad range of pH and

### 6.1 Isolation of pH-dependent signal contributions from concomitant effects

$B_1$  (pH = 6.0 to 8.0 and  $B_1 = 0.6$  to  $1.4 \mu\text{T}$ ), similar to the 3-point method [147], thus, representing a good compromise between accuracy and stability. The accuracy of this approach was verified by the observed symmetry of  $\text{MTR}_{\text{Rex}}(\text{pH})$  resulting from the extracted amide and guanidyl signals (Figure 5.4a and b), in coherence with theory (Figure 3.1c). The stability was shown by the resulting  $k_c$  which were approximately constant over a broad range of  $B_1$  (Figure 5.4c and d). For  $B_1 < 0.6 \mu\text{T}$ , the amide and guanidyl signals were not strong enough resulting in insufficient SNR, whereas for  $B_1 > 1.4 \mu\text{T}$  the peak broadening was too pronounced (equation (2.75)), thus, compromising a reliable fit extraction.

#### Z-spectra fit analysis

To extract the amide and guanidyl signals, also several other approaches were investigated and compared to each other before committing to the proposed separate linear and Lorentzian fit model. Alternatives, which were also tested with various combinations of each other, ranged from:

- Different fit model approaches (e.g. 2nd to 4th order polynomial and Lorentzian fits, or multiple Lorentzian fitting approaches).
- Combined versus separate amide and guanidyl fit models (i.e. combined versus separate fitting procedures).
- 2-step fitting procedures, in which the pH-independent Z-spectra background is fitted in a first step. After background subtraction, the remaining amide and guanidyl signals are isolated using a second fit which e.g. also allows for a regularization process.

However, compared to the separate linear and Lorentzian fit model, none of the above mentioned approaches simultaneously allowed for an accurate and stable signal extraction over the aforementioned necessary broad range of pH and  $B_1$  in porcine brain lysates. In particular, a combined fit model approach using higher order polynomial functions for the background was not stable enough which was most noticeable for either too high or too low pH values, i.e. at  $\text{pH} \leq 6$  for amide and at  $\text{pH} \geq 7.5$  for guanidyl protons, where no distinct amide or guanidyl signals are any longer detectable in the Z-spectra (Figure 5.2).

Interestingly, in the aforementioned pH regions, higher order polynomial functions as well as multiple Lorentzian fitting approaches led to a non-physical and pH-independent

bias, i.e. an overestimation of the  $MTR_{\text{Rex}}(\text{pH})$  values. One possible explanation for this observation is the presence of pH-independent underlying downfield rNOE signals at the frequency offsets of the amide and guanidyl signals. Essentially, the overall exchange rate of the rNOE magnetization transfer pathway is pH-independent [148]. This is due to the relatively slow pH-independent intra molecular spin diffusion in the order of  $\sim (2 - 5)$  Hz [107] acting like the bottle neck of the entire MT pathway of rNOE processes (subsection 2.3.2). Therefore, the aim of the utilized linear function was specifically not to follow the curvature of the DS, but instead to separate the pH-dependent signal contributions at 3.6 and 2.0 ppm from the background of all other confounding, pH-independent contributions (i.e. DS, MTC, rNOE).

Furthermore, apart from the prominent amide and guanidyl signals, another pH-dependent contribution due to fast exchanging amine protons was observed to the Z-spectra of porcine brain lysates at  $\Delta\omega_{\text{amine}} \approx 2.7$  ppm, in coherence with literature [87]. Although the amine signal was too broad to be resolved as a clear peak, it still significantly varied as a function of pH and also  $B_1$  (Figure 5.1a), thus, preventing a combined fit analysis. Importantly, it was found that a separate fit of the amide and guanidyl CEST signal was essential to avoid interfering contributions from the amine signal, i.e. by excluding the frequency range between 2.5 and 2.9 ppm from the fits (Figure 5.2, gray and black lines). Also, it was crucial to use separate fit parameters for fitting of Z-spectra acquired at different  $B_1$  (Table 4.6). This was necessary to account for the different Z-values at different  $B_1$  and the peak broadening with increasing  $B_1$  (cf. squares and stars in Figure 5.2).

### Z-spectra fit model prerequisites for a reliable pH mapping

In summary, to allow for a reliable pH mapping, any utilized fit model must simultaneously satisfy the following prerequisites:

- (i) Extraction of only the pH-dependent signal contributions of the amide and guanidyl CEST signals from the background of all other confounding, pH-independent contributions to the Z-spectra (i.e. DS, MTC, rNOE).
- (ii) Avoidance of the superimposing and interfering pH-dependent amine CEST signal contribution resonating at  $\Delta\omega_{\text{amine}} \approx 2.7$  ppm.
- (iii) Application of specifically tailored fit parameters for fitting of Z-spectra acquired at different  $B_1$ .

Importantly, it was observed that the proposed separate linear and Lorentzian fit model satisfies these requirements. Moreover, compared to the examinations performed in porcine brain lysates, the range of offsets  $\Delta\omega$  included in the fitting procedure for examinations *in vivo* was slightly increased to account for the peak broadening with increasing  $B_1$ . The peak broadening was more pronounced for the amide signal due to its lower exchange rate, in coherence with theory (equation (2.75)). In addition, the applicable offset range for the guanidyl signal was limited on the right side by the DS. Thus, the offset range for the guanidyl signal was only slightly adjusted by 0.1 ppm for the *in vivo* mice examinations at  $B_1 \geq 1 \mu\text{T}$  (cf. Tables 4.6 and 4.7).

#### 6.1.2 Concentration independence

In order to obtain concentration independence, typically, the  $\text{CEST}_{\text{ratio}}$  [59] is utilized which exploits the ratio of the same CEST signal at two different  $B_1$  (subsection 3.4.1). By definition, the  $\text{CEST}_{\text{ratio}}$  is independent of the relative proton fraction ( $f_s$ ) of the examined signal, i.e. concentration-independent. This established ratiometric approach has been employed for  $\text{pH}_i$  mapping using endogenous CEST signals [60, 61], but also for  $\text{pH}_e$  mapping using exogenous contrast agents (CA) [59, 76].

On the contrary, in this thesis, the  $\text{CEST}_{\text{ratio}}$  approach was extended by implementing a contrast- $B_1$ -correction fit model directly based on the  $\text{MTR}_{\text{Rex}}$  theory [57, 58, 90] (subsection 3.4.2). In the used contrast- $B_1$ -correction fit model, the tissue concentration-dependent factor  $f_s$  is compensated by the fit parameter  $a$  and the exchange rate  $k_{\text{ex}}$  is given directly by the fit parameter  $b$  (equation (3.16)). For both, the amide and guanidyl signal separately, this approach was found to be stable over a broad range of pH (Figure 5.3). Importantly, this approach allows for concentration-independent, reliable extraction of  $k_{\text{ex}}$  from CEST data acquired at more than only two  $B_1$  [16, 59]. Altogether, the implemented contrast- $B_1$ -correction fit model allows to increase the accuracy of experimentally determining  $k_{\text{ex}}$  and, thus, pH which is particularly relevant in the presence of noisy data e.g. *in vivo* (Figure 5.11).

To additionally compensate for SD and relaxation effects, the combination of the  $\text{CEST}_{\text{ratio}}$  with the  $\text{MTR}_{\text{Rex}}$  metric has already been proposed, although only using the guanidyl signal [60, 61]. In this thesis, the amide and guanidyl signals were combined to further increase the pH sensitivity (section 3.6). The combination of both the amide and guanidyl signal to enhance the pH sensitivity has already been proposed [64] which, however, in-

volved calculating a difference of both signals. The calculation of a difference between the amide and guanidyl signal is not independent of concentration as each separate signal can originate from different proteins and peptides which may occur in strongly different concentrations depending e.g. on the specific tissue type under investigation. Moreover, methods directly using the amide and amine signals have been proposed [65, 149–151], also incorporating the guanidyl signal to further enhance the pH sensitivity [152]. Nevertheless, these methods have been shown to only reliably measure relative pH values, as opposed to quantitative, i.e. absolute, pH values.

In contrast, the developed method uses the separate, concentration-independent and quantitative calculation of  $\text{pH}_{\text{amide}}$  and  $\text{pH}_{\text{gua}}$ , respectively (section 3.1), followed by a weighted combination of both individually obtained pH maps into a final pH map, i.e.  $\text{pH}_{\text{combi}}$  (section 3.6). In this manner, a broader range of high pH sensitivity was possible ( $\text{pH} = 6.2$  to  $8.0$ ) while simultaneously ensuring concentration independence (Figure 5.8). Regarding the application to pathological tissues, the applied separate fit model for the amide and guanidyl signal is capable of handling relative concentration changes. In particular, as the observed variations in the porcine brain lysate data were much stronger than in the used in vivo tumor model (cf. Figures 5.2 and 5.11a), which is why realistic relative concentration changes can be assumed to be handled by the utilized separate linear and Lorentzian fit model.

## 6.2 A novel model using a single $k_c$ describing one CEST pool

The entire model is based on the finding that the dependency of the exchange rate ( $k_{\text{ex}}$ ) on pH is completely characterized by only one rate constant ( $k_c$ ), i.e. one for amide and one for guanidyl protons at any given fixed temperature (chapter 3). With previous calibration of  $k_c$ , this theoretical framework enables a direct translation of extracted  $k_{\text{ex}}$  into pH, i.e. via  $\text{pH} = \log_{10} \left[ \frac{k_{\text{ex}}}{k_c} \right]$ .

### 6.2.1 Underlying assumptions

The developed method is based on the following assumptions:

- (1) The  $\text{pH}_{\text{combi}}$  measurements in vivo are mostly sensitive to  $\text{pH}_i$ .

- (2) The pH dependencies of the amide and guanidyl CEST pool, respectively, are each completely described by a single  $k_c$ .
- (3) The  $k_c$  of amide and guanidyl protons calibrated in porcine brain lysates are transferable for examinations in vivo.
- (4) The temperature dependency of  $k_c$  and  $k_{ex}$  is negligible compared to other influences in vivo.

### 6.2.2 Sensitivity towards $pH_i$

Regarding assumption (1), it has been demonstrated that endogenous amide and guanidyl signals are primarily associated with mobile proteins and peptides within cells [46, 47, 50, 52, 53], whereas additionally, the guanidyl signal is also related to creatine [39, 40, 54, 55] which is also primarily intracellular. However, other contributions e.g. from the extracellular compartment to the amide and guanidyl signal can not be completely excluded, in particular, in cancer or other pathological tissues with abnormal cellular structures.

### 6.2.3 Describing the amide and guanidyl signals with one $k_c$ each

Regarding assumption (2), currently, it is not yet clear if guanidyl groups in creatine and proteins have different exchange rates. In this thesis, the calibrated  $k_c$  value of the guanidyl signal in creatine model solutions ( $89 \pm 3 \mu\text{Hz}$ ) significantly differed from the  $k_c$  value of the guanidyl signal in porcine brain lysates ( $53.2 \pm 3.7 \mu\text{Hz}$ ), thus, indicating different exchange rates. However, the observed discrepancy of  $k_c$  between porcine brain lysates and creatine model solutions could be explained by the different chemical environments of porcine brain lysates and creatine model solutions leading to different  $pK$  (section 2.6). Regarding the exchange rates of proteins, a weaker increase of the guanidyl signal as a function of  $B_1$  has already been observed in knockout mice with a creatine deficiency [53]. However, the data in [53] only hints towards different guanidyl exchange rates in proteins compared to creatine as no actual quantification of exchange rates was performed. In fact, a dispersion of the underlying exchange rates due to potentially more than one  $k_c$  describing a single CEST pool would affect the accuracy of the developed method.

### Influence of a $k_c$ dispersion | Observed symmetry of $MTR_{\text{Rex}}$

In principle, a dispersion of various exchange processes for one proton species may occur *in vivo*, especially for the guanidyl signal as it exhibits contributions of proteins but also creatine. However, the rather simple approach of assuming only a single  $k_c$  for describing one CEST signal was experimentally validated by the observed symmetry of  $MTR_{\text{Rex}}$  as a function of pH (Figure 5.4a, b), in good coherence with theory (Figure 3.1c). Especially, as both the isolated amide and guanidyl CEST signal showed the expected distinct maximum and, in addition, the resulting  $k_c$  calculated from the position of  $\text{pH}_{\text{max}}$  at various  $B_1$  were approximately constant (Figure 5.4c, d). This unambiguously shows that there is no large dispersion of exchange rates present in either the amide or the guanidyl signal. Therefore, the valid assumption of describing the endogenous amide and guanidyl CEST signal *in vivo* using only a single  $k_c$  is another fundamental finding of this thesis. In particular, as this result was not obtained using simple model solutions but, in fact, using complex *in vivo*-like model suspensions produced from porcine brain lysates. In contrast, a hypothetical dispersion of exchange rates within one CEST signal (i.e. more than only one underlying  $k_c$ ) would lead to more than one  $k_{\text{ex,max}}$  (equation (3.4)) and ultimately would result in more than one maximum of the CEST signal as a function of pH (equation (3.6)) which, however, was not observed in the experimental data (Figure 5.4a and b).

Furthermore, the porcine brain lysates used for the calibration experiments were continuously chilled using ice during preparation and, in addition, examined directly after preparation to ensure that all mobile proteins and peptides as well as metabolites, like creatine, stay intact. Also, from a chemical point of view, this result is in accordance with very early findings of Liepinsh and Otting in 1996 [97] which demonstrated that the guanidyl group of arginine (i.e. the only guanidyl group in proteins and peptides) is inert against catalysts of other amino acid side chain protons.

#### 6.2.4 Transferability of *in vitro*-calibrated $k_c$ for examinations *in vivo*

Regarding assumption (3), in this thesis, porcine brain lysates were employed for calibration of  $k_c$ . Porcine brain lysates have already been shown to reliably mimic the *in vivo* situation in terms of water relaxation properties and observable signals in the Z-spectrum [135] (cf. Figure 5.1a and b with Figure 5.11a). However, the *in vitro* calibration procedure still implies the assumption that  $k_c$  *in vivo* does not depend on (i) further catalytic processes due to surrounding compounds such as buffers or salts, (ii) the mean molecu-

lar size [153], (iii) the mean composition of proteins, i.e. the proteome, or even (iv) the distinct protein folding state [49, 154, 155], which have all been shown to influence the exchange rates.

Regarding (i), it has been demonstrated that the amide and guanidyl signals are not catalyzed by phosphate and do not depend on buffer concentrations [40, 156]. Regarding (ii-iv), porcine brain lysates were specifically utilized in order to mimic the in vivo composition of proteins and peptides as good as experimentally feasible. In particular, the transferability of the in vitro-calibrated  $k_c$  of amide and guanidyl protons for examinations in vivo was supported by the physiologically plausible  $\text{pH}_i$  values of approximately 7.2 found in tumor lesions (Figure 5.12). Remarkably, the determined  $\text{pH}_i$  values were independent of tumor size and in good agreement with tumor  $\text{pH}_i$  values found in literature ranging from 7.1 to 7.6 [19, 20, 25, 27]. The in porcine brain lysates calibrated  $k_c$  of  $3.2 \pm 0.5$  and  $53.2 \pm 3.7$   $\mu\text{Hz}$  for amide and guanidyl protons, respectively, correspond to exchange rates of  $k_{\text{ex}} = 40$  and  $670$  Hz at  $\text{pH} = 7.1$  and  $T = 37^\circ\text{C}$  for amide and guanidyl protons, respectively. The corresponding exchange rates are in good agreement with literature values found in the range of 30 to 280 Hz [31, 40, 46, 58, 105, 112–114] and 600 to 1600 Hz [38, 40, 97, 112]) for amide and guanidyl protons, respectively, further supporting the developed method.

To assess the specificity of detecting  $\text{pH}_i$  in vivo using the developed method, in the future e.g. other treatments or inhalation of  $\text{CO}_2$  inducing an intracellular acidification could be employed as a positive control [149–152, 157], since the used treatment did clearly not work (Figure 5.13b). In particular, as treatments inducing an intracellular acidification of up to 0.48 relative  $\text{pH}$ -values have been demonstrated [150] which, in principle, should be detectable via the  $\text{pH}_{\text{combi}}$  approach showing an  $\text{pH}$  accuracy of around  $\pm 0.2$   $\text{pH}$  units (cf. error bars in gray shaded region of Figure 5.8e).

### 6.2.5 Influence of temperature

Regarding assumption (4), as the developed method relies on the exact value of  $k_c$  and  $k_{\text{ex}}$ , the exponential temperature dependency of the exchange rates [40, 102] is a limitation which has to be taken into account. For  $k_c$ , in particular, the underlying dominantly base-catalyzed exchange rate constant  $k_b(T)$  in equation (3.1) exhibits a exponential temperature dependency which, ultimately, is due to the strong temperature dependency of the corresponding  $\text{p}K$  value (subsection 2.6). Consequently, it is a crucial step that the

## 6 Discussion

calibration of  $k_c$  in vitro and the actual pH mapping in vivo are carried out at the same temperature. Furthermore, the specificity of measuring pH depends on the accuracy of extracting  $k_{ex}$ . In general, an increase of  $k_{ex}$  by a factor of 2 corresponds to an increase of 0.3 pH units, as  $\log_{10}(2) \approx 0.3$ . Regarding the increase of  $k_{ex}$  due to temperature, for guanidyl protons a doubling of  $k_{ex}$  was observed for a temperature increase of approximately 6°C in [40].

In this thesis, all in vitro and in vivo examinations were stabilized at  $T = 37.0 \pm 0.2^\circ\text{C}$ . Estimated from [40], the temperature uncertainty of 0.2°C results in a pH uncertainty of approximately  $\pm 0.01$  pH units for guanidyl protons which is negligible in comparison to the observed  $\text{pH}_{\text{combi}}$  uncertainty of  $\pm 0.2$  pH units (Figure 5.8e). Also estimated from [40], the observed  $\text{pH}_{\text{combi}}$  uncertainty of  $\pm 0.2$  pH units corresponds to a temperature uncertainty of approximately 4°C. Thus, any realistic temperature variations across e.g. a tumor ROI in vivo are negligible compared to the overall  $\text{pH}_{\text{combi}}$  measurement uncertainties. Nevertheless, as the in vivo temperature was measured using a rectal temperature sensor, the actual temperature inside the tumor lesions might systematically differ. For this reason, any potential systematic temperature differences were reduced by using warm air blown into the small animal imaging chamber instead of a heating pad, which enabled a more homogeneous temperature profile across the tumor lesions.

The developed method can also be used at different temperatures. However, in such a case the respective  $k_c$  have to be newly calibrated at the desired temperature. Additionally, in principle, the developed method could also be used for non-invasive mapping of temperature, specifically, due to the exponential temperature dependency of  $k_{ex}$ . Although, for a reliable temperature measurement a significantly higher accuracy for experimental determination of  $k_{ex}$  would be required.

### 6.2.6 The sensitivity of the $\text{pH}_{\text{combi}}$ approach

It was found, that the derivative of the  $\text{CEST}_{\text{ratio}}$  as a function of pH (Figure 3.4a) represents the pH sensitivity which also can be employed for determination of reliable weightings  $w_{\text{amide}}$  and  $w_{\text{gua}}$  for the proposed  $\text{pH}_{\text{combi}}$  approach (section 3.6). Remarkably, the  $\text{pH}_{\text{combi}}$  approach even enabled reliable measurement of pH in regions where neither  $\text{pH}_{\text{amide}}$ , nor  $\text{pH}_{\text{gua}}$  could reliably measure pH, i.e. at around  $\text{pH}_{\text{titrated}} = 7.3$  (Figure 5.8 e), which is an especially important pH range as it is relevant in vivo. Ultimately, the robustness and reliability of the  $\text{pH}_{\text{combi}}$  approach can be attributed to the suitable exchange

rate regimes of amide and guanidyl protons under physiological conditions (i.e. exchange rates in the slow to intermediate exchange regime yielding measurable  $k_{ex}$ ).

The pH sensitivity of the developed method relies on the extracted  $k_{ex}$  which is achieved using several post processing steps (subsection 4.4.2). In principle, a higher pH sensitivity could be obtained by directly using the isolated  $MTR_{Rex}$  signal amplitude strength. However, although  $MTR_{Rex}$  has a distinct dependency on pH (Figure 3.1b), pH can not be determined from the value of  $MTR_{Rex}$  at only one  $B_1$  because the amplitude of  $MTR_{Rex}$  (equation (3.10)) is scaled by the tissue-specific value of  $f_s/R_{1w}$ . This is the reason why the actual  $MTR_{Rex}$  amplitude can not be translated directly into a pH sensitivity although the amplitude itself strongly depends on pH. Moreover, as determined in section 3.5, the pH sensitivity of the amide and guanidyl signals is represented by the slope and range of their corresponding  $CEST_{ratio}$  which, importantly, is independent of the absolute  $MTR_{Rex}$  signal strength. The value of the  $CEST_{ratio}(pH)$  depends on the relative change of  $MTR_{Rex}(pH)$  with varying  $B_1$  at a fixed pH (i.e. the  $B_1$ -dispersion at each pH). This explains, why the amide CEST signal exhibits a low pH sensitivity at e.g.  $pH = 7.0$  even though the amide CEST signal itself is significantly pronounced enough for a reliable isolation and calculation of  $MTR_{Rex}$  (Figure 5.4a).

### 6.2.7 Further applications

The novel calibration method for  $k_c$  determined in this thesis (equation (3.7)) can, in principle, equally well be applied to dominantly acid-catalyzed exchange processes. In fact, the method can even be applied to a combination of acid- and base-catalyzed exchange processes which, however, would result in two distinct maxima of  $MTR_{Rex}$  as a function of pH. By acquisition of just a single- $B_1$   $MTR_{Rex}$  image of a multi-pH phantom, the developed approach enables a stable and accurate, complete characterization of the pH dependency of exchange processes. In principle, this enables a high implementation rate for sample quantification which is of interest for the investigation of e.g. exchange processes under various molecular environments. In particular, this procedure could e.g. be utilized for the design of novel paraCEST agents [158].

Importantly, the developed method is not limited to examinations in tumors only, but can as well be employed for investigations of e.g. stroke, neurodegenerative diseases, or any sort of other pathologies showing alterations in  $pH_i$ .

## 6.3 Remaining challenges

### Further $B_1$ optimization for an enhanced pH sensitivity

In this thesis, *in vivo* Z-spectra were acquired at  $B_1 = 0.6, 1.0$  and  $1.4 \mu\text{T}$ , respectively, to exploit the whole range of experimentally feasible  $B_1$  while simultaneously reducing the total acquisition time of *in vivo* examinations. Acquisition of data at even more  $B_1$  would lead to a more reliable extraction of  $k_{\text{ex}}$  and, thus, pH as the labeling efficiency  $\alpha(B_1)$  would be sampled at more  $B_1$  (Figure 3.2). The longer acquisition time due to the acquisition of Z-spectra at more  $B_1$  could be compensated by omitting frequency offsets which are not needed for a reliable extraction of  $k_{\text{ex}}$ . Additionally, due to the different exchange rates of amide and guanidyl protons under physiological conditions (i.e.  $\text{pH} \approx 7.2$ ), the used  $B_1$  could be further optimized so that  $\alpha(B_1)$  of each proton species is sampled at the respective interesting  $B_1$  regions.

Importantly, in general the entire experimentally feasible  $B_1$  range should be exploited for extraction of  $k_{\text{ex}}$ . However, for amide protons particularly, more data should be acquired using lower  $B_1$  (e.g.  $0.6 \leq B_1 \leq 1.0$ ), as the labeling efficiency  $\alpha$  of amide protons under physiological conditions reaches FS (i.e.  $\alpha = 1$ ) already at around  $B_1 \approx 1 \mu\text{T}$  (Figure 5.3c, green stars). Therefore, the relevant pH-dependent information of  $\alpha(B_1)$  for amide proton exchange rates under physiological conditions lies more towards the lower  $B_1$  end (Figure 3.2, in between yellow and green line). In contrast, for guanidyl protons, more data should be acquired using the entire experimentally feasible  $B_1$  range, as the FS limit is not reached for guanidyl proton exchange rates under physiological conditions. Essentially this would allow for a more precise sampling of the  $\alpha(B_1)$  curve in those  $B_1$  regions which are more sensitive to the respective exchange rates of each protons species.

### Enhanced calibration of $k_c$

For calibration of  $k_c$ , porcine brain lysate samples with values of  $\text{pH}_{\text{titrated}} > 8$  could be included. In particular, this would allow for a more stable  $\text{pH}_{\text{max}}$  fitting procedure of  $\text{MTR}_{\text{Rex}}(\text{amide})$  and, consequently, an enhanced calibration of  $k_c$  for amide protons (Figure 5.4a). Moreover, instead of fitting  $\text{pH}_{\text{max}}$  for multiple  $B_1$  separately, the  $B_1$  dependency of  $\text{pH}_{\text{max}}$  (equation (3.6)) can be used to simultaneously fit the pH and the  $B_1$  dimension, i.e. via a 2D fit. This should further increase the accuracy of calibrating  $k_c$ .

### Reduction of motion-induced artifacts

It was observed that inevitable abdominal motion due to breathing of the mice led to significant artifacts in the Z-spectra. This was due to the utilized tumor model in which the xenograft tumors are injected subcutaneously into the right flank of the mice. In the future, further reduction of motion-induced artifacts can be achieved by using the developed method in combination with respiratory gating. For pulsed saturations, in particular, respiratory gating allows for an MR image acquisition only during the exhaled breathing state, and consequently, compensation of respiratory motion during examinations. Also, other tumor models which are not situated in the abdominal region but e.g. in the brain could be investigated where significantly less motion occurs.

In this thesis, all image acquisition was performed using 2D readouts. However, the method can also be used for volumetric mapping of  $\text{pH}_i$  by using a 3D image readout after presaturation. Using a 3D image acquisition would allow for image co-registration during post processing [45, 159] and, thus, more reliable  $\text{pH}_i$  mapping.

### Influence of $R_{2s}$

In this thesis, a fixed value of  $R_{2s} = 100$  Hz was used for the determination of  $k_{\text{ex}}$  of both the amide and guanidyl signal, which is in agreement with the broad range of values found in literature ranging from  $R_{2s} = 0$  to 120 Hz [57, 58, 61, 74, 90, 125, 126]. For the determination of  $\text{pH}_{\text{gua}}$ , the used fixed value of  $R_{2s}$  does not have a large influence, as  $k_{\text{ex}}(\text{gua}) \gg R_{2s}$ . In contrast, for the determination of  $\text{pH}_{\text{amide}}$ , the used value of  $R_{2s}$  has a stronger influence as the  $k_{\text{ex}}$  of amide protons is in the order of  $R_{2s}$ . Therefore, a more accurate  $R_{2s}$  would result in a more accurate  $\text{pH}_{\text{combi}}$  mapping, in particular, due to the more accurate calculation of  $\text{pH}_{\text{amide}}$ . In principle,  $R_{2s}$  can be experimentally determined from a fit of multi-pH  $\text{MTR}_{\text{Rex}}$  data via equation (3.13). However, due to the large fit uncertainty of determining  $\Gamma$  (equation (3.11)) from  $\text{MTR}_{\text{Rex}}(\text{pH})$  (equation (3.9)) this was not experimentally feasible.

### Calibration in vivo using $^{31}\text{P}$ -MRSI

In the future, the calibration carried out in porcine brain lysates can be directly validated in vivo by correlating the  $\text{pH}_{\text{combi}}$  maps with well established  $^{31}\text{P}$ -MRSI  $\text{pH}_i$  imaging methods [26, 27, 65, 160]. This would also allow for assessing the specificity of  $\text{pH}_{\text{combi}}$

towards  $\text{pH}_i$ , as  $^{31}\text{P}$ -MRSI, in principle, can discriminate between  $\text{pH}_e$  and  $\text{pH}_i$  [27].

## 6.4 Towards application in humans

The successful application to in vivo tumor models was an important milestone towards the application in humans, where the developed method, in principle, can equally well be applied. For CEST-MRI examinations in humans, a pulsed presaturation is a prerequisite due to patient safety and hardware limitations. Consequently, the demonstrated applicability of using a pulsed presaturation for  $\text{pH}_{\text{gua}}$  mapping in creatine model solutions further supports the translation of the developed method to whole-body MR scanners and, thus, the prospective application in humans.

### 6.4.1 Further evaluation of using a pulsed presaturation

In creatine model solutions, the pulse shape of the presaturation ( $c_2$ ) was identified as a new parameter to shift the pH sensitivity of  $\text{pH}_{\text{gua}}$  to higher pH values (Figure 5.17), in coherence with theory (Figure 3.3d). This indicates that  $c_2$  introduces a new possibility of shifting the pH sensitivity to higher pH without relevant interfering peak broadening (Figure 5.15b). In contrast, shifting the pH sensitivity by increasing  $B_{1,\text{high}}$  is impracticable for applications in vivo due to excessive peak broadening (equation (2.75)) resulting in an impeded reliable extraction of the guanidyl signal from other superimposing signals in the in vivo Z-spectrum.

However, it should be examined if the pH sensitivity shift really is due to the decreasing  $c_2$  at a constant  $\overline{B}_1$  (equation (4.2)) or maybe just due to a potentially increased effective  $B_1$  (i.e. FA equivalent  $B_1$ ). Thus, the effect of the same effective  $B_1$  using a cw and pulsed presaturation should be further investigated. In addition, the peak broadening with increasing  $\overline{B}_1$  versus decreasing  $c_2$  should be investigated under in vivo-like conditions, i.e. using porcine brain lysates. This can be achieved by choosing two different  $c_2$  exhibiting (i) an identical effective  $B_1$  and (ii) an identical effective DC. Adjustment of the effective  $B_1$  (i) can be accomplished by variation of the  $B_1$  amplitude and  $c_2$  (i.e. via  $B_1/c_2$ , subsection 3.2). Adjustment of the effective DC (ii) can be accomplished by variation of the delay time  $t_d$  and  $c_1$ . By comparing the Z-spectra acquired in such a manner, the experimental feasibility of the pulsed method for prospective examinations in humans can be further assessed.

Furthermore, different  $c_2$  could be used for data acquisition at different  $B_1$ , or for the amide and guanidyl signal sampling in the Z-spectra (e.g. pulsed for guanidyl and cw for amide protons) to enhance the pH specificity of each proton species in the physiologically relevant range.

## 6.4.2 pH<sub>i</sub> mapping in humans

### Spectral resolution at lower magnetic fields

Although the developed method is, in principle, independent of  $B_0$ , it exploits the high spectral selectivity of the amide and guanidyl CEST signals at  $B_0 = 9.4$  T. Regarding the pH sensitivity of the CEST signals, there is no dependency on  $B_0$  from theory. However, the proposed fit model does not aim at following the curvature of the DS, but rather to separate the selective pH-dependent resonances at 3.6 and 2.0 ppm from the background of all other contributions to the Z-spectra (i.e. DS, CE, rNOE, MTC). Thus, the major limiting factor for the translation of the proposed method to lower magnetic fields is the spectral resolution required to reliably extract the amide and guanidyl signal from the background of superimposing signals in the Z-spectrum. Also, at lower magnetic field strength the DS broadens and overlaps even more with the guanidyl signal and maybe also with the amide signal, further impeding a straightforward translation.

However, at  $B_0 = 7$  T, in vivo Z-spectra still exhibit clear resonances of the amide and guanidyl signal allowing for a reliable signal extraction which, therefore, should also offer the potential of pH<sub>i</sub> mapping using the developed method. In contrast, at  $B_0 = 3$  T, the required spectral resolution will most likely not be sufficient [161]. Thus, the expected limit is  $B_0 = 7$  T which, importantly, is by now also approved for clinical use. Nevertheless, most likely also the fit parameters will have to be adjusted in order to account for the respective spectral widths of the amide and guanidyl signals at  $B_0 = 7$  T.

### steady-state CEST-MRI using a reduced presaturation time

In the future, the acquisition time can be reduced e.g. by incorporating methods allowing for a steady-state CEST-MRI using a reduced  $t_{sat}$  [162–165]. In particular, this would enable a quantitative evaluation procedure of CEST signals and, thus, pH<sub>i</sub> mapping while simultaneously allowing for an improved clinical applicability.



## 7 Summary and Conclusion

In principle, chemical exchange saturation transfer (CEST) magnetic resonance imaging (MRI) enables mapping of intracellular pH ( $\text{pH}_i$ ), which is a particularly valuable biomarker for the assessment of cancer as  $\text{pH}_i$  is typically increased in tumors. However, so far, the application of CEST-based  $\text{pH}_i$  mapping in cancerous tissue was prevented by concomitant effects such as intrinsically unknown concentration changes, other superimposing CEST signals, magnetization transfer contrast (MTC), and spillover dilution (SD), which can all strongly vary in an unpredictable manner in tumors. For this purpose, in this thesis, a novel method was developed based on the spillover-corrected and relaxation-compensated CEST signal ( $\text{MTR}_{\text{Rex}}$ ) of amide and guanidyl protons, i.e. using endogenous CEST signals primarily associated with mobile proteins and peptides within cells, which simultaneously compensates for all aforementioned concomitant effects, thus, enabling for the first time non-invasive, high-resolution, quantitative  $\text{pH}_i$  mapping of tumors in vivo.

To this end, a novel model was developed which is based on the finding that the dependency of the magnetization transfer exchange rate ( $k_{\text{ex}}$ ) on pH is completely characterized by only one rate constant ( $k_c$ ), i.e. for amide and guanidyl protons at any given fixed temperature (e.g.  $37^\circ\text{C}$  in vivo). This theoretical framework enabled a direct translation of extracted  $k_{\text{ex}}$  into pH, i.e. via  $\text{pH} = \log_{10} \left[ \frac{k_{\text{ex}}}{k_c} \right]$  with previous calibration of  $k_c$ . By analytically examining  $\text{MTR}_{\text{Rex}}$  as a function of pH, it was determined that  $\text{MTR}_{\text{Rex}}(\text{pH})$  has a symmetric shape with a well-defined amplitude and full width at half maximum (FWHM), which is a fundamental finding of this thesis yielding further insights into the nature of CEST. Furthermore, it was identified that the position of the maximum ( $\text{pH}_{\text{max}}$ ) of  $\text{MTR}_{\text{Rex}}(\text{pH})$  allows for a calibration of  $k_c$  in vitro. Remarkably, it was found that  $\text{pH}_{\text{max}}$  is completely independent of tissue specific parameters and only depends on the effective RF amplitude ( $B_1$ ) determined by the experimenter. In this context, it was recognized that the intrinsically different  $k_c$  of amide and guanidyl protons inevitably result in different ranges of high pH sensitivity. Consequently, the individually obtained pH maps ( $\text{pH}_{\text{amide}}$  and  $\text{pH}_{\text{gua}}$ ) were combined into a final pH map ( $\text{pH}_{\text{combi}}$ ) using a weighted combination

## 7 Summary and Conclusion

approach based on the theoretical relative pH sensitivity of each signal ( $w_{amide}$  and  $w_{gua}$ ). The robustness and reliability of  $pH_{combi}$  could be attributed to the suitable exchange rate regimes of amide and guanidyl protons under physiological conditions, i.e. the slow to intermediate exchange regime yielding measurable  $k_{ex}$ . Moreover, by extending the pH mapping theory to a pulsed presaturation, it was identified that the pH sensitivity can be tuned by variation of the presaturation pulse shape ( $c_2$ ), which is particularly interesting for prospective examinations in humans where a pulsed presaturation is a prerequisite due to patient safety.

In order to demonstrate the applicability of the developed method under in vivo-like conditions, porcine brain lysates exhibiting in vivo-like Z-spectra, i.e. comparatively small CEST signals and large MTC, were investigated at various titrated pH values ( $pH_{titrated}$ ) and tissue concentrations. Within the scope of this thesis, a custom-built CEST pulse sequence was implemented on the 9.4 T small animal MR scanner situated at the DKFZ in Heidelberg which was used to perform all measurements. In porcine brain lysates, an extensive optimization of the acquisition protocol, fitting and processing procedure enabled a robust and reliable extraction of the pH-dependent amide and guanidyl signals from the background, which was achieved using linear and Lorentzian fits and was stable over a broad range of pH and  $B_1$  ( $pH = 6.0$  to  $8.0$  and  $B_1 = 0.5$  to  $1.5 \mu T$ ). The rather simple approach of assuming a single  $k_c$  for one CEST signal was validated by the observed symmetry of the  $MTR_{Rex}(pH)$  curves obtained from data at multiple pH and  $B_1$  showing one distinct maximum as a function of pH, in coherence with theory. In particular, this finding implied translatability for application in vivo, as it was obtained using complex model suspensions mimicking the in vivo composition of proteins and peptides. Utilizing the extracted  $MTR_{Rex}(pH, B_1)$  values, the calibration of  $k_c$  yielded a value of  $3.2 \pm 0.5$  and  $53.2 \pm 3.7 \mu Hz$  for the amide and the guanidyl signal, respectively.

Having performed the calibration of the amide and guanidyl signals in porcine brain lysates, concentration-independent pH mapping was accomplished for each signal individually ( $pH_{amide}$  and  $pH_{gua}$ ) by experimental determination of  $k_{ex}$ . In this thesis, a contrast- $B_1$ -correction fit model based on the  $MTR_{Rex}$  theory was implemented, which allowed for concentration-independent determination of  $k_{ex}$  with data acquired at more than two  $B_1$ . This approach was found to be crucial to increase the accuracy of experimental determination of  $k_{ex}$ , and therefore pH, especially in the case of noisy data in vivo. In coherence with theory, a good signal correlation was observed for  $pH_{amide}$  and  $pH_{gua}$

in the range of  $\text{pH}_{\text{titrated}} = 7.3$  to  $8.0$  and  $6.2$  to  $7.3$ , respectively. To enable a reliable pH measurement over a broader range of physiologically relevant pH values, the individually acquired  $\text{pH}_{\text{amide}}$  and  $\text{pH}_{\text{gua}}$  maps were combined into  $\text{pH}_{\text{combi}}$  using  $w_{\text{amide}}$  and  $w_{\text{gua}}$ . In this manner, calculation of  $\text{pH}_{\text{combi}}$  in porcine brain lysates allowed for a robust and reliable pH mapping in the physiologically relevant range of  $\text{pH}_{\text{titrated}} = 6.2$  to  $8.0$ . Remarkably, the employed  $w_{\text{amide}}$  and  $w_{\text{gua}}$  also enabled reliable  $\text{pH}_{\text{combi}}$  measurements around  $\text{pH} \approx 7.3$ , where neither  $\text{pH}_{\text{amide}}$  nor  $\text{pH}_{\text{gua}}$  individually were particularly sensitive and which, importantly, is an especially relevant pH range in vivo.

In order to demonstrate the applicability in vivo, tumor-bearing mice were investigated. Therefore, the calibrated  $k_c$  and weightings found in porcine brain lysates were assumed to be transferable for examinations in vivo. With the insights obtained from examinations in porcine brain lysates, the experimental setup, acquisition protocol and fit models were slightly optimized to also enable a robust and reliable  $\text{pH}_{\text{combi}}$  mapping in vivo. Using the optimized setup,  $n = 19$  examinations of tumor-bearing mice at  $B_0 = 9.4$  T yielded a physiologically plausible median  $\text{pH}_i$  of approximately  $7.2$  inside tumor lesions, independent of tumor size and in good agreement with tumor  $\text{pH}_i$  values found in literature. The physiologically plausible  $\text{pH}_i$  values supported the transfer of the in vitro-calibrated  $k_c$  and theoretically derived  $\text{pH}_{\text{combi}}$  weightings. In addition, in order to assess whether the developed  $\text{pH}_{\text{combi}}$  mapping method can detect a change of  $\text{pH}_i$  in vivo, the tumor lesions of  $n = 3$  treated and  $n = 3$  control mice were investigated. The idea of the treatment was to stop tumor growth by specifically inducing a significant decrease of  $\text{pH}_i$  in the tumor cells. The used treatment was not effective which was clearly indicated by the approximately same tumor growth of the treatment and control group. Interestingly, in coherence with the failed treatment, the  $\text{pH}_{\text{combi}}$  tumor region of interest (ROI) analysis detected no significant changes in  $\text{pH}_i$ , thus highlighting the applicability of the developed method for relevant investigations in vivo.

In an effort towards translating the developed method for examinations in humans, creatine model solutions, representing a simple model system for the guanidyl signal, were investigated at various  $\text{pH}_{\text{titrated}}$  using a pulsed presaturation scheme with various  $c_2$ . In creatine model solutions, a shift in the pH sensitivity of  $\text{pH}_{\text{gua}}$  towards higher pH was observed for decreasing  $c_2$ , i.e. sharper presaturation pulses, in coherence with theory. In particular, applicability of the pulsed pH mapping method was demonstrated for  $c_2 = 0.42$  which, by shifting the  $\text{pH}_{\text{gua}}$  sensitivity to the physiological pH range, enabled reliable

## 7 Summary and Conclusion

calculation of  $\text{pH}_{\text{gua}}$  maps in the range of  $\text{pH}_{\text{titrated}} = 6.5$  to  $7.5$  without the need for  $\text{pH}_{\text{amide}}$ . These preliminary findings using a pulsed presaturation support the translatability of the developed method to whole-body MR scanners and, consequently, the prospective application in humans.

Altogether, the developed method now allows assessing the potential of  $\text{pH}_i$  as a valuable imaging biomarker for cancer diagnosis, treatment planning and monitoring, respectively. In fact, the approach is not only restricted to applications in tumors but, in principle, can also be applied for the investigation of other pathologies showing alterations in  $\text{pH}_i$ , e.g. stroke or neurodegenerative diseases, in which it might provide further physiological insights.

# A Appendix

## A.1 Measurement of labile proton fraction $f_s$

### A.1.1 Quantification for one CEST pool

As established in section 3.3, for a fixed  $R_{2s}$  and by additionally acquiring a  $T_1$  map<sup>1</sup> (i.e.  $T_{1w} = R_{1w}^{-1}$ ), one can experimentally determine the labile proton fraction  $f_s$  of the amide or guanidyl signal from the fit parameters of the amplitude and FWHM of  $MTR_{\text{Rex}}$  as a function of pH (i.e. via  $A$  and  $\Gamma$  in equation (3.12)). However, calculation of  $f_s$  via equation (3.12) can only be performed in model suspensions or solutions with well-known  $\text{pH}_{\text{titrated}}$  values (i.e. only feasible in multi-pH phantoms).

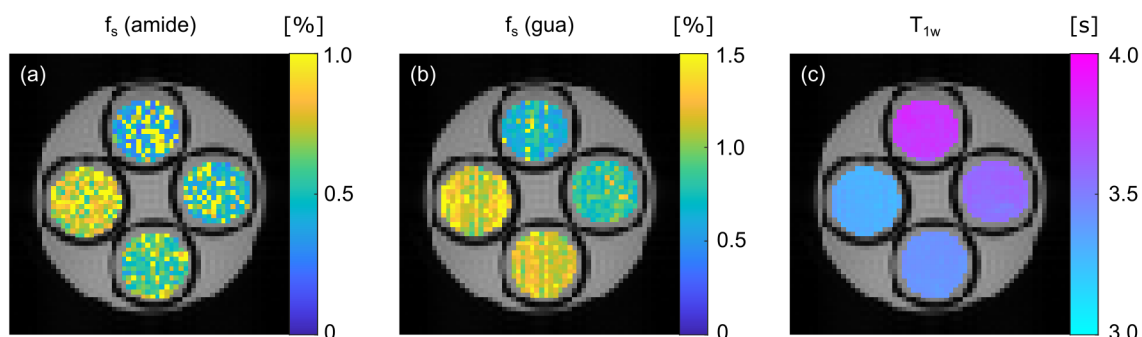


**Figure A.1:** Measurement of the labile proton fraction ( $f_s$ ) for the amide and guanidyl CEST signal in porcine brain lysates at various tissue concentrations ( $C_{\text{tissue}}$ ) with a fixed pH of  $\text{pH}_{\text{titrated}} = 7$  (a and b, respectively). An additional acquisition of a  $T_1$  map of the water signal (c) enables calculation of  $f_s$  via equation (A.1). For clockwise increasing  $C_{\text{tissue}}$ , an increasing  $f_s$  of the amide as well as guanidyl signal is observed, whereas  $T_1$  of water decreases (values of  $C_{\text{tissue}}$  are illustrated in Figures 5.6b and 5.8b, respectively).

<sup>1</sup> For instance, via a saturation recovery or inversion recovery sequence.

## A Appendix

Alternatively,  $f_s$  can also be experimentally determined via

$$f_s = MTR_{Rex} \cdot R_{1w} \cdot \frac{(\gamma B_1)^2 + k_{ex}(k_{ex} + R_{2s}) \cdot c_2^2}{DC \cdot c_1 \cdot k_{ex} \cdot (\gamma B_1)^2}. \quad (\text{A.1})$$

Again,  $MTR_{Rex}$  refers to either the amide or the guanidyl CEST signal. Remarkably, equation (A.1) enables calculation of  $f_s$  without the need for various well-known  $\text{pH}_{\text{titrated}}$  values (Figure A.1a and b). The more robust measurement of  $f_s(\text{gua})$  compared to  $f_s(\text{amide})$  (cf. Figure A.1b with a) is due the higher pH sensitivity of the guanidyl signal compared to the amide signal at  $\text{pH} = 7$  (Figures 3.4a and 5.5e, f) enabling a more robust extraction of  $k_{ex}(\text{gua})$  compared to  $k_{ex}(\text{amide})$  at  $\text{pH} = 7$  (cf. Figure 5.5d with c).

### A.1.2 Ratio between two CEST pools

Moreover, the ratio between the labile proton fraction of amide and guanidyl protons can be calculated without the need for an additionally acquired  $T_1$  map via

$$\frac{f_s(\text{amide})}{f_s(\text{gua})} = \frac{MTR_{Rex}(\text{amide})}{MTR_{Rex}(\text{gua})} \cdot \frac{k_{ex}(\text{gua})}{k_{ex}(\text{amide})} \cdot \frac{(\gamma B_1)^2 + k_{ex}(\text{amide}) \cdot (k_{ex}(\text{amide}) + R_{2s}(\text{amide})) \cdot c_2^2}{(\gamma B_1)^2 + k_{ex}(\text{gua}) \cdot (k_{ex}(\text{gua}) + R_{2s}(\text{gua})) \cdot c_2^2}. \quad (\text{A.2})$$

## A.2 Complete lists of frequency offsets for sampling of Z-spectra

All presaturation frequency offsets  $\Delta\omega$  are presented in the unit [ppm]. For Z-spectra normalization, two  $M_0$  images were acquired at -300 ppm (i.e. one at the beginning and one at the end of each scan).

- **Porcine brain lysates**

Session 1,  $\#\Delta\omega = 92$  (+2  $M_0$ ):

(-300), 100, 75, 50, 30, 17, 10, 7, 6, 5.3, 4.9, 4.6, 4.4, 4.3, 4.2, 4.1, 4, 3.9, 3.8, 3.75, 3.7, 3.65, 3.6, 3.55, 3.5, 3.45, 3.4, 3.3, 3.2, 3.1, 3, 2.9, 2.85, 2.8, 2.75, 2.7, 2.65, 2.6, 2.55, 2.5, 2.4, 2.3, 2.2, 2.15, 2.1, 2.05, 2, 1.95, 1.9, 1.85, 1.8, 1.7, 1.6, 1.5, 1.4, 1.3, 1.2, 1.1, 1, 0.9, 0.8, 0.7, 0.6, 0.5, 0.4, 0.3, 0.2, 0.1, 0.05, 0, -0.05, -0.1, -0.2, -0.4, -0.6, -0.9, -1.2, -1.5, -1.8, -2.3, -2.8, -3.5, -4.2, -4.9, -5.6, -6.3, -7, -10, -17, -30, -50, -75, -100, (-300).

### A.3 Complete lists of simulation parameters used in Figures

Session 2,  $\#\Delta\omega = 48$  ( $+2 M_0$ ):

(-300), 10, 6, 4.6, 4.4, 4.2, 4, 3.9, 3.8, 3.75, 3.7, 3.65, 3.6, 3.55, 3.5, 3.45, 3.4, 3.3, 3.2, 3, 2.9, 2.7, 2.5, 2.4, 2.3, 2.2, 2.15, 2.1, 2.05, 2, 1.95, 1.9, 1.85, 1.8, 1.7, 1.6, 1.5, 1.3, 1.1, 1, 0.8, 0.6, 0.4, 0.2, 0.1, 0, -0.1, -0.2, -0.4, (-300).

Session 3,  $\#\Delta\omega = 58$  ( $+2 M_0$ ):

(-300), 10, 9, 8, 7, 6, 5.5, 5, 4.6, 4.4, 4.2, 4, 3.9, 3.8, 3.75, 3.7, 3.65, 3.6, 3.55, 3.5, 3.45, 3.4, 3.3, 3.2, 3.1, 3, 2.9, 2.8, 2.7, 2.6, 2.5, 2.4, 2.3, 2.2, 2.15, 2.1, 2.05, 2, 1.95, 1.9, 1.85, 1.8, 1.7, 1.6, 1.5, 1.4, 1.3, 1.2, 1.1, 1, 0.8, 0.6, 0.4, 0.2, 0.1, 0, -0.1, -0.2, -0.4, (-300).

- **Tumor-bearing mice**,  $\#\Delta\omega = 42$  ( $+2 M_0$ ):

(-300), 10, 8.5, 7, 6, 5.5, 5, 4.6, 4.3, 4.1, 4, 3.9, 3.8, 3.7, 3.6, 3.5, 3.4, 3.3, 3.2, 3.1, 2.9, 2.7, 2.5, 2.4, 2.3, 2.2, 2.1, 2, 1.9, 1.8, 1.7, 1.6, 1.5, 1.4, 1.3, 1.2, 1.1, 1, 0.9, 0.7, 0.5, 0.3, 0.1, (-300).

- **Creatine model solutions**,  $\#\Delta\omega = 82$  ( $+2 M_0$ ):

(-300), 7, 6, 5, 4.5, 4, 3.5, 3, 2.9, 2.8, 2.7, 2.6, 2.5, 2.4, 2.3, 2.2, 2.15, 2.1, 2.025, 2.05, 2.075, 2, 1.975, 1.95, 1.925, 1.9, 1.85, 1.8, 1.7, 1.6, 1.5, 1.4, 1.3, 1.2, 1.1, 1, 0.9, 0.8, 0.7, 0.6, 0.5, 0.4, 0.3, 0.2, 0.175, 0.15, 0.125, 0.1, 0.075, 0.05, 0.025, 0, -0.025, -0.05, -0.075, -0.1, -0.125, -0.15, -0.175, -0.2, -0.3, -0.4, -0.5, -0.6, -0.7, -0.8, -0.9, -1, -1.2, -1.4, -1.6, -1.8, -2, -2.25, -2.5, -2.75, -3, -3.5, -4, -4.5, -5, -6, -7, (-300).

- **All WASABI measurements**,  $\#\Delta\omega = 25$  ( $+2 M_0$ ):

(-300), 1.2, 1.1, 1.0, 0.9, 0.8, 0.7, 0.6, 0.5, 0.4, 0.3, 0.2, 0.1, 0, -0.1, -0.2, -0.3, -0.4, -0.5, -0.6, -0.7, -0.8, -0.9, -1.0, -1.1, -1.2, (-300).

## A.3 Complete lists of simulation parameters used in Figures

All simulation parameters other than those explicitly stated in the Figure captions, legends or unambiguously assigned anywhere else within the Figures are specified in the following.

**Figure 3.1:**

$$k_c = 30 \mu\text{Hz},$$

$$B_1 = 1 \mu\text{T},$$

$$R_{2s} = 0 \text{ Hz},$$

$$R_{1w} = 1 \text{ Hz},$$

$$f_s = 0.018,$$

$$\text{DC} = c_1 = c_2 = 1.$$

**Figure 3.4:**

$$k_c(\textit{amide}) = 3.2 \mu\text{Hz},$$

$$k_c(\textit{gua}) = 53.2 \mu\text{Hz},$$

$$B_{1,\textit{high}}(\textit{amide}) = B_{1,\textit{high}}(\textit{gua}) = 1.4 \mu\text{T},$$

$$B_{1,\textit{low}}(\textit{amide}) = B_{1,\textit{low}}(\textit{gua}) = 0.6 \mu\text{T},$$

$$R_{2s}(\textit{amide}) = R_{2s}(\textit{gua}) = 100 \text{ Hz},$$

$$\text{DC} = c_1 = c_2 = 1.$$

**Figure 5.5a-d, black lines:**

$$k_c(\textit{amide}) = 3.2 \mu\text{Hz},$$

$$k_c(\textit{gua}) = 53.2 \mu\text{Hz},$$

$$R_{2s}(\textit{amide}) = R_{2s}(\textit{gua}) = 100 \text{ Hz},$$

$$c_2 = 1.$$

# List of Figures

2.1	Zeeman energy level splitting in a static magnetic field . . . . .	9
2.2	Rotating frame of reference and effective magnetic field ( $\vec{B}_{eff}$ ) . . . . .	14
2.3	Fourier transform of the free induction decay (FID) . . . . .	18
2.4	$^1\text{H}$ NMR spectrum of the human brain at $B_0 = 7$ T and chemical shift (CS) [96] . . . . .	19
2.5	Exchange rates $k_{ex}$ of various functional groups as function of pH [101] .	27
2.6	Exchange-relayed nuclear Overhauser effect (rNOE) and semi-solid magnetization transfer (ssMT) [30] . . . . .	29
2.7	The CEST-MRI data set [58] . . . . .	32
2.8	The in vivo Z-spectrum . . . . .	33
2.9	The cw and pulsed CEST pulse sequences . . . . .	35
2.10	Two-pool model . . . . .	37
3.1	$k_{ex}$ dependency on pH, symmetry of $MTR_{Rex}(pH)$ and calibration of $k_c$ .	50
3.2	Labeling efficiency $\alpha$ as a function of $k_{ex}$ and $B_1$ . . . . .	54
3.3	$CEST_{ratio}$ as a function of pH and influence of $B_{1,high}$ , $B_{1,low}$ , $k_c$ and $c_2$ . .	57
3.4	Theoretical pH sensitivities of amide and guanidyl protons   visualization of the $pH_{combi}$ approach . . . . .	60
4.1	9.4 T small animal MR scanner at the DKFZ and $^1\text{H}$ RF coil . . . . .	64
4.2	Multi-chamber phantom . . . . .	67
4.3	Dounce homogenizer used for sample preparation of porcine brain lysates	68
4.4	Various presaturation pulse shapes $c_2$ used for pulsed CEST experiments .	74
4.5	In vivo positioning procedure of FOV and adjustment volume . . . . .	78
4.6	pH mapping workflow   CEST data post-processing . . . . .	79
5.1	Influence of pH and $C_{tissue}$ on Z-spectra of porcine brain lysates . . . . .	93
5.2	Separate amide and guanidyl signal extraction from Z-spectra of porcine brain lysates at various pH and $B_1$ . . . . .	95

List of Figures

5.3	Contrast- $B_1$ -correction of $MTR_{\text{Rex}}(\text{amide})$ and $MTR_{\text{Rex}}(\text{gua})$ in porcine brain lysates at various pH and $B_1$ . . . . .	97
5.4	Calibration of $k_c$ in porcine brain lysates . . . . .	99
5.5	$CEST_{\text{ratio}}$ , $k_{\text{ex}}$ and correlation of $\text{pH}_{\text{amide}}$ and $\text{pH}_{\text{gua}}$ with $\text{pH}_{\text{titrated}}$ in porcine brain lysates . . . . .	102
5.6	$\text{pH}_{\text{amide}}$ and $\text{pH}_{\text{gua}}$ maps in porcine brain lysates at various pH and $C_{\text{tissue}}$	103
5.7	Weightings of $\text{pH}_{\text{amide}}$ and $\text{pH}_{\text{gua}}$ for $\text{pH}_{\text{combi}}$ mapping in porcine brain lysates at various pH and $C_{\text{tissue}}$ . . . . .	105
5.8	Correlation of $\text{pH}_{\text{combi}}$ with $\text{pH}_{\text{titrated}}$ and concentration-independence of $\text{pH}_{\text{combi}}$ in porcine brain lysates . . . . .	106
5.9	Steady-state condition in tumor lesions . . . . .	109
5.10	Tumor ROI definition   in vivo $B_0$ and $B_1$ map . . . . .	112
5.11	In vivo signal extraction, contrast- $B_1$ -correction and $\text{pH}_{\text{combi}}$ . . . . .	113
5.12	$\text{pH}_i$ mapping in tumor lesions of different sizes . . . . .	114
5.13	Treatment course of $\text{pH}_i$ in tumor lesions of treated and control mice measured via $\text{pH}_{\text{combi}}$ and corresponding tumor growth . . . . .	116
5.14	Time course of $\text{pH}_{\text{combi}}$ maps of control mice . . . . .	117
5.15	Z-spectra as a function of pH and presaturation pulse shape $c_2$ in creatine model solutions . . . . .	119
5.16	Effect of $c_2$ on $MTR_{\text{Rex}}$ , $k_c$ and $CEST_{\text{ratio}}$ in creatine model solutions at various pH . . . . .	120
5.17	Correlation of $\text{pH}_{\text{gua}}$ and $\text{pH}_{\text{titrated}}$ for cw and $c_2 = 0.42$ in creatine model solutions   shift of pH sensitivity . . . . .	122
A.1	Quantification of $f_s$ for amide and guanidyl protons in porcine brain lysates at various $C_{\text{tissue}}$ . . . . .	I

## List of Tables

4.1	pH series of porcine brain lysate model suspensions . . . . .	69
4.2	Concentration series of porcine brain lysate model suspensions . . . . .	70
4.3	pH series of creatine model solutions . . . . .	70
4.4	Optimized MRI readout parameters . . . . .	75
4.5	Optimized CEST acquisition parameters . . . . .	77
4.6	Fit parameters used for extraction of $Z_{lab}$ and $Z_{ref}$ in porcine brain lysates	84
4.7	Fit parameters used for extraction of $Z_{lab}$ and $Z_{ref}$ in tumor-bearing mice .	85
4.8	Fit parameters of the $MTR_{REX}$ -based contrast- $B_1$ -correction . . . . .	86
4.9	Fit parameters for the calibration of $k_c$ . . . . .	89
5.1	Calibrated values of $k_c$ for amide and guanidyl protons in porcine brain lysates at $T = 37 \pm 0.2^\circ\text{C}$ . . . . .	100
5.2	Experimentally determined $pH_i$ in tumor lesions of different sizes . . . . .	115



## Bibliography

- [1] I. I. Rabi, J. R. Zacharias, S. Millman, and P. Kusch. “A New Method of Measuring Nuclear Magnetic Moment”. In: *Physical Review* 53 (1938), pp. 318–318.
- [2] F. Bloch, W. W. Hansen, and Martin Packard. “Nuclear Induction”. In: *Physical Review* 69 (1946), pp. 127–127.
- [3] E. M. Purcell, H. C. Torrey, and R. V. Pound. “Resonance Absorption by Nuclear Magnetic Moments in a Solid”. In: *Physical Review* 69 (1946), pp. 37–38.
- [4] W. G. Proctor and F. C. Yu. “The Dependence of a Nuclear Magnetic Resonance Frequency upon Chemical Compound”. In: *Physical Review* 77 (1950), pp. 717–717.
- [5] WC Dickinson. “Dependence of the F 19 nuclear resonance position on chemical compound”. In: *Physical Review* 77.5 (1950), p. 736.
- [6] P. C. Lauterbur. “Image Formation by Induced Local Interactions: Examples Employing Nuclear Magnetic Resonance”. en. In: *Nature* 242 (1973), pp. 190–191.
- [7] Peter Mansfield and Peter K Grannell. “NMR ‘diffraction’ in solids?”. In: *Journal of Physics C: solid state physics* 6.22 (1973), p. L422.
- [8] Ahmedin Jemal, Melissa M Center, Carol DeSantis, and Elizabeth M Ward. “Global patterns of cancer incidence and mortality rates and trends”. In: *Cancer Epidemiology and Prevention Biomarkers* 19.8 (2010), pp. 1893–1907.
- [9] Jacques Ferlay, Isabelle Soerjomataram, Rajesh Dikshit, Sultan Eser, Colin Mathers, Marise Rebelo, Donald Maxwell Parkin, et al. “Cancer incidence and mortality worldwide: sources, methods and major patterns in GLOBOCAN 2012”. In: *International journal of cancer* 136.5 (2015), E359–E386.
- [10] Robert F Schmidt, Gerhard Thews, Florian Lang, et al. *Physiologie des Menschen*. Vol. 10. Springer, 1987.
- [11] Bruce Alberts, Alexander Johnson, Julian Lewis, David Morgan, Martin Raff, Keith Roberts, and Peter Walter. *Molekularbiologie der Zelle*. Vol. 3. VCh Weinheim, 1995.

## Bibliography

- [12] Walter F Boron and Emile L Boulpaep. *Medical physiology E-book*. Elsevier Health Sciences, 2016.
- [13] Jeremy M Berg, John L Tymoczko, et al. *Stryer biochemie*. Vol. 8. Springer, 2018.
- [14] R.J. Gillies, N. Raghunand, M.L. Garcia-Martin, and R.A. Gatenby. “pH imaging”. In: *IEEE Engineering in Medicine and Biology Magazine* 23 (2004), pp. 57–64.
- [15] Arig Ibrahim Hashim, Xiaomeng Zhang, Jonathan W Wojtkowiak, Gary V Martinez, and Robert J Gillies. “Imaging pH and metastasis”. In: *NMR in biomedicine* 24.6 (2011), pp. 582–591.
- [16] KowsalyaDevi Pavuluri and Michael T McMahon. “pH imaging using chemical exchange saturation transfer (CEST) MRI”. In: *Israel Journal of Chemistry* 57.9 (2017), pp. 862–879.
- [17] Bradley A Webb, Michael Chimenti, Matthew P Jacobson, and Diane L Barber. “Dysregulated pH: a perfect storm for cancer progression”. In: *Nature Reviews Cancer* 11.9 (2011), pp. 671–677.
- [18] Douglas Hanahan and Robert A Weinberg. “Hallmarks of cancer: the next generation”. In: *cell* 144.5 (2011), pp. 646–674.
- [19] Mehdi Damaghi, Jonathan W Wojtkowiak, and Robert J Gillies. “pH sensing and regulation in cancer”. In: *Frontiers in physiology* 4 (2013), p. 370.
- [20] Marina V Shirmanova, Irina N Druzhkova, Maria M Lukina, Mikhail E Matlashov, Vsevolod V Belousov, Ludmila B Snopova, Natalia N Prodanetz, et al. “Intracellular pH imaging in cancer cells in vitro and tumors in vivo using the new genetically encoded sensor SypHer2”. In: *Biochimica et Biophysica Acta (BBA)-General Subjects* 1850.9 (2015), pp. 1905–1911.
- [21] KA White, BK Grillo-Hill, and DL Barber. “Dysregulated pH dynamics enables cancer cell behaviors”. In: *J Cell Sci* 130 (2017), pp. 663–669.
- [22] Mohit Sharma, Madhusudan Astekar, Sonal Soi, Bhari S Manjunatha, Devi C Shetty, and Raghu Radhakrishnan. “pH gradient reversal: an emerging hallmark of cancers”. In: *Recent patents on anti-cancer drug discovery* 10.3 (2015), pp. 244–258.
- [23] Marion Stubbs, Loreta Rodrigues, Franklyn A Howe, Jian Wang, Kyu-Shik Jeong, Richard L Veech, and John R Griffiths. “Metabolic consequences of a reversed pH gradient in rat tumors”. In: *Cancer research* 54.15 (1994), pp. 4011–4016.

- [24] Tianyu Zheng, Marja Jäätelä, and Bin Liu. “pH gradient reversal fuels cancer progression”. In: *The International Journal of Biochemistry & Cell Biology* 125 (2020), p. 105796.
- [25] Katharina J Wenger, Elke Hattingen, Kea Franz, Joachim P Steinbach, Oliver Bähr, and Ulrich Pilatus. “Intracellular pH measured by  $^{31}\text{P}$ -MR-spectroscopy might predict site of progression in recurrent glioblastoma under antiangiogenic therapy”. In: *Journal of Magnetic Resonance Imaging* 46.4 (2017), pp. 1200–1208.
- [26] Andreas Korzowski and Peter Bachert. “High-resolution  $^{31}\text{P}$  echo-planar spectroscopic imaging in vivo at 7 T”. In: *Magnetic resonance in medicine* 79.3 (2018), pp. 1251–1259.
- [27] Andreas Korzowski, Nina Weinfurter, Sebastian Mueller, Johannes Breitling, Steffen Goerke, Heinz-Peter Schlemmer, Mark E Ladd, et al. “Volumetric mapping of intra-and extracellular pH in the human brain using  $^{31}\text{P}$  MRSI at 7T”. In: *Magnetic resonance in medicine* 84.4 (2020), pp. 1707–1723.
- [28] Steven D Wolff and Robert S Balaban. “NMR imaging of labile proton exchange”. en. In: *Journal of Magnetic Resonance (1969)* 86 (1990), pp. 164–169.
- [29] K.M Ward, A.H Aletras, and R.S Balaban. “A New Class of Contrast Agents for MRI Based on Proton Chemical Exchange Dependent Saturation Transfer (CEST)”. In: *Journal of Magnetic Resonance* 143 (2000), pp. 79–87.
- [30] Peter C. M. van Zijl and Nirbhay N. Yadav. “Chemical exchange saturation transfer (CEST): What is in a name and what isn’t?” en. In: *Magnetic Resonance in Medicine* 65 (2011), pp. 927–948.
- [31] Guanshu Liu, Xiaolei Song, Kannie W. Y. Chan, and Michael T. McMahon. “Nuts and bolts of chemical exchange saturation transfer MRI”. en. In: *NMR in Biomedicine* (2013), n/a–n/a.
- [32] M. T. McMahon, A. A. Gilad, J. W. M. Bulte, and P. C. M. van Zijl. *Chemical Exchange Saturation Transfer Imaging*. Pan Stanford Publishing Pte. Ltd., 2016.
- [33] Michael T McMahon, Assaf A Gilad, Jeff WM Bulte, and Peter CM Van Zijl. *Chemical exchange saturation transfer imaging: advances and applications*. CRC Press, 2017.

## Bibliography

- [34] Kannie W. Y. Chan, Michael T. McMahon, Yoshinori Kato, Guanshu Liu, Jeff W. M. Bulte, Zaver M. Bhujwala, Dmitri Artemov, et al. “Natural D-Glucose as a Biodegradable MRI Contrast Agent for Detecting Cancer”. en. In: *Magnetic Resonance in Medicine* 68.6 (2012), pp. 1764–1773.
- [35] Xiang Xu, Nirbhay N Yadav, Linda Knutsson, Jun Hua, Rita Kalyani, Erica Hall, John Laterra, et al. “Dynamic glucose-enhanced (DGE) MRI: translation to human scanning and first results in glioma patients”. In: *Tomography: a journal for imaging research* 1.2 (2015), p. 105.
- [36] Daniel Paech, Patrick Schuenke, Christina Koehler, Johannes Windschuh, Sibumundiyanapurath, Sebastian Bickelhaupt, David Bonekamp, et al. “T1 $\rho$ -weighted Dynamic Glucose-enhanced MR Imaging in the Human Brain”. In: *Radiology* 285.3 (2017), pp. 914–922.
- [37] P. Schuenke, C. Koehler, A. Korzowski, J. Windschuh, P. Bachert, M. E. Ladd, S. Mundiyanapurath, et al. “Adiabatically prepared spin-lock approach for T1 $\rho$ -based Dynamic Glucose Enhanced MRI at ultrahigh fields”. In: *Magnetic Resonance in Medicine* 78.1 (2017), pp. 215–225.
- [38] Mohammad Haris, Ravi Prakash Reddy Nanga, Anup Singh, Kejia Cai, Feliks Kogan, Hari Hariharan, and Ravinder Reddy. “Exchange rates of creatine kinase metabolites: feasibility of imaging creatine by chemical exchange saturation transfer MRI”. In: *NMR in Biomedicine* 25 (2012), pp. 1305–1309.
- [39] Mohammad Haris, Anup Singh, Kejia Cai, Feliks Kogan, Jeremy McGarvey, Catherine DeBrosse, Gerald A Zsido, et al. “A technique for in vivo mapping of myocardial creatine kinase metabolism”. In: *Nature medicine* 20.2 (2014), pp. 209–214.
- [40] Steffen Goerke, Moritz Zaiss, and Peter Bachert. “Characterization of creatine guanidinium proton exchange by water-exchange (WEX) spectroscopy for absolute-pH CEST imaging in vitro”. en. In: *NMR in Biomedicine* 27 (2014), pp. 507–518.
- [41] Lin Chen, Peter B Barker, Robert G Weiss, Peter CM van Zijl, and Jiadi Xu. “Creatine and phosphocreatine mapping of mouse skeletal muscle by a polynomial and Lorentzian line-shape fitting CEST method”. In: *Magnetic resonance in medicine* 81.1 (2019), pp. 69–78.

- [42] Kejia Cai, Mohammad Haris, Anup Singh, Feliks Kogan, Joel H. Greenberg, Hari Hariharan, John A. Detre, et al. “Magnetic resonance imaging of glutamate”. en. In: *Nature Medicine* 18 (2012), pp. 302–307.
- [43] Mohammad Haris, Kavindra Nath, Kejia Cai, Anup Singh, Rachelle Crescenzi, Feliks Kogan, Gaurav Verma, et al. “Imaging of glutamate neurotransmitter alterations in Alzheimer’s disease”. en. In: *NMR in Biomedicine* 26 (2013), pp. 386–391.
- [44] David R Roalf, Ravi Prakash Reddy Nanga, Petra E Rupert, Hari Hariharan, Megan Quarmley, Monica E Calkins, Erich Dress, et al. “Glutamate imaging (GluCEST) reveals lower brain GluCEST contrast in patients on the psychosis spectrum”. In: *Molecular psychiatry* 22.9 (2017), pp. 1298–1305.
- [45] Philip S. Boyd, Johannes Breitling, Ferdinand Zimmermann, Andreas Korzowski, Moritz Zaiss, Patrick Schuenke, Nina Weinfurter, et al. “Dynamic glucose-enhanced (DGE) MRI in the human brain at 7 T with reduced motion-induced artifacts based on quantitative  $R1\rho$  mapping”. In: *Magnetic resonance in medicine* 84.1 (2020), pp. 182–191.
- [46] Jinyuan Zhou, Jean-Francois Payen, David A. Wilson, Richard J. Traystman, and Peter C. M. van Zijl. “Using the amide proton signals of intracellular proteins and peptides to detect pH effects in MRI”. en. In: *Nature Medicine* 9 (2003), pp. 1085–1090.
- [47] Kun Yan, Zongming Fu, Chen Yang, Kai Zhang, Shanshan Jiang, Dong-Hoon Lee, Hye-Young Heo, et al. “Assessing Amide Proton Transfer (APT) MRI Contrast Origins in 9 L Gliosarcoma in the Rat Brain Using Proteomic Analysis”. en. In: *Molecular Imaging and Biology* (Jan. 2015), pp. 1–9.
- [48] Steffen Goerke, Moritz Zaiss, Johannes Windschuh, Karel D. Klika, and Peter Bachert. “Two dimensional CEST spectroscopy of proteins”. In: *Proceedings of the Symposium on Chemical Exchange Saturation Transfer PENN-CEST, Philadelphia, PA, USA* (2015).
- [49] Steffen Goerke, Moritz Zaiss, Patrick Kunz, Karel D. Klika, Johannes D. Windschuh, Axel Mogk, Bernd Bukau, et al. “Signature of protein unfolding in chemical exchange saturation transfer imaging”. en. In: *NMR in Biomedicine* 28 (2015), pp. 906–913.

## Bibliography

- [50] Steffen Goerke, Johannes Breitling, Moritz Zaiss, Johannes Windschuh, Patrick Kunz, Patrick Schuenke, Daniel Paech, et al. “Dual-frequency irradiation CEST-MRI of endogenous bulk mobile proteins”. In: *NMR in Biomedicine* 31.6 (2018), e3920.
- [51] K.m. Ward and R.s. Balaban. “Determination of pH using water protons and chemical exchange dependent saturation transfer (CEST)”. en. In: *Magnetic Resonance in Medicine* 44.5 (2000), pp. 799–802.
- [52] Xiao-Yong Zhang, Jingping Xie, Feng Wang, Eugene C Lin, Junzhong Xu, Daniel F Gochberg, John C Gore, et al. “Assignment of the molecular origins of CEST signals at 2 ppm in rat brain”. In: *Magnetic resonance in medicine* 78.3 (2017), pp. 881–887.
- [53] Lin Chen, Haifeng Zeng, Xiang Xu, Nirbhay N Yadav, Shuhui Cai, Nicolaas A Puts, Peter B Barker, et al. “Investigation of the contribution of total creatine to the CEST Z-spectrum of brain using a knockout mouse model”. In: *NMR in Biomedicine* 30.12 (2017), e3834.
- [54] Lin Chen, Zhiliang Wei, Shuhui Cai, Yuguo Li, Guanshu Liu, Hanzhang Lu, Robert G Weiss, et al. “High-resolution creatine mapping of mouse brain at 11.7 T using non-steady-state chemical exchange saturation transfer”. In: *NMR in Biomedicine* 32.11 (2019), e4168.
- [55] Lin Chen, Michael Schär, Kannie WY Chan, Jianpan Huang, Zhiliang Wei, Hanzhang Lu, Qin Qin, et al. “In vivo imaging of phosphocreatine with artificial neural networks”. In: *Nature communications* 11.1 (2020), pp. 1–10.
- [56] Joshua M Goldenberg and Mark D Pagel. “Assessments of tumor metabolism with CEST MRI”. In: *NMR in Biomedicine* 32.10 (2019), e3943.
- [57] Moritz Zaiss and Peter Bachert. “Exchange-dependent relaxation in the rotating frame for slow and intermediate exchange – modeling off-resonant spin-lock and chemical exchange saturation transfer”. en. In: *NMR in Biomedicine* 26 (2013), pp. 507–518.
- [58] Moritz Zaiss and Peter Bachert. “Chemical exchange saturation transfer (CEST) and MR Z-spectroscopy in vivo: a review of theoretical approaches and methods”. en. In: *Physics in Medicine and Biology* 58 (2013), R221–R269.

- [59] Dario L Longo, Phillip Zhe Sun, Lorena Consolino, Filippo C Michelotti, Fulvio Uggeri, and Silvio Aime. “A general MRI-CEST ratiometric approach for pH imaging: demonstration of in vivo pH mapping with iobitridol”. In: *Journal of the American Chemical Society* 136.41 (2014), pp. 14333–14336.
- [60] Eugenia Rerich, Moritz Zaiss, Andreas Korzowski, Mark E Ladd, and Peter Bachert. “Relaxation-compensated CEST-MRI at 7 T for mapping of creatine content and pH—preliminary application in human muscle tissue in vivo”. In: *NMR in Biomedicine* 28.11 (2015), pp. 1402–1412.
- [61] Phillip Zhe Sun, Gang Xiao, Iris Yuwen Zhou, Yingkun Guo, and Renhua Wu. “A method for accurate pH mapping with chemical exchange saturation transfer (CEST) MRI”. In: *Contrast media & molecular imaging* 11.3 (2016), pp. 195–202.
- [62] Francesca Arena, Pietro Irrera, Lorena Consolino, Sonia Colombo Serra, Moritz Zaiss, and Dario Livio Longo. “Flip-angle based ratiometric approach for pulsed CEST-MRI pH imaging”. In: *Journal of Magnetic Resonance* 287 (2018), pp. 1–9.
- [63] Annasofia Anemone, Lorena Consolino, Francesca Arena, Martina Capozza, and Dario Livio Longo. “Imaging tumor acidosis: a survey of the available techniques for mapping in vivo tumor pH”. In: *Cancer and Metastasis Reviews* 38.1 (2019), pp. 25–49.
- [64] Tao Jin, Ping Wang, T Kevin Hitchens, and Seong-Gi Kim. “Enhancing sensitivity of pH-weighted MRI with combination of amide and guanidyl CEST”. In: *Neuroimage* 157 (2017), pp. 341–350.
- [65] Nevin McVicar, Alex X Li, Daniela F Goncalves, Miranda Bellyou, Susan O Meakin, Marco AM Prado, and Robert Bartha. “Quantitative tissue pH measurement during cerebral ischemia using amine and amide concentration-independent detection (AACID) with MRI”. In: *Journal of Cerebral Blood Flow & Metabolism* 34.4 (2014), pp. 690–698.
- [66] Enfeng Wang, Yin Wu, Jerry S Cheung, Takahiro Igarashi, Limin Wu, Xiaoan Zhang, and Phillip Zhe Sun. “Mapping tissue pH in an experimental model of acute stroke—Determination of graded regional tissue pH changes with non-invasive quantitative amide proton transfer MRI”. In: *NeuroImage* 191 (2019), pp. 610–617.

## Bibliography

- [67] Robert J Harris, Timothy F Cloughesy, Linda M Liau, Robert M Prins, Joseph P Antonios, Debiao Li, William H Yong, et al. “pH-weighted molecular imaging of gliomas using amine chemical exchange saturation transfer MRI”. In: *Neuro-oncology* 17.11 (2015), pp. 1514–1524.
- [68] Benjamin M Ellingson, Jingwen Yao, Catalina Raymond, Ararat Chakhoyan, Kasra Khatibi, Noriko Salamon, J Pablo Villablanca, et al. “pH-weighted molecular MRI in human traumatic brain injury (TBI) using amine proton chemical exchange saturation transfer echoplanar imaging (CEST EPI)”. In: *NeuroImage: Clinical* 22 (2019), p. 101736.
- [69] Robert J Harris, Jingwen Yao, Ararat Chakhoyan, Catalina Raymond, Kevin Leu, Linda M Liau, Phioanh L Nghiemphu, et al. “Simultaneous pH-sensitive and oxygen-sensitive MRI of human gliomas at 3 T using multi-echo amine proton chemical exchange saturation transfer spin-and-gradient echo echo-planar imaging (CEST-SAGE-EPI)”. In: *Magnetic resonance in medicine* 80.5 (2018), pp. 1962–1978.
- [70] Moritz Zaiss, Goran Angelovski, Eleni Demetriou, Michael T McMahon, Xavier Golay, and Klaus Scheffler. “QUEST and QUEST revisited—fast and accurate quantitative CEST experiments”. In: *Magnetic resonance in medicine* 79.3 (2018), pp. 1708–1721.
- [71] Michael T McMahon, Assaf A Gilad, Jinyuan Zhou, Phillip Z Sun, Jeff WM Bulte, and Peter CM Van Zijl. “Quantifying exchange rates in chemical exchange saturation transfer agents using the saturation time and saturation power dependencies of the magnetization transfer effect on the magnetic resonance imaging signal (QUEST and QUEST): pH calibration for poly-L-lysine and a starburst dendrimer”. In: *Magnetic Resonance in Medicine: An Official Journal of the International Society for Magnetic Resonance in Medicine* 55.4 (2006), pp. 836–847.
- [72] Phillip Zhe Sun, Jinyuan Zhou, Weiyun Sun, Judy Huang, and Peter CM Van Zijl. “Detection of the ischemic penumbra using pH-weighted MRI”. In: *Journal of Cerebral Blood Flow & Metabolism* 27.6 (2007), pp. 1129–1136.
- [73] Phillip Zhe Sun. “Demonstration of magnetization transfer and relaxation normalized pH-specific pulse-amide proton transfer imaging in an animal model of acute stroke”. In: *Magnetic Resonance in Medicine* 84.3 (2020), pp. 1526–1533.

- [74] Phillip Zhe Sun and A. Gregory Sorensen. “Imaging pH using the chemical exchange saturation transfer (CEST) MRI: Correction of concomitant RF irradiation effects to quantify CEST MRI for chemical exchange rate and pH”. en. In: *Magn Reson Med* 60.2 (2008), pp. 390–397.
- [75] Hahnsung Kim, Lisa C Krishnamurthy, and Phillip Zhe Sun. “Brain pH imaging and its applications”. In: *Neuroscience* 474 (2021), pp. 51–62.
- [76] Dario Livio Longo, Pietro Irrera, Lorena Consolino, Phillip Zhe Sun, and Michael T McMahon. “Renal pH imaging using chemical exchange saturation transfer (CEST) MRI: basic concept”. In: *Preclinical MRI of the Kidney* (2021), p. 241.
- [77] Kowsalya Devi Pavuluri, Lorena Consolino, Dario Livio Longo, Pietro Irrera, Phillip Zhe Sun, and Michael T McMahon. “Renal pH mapping using chemical exchange saturation transfer (CEST) MRI: experimental protocol”. In: *Preclinical MRI of the Kidney*. Humana, New York, NY, 2021, pp. 455–471.
- [78] Enfeng Wang, Yin Wu, Jerry S Cheung, Iris Yuwen Zhou, Takahiro Igarashi, Xiaolan Zhang, and Phillip Zhe Sun. “pH imaging reveals worsened tissue acidification in diffusion kurtosis lesion than the kurtosis/diffusion lesion mismatch in an animal model of acute stroke”. In: *Journal of Cerebral Blood Flow & Metabolism* 37.10 (2017), pp. 3325–3333.
- [79] Renhua Wu, Gang Xiao, Iris Yuwen Zhou, Chongzhao Ran, and Phillip Zhe Sun. “Quantitative chemical exchange saturation transfer (qCEST) MRI–omega plot analysis of RF-spillover-corrected inverse CEST ratio asymmetry for simultaneous determination of labile proton ratio and exchange rate”. In: *NMR in biomedicine* 28.3 (2015), pp. 376–383.
- [80] Yin Wu, Iris Y Zhou, Takahiro Igarashi, Dario L Longo, Silvio Aime, and Phillip Zhe Sun. “A generalized ratiometric chemical exchange saturation transfer (CEST) MRI approach for mapping renal pH using iopamidol”. In: *Magnetic resonance in medicine* 79.3 (2018), pp. 1553–1558.
- [81] Limin Wu, Liang Jiang, and Phillip Zhe Sun. “Investigating the origin of pH-sensitive magnetization transfer ratio asymmetry MRI contrast during the acute stroke: Correction of T1 change reveals the dominant amide proton transfer MRI signal”. In: *Magnetic resonance in medicine* 84.5 (2020), pp. 2702–2712.

## Bibliography

- [82] Dario Livio Longo, Enza Di Gregorio, Riccardo Abategiovanni, Alberto Ceccon, Michael Assfalg, Henriette Molinari, and Silvio Aime. “Chemical exchange saturation transfer (CEST): an efficient tool for detecting molecular information on proteins’ behaviour”. In: *Analyst* 139 (2014), pp. 2687–2690.
- [83] Robert J Harris, Timothy F Cloughesy, Linda M Liao, Phioanh L Nghiemphu, Albert Lai, Whitney B Pope, and Benjamin M Ellingson. “Simulation, phantom validation, and clinical evaluation of fast pH-weighted molecular imaging using amine chemical exchange saturation transfer echo planar imaging (CEST-EPI) in glioma at 3 T”. In: *NMR in Biomedicine* 29.11 (2016), pp. 1563–1576.
- [84] Hahnsung Kim, Yin Wu, Daisy Villano, Dario Livio Longo, Michael T McMahon, and Phillip Zhe Sun. “Analysis protocol for the quantification of renal pH using chemical exchange saturation transfer (CEST) MRI”. In: *Preclinical MRI of the Kidney* (2021), p. 667.
- [85] Liu Qi Chen and Mark D Pagel. “Evaluating pH in the extracellular tumor microenvironment using CEST MRI and other imaging methods”. In: *Advances in radiology* 2015 (2015).
- [86] Jinyuan Zhou and Peter van Zijl. “Defining an acidosis-based ischemic penumbra from pH-weighted MRI”. In: *Translational stroke research* 3.1 (2012), pp. 76–83.
- [87] Y Liu, B Zhao, and XY Zhang. “A comparison of several tumor endogenous pH mapping methods using CEST at 11.7 T”. In: *Proceedings of the 29th Annual Meeting of the International Society for Magnetic Resonance in Medicine* 29.1467 (2021).
- [88] Liu Qi Chen, Edward A Randtke, Kyle M Jones, Brianna F Moon, Christine M Howison, and Mark D Pagel. “Evaluations of tumor acidosis within in vivo tumor models using parametric maps generated with acidoCEST MRI”. In: *Molecular Imaging and Biology* 17.4 (2015), pp. 488–496.
- [89] Liu Qi Chen, Mark D. Pagel, Liu Qi Chen, and Mark D. Pagel. “Evaluating pH in the Extracellular Tumor Microenvironment Using CEST MRI and Other Imaging Methods, Evaluating pH in the Extracellular Tumor Microenvironment Using CEST MRI and Other Imaging Methods”. en. In: *Advances in Radiology, Advances in Radiology* Article ID 206405 (2015).

- [90] Moritz Zaiss, Junzhong Xu, Steffen Goerke, Imad S. Khan, Robert J. Singer, John C. Gore, Daniel F. Gochberg, et al. “Inverse Z-spectrum analysis for spillover-, MT-, and T1-corrected steady-state pulsed CEST-MRI – application to pH-weighted MRI of acute stroke”. en. In: *NMR in Biomedicine* 27 (2014), pp. 240–252.
- [91] Charles P. Slichter. *Principles of Magnetic Resonance*. 3. edition. Springer-Verlag Berlin Heidelberg, 1990.
- [92] E. Mark Haacke, Robert W. Brown, Michael R. Thompson, and Ramesh Venkatesan. *Magnetic Resonance Imaging: Physical Principles and Sequence Design*. Englisch. 1st edition. New York, NY, USA: John Wiley & Sons, 1999.
- [93] Matt A. Bernstein, Kevin F. King, and Xiaohong Joe Zhou. *Handbook of MRI Pulse Sequences*. en. Elsevier, Sept. 2004.
- [94] Robin A. de Graaf. *In Vivo NMR Spectroscopy: Principles and Techniques*. en. 2nd edition. Chichester, England: John Wiley & Sons, 2008.
- [95] F. Bloch. “Nuclear Induction”. In: *Physical Review* 70.7-8 (1946), p. 460.
- [96] Ivan Tkáč, Gülin Öz, Gregor Adriany, Kamil Uğurbil, and Rolf Gruetter. “In vivo <sup>1</sup>H NMR spectroscopy of the human brain at high magnetic fields: metabolite quantification at 4T vs. 7T”. In: *Magnetic Resonance in Medicine: An Official Journal of the International Society for Magnetic Resonance in Medicine* 62.4 (2009), pp. 868–879.
- [97] Edvards Liepinsh and Gottfried Otting. “Proton exchange rates from amino acid side chains— implications for image contrast”. en. In: *Magnetic Resonance in Medicine* 35 (1996), pp. 30–42.
- [98] Jinyuan Zhou and Peter C. M. van Zijl. “Chemical exchange saturation transfer imaging and spectroscopy”. In: *Progress in Nuclear Magnetic Resonance Spectroscopy* 48 (2006), pp. 109–136.
- [99] P. W. Atkins and Julio de Paula. *Physikalische Chemie*. 4. Auflage. Weinheim, Deutschland: WILEY-VCH, 2006.
- [100] H BIELKA GDR, N Sharon, and EC WEBB Australia. “Nomenclature and symbolism for amino acids and peptides”. In: *Pure and Applied Chemistry* 56 (1984), pp. 595–624.
- [101] Kurt Wuethrich. *NMR of Proteins and Nucleic Acids*. 1st edition. New York, NY, USA: John Wiley & Sons, 1986.

## Bibliography

- [102] Yawen Bai, John S. Milne, Leland Mayne, and S. Walter Englander. “Primary structure effects on peptide group hydrogen exchange”. en. In: *Proteins: Struct, Funct, Bioinf* 17.1 (1993), pp. 75–86.
- [103] I. Solomon. “Relaxation Processes in a System of Two Spins”. In: *Physical Review* 99 (1955), pp. 559–565.
- [104] Peter C. M. van Zijl, Jinyuan Zhou, Noriko Mori, Jean-Francois Payen, David Wilson, and Susumu Mori. “Mechanism of Magnetization Transfer During On-Resonance Water Saturation. A New Approach to Detect Mobile Proteins, Peptides, and Lipids”. en. In: *Magnetic Resonance in Medicine* 49 (2003), pp. 440–449.
- [105] Jiadi Xu, Nirbhay N. Yadav, Amnon Bar-Shir, Craig K. Jones, Kannie W. Y. Chan, Jiangyang Zhang, P. Walczak, et al. “Variable Delay Multi-Pulse Train for Fast Chemical Exchange Saturation Transfer and Relayed-Nuclear Overhauser Enhancement MRI”. en. In: *Magnetic Resonance in Medicine* 71 (2014), pp. 1798–1812.
- [106] S Mori, J M Berg, and P C van Zijl. “Separation of intramolecular NOE and exchange peaks in water exchange spectroscopy using spin-echo filters”. eng. In: *Journal of biomolecular NMR* 7 (1996), pp. 77–82.
- [107] Joshua I. Friedman, Ding Xia, Ravinder R. Regatte, and Alexej Jerschow. “Transfer Rate Edited experiment for the selective detection of Chemical Exchange via Saturation Transfer (TRE-CEST)”. In: *Journal of Magnetic Resonance* 256 (2015), pp. 43–51.
- [108] Steven D Wolff and Robert S Balaban. “Magnetization transfer contrast (MTC) and tissue water proton relaxation in vivo”. In: *Magnetic Resonance in Medicine* 10 (1989), pp. 135–144.
- [109] Greg J. Stanisz, Ewa E. Odobina, Joseph Pun, Michael Escaravage, Simon J. Graham, Michael J. Bronskill, and R. Mark Henkelman. “T1, T2 relaxation and magnetization transfer in tissue at 3T”. en. In: *Magnetic Resonance in Medicine* 54 (2005), pp. 507–512.
- [110] R. M. Henkelman, G. J. Stanisz, and S. J. Graham. “Magnetization transfer in MRI: a review”. en. In: *NMR in Biomedicine* 14 (2001), pp. 57–64.

- [111] Jinyuan Zhou, David A. Wilson, Phillip Zhe Sun, Judith A. Klaus, and Peter C. M. van Zijl. “Quantitative Description of Proton Exchange Processes Between Water and Endogenous and Exogenous Agents for WEX, CEST, and APT Experiments”. en. In: *Magnetic Resonance in Medicine* 51 (2004), pp. 945–952.
- [112] Michael T. McMahon, Assaf A. Gilad, Jinyuan Zhou, Phillip Z. Sun, Jeff W. M. Bulte, and Peter C. M. van Zijl. “Quantifying exchange rates in chemical exchange saturation transfer agents using the saturation time and saturation power dependencies of the magnetization transfer effect on the magnetic resonance imaging signal (QUEST and QUESP): pH calibration for poly-L-lysine and a starburst dendrimer”. en. In: *Magn Reson Med* 55.4 (2006), pp. 836–847.
- [113] Dapeng Liu, Jinyuan Zhou, Rong Xue, Zhentao Zuo, Jing An, and Danny J. J. Wang. “Quantitative characterization of nuclear overhauser enhancement and amide proton transfer effects in the human brain at 7 tesla”. en. In: *Magnetic Resonance in Medicine* 70 (2013), pp. 1070–1081.
- [114] Xiang Xu, Jae-Seung Lee, and Alexej Jerschow. “Ultrafast Scanning of Exchangeable Sites by NMR Spectroscopy”. en. In: *Angewandte Chemie International Edition in English* 52 (2013), pp. 8281–8284.
- [115] Harden M. McConnell. “Reaction Rates by Nuclear Magnetic Resonance”. In: *The Journal of Chemical Physics* 28 (1958), pp. 430–431.
- [116] Daniel Abergel and Arthur G. Palmer. “Approximate Solutions of the Bloch–McConnell Equations for Two-Site Chemical Exchange”. en. In: *ChemPhysChem* 5 (2004), pp. 787–793.
- [117] Oleg Trott and Arthur G. Palmer III. “R1 Relaxation outside of the Fast-Exchange Limit”. In: *Journal of Magnetic Resonance* 154 (2002), pp. 157–160.
- [118] P. Z. Sun, J. Zhou, J. Huang, and P. van Zijl. “Simplified quantitative description of amide proton transfer (APT) imaging during acute ischemia”. In: *Magnetic Resonance in Medicine* 57.2 (2007), pp. 405–410.
- [119] Moritz Zaiss and Peter Bachert. “Exchange-dependent relaxation in the rotating frame for slow and intermediate exchange—modeling off-resonant spin-lock and chemical exchange saturation transfer”. In: *NMR in Biomedicine* 26.5 (2012), pp. 507–518.
- [120] Charles E Mortimer and Ulrich Müller. “Das Basiswissen der Chemie”. In: *Stuttgart, New York* 122015 (2003), p. 103.

## Bibliography

- [121] Philip S. Boyd, Johannes Breitling, Andreas Korzowski, Moritz Zaiss, Vanessa L. Franke, Karin Mueller-Decker, Andrey Glinka, et al. “Mapping intracellular pH in tumors using amide and guanidyl CEST-MRI at 9.4 T”. In: *Magnetic Resonance in Medicine* 87.5 (2022), pp. 2436–2452.
- [122] Donald E. Woessner, Shanrong Zhang, Matthew E. Merritt, and A. Dean Sherry. “Numerical solution of the Bloch equations provides insights into the optimum design of PARACEST agents for MRI”. en. In: *Magn Reson Med* 53.4 (2005), pp. 790–799.
- [123] Tao Jin, Ping Wang, Xiaopeng Zong, and Seong-Gi Kim. “Magnetic resonance imaging of the Amine–Proton EXchange (APEX) dependent contrast”. In: *Neuroimage* 59.2 (2012), pp. 1218–1227.
- [124] Tao Jin and Seong-Gi Kim. “Approximated analytical characterization of the steady-state chemical exchange saturation transfer (CEST) signals”. In: *Magnetic resonance in medicine* 82.5 (2019), pp. 1876–1889.
- [125] Kimberly L. Desmond and Greg J. Stanisz. “Understanding quantitative pulsed CEST in the presence of MT”. eng. In: *Magnetic Resonance in Medicine: Official Journal of the Society of Magnetic Resonance in Medicine / Society of Magnetic Resonance in Medicine* 67.4 (Apr. 2012), pp. 979–990.
- [126] Moritz Zaiss, Annasofia Anemone, Steffen Goerke, Dario Livio Longo, Kai Herz, Rolf Pohmann, Silvio Aime, et al. “Quantification of hydroxyl exchange of D-Glucose at physiological conditions for optimization of glucoCEST MRI at 3, 7 and 9.4 Tesla”. In: *NMR in Biomedicine* 32.9 (2019), e4113.
- [127] Jan-Eric Meissner, Steffen Goerke, Eugenia Rerich, Karel D. Klika, Alexander Radbruch, Mark E. Ladd, Peter Bachert, et al. “Quantitative pulsed CEST-MRI using Omega-plots”. en. In: *NMR in Biomedicine* (2015).
- [128] Eleni Demetriou, Mohamed Tachrount, Moritz Zaiss, Karin Shmueli, and Xavier Golay. “PRO-QUEST: a rapid assessment method based on progressive saturation for quantifying exchange rates using saturation times in CEST”. In: *Magnetic Resonance in Medicine* 80.4 (2018), pp. 1638–1654.
- [129] Eleni Demetriou, Aaron Kujawa, and Xavier Golay. “Pulse sequences for measuring exchange rates between proton species: From unlocalised NMR spectroscopy to chemical exchange saturation transfer imaging”. In: *Progress in Nuclear Magnetic Resonance Spectroscopy* 120 (2020), pp. 25–71.

- [130] Zhongliang Zu. “Ratiometric NOE (- 1.6) contrast in brain tumors”. In: *NMR in Biomedicine* 31.12 (2018), e4017.
- [131] Johannes Windschuh, Moritz Zaiss, Jan-Eric Meissner, Daniel Paech, Alexander Radbruch, Mark E. Ladd, and Peter Bachert. “Correction of B1-inhomogeneities for relaxation-compensated CEST imaging at 7T”. en. In: *NMR in Biomedicine* 28 (2015), pp. 529–537.
- [132] Marco Nolden, Sascha Zelzer, Alexander Seitel, Diana Wald, Michael Müller, Alfred M Franz, Daniel Maleike, et al. “The medical imaging interaction toolkit: challenges and advances”. In: *International journal of computer assisted radiology and surgery* 8.4 (2013), pp. 607–620.
- [133] Steffen Görke. *Einfluss von Entfaltung und Aggregation auf den <sup>1</sup>H-Magnetisierungstransfer zwischen Proteinen und freiem Wasser*. Fakultät für Physik und Astronomie, Ruprecht-Karls-Universität Heidelberg, Dissertation, 2015.
- [134] Johannes Windschuh. *Isolation of Unbiased Chemical Exchange Saturation Transfer Effects at 7 T and Application to Brain Tumors*. Fakultät für Physik und Astronomie, Ruprecht-Karls-Universität Heidelberg, Dissertation, 2016.
- [135] Moritz Zaiss, Johannes Windschuh, Steffen Goerke, Daniel Paech, Jan-Eric Meissner, Sina Burth, Philipp Kickingereeder, et al. “Downfield-NOE-suppressed amide-CEST-MRI at 7 Tesla provides a unique contrast in human glioblastoma”. In: *Magnetic resonance in medicine* 77.1 (2017), pp. 196–208.
- [136] Lilli Leonor Diederichs. *Implementation of pulsed presaturation for optimizing the pH sensitivity of guanidyl CEST-MRI for absolute pH mapping at 9.4 T*. Faculty of Physics and Astronomy, Ruperto-Carola University of Heidelberg, Bachelor Thesis, 2022.
- [137] Sebastian Müller. *Gewebeäquivalente Einstellung von Relaxationszeiten in Phantomen mit festgelegtem pH-Wert für Messungen bei verschiedenen Feldstärken und Temperaturen*. Fakultät für Physik und Astronomie, Ruprecht-Karls-Universität Heidelberg, Bachelorarbeit, 2016.
- [138] Daniel F Gochberg, Mark D Does, Zhongliang Zu, and Christopher L Lankford. “Towards an analytic solution for pulsed CEST”. In: *NMR in Biomedicine* 31.5 (2018), e3903.

## Bibliography

- [139] Christopher L Lankford, Elizabeth A Louie, Zhongliang Zu, Mark D Does, and Daniel F Gochberg. “A hybrid numeric-analytic solution for pulsed CEST”. In: *NMR in Biomedicine* 35.1 (2022), e4610.
- [140] Patrick Schuenke, Johannes Windschuh, Volkert Roeloffs, Mark E Ladd, Peter Bachert, and Moritz Zaiss. “Simultaneous mapping of water shift and B1 (WASABI)—Application to field-Inhomogeneity correction of CEST MRI data”. In: *Magnetic resonance in Medicine* 77.2 (2017), pp. 571–580.
- [141] Kimberly L. Desmond, Firas Moosvi, and Greg J. Stanisz. “Mapping of Amide, Amine, and Aliphatic Peaks in the CEST Spectra of Murine Xenografts at 7 T”. en. In: *Magnetic Resonance in Medicine* 71 (2013), pp. 1841–1853.
- [142] Craig K. Jones, Alan Huang, Jiadi Xu, Richard A.E. Edden, Michael Schaer, Jun Hua, Nikita Oskolkov, et al. “Nuclear Overhauser enhancement (NOE) imaging in the human brain at 7T”. In: *NeuroImage* 77 (2013), pp. 114–124.
- [143] Moritz Zaiss, Johannes Windschuh, Daniel Paech, Jan-Eric Meissner, Sina Burth, Benjamin Schmitt, Philip Kickingereder, et al. “Relaxation-compensated CEST-MRI of the human brain at 7T: Unbiased insight into NOE and amide signal changes in human glioblastoma”. In: *NeuroImage* 112 (2015), pp. 180–188.
- [144] Ran Sui, Lin Chen, Yuguo Li, Jianpan Huang, Kannie WY Chan, Xiang Xu, Peter CM van Zijl, et al. “Whole-brain amide CEST imaging at 3T with a steady-state radial MRI acquisition”. In: *Magnetic resonance in medicine* 86.2 (2021), pp. 893–906.
- [145] Johannes Windschuh, Moritz Zaiss, Jan-Eric Meissner, Daniel Paech, Alexander Radbruch, Mark E Ladd, and Peter Bachert. “Correction of B1-inhomogeneities for relaxation-compensated CEST imaging at 7 T”. In: *NMR in biomedicine* 28.5 (2015), pp. 529–537.
- [146] Philip S. Boyd, Lilli Diederichs, Johannes Breitling, Mark E. Ladd, Peter Bachert, and Steffen Goerke. “Presaturation pulse shape enables shifting the pH sensitivity of guanidyl CEST-MRI for absolute pH mapping at 9.4 T”. In: *Proceedings of the 30th Annual Meeting of the International Society for Magnetic Resonance in Medicine* 30.2803 (2022).
- [147] Tao Jin, Ping Wang, Xiaopeng Zong, and Seong-Gi Kim. “MR Imaging of the Amide-Proton Transfer Effect and the pH-Insensitive Nuclear Overhauser Effect at 9.4 T”. en. In: *Magnetic Resonance in Medicine* 69 (2013), pp. 760–770.

- [148] Tao Jin and Seong-Gi Kim. “Role of chemical exchange on the relayed nuclear Overhauser enhancement signal in saturation transfer MRI”. In: *Magnetic Resonance in Medicine* 87.1 (2022), pp. 365–376.
- [149] Mohammed Albatany, Alex Li, Susan Meakin, and Robert Bartha. “Dichloroacetate induced intracellular acidification in glioblastoma: in vivo detection using AACID-CEST MRI at 9.4 Tesla”. In: *Journal of neuro-oncology* 136.2 (2018), pp. 255–262.
- [150] Mohammed Albatany, Alex Li, Susan Meakin, and Robert Bartha. “In vivo detection of acute intracellular acidification in glioblastoma multiforme following a single dose of cariporide”. In: *International Journal of Clinical Oncology* 23.5 (2018), pp. 812–819.
- [151] Mohammed Albatany, Susan Meakin, and Robert Bartha. “The Monocarboxylate transporter inhibitor Quercetin induces intracellular acidification in a mouse model of Glioblastoma Multiforme: In-vivo detection using magnetic resonance imaging”. In: *Investigational New Drugs* 37.4 (2019), pp. 595–601.
- [152] Mohammed Albatany, Susan Meakin, and Robert Bartha. “Brain pH Measurement Using AACID CEST MRI Incorporating the 2 ppm Amine Resonance”. In: *Tomography* 8.2 (2022), pp. 730–739.
- [153] Steffen Goerke, Johannes Breitling, Karel D Klika, Mark E Ladd, and Peter Bachert. “Dependence of rNOE-CEST signals on molecular weight”. In: *Proc. Jt. Annu. Meet. ISMRM-ESMRMB* 2228 (2018).
- [154] Moritz Zaiss, Patrick Kunz, Steffen Goerke, Alexander Radbruch, and Peter Bachert. “MR imaging of protein folding in vitro employing Nuclear-Overhauser-mediated saturation transfer”. en. In: *NMR in Biomedicine* 26 (2013), pp. 1815–1822.
- [155] Steffen Goerke, Katharina S Milde, Raul Bukowiecki, Patrick Kunz, Karel D Klika, Thomas Wiglenda, Axel Mogk, et al. “Aggregation-induced changes in the chemical exchange saturation transfer (CEST) signals of proteins”. In: *NMR in Biomedicine* 30.1 (2017), e3665.
- [156] Jingwen Yao, Chencai Wang, and Benjamin M Ellingson. “Influence of phosphate concentration on amine, amide, and hydroxyl CEST contrast”. In: *Magnetic Resonance in Medicine* 85.2 (2021), pp. 1062–1078.

## Bibliography

- [157] Alan W. Bown. “CO<sub>2</sub> and intracellular pH”. In: *Plant, Cell & Environment* 8.6 (1985), pp. 459–465.
- [158] Donald E Woessner, Shanrong Zhang, Matthew E Merritt, and A Dean Sherry. “Numerical solution of the Bloch equations provides insights into the optimum design of PARACEST agents for MRI”. In: *Magnetic Resonance in Medicine: An Official Journal of the International Society for Magnetic Resonance in Medicine* 53.4 (2005), pp. 790–799.
- [159] Johannes Breitling, Andreas Korzowski, Neele Kempa, Philip S. Boyd, Daniel Paech, Heinz-Peter Schlemmer, Mark E. Ladd, et al. “Motion correction for 3D CEST imaging without direct water saturation artifacts”. In: *NMR in Biomedicine* (2022), e4720.
- [160] Jan-Rüdiger Schüre, Manoj Shrestha, Stella Breuer, Ralf Deichmann, Elke Hattungen, Marlies Wagner, and Ulrich Pilatus. “The pH sensitivity of APT-CEST using phosphorus spectroscopy as a reference method”. In: *NMR in Biomedicine* 32.11 (2019), e4125.
- [161] Steffen Goerke, Yannick Soehngen, Anagha Deshmane, Moritz Zaiss, Johannes Breitling, Philip S. Boyd, Kai Herz, et al. “Relaxation-compensated APT and rNOE CEST-MRI of human brain tumors at 3 T”. In: *Magnetic resonance in medicine* 82.2 (2019), pp. 622–632.
- [162] Johannes Breitling, Steffen Goerke, Jan-Eric Meissner, Andreas Korzowski, Patrick Schuenke, Mark E. Ladd, and Peter Bachert. “Steady-state CEST-MRI using a reduced saturation period”. In: *Proceedings of the 26th Annual Meeting of the International Society for Magnetic Resonance in Medicine* 26.2240 (2018).
- [163] Phillip Zhe Sun. “Quasi-steady-state chemical exchange saturation transfer (QUASS CEST) MRI analysis enables T<sub>1</sub> normalized CEST quantification—Insight into T<sub>1</sub> contribution to CEST measurement”. In: *Journal of Magnetic Resonance* 329 (2021), p. 107022.
- [164] Phillip Zhe Sun. “Quasi-steady-state CEST (QUASS CEST) solution improves the accuracy of CEST quantification: QUASS CEST MRI-based omega plot analysis”. In: *Magnetic Resonance in Medicine* 86.2 (2021), pp. 765–776.
- [165] Phillip Zhe Sun. “Quasi-steady state chemical exchange saturation transfer (QUASS CEST) analysis—correction of the finite relaxation delay and satura-

tion time for robust CEST measurement”. In: *Magnetic Resonance in Medicine* 85.6 (2021), pp. 3281–3289.



# List of Scientific Publications

I want to point out that parts of this thesis have already been published in the peer-reviewed journal article “Mapping intracellular pH in tumors using amide and guanidyl CEST-MRI at 9.4 T” [121] and the conference contribution “Presaturation pulse shape enables shifting the pH sensitivity of guanidyl CEST-MRI for absolute pH mapping at 9.4 T” [146].

## Journal articles

Breitling, Johannes; Korzowski, Andreas; Kempa, Neele; **Boyd, Philip S.**; Paech, Daniel; Schlemmer, Heinz-Peter; Ladd, Mark E.; Bachert, Peter and Goerke, Steffen: *Motion correction for 3D CEST imaging without direct water saturation artifacts*. NMR in Biomedicine. 2022, online, ahead of print. doi:10.1002/nbm.4720.

**Boyd, Philip S.**; Breitling, Johannes; Korzowski, Andreas; Zaiss, Moritz; Franke, Vanessa L.; Mueller-Decker, Karin; Glinka, Andrey; Ladd, Mark E.; Bachert, Peter and Goerke, Steffen: *Mapping intracellular pH in tumors using amide and guanidyl CEST-MRI at 9.4 T*. Magnetic Resonance in Medicine. 2022;87:2436–2452.

**Boyd, Philip S.**; Breitling, Johannes; Zimmermann, Ferdinand; Korzowski, Andreas; Zaiss, Moritz; Schuenke, Patrick; Weinfurtner, Nina; Schlemmer, Heinz-Peter; Ladd, Mark E.; Bachert, Peter; Paech, Daniel and Goerke, Steffen: *Dynamic Glucose-Enhanced (DGE) MRI in the human brain at 7 T with reduced motion-induced artifacts based on quantitative  $R_{1\rho}$  mapping*. Magnetic Resonance in Medicine. 2020;84:182–191.

Goerke, Steffen; Soehngen, Yannick; Deshmane, Anagha; Zaiss, Moritz; Breitling, Johannes; **Boyd, Philip S.**; Herz, Kai; Zimmermann, Ferdinand; Klika, Karel D.; Schlemmer, Heinz-Peter; Paech, Daniel; Ladd, Mark E. and Bachert, Peter: *Relaxation-compensated APT and rNOE CEST-MRI of human brain tumors at 3 T*. Magnetic Resonance in Medicine. 2019;82:622–632.

**Boyd, Philip S.;** Struve, Nina; Bach, Margund; Eberle, Jan Philipp; Gote, Martin; Schock, Florian; Cremer, Christoph; Kriegs, Malte and Hausmann, Michael: *Clustered localization of EGFRvIII in glioblastoma cells as detected by high precision localization microscopy*. *Nanoscale*. 2016; 8:20037–20047.

## Conference and workshop contributions

**Boyd, Philip S.;** Diederichs, Lilli; Breitling, Johannes; Ladd, Mark E.; Bachert, Peter and Goerke, Steffen: *Presaturation pulse shape enables shifting the pH sensitivity of guanidyl CEST-MRI for absolute pH mapping at 9.4 T*. Proceedings of the 30th Annual Meeting of the International Society for Magnetic Resonance in Medicine, London, UK 2022; Poster #2803. (Digital Poster | Video Presentation)

**Boyd, Philip S.;** Breitling, Johannes; Laier, Stephanie; Mueller-Decker, Karin; Glinka, Andrey; Ladd, Mark E.; Bachert, Peter and Goerke, Steffen: *Mapping of intracellular pH in vivo using amide and guanidyl CEST-MRI at 9.4 T*. Proceedings of the 29th Annual Meeting of the International Society for Magnetic Resonance in Medicine, Vancouver, Canada 2021; Poster #1463. (Digital Poster | Video Presentation)

Breitling, Johannes; Korzowski, Andreas; Kempa, Neele; **Boyd, Philip S.;** Ladd, Mark E.; Bachert, Peter and Goerke, Steffen: *Motion correction for 3D CEST imaging without direct water saturation artefacts*. Proceedings of the 29th Annual Meeting of the International Society for Magnetic Resonance in Medicine, Vancouver, Canada 2021; Poster #0146.

Franke, Vanessa L.; Platek, Justyna; **Boyd, Philip S.;** Laier, Stephanie; Mueller-Decker, Karin; Glinka, Andrey; Ladd, Mark E.; Goerke, Steffen; Bachert, Peter and Korzowski, Andreas: *<sup>31</sup>P MRSI in tumor-bearing mice at 9.4 T*. Proceedings of the 29th Annual Meeting of the International Society for Magnetic Resonance in Medicine, Vancouver, Canada 2021; Poster #0929.

**Boyd, Philip S.;** Breitling, Johannes; Laier, Stephanie; Mueller-Decker, Karin; Glinka, Andrey; Ladd, Mark E.; Bachert, Peter and Goerke, Steffen: *Concentration-independent mapping of absolute pH values in vivo using amide and guanidyl CEST-MRI at 9.4 T*. Proceedings of the 8th International Workshop on Chemical Exchange Satu-

ration Transfer Imaging, Atlanta, USA 2020; Oral Presentation #12. (Talk | Video Presentation)

Breitling, Johannes; Korzowski, Andreas; Kempa, Neele; **Boyd, Philip S.**; Ladd, Mark E.; Bachert, Peter and Goerke, Steffen: *Improved motion correction for CEST imaging by identifying and mitigating direct water saturation artefacts*. Proceedings of the 8th International Workshop on Chemical Exchange Saturation Transfer Imaging, Atlanta, USA 2020; Digital Poster #28.

**Boyd, Philip S.**; Breitling, Johannes; Ladd, Mark E.; Bachert, Peter and Goerke, Steffen: *Concentration-independent absolute pH mapping using amide CEST-MRI at 9.4 T*. Proceedings of the 28th Annual Meeting of the International Society for Magnetic Resonance in Medicine, Paris, France 2020; Poster #3128. (Digital Poster | Video Presentation)

**Boyd, Philip S.**; Breitling, Johannes; Zimmermann, Ferdinand; Korzowski, Andreas; Zaiss, Moritz; Schuenke, Patrick; Weinfurter, Nina; Schlemmer, Heinz-Peter; Ladd, Mark E.; Bachert, Peter; Paech, Daniel and Goerke, Steffen: *Acquisition protocol for glucoCESL MRI in the human brain at 7 T with reduced motion-induced artifacts*. Proceedings of the 27th Annual Meeting of the International Society for Magnetic Resonance in Medicine, Montreal, Canada 2019; Poster #5009. (Digital Poster)

Goerke, Steffen; Soehngen, Yannick; Deshmane, Anagha; Zaiss, Moritz; Breitling, Johannes; **Boyd, Philip S.**; Herz, Kai; Zimmermann, Ferdinand; Klika, Karel D.; Ladd, Mark E. and Bachert, Peter: *Relaxation-compensated APT and rNOE CEST-MRI of human brain tumors at 3 T*. Proceedings of the 27th Annual Meeting of the International Society for Magnetic Resonance in Medicine, Montreal, Canada 2019; Poster #4013. (Digital Poster)

Breitling, Johannes; Goerke, Steffen; Zaiss, Moritz, Soehngen, Yannick; Deshmane, Anagha; Herz, Kai; **Boyd, Philip S.**; Ladd, Mark E. and Bachert, Peter: *Optimized dualCEST-MRI for imaging of endogenous bulk mobile proteins in the human brain*. Proceedings of the 7th International Workshop on Chemical Exchange Saturation Transfer Imaging, Beijing, China 2018; Poster #4.



## Acknowledgements | Danksagung

A PhD is like a roller coaster – with plenty of ups and downs. Sometimes, quite frankly, *it can feel* like an impossible undertaking. Then again, at other times and fortunately far more often, *like the best adventure ever*. Throughout my entire PhD, from its initial idea to the final sentence of this dissertation, so many people have accompanied me on this journey in one way or another. Therefore, I would like to take this opportunity to thank everybody involved in this journey without whom this would not have been possible. I am very grateful for having received a great deal of support during this time and for everyone who made this a magnificent experience.

First and foremost, I would like to thank you, Prof. Peter Bachert, for offering me the opportunity to become your PhD student and prolong my scientific path as part of your research group after my masters degree. Thank you for your trust and continuous support, which allowed me to research this topic with plenty of freedom and, ultimately, experience this wonderful journey. Your enthusiasm for (NMR) physics really is contagious and I always enjoyed your physics – as well as non-physics – fun facts.

Moreover, I would like to thank you, Prof. Michael Hausmann, for taking the time and kindly accepting to be the second referee for my doctoral thesis. In particular, because I basically started my scientific path as a bachelor student in your group, it's a pleasure to be able to finish off my studies in this manner.

Steffen, thank you so much for everything you taught me during the last couple of years. Not only did you introduce me to the fascinating world of CEST and, in particular, pH imaging, but also basically showed me how to think like a real scientist. Thank you for your endless support, supervising me during this journey, nudging me into the right direction when I seemed to be lost and just being there as a tutor, motivator, critic and friend. Your and Moritz' preliminary work on pH imaging was the starting point of this whole adventure.

Andi and Johannes, thank you for all the fruitful ideas and considerations in countless brain-storming sessions as well as guiding advice helping me getting things to work. Thank you, Andi, for supervising me in the final months of my thesis and for all the valuable conversations.

Steffi, Melanie, Renate, Julia, Karin and Andrey, I would like to thank you for your help in realizing the mice examinations and cell culturing. Not a single in vivo measurement would have been possible without you, thanks for the great collaboration. In this regard, I would also like to acknowledge the contribution of all mice to this research project.

Roland, Martha, Dima, Inna, Viktoria and Manfred, I would like to thank you for realizing the glucoCESL-MRI mice examinations which, unfortunately, could not be completed before writing up this thesis. Thanks for the great collaboration and I'm looking forward to the final examinations.

In addition, I would like to thank the Deutsche Forschungsgemeinschaft (DFG) for their generous financial support over the past three years (DFG; GO 2172/1-1).

A special thank you goes to my entire research group including all former colleagues, i.e. the real Speki-CESTler, for your support, constructive criticism, creative insights and, most notably, for the awesome atmosphere within the group. In particular, I want to thank you, Vanessa, for joining my on this sometimes crazy roller coaster ride and just for being a great work spouse. Each and every one of you made this journey so much more enjoyable and I could (almost always) count on a relaxed and friendly environment, thank you guys for all the good vibes. :-)

Also, I would like to thank all my friends for accompanying me during, but also before and hopefully until long after this thesis. Thanks for just being yourself and all the great times we have together – I know that I can always count on you – you're the best!

Finally, I would like to thank my whole family and, in particular, my parents. Thank you for your enduring encouragement, continuous empathy and universal support. And Ines, I want to thank you from the bottom of my heart for the best support I could have ever imagined. Thank you for always being by my side, your motivation, patience and love.

# Declaration | Erklärung

I, hereby, affirm that I have written this work independently and without the use of resources and media other than those quoted.

Ich versichere hiermit, dass ich diese Arbeit selbstständig verfasst habe und keine anderen als die angegebenen Quellen und Hilfsmittel benutzt habe.

Heidelberg, den .....

.....

Philip Sebastian Boyd

